Generation and interaction of suprathermal electrons in inertial confinement fusion

Edoardo Rovere

université de BORDEAUX

THESIS

SUBMITTED IN PARTIAL FULFILLMENT OF THE REQUIREMENTS
FOR THE DEGREE OF

Doctor of Philosophy in Plasma Physics

UNIVERSITÉ DE BORDEAUX, ÉCOLE DOCTORALE DES SCIENCES ET DE L'INGÉNIEUR
SECTION : ASTROPHYSIQUE, PLASMAS, NUCLÉAIRE

GÉNÉRATION ET INTERACTION DES ÉLECTRONS SUPRA-THERMIQUES EN FUSION PAR CONFINEMENT INERTIEL

GENERATION AND INTERACTION OF SUPRATHERMAL ELECTRONS IN INERTIAL CONFINEMENT FUSION

---

by

Edoardo Rovere

supervised by

Ph. Nicolaï

A. Casner

A. Colaïtis

Defended the 7th June 2023, Talence (France)
Board of examiners:

Hüller, S.	Research Director, CPHT (Paris)	**Reviewer**
Palastro, J. M.	Senior Scientist, LLE Rochester (US)	**Reviewer**
Depierreux, S.	Research Engineer, CEA (Arpajon)	**Examiner**
D'Humieres, E.	Professor, CELIA	**Examiner**
Nicolaï, Ph.	Research Director, University of Bordeaux	**Director**
Casner, A.	Research Director, CEA (Le Barp)	**CoDirector**
Colaitis, A.	Researcher, Université de Bordeaux, CNRS, CELIA	**Invited**

Communications related to this thesis

Several parts of this work have been communicated to the scientific community. We give here a list of the publications in peer-reviewed journals, alongside a list of presentations in conferences.

List of publications:

- E.Rovere, A.Colaïtis, R.K.Follett and A.Casner, *Hot electron scaling for two-plasmon decay in ICF plasmas*. In: Physics of Plasmas Vol. 30, 042104 (2023). doi: 10.1063/5.0128052. eprint: https://doi.org/10.1063/5.0128052. url: https://doi.org/10.1063/5.0128052.

List of first author presentations at conferences:

- Oral presentation (virtual) at 48^{th} Edition for the European Physical Society, 27^{th} June - 1^{st} July, 2022. *"Scaling of hot electron generation for two-plasmon decay in ICF plasmas"*.
- Oral presentation (live) at 50^{th} Edition Anomalous Absorption Conference, Pennsylvania (US), 6^{th} - 10^{th} June, 2022. *"Scaling of hot electron generation for two-plasmon decay in ICF plasmas"*.
- Oral presentation (virtual) at 63^{rd} Edition for the American Physics Society, Division of Plasma Physics, 8^{th} - 12^{th} November, 2021. *"Scaling of hot electron generation mechanisms from two-plasmon decay in ICF plasmas"*.
- Oral presentation (live) at 11^{th} Edition Forum ILP, Corsica (FR), 27^{th} September - 1^{st} October, 2021. *"Scaling of hot electron generation mechanisms from two-plasmon decay in ICF plasmas"*.
- Oral presenation (virtual) at 16^{th} Edition Direct Drive and Fast Ignition Workshop, 22^{nd} - 24^{th} March, 2021. *"Hot electron generation from the two-plasmon decay laser-plasma instability"*.
- Poster presentation at The Royal Society, London (UK), 2^{nd} - 3^{rd} March, 2020. *"Modeling of hot electron generation in hydrodynamic codes"*.

Acknowledgements

Looking back, when people asked me "what do you want to do when you grow up?", I would have given them a different answer than "nuclear fusion". In elementary school, my first preferences were mineralogy and archeology. However, since middle school I met extraordinary people who pivoted my interest towards energy production, all the way to university, which made me narrow down the field I would have decided to partake more and more. These people, Paola Aimon (middle school), Salvatore Mattina (high school) and Matteo Passoni (university), are the ones I would like to thank first. It was fascinating to study the exploitation of the natural resources we have available around us and turn them into the lifeblood of society, electricity. It was fascinating to learn about giant machines built with astounding precision, and the extreme conditions in which they are designed for, great feats of human ingenuity. Now, after completing my PhD in a field at the very cutting edge of said ingenuity, where temperatures of tens of millions of degrees Celsius occur in the span of picoseconds and at the scale of millimeters, I am convinced I took the right decision in pursuing this career, and I have to thank the people that supported me in this journey for it.

From the people I worked with, first of all I would like to thank Alexis Casner, my previous thesis director, that offered me this opportunity. I will remember the many advice he gave me when the PhD started to become tougher, during my first paper and thesis redactions, and I will always remember his passion for science and for reading scientific papers, which he tried to share with me in more than one occasion.

The second person I would like to thank is Arnaud Colaïtis, my thesis supervisor. He was the one who suggested this PhD experience, and I am thankful for the dedication and seriousness in how he followed me. I will remember his wide scientific knowledge and flexibility in problem-solving, and I thank him for the many times I came to his office asking him questions, for which he was always available to answer. I also want to thank him for pushing me into attending multiple conferences and presenting my work to the scientific community on multiple occasions, as well as writing my first scientific paper, and to patiently listen to all my concerns while I was writing. Aside from work, I also discovered we had similar hobbies, and I thank him for the evenings spent together with half of the lab's nuclear fusion PhDs and postdocs to play Dungeons and Dragons together ;) . It has been a pleasure working and knowing him, and I hope I could work with him again in the future.

I also would like to thank Philippe Nicolaï for taking the role of thesis director after Alexis had to leave CELIA, as well as his help in organizing the defense committee, supervising the thesis work and presentation. Moreover, I thank him for encouraging me to speak a bit more of French at the lab.

Then I would like to thank the people that I met and discussed with during my PhD: I would like to thank Olimpia Budriga for her willingness to help to perform PIC simulations to confront with my results. Moreover, special thanks to Russell Follett, with which I discussed much about the simulation code used in my work and for being co-author for my first scientific paper, and

Vladimir Tikhonchuk, with which I had many discussions about plasma physics theory. I am sure their help and insight improved the quality of the work.

I would like to thank the jury members: the reviewers Stefan Huller, John M. Palastro, as well as the examiners Sylvie Depierreux and Emmanuel D'Humieres, which I am honored to have presented my work to. Particularly, I thank the reviewers Huller and Palastro for the time taken to read and correct the manuscript, and to Emmanuel D'Humieres for presenting to me and Arnaud Olimpia, and to organize our meetings to obtain the PIC simulations. Also, many thanks for Sylvie Depierreux not only for providing a more experimental approach to my work in the defense questions, but also for suggesting where to find suitable opportunities for a postdoc after the defense.

Moreover, I would like to thank all my colleagues and friends at CELIA, both postdocs and PhDs at the time. Alessandro Tentori and Paul Lageyre, with which I had some interesting discussions of science, politics and much more (e comunque Ale, io rimango dell'opinione che la musica trash dei primi anni 2000 non si puo' sentire!), Donaldi Mancelli, for his shenanigans and for being the "mischievous soul" of the lab (and the one who dragged me out of my shell to go drink with the others), but also for his professionality when working, Thibault Goudal and Victorien Bouffetier for their availability and help when I was a rookie in another country, looking to set up my bank account and find a home; without you I don't know what I would have done, thank you. Luke Ceurvorst, I hope you are doing great at Rochester; Lena, Alexandre, Corisande, Adrien, Stephane, Gabriele, Pedro, Thomas, Micha, Gabriel, Francesco, (Jesus) Christos, Phillip, Alana and all the others. Special thanks to Diego Viala and Romain Liotard, to which I wish an amazing thesis defense, and to Duncan Barlow to which I whish a good continuation of his career to the last one.

I wish to thank the two friends I made in Bordeaux outside of the laboratory, Vincent and Yann, to who I wish the best in life, work, good card draws and Nat 20s.

Finally, I would like to thank my most special people, my family. My father Ivano and my mother Emanuela, for encouraging and supporting this path that I chose even since before I entered university. I would not be sure if I would have made it here without their support, and for that I will be forever thankful. I would like to thank my sister Beatrice, who completed her studies during this period, for keeping an eye on our family while I was gone, and to which I wish the best for her future career. Special thanks to my grandmother Rosalinda, who prays for our wellbeing every time she hears me and my sister have something difficult going on, and even to my dog Tobia for having been a good boy while I was away.

Contents

Chapter 1

Introduction

1.1 Controlled fusion

1.1.1 Context

In recent years, controlled *Inertial Confinement Fusion* (ICF) has gained increased interest in the light of experiments carried out at the *National Ignition Facility* (NIF) at the Lawrence Livermore National Laboratories (California, US). In particular, the implosion experiment *N210808* [1, 2] produced a fusion yield of 1.37 MJ, compared to the 1.9 MJ injected from the facility's laser assembly. This was 8 times higher than the previous shot, and taking into account the losses, it overcame the threshold for *scientific ignition*, for which the fusion energy is higher than the on-target laser energy. While the *engineering yield* for ignition (defined with respect to the electric power injected in the machine) is still far from being close to unity, this experiment is an important milestone for a future development of nuclear fusion for the purpose of energy production. Reasons for this achievement were the outstanding quality of the target, with a low number of imperfections such as "pits" and "voids", and a high control of the low mode symmetry of the laser drive. This shot has been followed by a second one, *N221213*, which further confirmed the overcoming of the scientific threshold.

These experiments are the current state of the art of ICF. This branch of research started immediately after the invention of the laser in 1957, when a proposal for a particular application appeared at the "Atoms for Peace" conference during the same year. This proposal was about using focused laser light as the drive to initiate thermonuclear fusion reactions, and it was a natural evolution after a period in which ICF was used for military applications, with the first ICF devices being hydrogen bombs invented in 1950. However, while hydrogen bombs use an X-Ray source such as fission reactions of radioactive plutonium, the invention of the laser opened the doors for a peaceful utilization of nuclear fusion reactions for the purpose of energy production, as was then proposed by J. Nuckolls in 1972 [3]. This was particularly attractive due to the high availability of the fuel (mainly deuterium) and the high theoretical yield. After 63 years from its proposal, the field of study called *Inertial Confinement Fusion* (ICF) developed a wide landscape of theoretical ground, encompassing fields such as the physics of solids, laser and plasma physics, hydrodynamics and more. Moreover, from a practical point of view, the construction of the laser systems, the realization of the ICF capsules and the facility itself, imply a wide field of studying from an engineering point of view. Finally, the realization of modern computers and its rapidly expanding innovation through *supercomputers* and *High Performance Computing* (HPC) in general opened the opportunity for simulations of complex ICF problems using increasingly more powerful computational capabilities, allowing for the description of phenomena both at "macroscopic" scales (millimeters and laser pulse duration of the order of nanoseconds) through a wide array of *hydrodynamic codes*, and "microscopic" scales (order of μm and ps) through *Particle-in-Cell* (PIC) and other reduced-scale codes.

Theoretical studies, simulations and experiments allow the study of physical phenomena such as the ICF target life cycle [4, 5], developing of shock waves, and the attempt at solving phenomena detrimental to the ICF target implosion, development of hydrodynamic instabilities the likes of *Rayleigh-Taylor* [6, 7, 8, 9], and more. The aforementioned phenomena occur at macroscopic scales, and are studied accordingly.

Moreover, ICF scenarios are characterized by *laser interaction parameters* $I\lambda^2$ (where I is the laser intensity and λ is the laser wavelength) in the range of $I\lambda^2 \simeq 10^{13} - 10^{16}$ Wμm^2/cm^2, with pulse durations of the order of $t_{pulse} \simeq 0.1 - 10$ ns. At these intensities, strong non-linear laser-plasma coupling can occur [10]. This is the field of study of *laser-plasma interactions*, and it encompasses a vast array of physical phenomena such as filamentation [11, 12, 13], *Cross-Beam Energy Transfer* (CBET) [14, 15, 16], laser-plasma instabilities [17, 18, 19, 20] such as *Stimulated Raman Scattering* (SRS) [21, 22, 23], *Two Plasmon Decay* (TPD) [24, 25, 26, 27, 28], and *Stimulated Brillouin Scattering* (SBS) [18, 29, 30, 31, 32]. Other studies of laser-plasma interactions include the kinetic effects such as the arising of a population of high energy electrons [33, 34, 35, 36], also called *hot electrons* (HEs), and development of plasma turbulence, both "weak", through secondary instabilities such as *Langmuir Decay Instability* (LDI) [37, 38, 39], and "strong", through the excitation of density depressions in the plasma profile called *cavitons*, which trap the plasma waves produced by the instabilities [40, 41] in a process called *Langmuir wave (LW) collapse* or *cavitation*.

The main purpose of this work is to investigate and characterize the hot electron generation in such plasmas. Their production mainly occurs via energy transfer from *Electron Plasma Waves* (EPWs) through a particular set of laser-plasma instabilities (LPIs) called *parametric instabilities*. These class of instabilities encompass the above-mentioned SRS, TPD and SBS, as well as the LDI instability, and they are characterized by an initial "pump" wave decaying into two "product" waves under certain matching conditions both in wave frequency and wave vector. Moreover, plasma turbulence in the form of LW collapse can lead to formation of density cavities, trapping the product EPWs. These cavities can generate HEs when the electrons passing within are able to resonate with the trapped EPW, weakening the field sustaining the cavity until it eventually collapses, leading to strong plasma turbulence. Overall, while the presence of a HE population could be beneficial in some ICF schemes (such as in *Shock Ignition* (SI), where they can enhance the ignitor shock pressure [42, 43, 44]), they are mainly a cause of concern, where their propagation can cause preheat of the ICF target, preventing its compression. In the SI scheme, this is especially detrimental due to the high values of $I\lambda^2$, leading to strong nonlinear laser-plasma couplings, with a copious amount of HEs produced. Therefore, the investigation of hot electron generation is of great importance for the feasibility of ICF, with the goal of studying their propagation afterwards and formulating mitigation and control strategies.

The instabilities previously mentioned have been extensively studied from a theoretical point of view [45, 46, 47]. The state-of-the-art literature on the topic of HE generation and propagation, is oriented towards several main goals; the investigation of HE generation in an experimental context, by measuring the signature of HE generation through hard X-Ray detectors [48, 49], with the consideration of different ICF target materials and the effects of adding *Smoothing by Spectral Dispersion* (SSD) to the laser light [43]; the measurement of the effects of preheat of the capsule [50, 51]; and the measurement and scaling of HE generation for different laser drive intensities [52, 53]. From the simulation point of view, the objective is to match more closely the experimental data, by the addition of more sophisticated phenomena such as SSD to the simulations [43], the effects on the parametric instabilities when multi-beam irradiation of the laser target take place [23, 54, 55], polarization effects [56], simulations at short and long density scale lengths [57]. Regarding the propagation of the generated HEs [58], Monte Carlo simulations [59] have been carried out in order to predict their propagation in the coronal plasma towards the ICF target. These simulations use several codes, from microscopic PIC codes such as EPOCH [60], Monte Carlo codes such as GEANT4 [61], and hybrid codes such as LPSE, the code used

in this work [62]. Another type of study has been to select a set of key laser-plasma conditions, from which simulations can be performed to extract HE quantities, in order to possibly develop predictive scaling laws. This has been done in the works of [43, 53, 63, 64, 65].

While HE generation is a cause of concern for fuel preheat, which worsen the target compressibility, the timing of HEs impacting the fuel can also provide beneficial effects to the compression in alternative ICF schemes. Therefore, the study of the HE population propagation and behavior at macroscopic scales (i.e. $\sim 10^{-3}$ m) is of great importance for the life of the ICF target, and it is necessary to provide a HE generation model in the form of databases and scaling laws obtained with reduced-scale codes, which can then be plugged into macroscopic hydrodynamic codes as inputs for HE propagation analysis.

Following such studies, a scaling analysis is proposed in this work for the SRS and TPD processes in 2D in a plasma irradiated by a single plane-wave laser beam in p-polarization, with variations of four laser plasma conditions (*electron plasma temperature* T_e, *ion-electron temperature ratio* T_i/T_e, *density scale length* L_n and *drive strength* η) for the derived hot electron quantities (*energy flux* Φ_{HE}, *conversion fraction* f_{HE} and *average temperature* T_{HE}), with the aim to build a database for such HE quantities mapped with the chosen laser-plasma conditions.

1.1.2 Principles of fusion devices

Fusion reactions are obtained when two ionized nuclei have enough energy to overcome the Coulomb force barrier they generate. After such potential barrier is overcome, at distances of the order of 1fm $\simeq 10^{-15}$m, another fundamental interaction called *strong force* takes over with a net attractive force that pulls the two nuclei together. This phenomenon is called *nuclear fusion*, and when the two nuclei join together, expulsion of matter (either neutrons or protons) and radiation (such as γ rays) occur, and energy is liberated in the fusion process. The most common fusion reaction in ICF is the one between *deuterium* and *tritium* (D-T), two hydrogen isotopes, resulting into [5]:

$$ {}^{2}_{1}\mathrm{D} + {}^{3}_{1}\mathrm{T} \rightarrow {}^{4}_{2}\mathrm{He}(3.5\ \mathrm{MeV}) + {}^{1}_{0}n(14.1\ \mathrm{MeV}), \tag{1.1} $$

where the energy liberated by the reaction because of the *mass defect law* [66] is partitioned between the newly formed helium nucleus (or *alpha particle*) and the emitted neutron. The easiest region to overcome the Coulomb barrier is for energies of ~ 300 keV. However, due to tunnel effect, reactions can occur even at lower energies, albeit at a reduced probability. There are other possible fusion reactions, the second most relevant here being the *deuterium-deuterium* (D-D) reaction, with a much lower cross section. While the energies required to achieve fusion reactions are of the order of hundreds of keV, a Maxwell-Boltzmann population with an average temperature of the order of ~ 10 keV can lead to significant reactions through the tail of the distribution. Therefore, a nuclei population that can undergo nuclear fusion reactions must possess an average temperature of the order of 10^8 K. At these temperatures, the constituents are found in form of a *plasma*, a state of matter in which electrons and nucleis' thermal velocities are much larger than their binding energy, allowing them to be separated in a population of individually charged particles.

These extreme conditions must be maintained in a localized region of space until the *fuel* (i.e. D-T or D-D) burns sufficiently. Due to the prohibitive temperatures achieved (for comparison, the center of the Sun possesses an estimated temperature of $\simeq 15 \times 10^6$ K), it is impossible to contain such a state of matter using material walls, and due to the thermal losses that would incur through heat propagation if it were in contact with a colder gas (such as air). The most efficient way is therefore to confine the locally charged plasma in a vacuum chamber (minimal heat transfer), either using magnetic fields (*Magnetic Confinement Fusion* or MCF) or using the mass inertia of a solid target (*Inertial Confinement Fusion* or ICF). Due to the different methods of confinement, facilities dedicated to MCF and ICF are fundamentally different.

The machines used in MCF use a toroidal shaped vacuum chamber surrounded by coils traversed by a current, producing both toroidal and poloidal fields that confine the plasma in a "donut" shape (or, more appropriately, a *torus*). These fields drive an initially neutral gas injected in the chamber that is heated up to the state of plasma by means of injection of neutral beams of particles or by stimulating harmonics of the electron and ion cyclotron frequencies. The magnetic fields of the coils oppose the plasma pressure that induces the plasma donut to expand, keeping it confined. The main advantage of MCF is having high confinement times, of the order of seconds, therefore raising the probability of fusion reactions albeit using low density gases in the chamber. However, these machines essentially work similarly to a transformer, with the primary being the magnetic coils and the secondary being the plasma in the chamber, following the Faraday-Neumann-Lenz law of the Maxwell equations. Therefore, present tokamaks cannot work in a continuous regime, but only when a gradient of electric field is applied to the coils. Moreover, the shape of the magnetic field lines induce drifting of particles towards the outer walls of the chamber. In order to solve this last problem, similar machines called *stellarators* have been realized, whose vacuum chamber shape and coils naturally follow the shape of the magnetic field lines. This eliminates particle drift, but the odd shape of the chamber increases building costs and assembling time.

The machines used in ICF use a solid fuel target covered by an outer shell of mid-Z material called *ablator*, and a gaseous core inside the inner shell, both composed by the desired fuel. A set of lasers uniformly irradiate the target, their high intensity ablating the outer shell and generating a pressure in the inner shell that pushes the fuel inward, therefore imploding onto itself. This *target implosion* compresses the gas fuel within the core, dramatically increasing density and temperature in its center, to the point of the formation of a *hot-spot* in which fusion reactions occur. The heating provided by the emitted α particles then deposit their energy in the outer dense fuel, triggering more reactions, until burning most of the fuel target. The confinement here is provided by the material shell inertia during the compression and ignition phases, which is feasible due to the high densities of the ICF targets, and allows for time duration of the order of nanoseconds for the entire process. The various ignition schemes will be discussed in more detail in the following sections.

Both schemes aim to achieve *ignition*, which is defined by reaching the limit of different figures of merit for each confinement method [4]. For MCF, the efficiency of the reactor Q is given by:

$$Q = \frac{P_{fus}}{P_{aux}}, \tag{1.2}$$

where P_{fus} is a theoretical constant output power in a steady state reactor, and P_{aux} is the power delivered to the plasma to maintain operating conditions, and compensating for the power losses. In this case, ignition is achieved when the α particles emitted by nuclear fusion deposit their energy in the surrounding plasma, heating it up to the ideal point where P_{aux} can be reduced to zero. In that, $\mathrm{Q} \to \infty$ is the so called *thermonuclear ignition* condition, where the heat produced by the fusion products keeps the reactions going and only spent fuel must be replaced by fresh fuel. In ICF, the figure of merit used is the *target energy gain*:

$$G = \frac{E_{fus}}{E_d}, \tag{1.3}$$

where E_{fus} is the energy released by the target, and E_d is the energy delivered to it by the driving laser beam in a short, powerful pulse. In order to achieve ignition feasible for power production, $\mathrm{G} \geq 30 - 100$. To make a comparison, NIF shot N221213 reached an energy gain of $\mathrm{G} = 1.54$.

A condition on ignition can be obtained by looking at the *Lawson criterion*, proposed by J.D. Lawson in 1957 [67] through the calculation of the energy balance of a fusion reaction, with the approximation of neglecting the losses by bremsstrahlung. Assuming a globally neutral

plasma (i.e. $n_e = n_i = n$, where $n_{e,i}$ is the electron/ion number density) as an ideal gas, the energy for a plasma at the average temperature T (in keV) corresponds to $\mathrm{E_k} = 3nTV$, where V is the volume of the system. We define the *energy confinement time* as $\tau_E \equiv E_k/P_{loss}$, where P_{loss} are the power losses of the system. Therefore, the power output generated by the system P_{out} must overcome the power lost P_{loss}, or in other words the temperature required for heating the plasma, in order to obtain a positive gain $P_{out}\tau_E > P_{loss}\tau_E = 3nTV$. Overall, for MCF the Lawson criterion can be written as:

$$n\tau_E T \simeq 3.3 \times 10^{15} \text{ [cm}^{-3} \text{ s keV]}, \tag{1.4}$$

with $8 < \mathrm{T} < 25$ keV, n_e being low ($\sim 10^{10}$ cm^{-3}) and τ_E being high ($\sim s$) in MCF. In ICF, the Lawson criterion can be expressed in a different form; the energy confinement time τ_E can be rewritten as a function of the material density ρ and the fuel radius R_f:

$$n\tau_E = \frac{1}{m_f c_s}\rho R_f, \tag{1.5}$$

with $c_s \equiv \sqrt{2T/m_f}$ being the isothermal sound velocity of the fuel (the temperature T is in eV). With this, the Lawson criterion for achieving ignition in ICF becomes:

$$\rho R_f T > 6 \left(\frac{\rho}{\rho_c}\right)^{\frac{1}{2}} \text{ [g cm}^{-2} \text{ keV]}, \tag{1.6}$$

where ρ_c is the critical density. The range of plasma temperatures to achieve this condition is $5 < T < 15$ keV. ρR_f, defined as *areal density*, is a relevant quantity in ICF, measured in g/cm^2.

1.1.3 Inertial confinement fusion and ignition schemes

We will now focus mainly on the ICF scheme. The fraction of burnt fuel can be expressed as:

$$\Phi \simeq \frac{\rho R_f}{H_B + \rho R_f}, \quad H_B \equiv \frac{8 c_s m_f}{\langle \sigma v \rangle}, \tag{1.7}$$

where H_B is defined as the *burn parameter*, depending on the average value $\langle \sigma v \rangle$, where σ is the material cross section. Eq. 1.7 shows that, in order to burn half of the fuel, ρR_f (and, by extension $n\tau_E$) is of the order of $2/\langle \sigma v \rangle$, which ties to the Lawson criterion by maximizing the areal density by either making the ICF target more dense, or larger.

Given a sphere of material, one can express the areal density as $\rho R_f = (3/(4\pi))^{1/3} m_f^{1/3} \rho^{2/3}$. Therefore two cases can occur: either requiring the fuel mass to be fixed and increase the density of the ICF target above solid density, or keep the same areal density (i.e. the same burning fraction Φ) and decrease the required fuel mass (which leads to less energy required to reach the desired temperatures). In ICF, the first option is the one considered, where the ICF target starts with solid-like densities, and it is then increased to values higher than solids.

This is achieved by irradiating a sphere of material composed of an outer ablative shell and an inner solid shell with a gaseous core, both made of fuel. As shown in Fig. 1.1, the laser beams ablate the outer shell, generating an overall inward force that compresses the fuel. This compression increases the density in the gaseous target towards the desired values of ρR_f, going from ~ 0.5 g/cm^2 to 50 g/cm^2, with an increase in density by a factor of ~ 100. The increase in density raises the temperature at the center of the ICF target's gaseous core, thereby creating a *hot-spot* in which nuclear reactions occur. This requires pressures in the hot-spot of the order of 100 GBar. The α heating then extends the *ignition front* by triggering further nuclear reactions away from the center in the dense fuel, increasing the burning fraction. This is the simplest ICF ignition scheme, called *hot-spot scheme*.

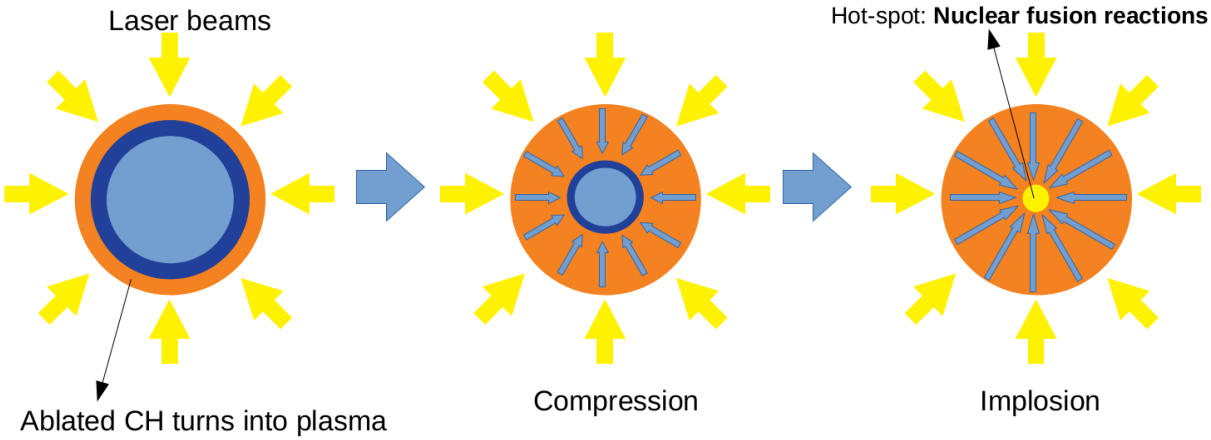

Figure 1.1: Hot spot ignition scheme.

The target acceleration and compression is due to the *ablation pressure* generated by the laser beams heating the outer target shell:

$$P_{abl} = 57(\eta_{abs}\frac{I_{15,W/cm^2}}{\lambda_{las,\mu m}})^{\frac{2}{3}}, \tag{1.8}$$

where η_{abs} is the fraction of absorbed laser energy, $I_{15,W/cm^2}$ is the laser intensity in vacuum (in units of 10^{15} W/cm^2) and $\lambda_{las,\mu m}$ is the laser wavelength in μm. At the critical density ρ_c, the laser light is reflected and the flow velocity and the acoustic velocity previously defined are equal, so that, we obtain: $\dot{m}_{abl}c_s \simeq \rho_c c_s^2 \simeq P_{abl} \propto (I/\lambda_{las})^{2/3}$, where $\dot{m}_{abl}$ is the *ablation mass rate*. Therefore, an increase in $\dot{m}_{abl}$ can be achieved either by using more intense lasers or by decreasing the wavelength.

The *implosion velocity* of the ICF target (i.e. the velocity of the shell during compression) is given by $u_{impl} \simeq \dot{m}_{abl}a_R/\rho$, where $a_R \equiv R_f/\Delta R_f$ is the *in-flight aspect ratio*, defined as the ratio between the outer shell and its thickness. The term "in-flight" refers to the profile of a_R, which changes during the compression of the fuel. One can therefore find the *convergence ratio* of the target, measuring the ratio of the initial radius of a certain interface (be it the outer or inner shell radius) to the radius of the same interface after compression has taken place and the shell stops converging, in a situation defined as *stagnation*. This quantity is given by:

$$C = \frac{u_{impl}}{\rho^{1/3}(\alpha A_f a_R)^{1/2}} = \frac{\dot{m}_{abl}a_R^{1/2}}{\rho^{4/3}(\alpha A_f)^{1/2}}, \tag{1.9}$$

where A_f is the nuclear mass of the fuel, and α is the *adiabat* of the reaction, defined as the ratio of the shell pressure and the Fermi pressure [5]. For DT fuel, this is given by:

$$\alpha \simeq \frac{P_{shell}}{2.2\rho^{5/2}}. \tag{1.10}$$

Equation 1.9 is very important for the design of an ignition scheme. The required pulse energy E_p in an ICF system can be shown to scale with the convergence ratio as $E_p \propto C^{-6}$ [4]. Therefore, the control of the convergence ratio is important for ICF design concerns. From Eq. 1.9, one can obtain high values of C by changing several parameters: for one, high C can be achieved by having high implosion velocities u_{impl}, meaning a higher ablation mass rate and therefore a higher laser intensity (which will drive a higher ablation pressure). Another method would be to keep the adiabat as low as possible, which means that the shell pressure must be low and therefore the target must be compressed as isentropically as possible. The last method would be to use a high in flight aspect ratio. Maximizing these quantities entails several issues. First,

increasing the in flight aspect ratio means making the shell thinner. A thinner target does not require high laser intensities, but during the *deceleration phase* (i.e. the moment after the shell accelerating towards the center and before stagnation), the arising of hydrodynamic instabilities such as Rayleigh-Taylor Instabilities may break apart the shell. Increasing instead the laser intensity and therefore the ablation pressure and mass rate would lead to strongly nonlinear laser-plasma couplings, some of which can transfer energy to the electron plasma population resulting in the emission of high-energy "hot" electrons (HEs). This *target preheating* by HEs modifies the adiabat, increasing it during compression, therefore worsening the convergence ratio and increasing the pulse energy required for achieving ignition. Moreover, the target preheating may lead to an anomalous heating of the inner shell, which can lead to colder fuel mixing with the hotter fuel at the center [58].

1.1.4 ICF schemes and their relation with Hot Electron generation

Up to now, we considered only the most common hot-spot ignition scheme. This scheme presents a laser pulse irradiating the fuel target, with peak laser intensities of the order of $I \simeq 10^{14} - 10^{15}$ W/cm^2. This scheme relies entirely on a single laser pulse in order to shape the target compression and its subsequent ignition. Therefore, an idea would be to decouple the compression and ignition phases by using two laser pulses to deliver energy to the target. A low energy pulse would deliver the energy in the compression phase; due to its lower energy, the work pdV exerted on the ICF capsule would be insufficient to ignite the hot-spot. After the target has been compressed, the energy must be delivered for ignition. The method used for delivering such energy distinguishes between the two alternative ignition schemes.

In *Shock Ignition* (SI) [42, 68, 69], a second, high intensity laser pulse is launched, of the order of $I \sim 10^{15} - 10^{16}$ W/cm^2, generating a shock wave that propagates in the capsule towards the center. This shock is timed so that the *ignitor shock* traveling towards the center (whose pressure is increasing due to its convergence) collides with the return shock caused by the compression pulse in the dense target, after having bounced at the center. When these two shocks collide, the result is an enhanced converging shock that then ignites the hot-spot. Moreover, the overall weaker rebounding shocks raises the density in the inner shell, and therefore the areal density ρR_f. This helps preventing α particles from leaving the target, facilitating the propagation of the burn wave. The main advantages of this scheme are the lower implosion velocity (i.e. less susceptibility to the Rayleigh-Taylor instability), and the lower total energy required, thus allowing for higher gains. However, the high intensity that drives the ignition phase is more prone to nonlinear coupling with the coronal plasma. This implies a stronger development of laser-plasma instabilities, and a copious amount of hot electrons generated towards the target. Several experiments [43, 48, 49] and simulations [57, 58] showed that there is the possibility of this HE population to provide a beneficial effect to the ignition as a whole. If the electrons collide against a denser ICF shell due to the propagating rebounding shock, the denser fuel shell could be enough to stop the electrons, therefore enhancing the ablation pressure and the overall convergence ratio, and enhancing the ignitor shock pressure. This timing is governed by the average energy of the traveling HEs, which needs to be low enough for the rebounding shock to sufficiently increase the shell density. The HE energy threshold above which preheat is a concern is not clearly defined, but generally assumed in the literature [57] to be around 100 keV. If the HEs overcome this threshold, they possess enough energy to impact the target before the shell increases in density due to the rebound shock. If that is the case, HEs are more likely to deposit their energy in deeper layers of the shell, causing fuel preheat and mixing.

In *fast ignition* [70, 71], after boring a hole towards the center of the capsule, the energy delivery of the ignition phase is given by a flux of hot electrons which are produced, among other phenomena, by laser-plasma instabilities. In this case, HE generation is highly desirable, since it is the main driving process to ignition. Due to the more direct energy delivery, this scheme lowers the issues of the development of hydrodynamic instabilities in the target, as well

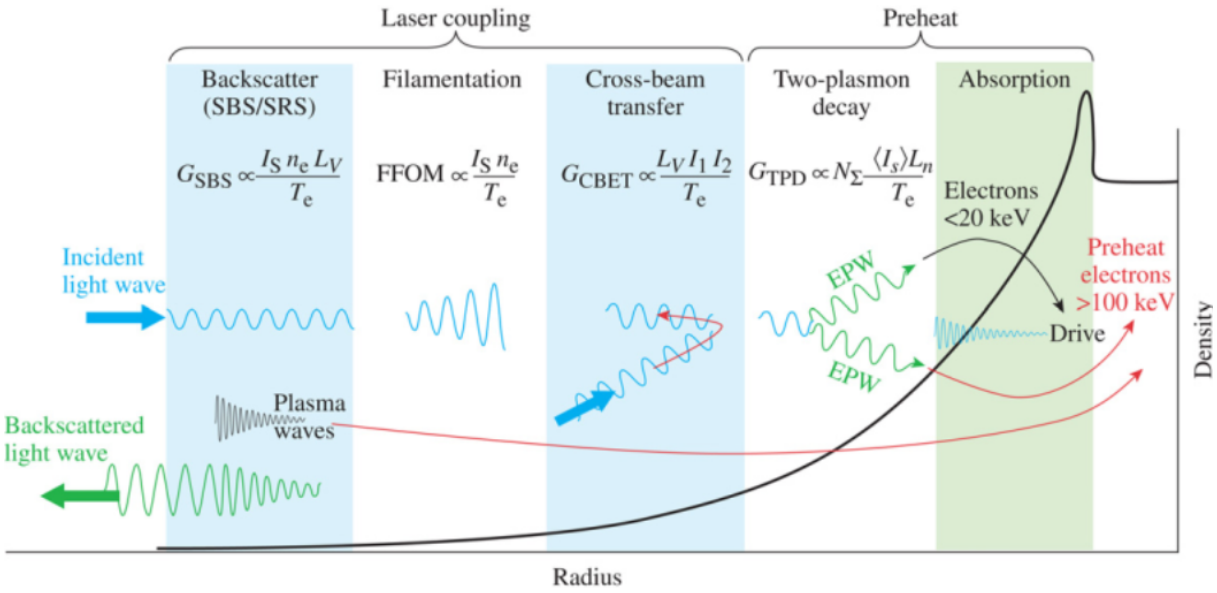

Figure 1.2: Development of laser plasma interactions in the coronal plasma (left is vacuum, right is the ICF target). Image taken from [72].

as propagation of shock waves. However, it is challenging to build the complex ICF target that allows for the electrons to transfer energy towards the target's center, to realize ultra-high intensity lasers required to generate the necessary HE population, and to keep the generated HEs focused enough for them to deposit energy in the hot-spot.

1.2 Laser plasma interactions

The interaction between a high-intensity laser and the outer shell of the ICF target proceeds to create a region of plasma around the ICF target called *coronal plasma*. The coronal plasma possesses an increased density the closer to the ICF target, in which the laser propagates until a *critical density* n_c is reached. It is defined as the density at which the electrons oscillating at the laser frequency generate a field strong enough that the laser waves cannot propagate beyond this density. The laser energy is mostly absorbed through *inverse bremsstrahlung* [4, 34] by the electrons, which quickly thermalize via collisions with the ions. This heat is then transferred from the coronal plasma to the denser part of the target by thermal conduction, driving the target compression and ignition phases.

1.2.1 Laser plasma instabilities

Before the critical density is reached however, an intense laser of the order of $I\lambda^2 \sim 10^{13} - 10^{16}$ Wμm^2/cm^2 experiences energy losses because of the nonlinear coupling between laser light and plasma taking place as discussed in sections 1.1 and 1.1.3, leading to the development of *laser plasma instabilities* (LPIs). Here a brief compendium of such instabilities is being summarized, putting emphasis on the ones that are capable of generating HEs through the creation of EPWs (see Fig. 1.2). The black curve represents the coronal plasma's density profile.

- *Filamentation*: this instability corresponds to the growth of density perturbations [11, 12, 13, 45, 73] and modulations generated either by the laser propagation, which "pushes" the plasma away from the region where the fields are the strongest (i.e. at the center of the beam), or by changes in the plasma refraction properties due to thermal heating, which focuses the laser light in a process called *self-focusing*. In both cases, the laser light grows

and exerts a force on the plasma in the plane orthogonal to the propagation direction of the laser beam. This force is called *ponderomotive force*, and it will be discussed in chapter 2. The filamentation instability takes place at any point in the plasma corona below critical density. This instability overall creates localized regions with strong fields that can trigger other instabilities.

- *Cross Beam Energy Transfer* (CBET): [14, 15, 16, 74, 75, 76, 77] when several beams irradiate the ICF target, their overlap can cause the energy transfer from a beam to the other. In particular, if one beam is ongoing and the other is outgoing, some of the laser energy destined to irradiate the target can be lost to the outgoing beam. This reduces the laser coupling, with less energy deposited to compress the target. Moreover, CBET breaks the symmetry of the irradiation, leading to an inhomogeneous pressure on the target surface and to hydrodynamic deformation of the ICF target, to the point of the puncturing the shell [78].

- *Parametric Instabilities* (PIs): when a certain threshold (different for each PI) is overcome, a wave can act as a "pump" decaying into two "product" waves, all of which must satisfy appropriate *matching conditions* both in frequency and wave vector. These matching conditions set the waves' energy and momentum conservation, and determine at which densities these instabilities occur. When they are satisfied, the product wave fields begin growing with a growth rate set by the instability. The product modes of each instability can either appear in a localized region of space and grow in time (*absolute* instability), or propagate and undergo spatial amplification (*convective* instability). Here we present the most common PIs, with a more detailed theoretical background given in chapter 2:

  - *Stimulated Brillouin Scattering* (SBS): [29, 30, 31, 32] after overcoming an intensity threshold condition, the laser light can couple with a density perturbation in the plasma, giving rise to an average current that generates a field beating with the laser light. The overall stronger field drives an even stronger density perturbation in a feedback loop [18, 45, 79]. In this case, the laser acts as a pump, generating an *Ion Acoustic Wave* (IAW) as density perturbation and a scattered *Brillouin light wave* as the beating wave. Due to the matching conditions, this instability develops absolutely at critical density, and convectively below n_c. This means that SBS is present almost everywhere in the coronal plasma, reducing the laser coupling with the target by advecting energy through the scattered light wave and plasma heating, due to the majority of the Brillouin emission being towards lower densities.
  - *Stimulated Raman Scattering* (SRS): [18, 21, 22, 23, 45, 79, 80] similarly to SBS, a threshold must be overcome in order for this instability to develop. The process is the same as SBS, however, in this case the laser pump decays into a scattered *Raman light wave* and an EPW. Due to the frequency matching conditions and the dispersion relation of each wave, absolute SRS develops at quarter critical density, and convective SRS at densities below $n_c/4$. The scattered Raman wave behaves similarly to the Brillouin one, mainly propagating towards lower densities. This means that the *backscattered SRS*, similarly to SBS, can advect energy away from the system. Moreover, the generated EPWs produce copious amounts of HEs, and they are one of the two most concerning HE generating processes as far as target preheat is concerned. This is one of the PIs mainly discussed and analyzed in this work.
  - *Two Plasmon Decay* (TPD): [19, 24, 25, 26, 27, 28, 45, 79, 81] the laser pump can decay into two EPWs as well, by driving a longitudinal plasma wave that beats with another plasma wave at a matching frequency and wave vector. While TPD grows absolutely around $n_c/4$, convective TPD is relatively weak compared to convective SRS. Therefore, TPD activity is usually limited in a localized region in space. The

two EPWs generated by TPD imply that the instability is capable of HE generation, and it is, alongside SRS, a major concern for preheating the target, as it will be seen throughout this work.

  - *Langmuir Decay Instability* (LDI): [37, 38, 39, 82] If the matching conditions allow it, an EPW can act as pump, decaying into another EPW and into an IAW. Since it requires an EPW as pump wave, LDI is dependent on another PI, such as SRS or TPD, and it is therefore called a *secondary instability*. Moreover, a product EPW can undergo another LDI and cascade until the associated matching conditions allow it. Since this instability involves only plasma waves, and it can produce successive decays through *LDI cascade* it is a source of "weak turbulence" in the plasma. Once again, the presence of EPWs can pose preheat concerns. Moreover, the cascade can generate strong turbulence in the following process.

- *Langmuir Wave* (LW) *collapse / cavitation*: [40, 41] when weak turbulence is established, the LDI cascade generates modes characterized by long wavelengths and small wave vectors. When this "condensation" reaches a critical field, the plasma begin forming density depressions pushed by the growing low-k EPW field, forming a *cavity / caviton*. This cavity traps the EPW inside, and acts as a resonator for the wave. At the same time, the cavity is sustained by the EPW field. When electrons cross the cavity and resonate with the EPW, there is a transfer of energy from the EPW to the electrons, which gain energy and can be accelerated to high energies [53, 83, 84], and the EPW undergoes damping. When the EPW field is damped enough, the cavity cannot be sustained by the field anymore, which collapses due to Coulomb forces. The shock wave from the collapsing cavity generates IAWs, resulting in a strongly turbulent plasma. Since this process is tied to the EPWs in the system, it mainly develops around the areas of activity of both SRS and TPD (i.e. from quarter critical density and below), and it also poses a preheat concern.

1.2.2 Resonance absorption

The process of *resonance absorption* (RA) [85, 86, 87] occurs when the laser light with an incidence angle of ϑ with respect to the target normal reaches its turning point. At this location, the light's wave number becomes vanishingly small at $n_0 = n_c \cos^2(\vartheta)$, and the wave splits into backward propagating light (reflected wave) and an evanescent wave towards the ICF capsule. If this evanescent wave reaches the critical density n_c with a polarization component parallel to the density gradient, it can excite longitudinal plasma modes (EPWs) that, being originated towards their own turning point at $n_{EPW} = n_c$, propagate away from the target [88]. These EPWs can in turn convert almost all their energy into hot electrons, accelerating a population at high energies. These electrons follow the EPW mode, moving towards lower densities. However, through electrostatic sheath there can be an acceleration of these electrons back towards higher densities. Being very close to the ICF capsule, this can pose preheat concerns. While this work focused exclusively on the physics of LPIs at *quarter critical density*, $n_c/4$, this instability can be an important source of HEs but mostly at initial times when the density scale length is small. Furthermore, the introduction of broadening of the laser bandwidth appears to be effective in mitigating the non-linear part of RA [88].

1.3 ICF simulations

Simulations are an essential tool for a variety of applications. They allow to formulate theoretical models and study the evolution of various processes in a controlled system, serve as experimental data verification and predict trends and results. ICF relevant simulations address different aspects of the ICF target and are resolved for different spatial and temporal scales.

Hydrodynamic codes are used for simulations at spatial scales of the order of the fuel target, 10^{-3} m, and time scales of the order of 10^{-9} s (i.e. the pulse duration). They usually employ hydrodynamic models that allow for the study of phenomena involving the ICF target as a whole, and they are used for observing hydrodynamic instabilities in the fuel, shock propagation at the macroscopic scale, and simulations of phenomena such as collisional absorption of laser light and reduced models of CBET. They can also model fluid instabilities such as Rayleigh-Taylor instabilities, as well as HE transport through the use of Monte Carlo models [59, 89]. Their advantages are not only the large scales that allow simulations of the complete problem, but also the lower computational times due to the models' simplicity. However, they are not suited for more detailed, smaller scale phenomena, such as the evolution of laser-plasma instabilities and HE generation, due to their inability to resolve the necessary scales [90].

On the other hand, some effects can be resolved only through a kinetic approach. A standard method is to couple the Maxwell equations with the resolution of discrete particle trajectories representing groups of ions and electrons. These are *Particle-In-Cell* (PIC) codes, in which the particles move in cells due to the fields defined at the mesh nodes, in turn used to update the fields and recompute the solution of the Maxwell equations. This feedback loop between particle kinetics and field solver allows for great precision and detail. However, the scales at play make each simulation computationally expensive. The domain size is of the order of $10^{-5} - 10^{-6}$ m in space and 10^{-12} s in time, and the typical grid steps is of the order of $10^{-8} - 10^{-9}$ m in space, and of the order of $10^{-17} - 10^{-18}$ s in time. Each cell contains $\simeq 10^{1} - 10^{2}$ particles each, whose trajectories must be computed at each time step (of the order of an as). This leads to computation times of the order of days to weeks for a single simulation, which makes these codes not suitable for studies with many parameters.

A way to conserve a kinetic aspect to the simulation while lowering the computational cost is to utilize *hybrid* approaches. One code that implements this approach is the Laser Plasma Simulation Environment (LPSE) used in this work. LPSE uses a system of field equations for the laser, Raman scattered light, EPWs and a hydrodynamic description of the IAWs (i.e. continuity and momentum equations). In order to simulate the particles, a kinetic module updates the particle trajectories according to the fields in the simulation domain. However, the macro-particle population is set to be much lower than PIC codes, at $10^{6} - 10^{7}$ particles. These particles, similarly to a PIC code, can evolve their trajectories and velocities according to the electromagnetic solutions given by the field solver. However, the particles in the code do not update the electric fields, and therefore there is no feedback from the particle, beside the calculation of a dynamic Landau damping evolution in time, tied to the electron velocity distribution function in the simulation. This simple feedback allows for faster and cheaper simulations at the cost of a reduced accuracy. Moreover, hybrid codes often use simplified wave models as well. LPSE uses the *Zakharov model* in order to not consider the entire Fourier wave spectrum, but only those waves that possess a frequency around a representative frequency chosen beforehand, allowing for further reduction in computational time. However, it also limits the observation of laser-plasma instabilities to a limited density interval, and does not allow a correct study of convective phenomena such as convective SRS. LPSE will be described in chapter 3.

The importance of HE phenomena in ICF implosions, through their interaction with plasma dynamics, warrant to account for their presence in hydrodynamic codes. However, they do not resolve the necessary scales to describe their generation consistently. Instead, one can formulate reduced models that relates laser and hydro parameters to HE characteristics, number of HEs, energy spectrum, angular spectrum, loss of laser transmission and local absorption of EPW energy. The formulation of such models requires to explore a large input parameter space, for which LPSE is well suited.

	Spatial scales [m]	Time scales [s]	Δx [m]	Δt [s]	Number of particles
hydro	10^{-3}	$10^{-8} - 10^{-11}$	$10^{-4} - 10^{-6}$	10^{-12}	N/A
hybrid	$10^{-4} - 10^{-6}$	$10^{-11} - 10^{-12}$	$10^{-8} - 10^{-9}$	10^{-15}	$10^{7} - 10^{8}$
PIC	$10^{-4} - 10^{-6}$	$10^{-11} - 10^{-12}$	$10^{-8} - 10^{-9}$	$10^{-17} - 10^{-18}$	10^{8}

Table 1.1: Comparison between scales of hydro codes, PIC codes and hybrid codes.

1.4 Objectives of this work

The main goal of this work is the *characterization of hot electrons generated by laser-plasma instabilities at quarter critical density.* In order to achieve this result, in this work several objectives, listed below, have been considered.

- The first objective is to determine hot electron generation mechanisms. Since in our intensity regime the electrons are accelerated by EPWs, SRS, TPD, LDI and cavitation are investigated in the region of quarter critical density. Validation of LPSE results is carried out, either through theory or PIC simulations and using previous literature to look for similar HE quantities in both simulations and experiments.
- The second objective is to characterize the HE production by identifying a set of key laser-plasma parameters, and extracting the HE quantities of interest from the simulations carried out according to input parameters. The goal is to form a database of such quantities with which to perform a complete parameter scan. For this purpose, the use of LPSE is more advantageous than using more expensive PIC codes.
- The third objective is to collect the data, investigate the changes that each parameter brings to the HE generation, providing a hypothesis on why these changes take place, with the support of the literature. Finally, a first attempt to derive scaling laws for the HE conversion fraction should be made.

1.5 Manuscript's structure

The investigation of HE generation and LPIs, as well as its scaling analysis according to different laser-plasma conditions has been divided in 3 main chapters.

- **Chapter II** We present in this chapter the required concepts of electromagnetism and plasma physics. We illustrate different plasma descriptions that can be adopted, explain the evolution of waves in the plasmas, their dispersion relations, reaching the definition for EPWs and IAWs. The EPWs and IAWs damping rates will be discussed as well. This will be done both for a "cold" and a "warm" plasma. In the case of a warm plasma, emphasis will be on the calculation of the Landau damping. We will look at the ponderomotive force as well, in order to setup the description of the parametric instabilities in a general way, by considering an infinite homogeneous plasma at the beginning, up until considering inhomogeneities and finite effects. After that, we will proceed to describe SRS, TPD, LDI and SBS. Coupled equations, growth rates, dispersion relations and threshold conditions are provided for all the instabilities.
- **Chapter III** The LPSE code is detailed here, explaining the Zakharov model and the derived field equations. Several examples of the fields solved by LPSE are brought up, both for SRS and TPD, with the goal to provide some degree of validation between LPSE and theory. After that, we begin to describe HE generation, the Landau damping calculation in LPSE and the explanation of weak plasma turbulence. A description of strong turbulence

and LW collapse follows, and is used to explain the kinetic module of LPSE: HPE. Finally, simulations to validate the kinetic module of the code are carried out.

- **Chapter IV** The presentation of the simulation results are given in this chapter. We begin by defining the parameter database used for the scaling analysis, and the subset of LPSE equations used to solve the problem. We discuss about the general simulation setup, density profile and boundary conditions, damping rates calculation and HPE module parameters. We then discuss the laser-plasma conditions that govern the parameter scan, the electron and ion-electron temperature ratio (T_e and T_i/T_e, respectively, the density scale length L_n and the drive strength η). A detailed analysis of a single LPSE simulation is carried out, with emphasis on the fields, the electron propagation and the energy metrics of the simulation. One important part is the extraction of the HE quantities through the fit of the electron energy flux. After this description, the first scaling analysis proposed will be for 2D TPD in presence of LDIs and LW collapse, where we list the different changes for different scans of the parameters considered, as well as inferring some simple scaling laws depending on the database parameters. After this, we pass onto a comparison between a sample of 2D and 3D simulations, in order to determine the effects of HE generation when raising the dimensions of the simulation box. After this, a similar scaling analysis to TPD, but with the inclusion of SRS as well, has been investigated and compared to the TPD only case. A small scaling law analysis is carried out for all the parameters involved, in an attempt to try to derive a multivariate law for predicting the HE conversion fractions. Finally, we present a comparison of LPSE results with a PIC simulation carried out with the SMILEI code [91]. The LPSE results are also compared with previous results from both simulation codes and experiments from the literature.

The conclusions of this work are presented in **Chapter V**.

Chapter 2

Theory of Laser-Plasma Instabilities

2.1 Elements of electromagnetism and plasma theory

2.1.1 Maxwell's equations: from a microscopic to a macroscopic description

The evolution in time and space of electric and magnetic fields is governed by the Maxwell's equations. J.C. Maxwell was the first one to propose a system of 20 equations in 1865 [92], but later work from O. Heaviside (1892) [93], H. Hertz and J.W. Gibbs [94] rearranged their form in the four-equations system mainly known in modern literature. At microscopic level, this system reads:

$$Gauss\ law: \nabla \cdot \boldsymbol{E}_{\mathbf{micr}} = 4\pi k_1 \rho_{\mathrm{micr}}, \tag{2.1a}$$

$$Gauss\ law\ for\ magnetism: \nabla \cdot \boldsymbol{B}_{\mathbf{micr}} = 0, \tag{2.1b}$$

$$Faraday - Neumann - Lenz\ law: \nabla \times \boldsymbol{E}_{\mathbf{micr}} = -k_3 \frac{\partial \boldsymbol{B}_{\mathbf{micr}}}{\partial t}, \tag{2.1c}$$

$$Ampere - Maxwell\ law: \nabla \times \boldsymbol{B}_{\mathbf{micr}} = 4\pi \frac{k_2}{k_3} \boldsymbol{J}_{\mathbf{micr}} + \frac{1}{c^2 k_3} \frac{\partial \boldsymbol{E}_{\mathbf{micr}}}{\partial t}., \tag{2.1d}$$

where $\mathbf{E}_{\mathrm{micr}}$ and $\mathbf{B}_{\mathrm{micr}}$ are the microscopic electric and magnetic fields in their vector form and $\rho_{\mathrm{micr}} \equiv \sum_i q_i \delta(\boldsymbol{x} - \boldsymbol{x_i(t)})$ and $\boldsymbol{J}_{\mathbf{micr}} \equiv \sum_i \boldsymbol{v_i(t)} q_i \delta(\boldsymbol{x} - \boldsymbol{x_i(t)})$ are the microscopic material's density and current density, respectively. $\delta(x)$ are Dirac's deltas. Eqs. 2.1 are not written in any specific unit system. These can be obtained by changing the values of the constants k_1, k_2 and k_3 according to a set of conditions (i.e. $k_1/k_2 = c^2$, where c is the speed of light in vacuum). In the case of the SI (*International System*) or the CGS (Centimeter-Gram-Second, also called *Gaussian*) systems of units, we can obtain them by defining the constants as in Tab. 2.1, where ϵ_0 is the electric permittivity and μ_0 is the magnetic permeability, both in vacuum. Unless explicitly specified, we will always refer to the CGS unit system. Eqs. 2.1, coupled with the *Lorentz's force*:

$$\boldsymbol{F}_{Lor,micr} = q\boldsymbol{E}_{\mathrm{micr}} + q\boldsymbol{v} \times \boldsymbol{B}_{\mathrm{micr}}, \tag{2.2}$$

constitute a system describing the self-consistent problem, at a microscopic level, of a charge population with density ρ and current density $\boldsymbol{J}$ being immersed in an electric and magnetic field, as well as generating their own, and feeling the effects of said field on themselves. In Eq. 2.2, q refers to the individual charge of a particle, and $\boldsymbol{v}$ to its velocity.

Since the system made by Eqs. 2.1 and 2.2 describes each individual particle, it is an unpractical description for large systems. Therefore, a *macroscopic description* which considers the particle as a population may be adopted. In order to consider a macroscopic description of these equations, a spatial averaging procedure can be introduced. Several spatial averages have been proposed in the work of authors such as Lorentz [95], Rosenfeld [96], Mazur [97], de Groot [98] and Russakoff [99]. The main idea behind these is to choose a finite scale length below

	k_1	k_2	k_3
SI	$\frac{1}{4\pi\epsilon_0} = 10^{-7}c^2$ [kg m^{3}s^{-4}A^2]	$\frac{\mu_0}{4\pi} = 10^{-7}$ [kg m s^{-2}A^{-2}]	1
Gauss	1	$\frac{1}{c^2}$ [s^{2}m^{-2}]	$\frac{1}{c}$ [s m^{-1}]

Table 2.1: Constants' values for the International System (SI) and the gaussian unit system.

which small fluctuations in the system can be neglected. We can therefore describe macroscopic quantities, at the cost of losing information (i.e. individual particle trajectories and velocities).

We define $\rho_{\text{micr}} \equiv \rho_m + \rho_{ext}$, where ρ_m is the charge density within the medium, and ρ_{ext} is an additional charge population not belonging to the macroscopic medium. Assuming the medium to be overall neutral, $\int_V \langle\rho_m\rangle d^3x = 0$, it is then possible to define a vector potential field $\boldsymbol{P}$:

$$\langle\rho_m\rangle \equiv -\nabla\cdot\boldsymbol{P}, \tag{2.3}$$

defined as the *polarization vector*. This vector is associated with the electric dipole moment: $\int_V \boldsymbol{x}\langle\rho_m\rangle d^3x = \int_V \boldsymbol{P} d^3x$. As such, Eq. 2.1a becomes:

$$\nabla\cdot\boldsymbol{E} \equiv \nabla\cdot\langle\boldsymbol{E}_{\mathbf{micr}}\rangle = -4\pi\nabla\cdot\boldsymbol{P} + 4\pi\langle\rho_{ext}\rangle. \tag{2.4}$$

Defining the *electric displacement* as $\boldsymbol{D} \equiv \boldsymbol{E} + 4\pi\boldsymbol{P}$ and $\langle\rho_{ext}\rangle \equiv \rho$, we obtain the *Gauss law for macroscopic media*:

$$\nabla\cdot\boldsymbol{D} = 4\pi\rho, \tag{2.5}$$

The same method can be applied to the Ampere-Maxwell's law. We can define $\langle\boldsymbol{J}_{\mathbf{micr}}\rangle \equiv \langle\boldsymbol{J_m}\rangle + \boldsymbol{J}$, where $\langle\boldsymbol{J_m}\rangle$ represents the average charge currents in the medium and $\boldsymbol{J} \equiv \langle\boldsymbol{J}_{ext}\rangle$ represents the average external currents. By using the *continuity equation*:

$$\frac{\partial\rho}{\partial t} + \nabla\cdot\boldsymbol{J} = 0, \tag{2.6}$$

and applying the time derivative to Eq. 2.5, we obtain:

$$\nabla\cdot\left(\frac{\partial\boldsymbol{D}}{\partial t} + 4\pi\boldsymbol{J}\right) = 0. \tag{2.7}$$

Therefore, a field $\boldsymbol{H}$ can be defined such that $\nabla\cdot(\nabla\times\boldsymbol{H}) = 0$, with the following expression:

$$\nabla\times\boldsymbol{H} = \frac{1}{c}\frac{\partial\boldsymbol{D}}{\partial t} + \frac{4\pi}{c}\boldsymbol{J}. \tag{2.8}$$

$\boldsymbol{H}$ is the *magnetizing field*, while the speed of light c appears because of dimensional purposes [66]. Eq. 2.8 is the Ampere-Maxwell law in a macroscopic description. Since the Ampere-Maxwell's equations for $\boldsymbol{B}$ (Eq. 2.1d) and $\boldsymbol{H}$ (Eq. 2.8) have a similar structure, we can obtain a "$\boldsymbol{B}-\boldsymbol{H}$" equation which reads:

$$\nabla\times\left(\frac{\boldsymbol{B}-\boldsymbol{H}}{4\pi}\right) = \frac{1}{c}\langle\boldsymbol{J_m}\rangle - \frac{1}{c}\frac{\partial}{\partial t}\left(\frac{\boldsymbol{D}-\boldsymbol{E}}{4\pi}\right). \tag{2.9}$$

In the same way as $(\boldsymbol{D}-\boldsymbol{E})/4\pi \equiv \boldsymbol{P}$, we can define the *magnetization vector* as the quantity $\boldsymbol{M} \equiv (\boldsymbol{B}-\boldsymbol{H})/4\pi$, such that:

$$\nabla\times\boldsymbol{M} = \frac{1}{c}\langle\boldsymbol{J_m}\rangle + \frac{1}{c}\frac{\partial\boldsymbol{P}}{\partial t}. \tag{2.10}$$

Similarly to the polarization vector $\boldsymbol{P}$, $\boldsymbol{M}$ is associated to the *magnetic dipole moment* $(c/2)\int_V(\boldsymbol{x}\times\langle\boldsymbol{J_m}\rangle)d^3x = \int_V \boldsymbol{M}d^3x$.

Modifying the description in this way, and averaging $\boldsymbol{E}$ and $\boldsymbol{B}$, we obtain the last two equations. Thus, the *macroscopic description of the Maxwell equations*, in gaussian units, reads:

$$\nabla \cdot \boldsymbol{D} = 4\pi\rho, \tag{2.11a}$$

$$\nabla \times \boldsymbol{E} = -\frac{1}{c}\frac{\partial \boldsymbol{B}}{\partial t}, \tag{2.11b}$$

$$\nabla \cdot \boldsymbol{B} = 0, \tag{2.11c}$$

$$\nabla \times \boldsymbol{H} = \frac{4\pi}{c}\boldsymbol{J} + \frac{1}{c}\frac{\partial \boldsymbol{D}}{\partial t}. \tag{2.11d}$$

2.1.2 Non-locality of the macroscopic system

Eqs. 2.11 do not constitute a closed system of equations. We therefore need *constitutive relations* between $\boldsymbol{P}$ and $\boldsymbol{E}$, and between $\boldsymbol{M}$ and $\boldsymbol{B}$. Expanding in series both $\boldsymbol{P}$ and $\boldsymbol{M}$, ignoring the 0-th term as a constant field and considering only the first order term, we obtain a non-local, linear relation between these quantities and their associated fields, through the *electric and magnetic susceptibilities* $\chi_e(\boldsymbol{x}, t)$ and $\chi_m(\boldsymbol{x}, t)$. These relations read:

$$\boldsymbol{P} = \iint \overline{\overline{\chi}}_e(\boldsymbol{x} - \boldsymbol{x'}, t - t') \cdot \boldsymbol{E}(\boldsymbol{x'}, t') d^3x' dt', \tag{2.12a}$$

$$\boldsymbol{M} = \iint \overline{\overline{\chi}}_m(\boldsymbol{x} - \boldsymbol{x'}, t - t') \cdot \boldsymbol{B}(\boldsymbol{x'}, t') d^3x' dt', \tag{2.12b}$$

where $\overline{\overline{\chi}}_e(\boldsymbol{x}, t)$ and $\overline{\overline{\chi}}_m(\boldsymbol{x}, t)$ are double tensors describing the medium anisotropies. According to Eqs. 2.12, the relation between $\boldsymbol{P}$ and $\boldsymbol{E}$ (and $\boldsymbol{M}$ and $\boldsymbol{B}$) is non-local, the non-locality being described by $\overline{\overline{\chi}}_e$. Therefore, $\boldsymbol{P}$ is not a function of $\boldsymbol{E}$, but its *functional*, describing anisotropies within the system.

From a mathematical point of view, Eqs. 2.12a and 2.12b are convolutions in space. Thus, under the assumption that $\boldsymbol{E}$ is a sum of monochromatic contributions and applying the Fourier transform both in time and space ($\nabla \to i\boldsymbol{k}$ and $\partial/\partial t \to -i\omega$), we obtain:

$$\boldsymbol{P}(\omega, \boldsymbol{k}) = \overline{\overline{\chi}}(\omega, \boldsymbol{k}) \cdot \boldsymbol{E}(\omega, \boldsymbol{k}), \tag{2.13}$$

Where, for simplicity, we dropped the notation $\overline{\overline{\chi}}_e$ in favor of $\overline{\overline{\chi}}$, under the assumption that the results for the magnetic field (subscript "m") can be derived in a similar way. This discussion describes the non-locality, or *dispersion*, of a response field both in space and time, and it is a general description that can be applied to other field couples. In particular, the relation between $\boldsymbol{D}$ and $\boldsymbol{E}$ reads:

$$\boldsymbol{D}(\omega, \boldsymbol{k}) = \overline{\overline{\epsilon}}(\omega, \boldsymbol{k}) \cdot \boldsymbol{E}(\omega, \boldsymbol{k}), \tag{2.14}$$

where $\overline{\overline{\epsilon}}$ is the *dielectric permittivity* tensor. Since $\boldsymbol{D} \equiv \boldsymbol{E} + 4\pi\boldsymbol{P}$, if we use Eqs. 2.13 and 2.14 in this definition, we obtain a relation between $\overline{\overline{\epsilon}}$ and the susceptibility $\overline{\overline{\chi}}$:

$$\overline{\overline{\epsilon}} = \overline{\overline{I}} + 4\pi\overline{\overline{\chi}}. \tag{2.15}$$

Considering the similar *generalized Ohm law*, which describes a relation between the fields $\boldsymbol{J}$ and $\boldsymbol{E}$, their relation is:

$$\boldsymbol{J}(\omega, \boldsymbol{k}) = \overline{\overline{\sigma}}(\omega, \boldsymbol{k}) \cdot \boldsymbol{E}(\omega, \boldsymbol{k}), \tag{2.16}$$

where $\overline{\overline{\sigma}}$ is the *conductivity* tensor. Finally, using Eq. 2.3 within the continuity equation (Eq. 2.6) and applying the Fourier equations, we obtain a relation between the current density and the polarization vector:

$$\boldsymbol{J}(\omega, \boldsymbol{k}) = -iw\boldsymbol{P}(\omega, \boldsymbol{k}), \tag{2.17}$$

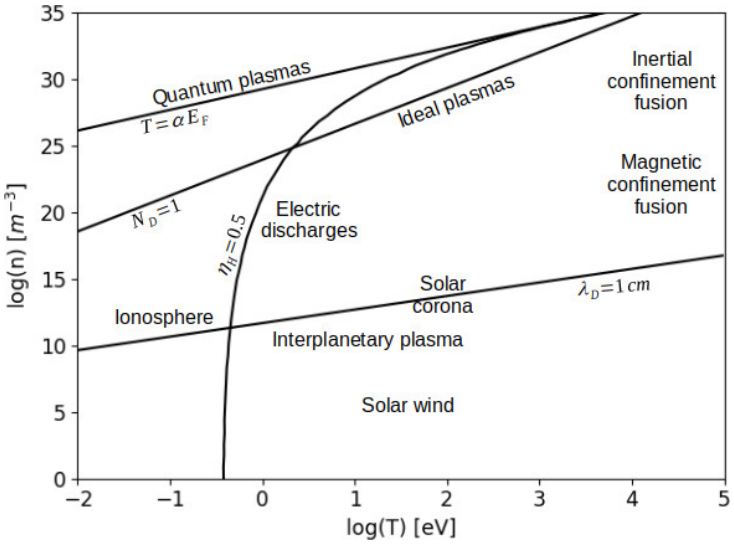

Figure 2.1: Plasma conditions chart [66]. The figure is divided in several sections The line $T = \alpha E_F$ divides the plasmas from quantum to classic plasmas, α being the fine constant structure and E_F the Fermi energy. The region under $N_D = 1$ is considered an ideal plasma, where each Debye sphere has a huge number of particles within. η_H is the ionization parameter, and separates partially ionized plasmas (left) from completely ionized ones (right), after at least 50% of the plasma is ionized. λ_D is the Debye length, and the region above this line implies that it is very small compared with the characteristic dimensions of the considered plasma.

which, using both Eq. 2.13 and 2.16, results in:

$$\bar{\bar{\epsilon}} = \bar{\bar{I}} + \frac{4\pi i}{\omega}\bar{\bar{\sigma}}. \tag{2.18}$$

These results will be useful in the following chapters, when the propagation of electromagnetic (and electrostatic) waves in a plasma will be considered.

2.1.3 Definition of a plasma

Alongside the most familiar states of matter of solid, liquid and gas there is the state of *plasma*. Theoretically, it is defined as a completely ionized gas, by heating a gas to very high temperatures [66]. A more practical definition of a plasma is when a macroscopic system (i.e., a macroscopically large number of particles) possesses a concentration of said charged particles high enough to strongly influence the physical properties of the system itself, such as its equilibrium and stability. In this system, space charge effects will exist within the system, and will cover a dominant role in its behavior and physical properties.

While there was already knowledge of "charged particles with a collective behavior" since Lord Rayleigh in 1906 [100], the term "plasma" was introduced by Langmuir [101] and later, Tonks [102] while both studying oscillations in electric discharges, despite the term "fourth state of matter" was coined much earlier by Crookes [103] in 1879, while observing ionized media created in a gas discharge, dubbing it an "ultra-gaseous state of matter".

Plasmas account for 99.9% of the observable matter [104] found in the universe, constituting the Earth ionosphere, stars, solar wind, solar corona, as well as intracluster and intergalactic media. Artificially, they are used for industrial and chemistry applications, such as laser ablation and plasma deposition [105], and studied for biomedical applications [106] and energy production via nuclear fusion reactions [5, 42]. As a consequence, plasmas enormously vary in their density and temperature conditions, ranging from $\simeq$ 30 orders of magnitude in the former, and $\simeq$ 7 orders in the latter, as shown in Fig. 2.1.

A brief introduction of what a plasma is has been provided in section 1.1. Plasmas can be assumed as a *locally charged, globally neutral* system, where the number of positive and negative charges, through Coulomb interactions, compensate any local charge imbalance. This assumption of *quasi-neutrality* implies that:

$$n_e = n_i = \sum_j n_j Z_j, \tag{2.19}$$

where n_e and n_i are the electron and ion density, respectively, and the index "j" takes into account multiple ion species within the plasma. A common approximation is to consider a plasma in *thermodynamic equilibrium*, which allows the approximation of the plasma particle distribution into the *Maxwell-Boltzmann distribution*:

$$f(\boldsymbol{v}) = \left(\frac{m}{2\pi T}\right)^{3/2} \exp\left(-\frac{m\boldsymbol{v}^2}{2T}\right), \tag{2.20}$$

where T is expressed in eV. Writing Eq. 2.20 in terms of the energy ε, recalling that $f(\epsilon)d\epsilon = f(\boldsymbol{v})d\boldsymbol{v} = 4\pi v^2 dv$, and defining $|\boldsymbol{v}_{Th}| = \sqrt{2\varepsilon/m}$ as the most probable speed, we obtain:

$$f(\varepsilon) = \frac{2}{\sqrt{\pi}} \frac{\sqrt{\varepsilon}}{T^{3/2}} \exp\left(-\varepsilon/T\right). \tag{2.21}$$

Aside from the thermodynamic equilibrium approximation leading to the results above, there might be conditions where the temperature between electrons and ions differs, but they both follow Maxwell-Boltzmann distributions. In such case, the system is not in thermodynamic equilibrium, but in *partial equilibrium*, where the two populations have two different average temperatures T_e and T_i. The most general case would be when there is no plasma thermal equilibrium at all, with electrons and ions following non-Maxwell Boltzmann distributions. In this case, the knowledge of average temperatures is insufficient to derive the overall plasma behavior. An important case in Inertial Confinement Fusion falls between partial equilibrium and non-equilibrium cases, in which a single population (i.e., the electrons), can be decomposed into a main *bulk* at thermal equilibrium, and a smaller population not in equilibrium with the rest of the bulk. This will be the case for *hot electron* generation, which we will talk about in more detail starting from Chapter 3.

2.1.3.1 Plasma frequency

The charge separation within the plasma means that there will be a response to density variations from charge neutrality. Assuming the ions as fixed, and moving a layer of electrons of thickness L at a distance x from the equilibrium position, two opposite charge layers will form. The electrostatic field generated will follow Gauss' law (Eq. 2.1a), where n is the plasma density. We will limit ourselves to the 1D case; therefore E can be reduced to a scalar. The electrons will be attracted by the ions towards their equilibrium position. The equation of motion for the electrons will simply be given by writing Newton's law for an electrostatic Coulomb force:

$$m_e \ddot{x} = -eE = -4\pi n_e e^2 x, \tag{2.22}$$

where n_e is the electron density. Eq. 2.22 is the equation of a free oscillator, characterized by a frequency (in CGS):

$$\omega_{pe} \equiv \sqrt{\frac{4\pi n_e e^2}{m_e}}, \tag{2.23}$$

defined as the electron *plasma frequency* and denoted ω_{pe}. For the ions, the *ion plasma frequency* is similar, where the only difference is the ion charge Ze: $\omega_{pi} \equiv \sqrt{4\pi n_i Z^2 e^2/m_i}$. The *total plasma frequency* is defined as $\omega_p \equiv \sqrt{\omega_{pe}^2 + \omega_{pi}^2}$. However, since $m_e \gg m_i$, the plasma frequency is almost always approximated as the electron plasma one: $\omega_p \sim \omega_{pe}$.

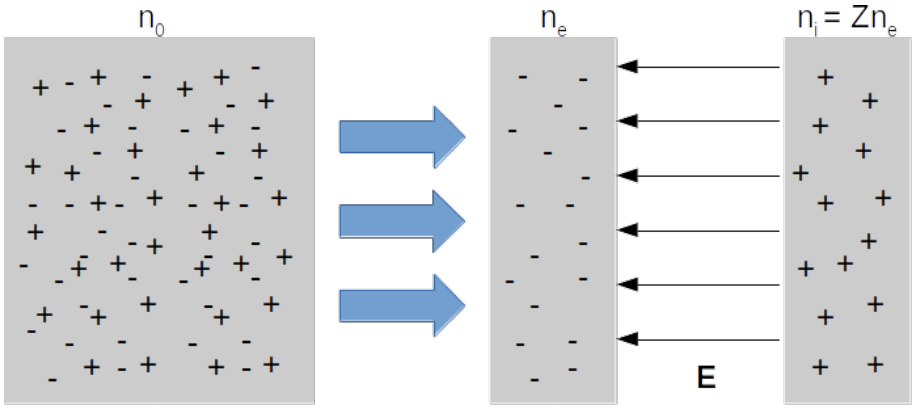

Figure 2.2: Space charge effect illustration with a negative charge population of density n_e, and a positive one of charge $n_i = Zn_e$.

2.1.4 Local space charge effects in a plasma: Yukawa potential

We now describe the behavior of electrically charged particles within a plasma. Considering Eq. 2.1a, we can obtain an expression for the *electrostatic scalar potential* ϕ, given by $\boldsymbol{E} \equiv -\nabla\phi$. A point charge in vacuum is described by $\phi(r) = q/r$, where q is the particle charge and r the radial distance from the origin of the reference frame. In a plasma, a charged particle interacts with all the others through Coulomb interactions. As such, local *space charge effects* will influence the particles' dynamics (Fig. 2.2). Considering a two species plasma composed by electrons and ions with charge number Z, the charge density ρ will be the sum of the electron density n_e, the ion density n_i, and the considered point charge $q\delta(\boldsymbol{x})$, where $\delta(\boldsymbol{x})$ is a Dirac's delta centered in the origin of our reference system. The result is the *Poisson's equation* $\nabla^2\phi = -4\pi\rho = 4\pi e(n_e - n_i) + 4\pi q\delta(\boldsymbol{x})$ where, assuming partial equilibrium, both n_e and n_i will have a Maxwell-Boltzmann distribution of the form $n = n_0 \exp(-q\phi/T)$, with different temperatures T_e and T_i, and n_0 is the density at $\phi = 0$. As such, Poisson's equation can be rewritten as:

$$\nabla^2\phi = 4\pi e n_0 \left[\exp\left(\frac{e\phi}{T_e}\right) - \exp\left(-\frac{Ze\phi}{T_i}\right)\right] - 4\pi q\delta(\boldsymbol{x}). \tag{2.24}$$

At long distances from the charge q, electrostatic effects are negligible compared with the thermal ones, $e\phi/T \ll 1$. Therefore, expanding in series and considering only the first order, we obtain:

$$\nabla^2\phi = 4\pi e^2 n_0 \left(\frac{1}{T_e} + \frac{Z}{T_i}\right)\phi, \tag{2.25}$$

where the term $4\pi\delta(\boldsymbol{x})$ disappears since $\delta(\boldsymbol{x}) = 0$ when $\boldsymbol{x} \neq 0$. We can define a characteristic length, called *Debye length* [107], along which space charge effects occur within a globally neutral plasma due to Coulomb potential energy, as well as thermal energy:

$$\lambda_D \equiv \left(\sum_j \frac{4\pi q_j^2 n_j}{T_j}\right)^{-\frac{1}{2}}, \tag{2.26}$$

where j represents the charged particle population (electrons or ion species). It must be noted that λ_D is not a constant, but depends on the plasma's properties (i.e., its temperature T and density n), and also on the forces of our system (i.e., electrostatic forces). In particular, if we consider a plasma in partial thermodynamic equilibrium (two different temperatures), with a single ion species (i.e. $n_e = Zn_i$), we obtain:

$$\lambda_D = \left(4\pi e^2 \left(\frac{n_e}{T_e} + \frac{n_i Z^2}{T_i}\right)\right)^{-\frac{1}{2}}. \tag{2.27}$$

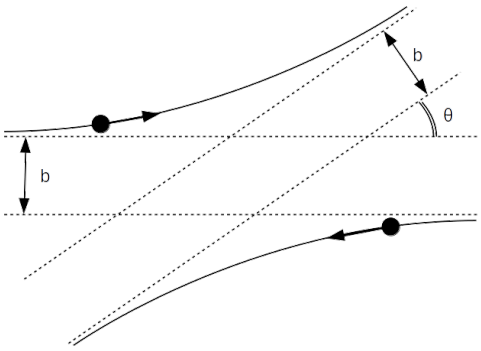

Figure 2.3: Rutherford scattering between particles.

With the introduction of λ_D, we can rearrange Eq. 2.25:

$$\nabla^2\phi - \frac{1}{\lambda_D^2}\phi \equiv \Box\phi = 0, \tag{2.28}$$

where $\Box\phi$ is the *d'Alembert operator* applied to the potential ϕ. Since the problem is in spherical symmetry, rewriting Eq. 2.28 in polar coordinates, and knowing that $\phi \to 0$ for $r \to \infty$, and $\phi \to q/r$ for $r \to 0$, we obtain the *Yukawa potential* [108]:

$$\phi(r) = \frac{q}{r}\exp\left(\frac{r}{\lambda_D}\right). \tag{2.29}$$

Eq. 2.29 describes the electrostatic potential experienced by a single particle within the plasma. After a characteristic length λ_D, the potential ϕ associated with a point charge vanishes exponentially. This is caused by the formation of a "screening charge" around the considered particle through Coulomb attraction, forming a sphere of radius λ_D called *Debye sphere*. Since the system is a plasma of density $n_0 = n_e + n_i$ for a single ion species plasma, we can evaluate the average number of particles N_D within a Debye sphere (with volume $(4\pi/3)\lambda_D^3$) as:

$$N_D \equiv (n_0)\frac{4\pi}{3}\lambda_D^3 \simeq 4.1 \times 10^{11} T^{\frac{3}{2}} n^{-\frac{1}{2}}, \tag{2.30}$$

where T is in eV and n is in m^{-3}. When $N_D \gg 1$, the plasma is considered an *ideal plasma*, in which thermal interactions are so strong that Coulomb interactions are negligible. Therefore, referring to Fig. 2.1, every plasma below the line $N_D = 1$ can be considered an ideal plasma.

2.1.5 Collisions between particles

Considering a plasma characterized by a density n, a test particle injected into it can experience a deflection in its trajectory through Coulomb forces. We define the *impact parameter* b as the separation between initial directions of the particles; it should be noted that, since the Coulomb force is a central force ($\propto r^{-2}$) and therefore the angular momentum is conserved, the impact parameter will be conserved as well ($|\boldsymbol{r} \times m\boldsymbol{v}| = bmv$). Thus, according to *Rutherford formula* [109], the scattering angle θ is determined by (Fig. 2.3):

$$tan\left(\frac{\theta}{2}\right) = \frac{1}{2}\frac{b_0}{b}, \tag{2.31}$$

where $b_0 \equiv 2(q_1 q_2)/(mv^2)$ is the *Landau distance* (q_i are the charges of the considered particles, v is the relative velocity between the two), defined as the value of b below which the angles of deflection become significant (e.g. $\theta(b = b_0) \simeq 53°$). It can be demonstrated that the case in which a particle experiences a deflection through multiple, small-angle collisions is dominant with

respect to singular, high-angle deflections [66]. Moreover, as seen in Section 2.1.4, each particle is shielded by the other particles in the plasma (Eq. 2.29), which limits Coulomb interactions of the central particle within a sphere with radius equal to λ_D. Therefore, a test particle within a plasma will have an impact parameter between $0 < b < \lambda_D$. Finally, considering the cumulative effects of low-angle collisions between two populations of test and target particles respectively, it can be demonstrated that there is no net variation of perpendicular velocity, $\langle \Delta v_\perp \rangle = 0$. What changes is the root mean square of the perpendicular velocity $\langle \Delta v_\perp^2 \rangle$, which is a characteristic dimension in diffusion processes, with $\langle v_\perp \rangle$ being constant. With all these considerations, we can define the *collisional frequency* ν_c as the rate of change of $\langle \Delta v_\perp^2 \rangle$, related to the initial collision velocity v^2:

$$\nu_c \equiv \frac{1}{v^2} \frac{d}{dt} \langle \Delta v_\perp^2 \rangle. \tag{2.32}$$

Working out the second part of Eq. 2.32, in particular the term $\langle \Delta v_\perp^2 \rangle$, the collision frequency reads, in gaussian units [66, 79]:

$$\nu_{ij} = 8\pi \left\langle \frac{n_j (q_i q_j)^2}{\mu^2 v^3} \ln \Lambda \right\rangle, \tag{2.33}$$

where v is the relative velocity between particle i and j, μ is the reduced mass between the two particles, and $\ln \Lambda$ is the *Coulomb logarithm*, which comes from the integration of the quantity $1/b$ between a minimum and maximum value of the impact parameter. The quantity Λ represents the ratio of such maximum and minimum impact parameters, and can be approximated as $\Lambda \sim 9 N_D$, where N_D is the number of particles inside a Debye sphere. Considering a Maxwell-Boltzmann velocity distribution for the particles, and that the Coulomb logarithm varies weakly with density and temperature, we obtain [110]:

$$\nu_{ij} = \frac{4}{3} \sqrt{2\pi} \langle n_j \rangle \frac{\langle q_i q_j \rangle^2}{\mu^2 (\langle v_j^2 \rangle / 3)^{3/2}} \ln \Lambda, \tag{2.34}$$

which becomes, for electron-electron collisions ($\mu \sim m_e/2$), for electron-ion collisions ($\mu \sim m_e$) and for ion-ion collisions ($\mu \sim m_i/2$) respectively:

$$\nu_{ee} = \frac{(4\pi)^2 \sqrt{2}}{6\sqrt{2}\pi^{3/2}} \frac{n_e e^4 \ln \Lambda_{ee}}{m_e^2 v_{Te}^3}, \tag{2.35a}$$

$$\nu_{ei} = \frac{(4\pi)^2}{6\sqrt{2}\pi^{3/2}} \frac{\langle Z^2 \rangle}{\langle Z \rangle} \frac{n_e e^4 \ln \Lambda_{ei}}{m_e^2 v_{Te}^3}, \tag{2.35b}$$

$$\nu_{ii} = \frac{(4\pi)^2 \sqrt{2}}{6\sqrt{2}\pi^{3/2}} \frac{\langle Z^4 \rangle}{\langle Z \rangle} \frac{n_e e^4 \ln \Lambda_{ii}}{m_i^2 v_{Ti}^3}, \tag{2.35c}$$

$$\tag{2.35d}$$

where $v_{Te} \equiv \sqrt{T_e/m_e}$ and $v_{Ti} \equiv \sqrt{T_i/m_i}$ are the root mean squares thermal velocities, in 1D, for both electrons and ions. The *average charge number* is defined as $\langle Z \rangle \equiv \sum_i Z_i f_i$, where f_i is the atomic fraction of the i-th species and Z_i is the atomic charge number. With this, we can define the additional quantities $\langle Z^2 \rangle \equiv \sum_i Z_i^2 f_i$ and $\langle Z^4 \rangle \equiv \sum_i Z_i^4 f_i$, respectively. Following the definition of $\langle Z \rangle$, it is implied in this description an *average ion description* is being used, where the ion species are represented by a single effective species of charge $Z_{\text{eff}} = \langle Z^2 \rangle / \langle Z \rangle$. Practically, ion-ion collision rate is almost always negligible (since $m_i \gg m_e$), while the electron-electron collision rate is similar to the electron-ion collision rate, but becomes negligible for materials for increasing Z_{eff}.

Braginskii [111, 112] was the first one to find the dependency of the collision frequency on the temperature ($\propto T^{-3/2}$) and on the Coulomb logarithm $\ln \Lambda$. Since then, several empirical

formulae for $\ln\Lambda$ have been proposed in literature [4, 79, 112, 113]. However, a general description of this parameter depends on the plasma temperature and density, relying on models to describe both the shielding conditions (e.g. Debye shielding, λ_D) and the quantum mechanics effects when close to the center of the Debye sphere. This is considered when the temperature increases to the point the De Broglie wavelength $\lambda_B \equiv h/\sqrt{2m_eT}$ (h being the Planck constant) becomes larger than the Landau distance b_0. Here we will provide the descriptions for Λ_{ei} and Λ_{ii} given by [79]:

$$\Lambda_{ei} = \frac{8\pi}{\sqrt{e}} n_e \lambda_{De}^3 \min\left(\frac{3}{\gamma}\frac{1}{\langle Z\rangle}, \frac{\sqrt{3}}{137}\frac{c}{v_{Te}}\right) = 1.69\times10^3 \frac{T_e\lambda_0}{(n_e/n_c)^{\frac{1}{2}}} \min\left[\left(\frac{T_e}{3.03\times10^{-3}\langle Z^2\rangle}\right)^{\frac{1}{2}}, 1\right], \tag{2.36a}$$

$$\begin{aligned}\Lambda_{ii} &= \frac{8\pi}{\sqrt{2e}} n_e \lambda_{De}^3 \frac{T_i}{T_e\langle Z\rangle^{\frac{1}{2}}} \min\left(\frac{3\sqrt{2}}{\gamma}\left(\frac{T_i}{T_e\langle Z^4\rangle}\right)^{\frac{1}{2}}, \frac{\sqrt{3}}{137}\frac{c}{v_{Te}}\left(\frac{m_i}{m_e}\right)^{\frac{1}{2}}\right) = \\ &= 5.12\times10^4 \frac{T_i\lambda_0}{(n_e/n_c)^{\frac{1}{2}}\langle Z\rangle^{\frac{1}{2}}} \min\left[\left(\frac{T_i}{2.77\langle Z^4\rangle}\right)^{\frac{1}{2}}, A^{\frac{1}{2}}\right].\end{aligned} \tag{2.36b}$$

2.1.6 Plasma descriptions

Starting from the equation of motion and Newton's law, we can begin a description of the plasma behavior. Writing the motion of each particle interacting with every other particle within the plasma through Lorentz forces [45], we obtain:

$$\dot{\boldsymbol{x}} = \boldsymbol{v}, \tag{2.37a}$$

$$\dot{\boldsymbol{v}} = \frac{q_j}{m_j}\left(\boldsymbol{E}_{\mathbf{micr}} + \frac{\boldsymbol{v}\times\boldsymbol{B}_{\mathbf{micr}}}{c}\right), \tag{2.37b}$$

where q_j and m_j are the particle charge and mass of the j-th species, and $\boldsymbol{E}_{\mathbf{micr}}$ and $\boldsymbol{B}_{\mathbf{micr}}$ refer to Eqs. 2.1. This system is impossible to solve, since the plasma behavior is described by a number of coupled equations of the order of N_{Av}, N_{Av} being the Avogadro number, each describing every particle trajectory and velocity in relation with the rest of the plasma. In this description, a lagrangian approach is used to describe the particles, through their trajectories and velocities, while the Maxwell equations follow an eulerian approach through the use of fields. Thus, an idea to solve the problem is to simplify it by applying a field (eulerian) description to the particles' populations as well through an averaging procedure, obtaining average charge and current densities. A way to bridge a lagrangian approach with an eulerian one is to define a microscopic distribution function in phase space, f_j, which describes the particle belonging to the j-th population in a small, 6-dimensional volume $d\boldsymbol{x}d\boldsymbol{v}$ in phase space, centered in $(\boldsymbol{x}, \boldsymbol{v})$:

$$f_j(\boldsymbol{x}, \boldsymbol{v}, t) \equiv \sum_i \delta(\boldsymbol{x} - \boldsymbol{x}_{ij})\delta(\boldsymbol{v} - \boldsymbol{v}_{ij}). \tag{2.38}$$

Applying the time derivative to both sides of Eq. 2.38, and recalling fundamental properties of Dirac's deltas (namely, $\partial(\delta(a-b))/\partial a = \partial(\delta(a-b))/\partial b$ and $g(a)\delta(a-b) = g(b)\delta(a-b)$, g being a continuous function evaluated in a and b):

$$\frac{\partial f_j}{\partial t} + \boldsymbol{v}\cdot\frac{\partial f_j}{\partial \boldsymbol{x}} + \frac{\partial}{\partial \boldsymbol{v}}\cdot\left(\frac{\boldsymbol{F}_j}{m_j}f_j\right) = 0, \tag{2.39}$$

where $\boldsymbol{F}_j$ is the Lorentz's force for microscopic fields. Eq. 2.39 is called *Klimontovich equation* [66, 114], and it has the form of a balance equation in phase space. Coupled with the Maxwell's

equations by appropriately redefining the charge density for the j-th population as $\rho_{micr,j} \equiv q_j \int f_j d^3\boldsymbol{v}$ and the charge current as $\boldsymbol{J}_{micr,j} \equiv q_j \int \boldsymbol{v} f_j d^3\boldsymbol{v}$, Eqs. 2.1 and 2.39 are the problem stated in Eqs. 2.37, but in a completely eulerian description. By doing so, it is possible to apply an average procedure to the elements of Eqs. 2.1 and 2.39, thus obtaining the *Boltzmann equation* [115]:

$$\frac{\partial f_j}{\partial t} + \boldsymbol{v} \cdot \frac{\partial f_j}{\partial \boldsymbol{x}} + \frac{q_j}{m_j}\left(\boldsymbol{E} + \frac{\boldsymbol{v}}{c} \times \boldsymbol{B}\right)\frac{\partial f_j}{\partial \boldsymbol{v}} = \left(\frac{\partial f_j}{\partial t}\right)_{\text{coll}}, \tag{2.40}$$

where the "micr" subscript has been dropped, since the quantities involved are average values ($x_{\text{micr}} \equiv x + \tilde{x}$, where $x \equiv \langle x_{\text{micr}} \rangle$ and $\tilde{x}$ is a perturbation of the quantity x_{micr}). The term $(\partial f_j/\partial t)_{\text{coll}}$ describes the short-range interactions, or collisions, of electromagnetic nature between charged particles. Eq. 2.40 can thus be written for every single particle species in the plasma, after also having specified the fields $\boldsymbol{E}$ and $\boldsymbol{B}$, as well as the shape of $(\partial f_j/\partial t)_{\text{coll}}$. However, this means that Eqs. 2.40 for each species and the field equations are coupled and must be solved simultaneously.

Starting from the kinetic description of Eq. 2.40, it is possible to reach a fluid description for distinct multiple species. Defining:

$$n_j \equiv \int f_j d^3v, \tag{2.41a}$$

$$\langle \psi_j \rangle \equiv \frac{1}{n_j}\int \psi(\boldsymbol{v}) f_j d^3v = \frac{\int \psi(\boldsymbol{v}) f_j d^3v}{\int f_j d^3v}, \tag{2.41b}$$

$$C_j = \sum_k C_{jk}, \tag{2.41c}$$

where $\langle \psi_j \rangle$ is a moment for the j-th particle population and C_j is a summed contribution over the other fluids belonging to the k-th fluid, and then multiplying Eq. 2.40 by ψ and integrating over d^3v, we obtain:

$$\frac{\partial}{\partial t}(n_j\langle\psi_j\rangle) + \nabla \cdot (n_j \langle \psi \boldsymbol{v} \rangle_j) - \frac{q_j}{m_j} n_j \left\langle \frac{\partial \psi}{\partial \boldsymbol{v}} \cdot \left(\boldsymbol{E} + \frac{\boldsymbol{v}}{c} \times \boldsymbol{B}\right)\right\rangle_j = n_j \langle C_j \psi \rangle_j, \tag{2.42}$$

which is the general equation for the moments in a *multiple fluid description*. Thus, depending on the form of ψ, different equations can be found:

$$\psi = 1\ , \quad \frac{\partial n_j}{\partial t} + \nabla \cdot (n_j \boldsymbol{u}_j) = 0, \tag{2.43a}$$

$$\psi = m_j \boldsymbol{v}\ , \quad \frac{\partial}{\partial t}(n_j \boldsymbol{u}_j) + \nabla : (n_j \overline{\overline{u_j u_j}}) + \nabla : \overline{\overline{P_j}} - \frac{q_j n_j}{m_j}\left(\boldsymbol{E} + \frac{\boldsymbol{U}_j}{c} \times \boldsymbol{B}\right) = n_j \langle C_j \boldsymbol{v} \rangle_j, \tag{2.43b}$$

$$\psi = \frac{m_j v^2}{2}\ , \quad \frac{\partial}{\partial t}\left(\frac{3}{2} n_j T_j + \frac{1}{2} m_j n_j u_j^2\right) + \nabla \cdot \left(\boldsymbol{q}_j + \overline{\overline{P_j}} : \boldsymbol{u}_j + \frac{3}{2} n_j T_j \boldsymbol{u_j} + \frac{1}{2} n_j m_j u_j^2 \boldsymbol{u}_j\right) = $$
$$= q_j n_j \boldsymbol{u}_j \cdot \boldsymbol{E} + \frac{1}{2} m_j n_j \langle C_j v^2 \rangle_j, \tag{2.43c}$$

where the operator ':' represents a double scalar product, $\boldsymbol{u}_j \equiv \langle \boldsymbol{v} \rangle_j$, $\overline{\overline{P_j}} \equiv \nabla p_j + \nabla : \overline{\overline{\Pi}}_j$ is equivalent to a pressure tensor ($p_j \equiv n_j T_j$ is the *hydrodynamic pressure*, while $\overline{\overline{\Pi}}_j$ is a tensor describing *viscous forces*), and $\boldsymbol{q}_j \equiv 1/2 m_j n_j \langle |\tilde{\boldsymbol{v}_j}|^2 \tilde{\boldsymbol{v}_j} \rangle_j$ is the *heat flux*, $\tilde{\boldsymbol{v}_j}$ being the fluctuations of velocity from the average $\boldsymbol{u}_j$. These three equations are the *mass continuity equation*, *momentum balance equation* and the *energy balance equation* for the j-th charged particle population, respectively. Eqs. 2.43 is not a closed system, since there is no equation provided for $\boldsymbol{q}_j$ nor $\overline{\overline{\Pi}}_j$. This is because the system 2.43 constitutes an *hierarchy* of equations, where the higher-order one describes some terms of the lower-order one. Thus, in order to close the system,

it is necessary to truncate it. One way to do that is to assume the medium behavior follow a *polytropic equation*, which reads [45]:

$$p_j n_j^{-\gamma} = \text{constant}, \tag{2.44}$$

where $\gamma \equiv (2+d_f)/d_f$, d_f being the number of *degrees of freedom* of the system. This equation can be used to truncate the system 2.43 to the second equation, ignoring the third one, if the viscous term from $\overline{\overline{\Pi_j}}$ can be considered negligible.

2.1.6.1 Collision term in the Boltzmann equation

The right hand term in Eq. 2.40 can also be written as:

$$\left(\frac{\partial f_j}{\partial t}\right)_{\text{coll}} = \sum_k C_{jk}, \tag{2.45}$$

where the sum takes into account that the collisions between particles can happen between both same or different species (index "k"). The complete shape of this term after having averaged the Klimontovich equation 2.39 is $\sum_k C_{j,k} \equiv (q_j/m_j)\langle(\tilde{\boldsymbol{E}} + \tilde{\boldsymbol{v}} \times \tilde{\boldsymbol{B}}/c)\partial \tilde{f}_j/\partial \boldsymbol{v}\rangle$, which, while exact, it is very complex to treat, thus it is not a useful description. As such, several models can be used to simplify its shape.

- The simplest model is setting the collision term to zero $(\partial f_j/\partial t)_{\text{coll}} = 0$, considering the plasma as collisionless. This is justified by considering that $\sum_k C_{jk}$ is of the order of Λ^{-1}, as described in Section 2.1.5. It can be shown [66] that $\Lambda \simeq N_D$, and that a collision frequency ν_{coll} related to the collision term, depends on $\nu_{\text{coll}} \sim \omega_p/\Lambda$ if we assume ν_{coll} as a similar shape as ν_{ei} in Section 2.1.5. As such, when $\Lambda \to \infty$, the collision term becomes negligible. Eq. 2.40 becomes the *Vlasov equation*:

$$\frac{\partial f_j}{\partial t} + \boldsymbol{v} \cdot \frac{\partial f_j}{\partial \boldsymbol{x}} + \frac{q_j}{m_j}\left(\boldsymbol{E} + \frac{\boldsymbol{v}}{c} \times \boldsymbol{B}\right)\frac{\partial f_j}{\partial \boldsymbol{v}} = 0, \tag{2.46}$$

- Another simple model is the *Krook model*, also called *relaxation time approximation*. In this model, the collision term is described by using a characteristic frequency ν_{jk} [104], so that:

$$\sum_k C_{jk} = \sum_k \nu_{jk}\left(f_j - f_{jk}^0\right), \tag{2.47}$$

  which implies that the distribution f_j tends to relax towards an equilibrium distribution f_{jk}^0, due to collisions, in a characteristic time $\tau_{jk} = \nu_{jk}^{-1}$. Following the derivation in [79], it is assumed that the distribution at equilibrium is a Maxwell-Boltzmann distribution that takes into account the interaction between particles:

$$f_{jk}^0 = n_j \left(\frac{m_j}{2\pi T_{jk}}\right)^{3/2} \exp -\frac{m_j(\boldsymbol{v} - \boldsymbol{u}_{jk})^2}{2T_{jk}}, \tag{2.48}$$

  where the quantities $\boldsymbol{u}_{jk}$ and T_{jk} (in eV) are defined as:

$$n_j \equiv \int f_j d^3v, \tag{2.49a}$$

$$(n_j m_j + n_k m_k)\boldsymbol{u}_{jk} = \int \boldsymbol{v}(m_j f_j + m_k f_k) d^3v, \tag{2.49b}$$

$$\frac{3}{2}(n_j + n_k)T_{jk} = \frac{1}{2}\int (\boldsymbol{v} - \boldsymbol{u}_{jk})^2 (m_j f_j + m_k f_k) d^3v, \tag{2.49c}$$

and represent average velocities and temperatures for an effective particle species, resulting from the average of the j-th and the k-th one.
We can define f_j as the superposition of the equilibrium plus a perturbation, $f_j \equiv f_j^0 + \tilde{f}_j$, where f_j^0 is the Maxwell-Boltzmann distribution at equilibrium for the j-th particle population, with a similar shape to Eq. 2.48, but without the k contribution. Developing in series the f_{jk}^0 distribution around $\boldsymbol{u}_{jk} = \mathbf{0}$ and $T_{jk} = T_j$, we obtain its approximated (to first order) form as:

$$(f_{jk}^0)_{\text{apx}} = f_j^0 + \delta\boldsymbol{u}_{jk} \cdot \left(\frac{\partial f_{jk}^0}{\partial \boldsymbol{v}}\right) + \delta T_{jk} \left(\frac{\partial f_{jk}^0}{\partial T_{jk}}\right), \tag{2.50}$$

where $\tilde{\boldsymbol{u}}_{jk}$ and $\tilde{T}_{jk}$ are defined as:

$$n_j^0 \equiv \int f_j^0 d^3v, \tag{2.51a}$$

$$(n_j^0 m_j + n_k^0 m_k)\delta\boldsymbol{u}_{jk} = \int \boldsymbol{v}(m_j\tilde{f}_j + m_k\tilde{f}_k)d^3v, \tag{2.51b}$$

$$\frac{3}{2}(n_j^0 + n_k^0)\delta T_{jk} = \frac{1}{2}\int \boldsymbol{v}^2(m_j\tilde{f}_j + m_k\tilde{f}_k)d^3v. \tag{2.51c}$$

Using the result of Eq. 2.50 as the truncated Krook operator, and considering that the temperature variation are of second order with respect to the velocity ($T_{jk\sim v_{jk}^2}$), we finally obtain:

$$\sum_k C_{jk} \sim \left(\sum_k C_{jk}\right)_{\text{apx}} = -\sum_k \nu_{jk}\left[\tilde{f}_j - \frac{m_j \boldsymbol{v}\cdot\delta\boldsymbol{u}_{jk}}{T_j} f_j^0\right]. \tag{2.52}$$

In particular, if we consider $j = e$ and $k = e, i$, we obtain that Eq. 2.52 is a sum of terms originated by both electron-electron $\nu_{jk} = \nu_{ee}$ and electron-ion $\nu_{jk} = nu_{ei}$ collisions, approximated to the electron-ion contribution only for high significant charge numbers Z_{eff} (see Section 2.1.5). By using this model for the collision term, Eq. 2.40 is also called *BGK equation*, from Bhatnagar, Gross, Krook. We will mainly use the BGK model and the Krook operator for describing collisions, due to its simplicity to treat.

- The BGK model is correct for collisions between charged and neutral particles, but not accurate when both particles are charged. In such case, the many, low-angle collisions are more significant than binary collisions. The collision term can be modeled, following [66], [46] and [116]:

$$\left(\frac{\partial f_j}{\partial t}\right)_{\text{coll}} = -\sum_{s=1}^{3}\frac{\partial}{\partial v_s}\left[F_s f_j + \frac{1}{2}\sum_{q=1}^{3}\frac{\partial}{\partial v_q}\left(D_{sq} f_j\right)\right], \tag{2.53}$$

where the indexes s and q are for the x,y,z axes. The first term on the left side of Eq. 2.53 is a friction term, where the vector $\boldsymbol{F}$ is a dynamic friction coefficient. The second term represents a diffusion term in velocity space, represented by the double tensor $\overline{\overline{D}}$, which is the diffusion coefficient. With this term, Eq. 2.40 becomes known as the *Fokker-Planck equation*. The friction coefficient can be approximated as $\boldsymbol{F} = -\nu_{ij}(\boldsymbol{v} - \boldsymbol{u})$, where $\boldsymbol{u}$ is the local drift velocity, and ν_{ij} is the collision frequency between particles. The diffusion coefficient can be simplified as $\overline{\overline{D}} = D\overline{\overline{I}}$.

The choice of this term changes the assumptions made on the collisions. We will see in section 2.2 that the choice of this term will have repercussions on the plasma response to a propagating electromagnetic wave.

2.2 Propagation of an electromagnetic wave in a plasma

2.2.1 Properties of a propagating wave

We now describe the most general properties for a propagating wave in a plasma. We will introduce the phase and group velocities belonging to a propagating wave, as well as their intensity. Moreover, we will describe the plasma response to a propagating wave, by modifying its dielectric permittivity accordingly. The concept of *inverse bremsstrahlung* will be introduced as well.

2.2.1.1 Group and phase velocities, wave intensity

Consider a monochromatic wave in the shape of $\boldsymbol{A} = A_0 \exp[i(\boldsymbol{k} \cdot \boldsymbol{x} - wt)]$, where $\boldsymbol{k}$ and ω are the mode wave vector and frequency, respectively, and propagating along the x axis, so that $\boldsymbol{k} = k\hat{\boldsymbol{x}}$ and $A = A_0 \exp[i(kx - \omega t)]$.
It is defined as *phase velocity* the speed at which an observer sees a constant phase for the wave A. Since the phase in this case is $(kx - \omega t)$:

$$\frac{d}{dt}(kx - \omega t) = k\frac{dx}{dt} - \omega = 0, \tag{2.54a}$$

$$v_{ph} \equiv \frac{\omega}{k}. \tag{2.54b}$$

The velocity v_{ph} can exceed the speed of light, but it is associated to a rigorously periodic wave, which carries no information.
Considering a simple modulated wave, by summing two waves $(\omega_1, \boldsymbol{k}_1)$ and $(\omega_1, \boldsymbol{k}_2)$ with a small difference $(\Delta\omega, \Delta\boldsymbol{k}) \ll (\omega_i, \boldsymbol{k_i})$ between the two, it is possible to describe the modulation of a *wave packet* composed by the two original waves. We can then derive that the modulated wave propagates with a *group velocity* $v_g = \Delta\omega/\Delta k$. When $\Delta k \to 0$:

$$v_g \equiv \frac{d\omega}{dk}. \tag{2.55}$$

While the phase velocity is the rate at which the wave phase is carried in space, the group velocity is defined as the velocity of popagation of its energy. In the great majority of cases, the group velocity is lower than the speed of light. However, there are cases in which v_g can be bigger than c, or even negative. In such cases, the term *anomalous dispersion* is used, the wave packet behavior is very complicated to describe, and the group velocity loses its physical meaning [66].
Finally, with these definitions it is possible to define the *refraction index*, which reads:

$$n \equiv \frac{c}{v_{ph}} = \frac{ck}{\omega}, \tag{2.56}$$

which describes the refraction of a light wave within the medium. In case of anisotropies in the material, the index of refraction becomes a double tensor, and it is thus needed to specify n for every propagation direction. Moreover, n can assume complex values and therefore be decomposed into $n = n_R + in_I$, where N_R describes the wave propagation in the material, and N_i describes its *damping*.

Finally, with these notions we can define the *wave intensity* as:

$$I \equiv \frac{cn|\boldsymbol{E}|^2}{8\pi}, \tag{2.57}$$

where c is the speed of light and n is the refraction index. This is an indication of the energy flux of an incident wave in a material, and it represents the magnitude of the *Poynting vector* [66].

2.2.1.2 Dielectric permittivity

Assuming the ions as fixed, we will now use the kinetic description for a plasma of Eq. 2.40 applied to fluctuations of the electron distribution function $\tilde{f}_e$ only, where $f_e \equiv f_e^0 + \tilde{f}_e$ (f_e^0 being a Maxwell Boltzmann distribution describing plasma at thermal equilibrium), using the Krook operator to model the collision term (BGK model). Assuming the magnetic fields are negligible with respect to the electric ones ($\boldsymbol{B} \sim 0$), and that $v_{ph} \gg v_{Te}$, we obtain [90]:

$$\frac{\partial \tilde{f}_e}{\partial t} - \frac{e}{m_e}\boldsymbol{E} \cdot \frac{\partial f_e^0}{\partial \boldsymbol{v}} = -\sum_{j=e,i} \nu_{ej} \left[\tilde{f}_e - \frac{m_e \boldsymbol{v} \cdot \delta \boldsymbol{u}_{ej}}{T_e} f_e^0 \right]. \tag{2.58}$$

Since $\nu_{ee} \ll \nu_{ei}$ for $Z_{\text{eff}} \gtrsim 4$, we can neglect the term depending on electron-electron collisions within the sum. Moreover, for the properties of Maxwell-Boltzmann distributions, $\partial f_e^0 / \partial \boldsymbol{v} = -m_e \boldsymbol{v} f_e^0 / T_e$. After these considerations, and applying the Fourier transform in time to Eq. 2.58, we obtain:

$$-i\omega \tilde{f}_e + \frac{e}{T_e}\boldsymbol{E} \cdot \boldsymbol{v} f_e^0 = -\nu_{ei} \tilde{f}_e. \tag{2.59}$$

Defining the polarization current density as $\boldsymbol{J}_{pol} \equiv e \int \boldsymbol{v} \tilde{f}_e d^3\boldsymbol{v}$, and noting that in Fourier space $\boldsymbol{J}_{pol} = i\omega \boldsymbol{P}_{pol}$ because of Eqs. 2.3 and 2.6, we obtain:

$$-i\omega \boldsymbol{P}_{pol} - \frac{e^2}{m_e} n_e^0 \boldsymbol{E} = -\nu_{ei} \boldsymbol{J}_{pol}, \tag{2.60}$$

where $n_e^0 = \int f_e^0 d^3v$. Remembering that $\boldsymbol{P} = \chi_e \boldsymbol{E}$, we can give an expression of the conductivity σ:

$$\boldsymbol{P}_{pol} = \sigma \boldsymbol{E} = -i\omega \chi_e \boldsymbol{E} = \frac{i\omega_{pe}^2}{4\pi(\omega + i\nu_{ei})} \boldsymbol{E}, \tag{2.61}$$

where $\omega_{pe} \equiv \sqrt{4\pi e^2 n_e^0 / m_e}$ is the electron plasma frequency. For the definition of Eq. 2.18, and considering the plasma as homogeneous and isotropic ($\overline{\overline{\epsilon}} = \epsilon \overline{\overline{I}}$), we obtain the expression of the *dielectric coefficient* as a function of the wave frequency ω:

$$\epsilon = 1 - \frac{\omega_{pe}^2}{\omega(\omega + i\nu_{ei})}, \tag{2.62}$$

Decomposing ϵ into a real and an imaginary component $\epsilon = \epsilon_R + i\epsilon_I$:

$$\epsilon_R = 1 - \frac{(\omega_{pe}^2/\omega^2)}{1 + (\nu_{ei}/\omega)^2} \sim 1 - \left(\frac{\omega_{pe}}{\omega}\right)^2, \tag{2.63a}$$

$$\epsilon_I = \frac{\nu_{ei}}{\omega} \frac{(\omega_{pe}/\omega)^2}{1 + (\nu_{ei}/\omega)^2} \sim \frac{\nu_{ei}}{\omega} \left(\frac{\omega_{pe}}{\omega}\right)^2. \tag{2.63b}$$

The approximate form of Eqs. 2.63 has been obtained in the case of low collisionality, or $\nu_{ei} \ll \omega$, which allowed to expand in Taylor series and keep the first order term only. In such a case, Eq. 2.63a describes the form of ϵ in the case of collisions being neglected. Since this implies neglecting thermal effects within the plasma, this is also called *cold plasma approximation*, and it is approximated by $\epsilon = \epsilon_R$. If collisions are small compared to the wave frequency, but non negligible, then ϵ includes its imaginary component approximated as in Eq. 2.63b as well.

2.2.2 Dispersion relation in a cold plasma

We now consider the propagation of an electromagnetic wave in a plasma. The electric and magnetic fields are of the form $\boldsymbol{E} = \boldsymbol{E}(\boldsymbol{x}) \exp(-iwt)$, and $\boldsymbol{B} = \boldsymbol{B}(\boldsymbol{x}) \exp(-iwt)$. Using the system of equations 2.11 with $\boldsymbol{D} = \boldsymbol{E}$ and $\boldsymbol{H} = \boldsymbol{B}$ (i.e., polarization and magnetization are

negligible in the considered plasma), and taking the second equation of the system 2.11 and using it in its fourth equation, we obtain:

$$\nabla \times (\nabla \times \boldsymbol{E}) = -\frac{1}{c^2}\left(4\pi \boldsymbol{J} + \frac{\partial \boldsymbol{E}}{\partial t}\right), \tag{2.64}$$

which is the *wave equation* of an electric field. As previously stated, in Fourier space we can use the transformations $\nabla \to i\boldsymbol{k}$ and $\partial/\partial t \to -iw$. Thus, applying the Fourier transform to Eq. 2.64, and using the relation between $\boldsymbol{J}$ and $\boldsymbol{E}$ in Eq. 2.16, we obtain the equation [66]:

$$\frac{c^2}{\omega^2}\boldsymbol{k} \times (\boldsymbol{k} \times \boldsymbol{E}) = -\left(\overline{\overline{I}} + \frac{4\pi i}{\omega}\overline{\overline{\sigma}}\right) : \boldsymbol{E} = -\overline{\overline{\epsilon}} : \boldsymbol{E}. \tag{2.65}$$

Moreover, in the last step we used the definition of $\overline{\overline{\epsilon}}$ (Eq. 2.18). Since $\nabla \times (\nabla \times \boldsymbol{X}) = \nabla(\nabla \cdot \boldsymbol{X}) + \nabla^2 \boldsymbol{X}$, the left hand side of Eq. 2.65 becomes:

$$\boldsymbol{k} \times (\boldsymbol{k} \times \boldsymbol{E}) = \boldsymbol{k}(\boldsymbol{k} \cdot \boldsymbol{E}) - k^2 \boldsymbol{E} = \overline{\overline{\boldsymbol{kk}}} : \boldsymbol{E} - k^2 \boldsymbol{E}, \tag{2.66}$$

where $\overline{\overline{\boldsymbol{kk}}}$ is a double tensor with elements $k_i k_j$ $(i, j = 1, 2, 3)$. Considering that $k_i k_j = k^2$ when $i = j$, it can be verified that $\overline{\overline{\boldsymbol{kk}}} : \boldsymbol{E} - k^2 \boldsymbol{E} = k^2(\overline{\overline{\boldsymbol{kk}}}/k^2 - \overline{\overline{I}}) : \boldsymbol{E}$, thus obtaining, from Eq. 2.65:

$$\left[\frac{c^2 k^2}{\omega^2}\left(\frac{\overline{\overline{\boldsymbol{kk}}}}{k^2} - \overline{\overline{I}}\right) + \overline{\overline{\epsilon}}\right] : \boldsymbol{E} = 0. \tag{2.67}$$

A similar derivation can be found for the $\boldsymbol{B}$ field. Eq. 2.67 is called *wave equation*, and it is a system of three scalar linear equations describing an electromagnetic wave propagation in an homogeneous plasma in three dimensions. The conditions of existence for this system for $\boldsymbol{E} \neq 0$ is that the determinant of the matrix in Eq. 2.67 must be set to 0. This equation is defined as *dispersion relation*:

$$D(\omega, \boldsymbol{k}) \equiv \det\left[\frac{c^2 k^2}{\omega^2}\left(\frac{\overline{\overline{\boldsymbol{kk}}}}{k^2} - \overline{\overline{I}}\right) + \overline{\overline{\epsilon}}(\omega, \boldsymbol{k})\right] = 0. \tag{2.68}$$

2.2.2.1 WKB theory

Consider an electric field of the form $\boldsymbol{E}(z) = E_x(z)\boldsymbol{e}_x + E_y(z)\boldsymbol{e}_y + E_z(z)\boldsymbol{e}_z$, where z is the direction of the wave propagation. The framework of the *WKB (Wentzel-Kramers-Brillouin) theory* is to seek transverse solutions $E_{x,y}(z)$ to the system 2.67 of the form:

$$E_x(z) = E_{x,0}(z) \exp\left[ik_v \int_0^z \Psi(x)dx\right], \tag{2.69}$$

where k_f is the wave number of the wave in vacuum. The same can be done for the y component. The field $E_{x,0}(z)$ and the function Ψ are under the hypothesis of slowly varying on a wavelength scale, or *Slowly Varying Envelope Approximation* (SVEA):

$$\left|\frac{d^2 E_{x,0}(z)}{dz^2}\right| \ll \left|k_v \Psi(z) \frac{E_{x,0}(z)}{dz}\right|, \tag{2.70a}$$

$$\left|\frac{d^2 \Psi(z)}{dz^2}\right| \ll \left|k_v \Psi(z) \frac{d\Psi(z)}{dz}\right|. \tag{2.70b}$$

We define $k(z) \equiv k_v \Psi(z)$. The transverse solutions to the system 2.67, inversely transformed in real space, will be reduced to the *Helmholtz equation* $(\Delta + \omega^2 \epsilon/c^2) E_{x,y}(z) = 0$. We define the first and second spatial derivatives as $(\bullet)'$ and $(\bullet)''$, respectively. Using the form of the transverse electric field in Eq. 2.69 within the Helmholtz equation, we obtain:

$$E''_{x,0} + 2ik_v E'_{x,0}\Psi + ik_v E_{x,0}\Psi' - k_v^2 E_{x,0}\Psi^2 + k_v^2 \epsilon(\omega, z) E_{x,0} = 0, \tag{2.71}$$

which, taking the 0-th and first order respectively and neglecting the second order terms according to the SVEA, we obtain:

$$\Psi = \sqrt{\epsilon(\omega, z)}, \tag{2.72a}$$

$$2E'_{x,0}\Psi + E_{x,0}\Psi' = 0 \quad \rightarrow \quad E_{x,0} = \frac{\text{const}}{\sqrt{\Psi}}. \tag{2.72b}$$

Taking as constant in Eq. 2.72b the amplitude of the transverse electric field in vacuum E_v, the solution of Eq. 2.69 assumes the form:

$$E_x(z) = \frac{E_v}{\epsilon(\omega, z)^{1/4}} \exp\left[ik_v \int_0^z \sqrt{\epsilon(\omega, z')}dz'\right]. \tag{2.73}$$

The result of Eq. 2.73 highlights that, the amplitude of a transverse electric field propagating within a plasma is amplified from the vacuum case by a factor of $\epsilon^{-1/4}$, in the SVEA approximation (Eq. 2.72a).

2.2.2.2 Inverse bremsstrahlung

The imaginary component in Eq. 2.63b indicates a *damping* process, transferring energy from the wave to the particles within the plasma. In this case, this transfer occurs through collisions, which are caused by particles that absorbed energy from the wave through a process called *inverse bremsstrahlung*. In the case of *bremsstrahlung* (*brake radiation*) a particle interacting with another through a collision of Coulombian nature will change its velocity. By the properties of an accelerating/decelerating charge, a particle will emit electromagnetic radiation during a collision, therefore advecting energy from the system. As a consequence of this loss in energy, the interacting particles will decelerate. In the process of *inverse bremsstrahlung*, a traveling wave will be absorbed by a particle, which is accelerated by the gain in energy. The second particle will then acquire energy through the Coulomb collision with the first one.
In Inertial Confinement Fusion scenarios, this mechanism couples the laser wave to the particles within the coronal plasma around the ICF target, resulting in an energy transfer to the particles which advects to the rest of the plasma through electron-ion collisions.
Following the WKB theory, the absorption coefficient for inverse bremsstrahlung κ_{IB}, in its simplest form, is given by [46, 47]:

$$\kappa_{IB} = 2\Im(k) = \frac{\nu_{ei}(n_c)}{c}\frac{n_e}{n_c}\left(1 - \frac{n_e}{n_c}\right)^{-1/2}, \tag{2.74}$$

where we used the definition of plasma frequency. Eq. 2.74 is valid for $n_e > n_c$, where n_c is the *critical density*, which we will provide a definition for in section 2.2.3.1. Substituting the expression of ν_{ei} from Eq. 2.35b, we obtain:

$$\kappa_{IB} \sim \frac{Z_{\text{eff}}}{T_e^{3/2}} n_e^2 \left(1 - \frac{n_e}{n_c}\right)^{-1/2}. \tag{2.75}$$

A more detailed form of the absorption coefficient has been provided by Johnston and Dawson [117], where the ν_{ei} rate is substituted by $\nu_{IB} = \nu_{ei} \ln\Lambda_{IB}/\ln\Lambda_{ei}$:

$$\kappa_{IB} = \frac{16\pi Z_{\text{eff}} n_e^2 e^6 \ln\Lambda_{IB}(\omega)}{3c\omega^2(2\pi m_e T_e)^{3/2})(1 - n_e/n_c)^{1/2}}, \tag{2.76}$$

where the related Coulomb logarithm $\ln\Lambda_{IB}$ is a function of ω. Moreover, we can substitute the expression of ϵ in Eq. 2.62 as:

$$\epsilon_{IB} = 1 - \frac{\omega_{pe}^2}{\omega(\omega + i\nu_{IB})}, \tag{2.77}$$

2.2.3 Solutions for the cold plasma approximation

Eq. 2.67 describes the relation between the frequency ω and the wave vector $\boldsymbol{k}$ of a wave propagating in a plasma. Assuming that the plasma is homogeneous and isotropic, $\overline{\overline{\epsilon}} = \epsilon\overline{\overline{I}}$. Moreover, we will not consider the temperature effects on the system, so that the shape of ϵ will be given by Eq. 2.68. In this case, the system is called a *cold plasma*. We assume wave propagation in the $\widehat{z}$ direction only, so that $\boldsymbol{k} = k\widehat{z}$ and $\overline{\overline{k\hat{k}}} = k^2\overline{\overline{\hat{z}\hat{z}}}$. Thus, Eq. 2.67 becomes:

$$\begin{pmatrix} \epsilon - (k^2c^2)/\omega^2 & 0 & 0 \\ 0 & \epsilon - (k^2c^2)/\omega^2 & 0 \\ 0 & 0 & \epsilon \end{pmatrix} \begin{pmatrix} E_x \\ E_y \\ E_z \end{pmatrix} = \begin{pmatrix} 0 \\ 0 \\ 0 \end{pmatrix}. \tag{2.78}$$

Following Eq. 2.68, the dispersion relation reads:

$$\epsilon \left(\epsilon - \frac{k^2c^2}{\omega^2} \right)^2 = 0, \tag{2.79}$$

which has two possible solutions:

- $\boldsymbol{\epsilon = 0}$. Applying this solution in Eq. 2.78 gives that $E_x, E_y = 0$, while $E_z \neq 0$. Therefore, the waves belonging to this solution exist in the $\boldsymbol{z}$ direction, and labeled as *longitudinal waves*. Combining this solution with the form of ϵ in a cold, collisionless plasma:

$$\epsilon = 1 - \frac{\omega_{pe}^2}{\omega^2} = 0 \quad or \quad \omega^2 = \omega_{pe}^2, \tag{2.80}$$

  where the electron plasma frequency ω_{pe} has been used since $\omega_p^2 = \omega_{pi}^2 + \omega_{pe}^2 \sim \omega_{pe}^2$, due to $m_i \gg m_e$. These waves are longitudinal waves caused by the oscillations ($\propto \omega_{pe} \propto \sqrt{n_e}$) of the electron population in the plasma, also called *plasma oscillations* or *Langmuir oscillations*, since they do not propagate in space.

- $\boldsymbol{\epsilon = c^2k^2/\omega^2}$. Eq. 2.78 gives $E_x, E_y \neq 0$ and $E_z = \boldsymbol{E} \cdot \boldsymbol{k} = 0$. These waves are called *transverse waves*. From Eq. 2.78, this means that:

$$1 - \frac{\omega_{pe}^2}{\omega^2} = \frac{c^2k^2}{\omega^2} \quad or \quad \omega^2 = \omega_{pe}^2 + k^2c^2. \tag{2.81}$$

  Differently from the longitudinal waves, the transverse ones propagate in space (depending on k). Moreover, it should be noted that, given the definitions of the refraction index N_{cold} (Eq. 2.56) and the definition of dielectric permittivity in a cold plasma, $\epsilon = \epsilon_R$ (Eq. 2.63):

$$N_{cold}(\omega) \equiv \frac{ck}{\omega} = \sqrt{1 - \frac{n_e}{n_c}} = \sqrt{\epsilon_R}. \tag{2.82}$$

  In this case, the refraction index is a purely real quantity, and as such there are no damping processes in the medium.

2.2.3.1 Interaction between plasma and waves: critical density.

In the transverse wave solution, Eq. 2.81 can be inverted to give:

$$k = \frac{\sqrt{\omega^2 - \omega_{pe}^2}}{c}. \tag{2.83}$$

If $\omega < \omega_{pe}$, the wave number k becomes imaginary. This means that the propagating wave term in space ($\propto \exp(ikx)$) will become a real-valued decreasing exponential, thus converting the

wave into a *evanescent wave*. Given the definition of the electron plasma frequency from Eq. 2.23, we can derive a condition on density:

$$n_c \equiv \frac{m_e \omega^2}{4\pi e^2} = \frac{1.11 \times 10^{21}}{\lambda_0}, \tag{2.84}$$

where ω is the transverse wave frequency. This threshold density at which $\omega = \omega_{pe}$ is called *critical density*, and it is the plasma density beyond which the laser cannot propagate anymore, but vanishes exponentially. The right side of Eq. 2.84 is the expression of n_c in practical units, where λ_0 is the incident wavelength in μm ($\omega = 2\pi c/\lambda_0$), and the resulting critical density is in cm^{-3}. With the result from Eq. 2.84 and the definition of plasma frequency, we can rewrite Eq. 2.62 as a function of the plasma density:

$$\epsilon = 1 - \frac{n_e}{n_c}. \tag{2.85}$$

In ICF scenarios, a normally incident laser wave will propagate in the coronal plasma around the fuel target up until $n_e = n_c$ ($n_e < n_c$ for obliquely incident plasmas), after which it will be reflected with a small fraction that vanishes exponentially at higher densities. Therefore, the energy coupling between laser and target must be mediated by the plasma through several energy transfer processes, one of which is considering the effects of temperature in the plasma.

2.2.4 Warm plasmas

We now include temperature effects in the plasma, which means including the effects of spatial dispersion as well. Since thermal effects predominantly influence waves with a phase velocity small with respect to the thermal velocity of the plasma particles, $v_{ph} \ll v_T$, the waves associated with them are mainly longitudinal (solution of Eq. 2.68 for the direction of propagation). Considering the continuity and momentum equations in Eqs. 2.43, neglecting the viscosity tensor and the collision term, and closing the system with the polytropic equation 2.44, we derive an expression for the small-amplitude fluctuations x_1 around an average quantity x_0, in the form $x = x_0 + x_1$. Finally, applying the Fourier transform to the system of equations, we can derive an expression for the electric conductivity:

$$\sigma = \frac{i}{\omega}\left[\sum_j \frac{n_{0j} q_j^2}{m_j}\left(1 - \frac{\gamma_j p_{0j}}{m_j n_{0j}}\frac{k^2}{\omega^2}\right)^{-1}\right], \tag{2.86}$$

where γ_j is the polytropic index of Eq. 2.44. Introducing the *acoustic velocity for the j-th species* as $c_{sj}^2 \equiv (\gamma_j p_{0j})/(n_{0j} m_j)$, following the definition of ϵ (Eq. 2.18) we obtain the expression for the *dielectric permittivity in a warm plasma*:

$$\epsilon = 1 - \sum_j \frac{\omega_{pj}^2}{\omega^2 - k^2 v_{0j}^2}, \tag{2.87}$$

where ω_{pj} is the plasma frequency for the j-th species (Eq. 2.23). Considering two fluid populations (the electrons and one ion species), the dispersion relation for the longitudinal modes gives an expression for the wave frequency:

$$\omega^2 = P\left[1 \pm \sqrt{1 - Q}\right], \tag{2.88a}$$

$$P = (1/2)\left[\omega_p^2 + k^2(v_{0e}^2 + v_{0i}^2)\right], \tag{2.88b}$$

$$Q = \frac{4k^2(\omega_{pe}^2 v_{0i}^2 + \omega_{pi}^2 v_{0e}^2 + k^2 v_{0i}^2 v_{0e}^2)}{[\omega_p^2 k^2 (v_{0e}^2 + v_{0i}^2)]^2}, \tag{2.88c}$$

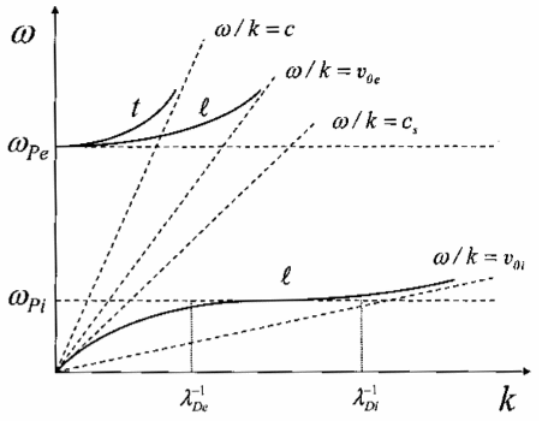

Figure 2.4: Dispersion relations for the transverse and longitudinal waves for warm, collisionless, $\boldsymbol{B}$-free plasmas. Image from [66].

where $\omega_p^2 \equiv \omega_{pe}^2 + \omega_{pi}^2$, from the definition of the total plasma frequency. Since $Q \propto m_e/m_i$, we can approximate Eq. 2.88 as $\omega^2 \simeq P[1 \pm (1 - Q/2)]$ and, considering that $v_{0i}^2 \ll v_{0e}^2$ as well, we obtain two solutions for the warm plasma wave frequency:

$$\omega_+^2 \simeq \omega_p^2 + k^2 v_{0e}^2, \tag{2.89a}$$

$$\omega_-^2 \simeq k^2 v_{0i}^2 \left[\frac{k^2 \omega_{pe}^2 / v_{0e}^2 + \omega_{pi}^2 / v_{0i}^2}{k^2 + \omega_p^2 / v_{0e}^2} \right]. \tag{2.89b}$$

It should be noted that, when introducing the temperature effects, these waves propagate in space with a group velocity $v_g = dw/dk \neq 0$, in contrast with the cold approximation. We now look at the two solutions of Eq. 2.89:

- From the first solution of 2.89, if k is small, we retrieve the plasma oscillations $\omega_+^2 \simeq \omega_{pe}^2$ found in the cold approximation. For high values of k we find $\omega_+^2 \simeq k^2 v_{0e}^2$, thus obtaining $\omega_+/k \simeq v_{0e}$, similar to a transverse wave. Considering $\gamma_e = 3$ (which means the system has only one degree of freedom, or a one-dimensional oscillation), we obtain the *Bohm-Gross dispersion frequency*:

  $$\omega_{EPW}^2 = \omega_+^2 = \omega_{pe}^2 + 3\frac{T_e}{m_e} k_{EPW}^2. \tag{2.90}$$

  These longitudinal traveling waves are called *Langmuir Waves* or *Electron Plasma Waves* (EPWs).

- Considering again a two-fluid system (electrons and single species ions), the second solution can be rewritten as a function of the Debye length for each particle population λ_{Dj}. From the kinetic theory [66], these waves propagate only for $T_e \gg T_i$, or $\lambda_{De}^{-1} \gg \lambda_{Di}^{-1}$, undergoing strong damping when the two temperatures are similar. The solution has a different form according to the value of the considered wave vector k. Focusing on $k \ll \lambda_{De}^{-1} \ll \lambda_{Di}^{-1}$, the frequency for the ions is:

  $$\omega_{IAW}^2 = \omega_-^2 = k_{IAW}^2 v_{0i}^2 \left(\frac{Z v_{0e}^2 m_e}{v_{0i}^2 m_i} + 1 \right) = k_{IAW}^2 \left(v_{0e}^2 \frac{Z m_e}{m_i} + v_{0i}^2 \right) \simeq k_{IAW}^2 c_s^2, \tag{2.91}$$

  where we defined the *ion acoustic velocity* c_s as:

  $$c_s^2 \equiv \frac{\gamma_e n_{0e} T_e + \gamma_i n_{0i} T_i}{n_{0e} m_e + n_{0i} m_i} \simeq \frac{Z\gamma_e T_e + \gamma_i T_i}{Z m_e + m_i} \simeq v_{0e}^2 \frac{Z m_e}{m_i} + v_{0i}^2, \tag{2.92}$$

where we approximated for $Zm_e \ll m_i$. Under the previous assumption of $T_e \gg T_i$, the term $v_{0e}^2 Zm_e/m_i$ from the second result of Eq. 2.92 can be rewritten as:

$$c_s^2 \simeq \frac{Z\gamma_e T_e}{m_i}. \tag{2.93}$$

From the kinetic theory, in this case it can be demonstrated that $\gamma_e = 1$, implying that the particles have an infinite number of degrees of freedom, therefore behaving as free particles, while $\gamma_i = 3$ (one degree of freedom, 1-D oscillation). These waves are called *Ion Acoustic Waves* (IAW).

For values of $\lambda_{De}^{-1} \ll k \ll \lambda_{Di}^{-1}$, we find that:

$$\omega_-^2 = \frac{v_{0i}^2}{\gamma_i \lambda_{Di}^2} = \omega_{pi}^2, \tag{2.94}$$

which are *ion plasma oscillations*, with no propagation ($v_g = 0$).

Finally, for $\lambda_{De}^{-1} \ll \lambda_{Di}^{-1} \ll k$, we have that k is dominant in the expression of ω_-^2, thus obtaining:

$$\omega_-^2 = k^2 v_{0i}^2 + \frac{v_{0i}^2}{\gamma_i \lambda_{Di}^2} = \omega_{pi}^2 + k^2 v_{0i}^2 \simeq k^2 v_{0i}^2, \tag{2.95}$$

where in the last iteration we assumed $k^2 \gg \lambda_{Di}^{-2}$. These traveling waves ($v_g \neq 0$) are called *ion plasma waves*.

In Figure 2.4 it is possible to see the waves described for a warm plasma, where the letters "t" and "l" correspond to transverse and longitudinal modes, respectively.

Finally, we briefly consider the addition of collisions. By doing so, we obtain an additional imaginary term in both Eqs. 2.90 and 2.91, which corresponds to a damping rate of the wave proportional to electron-ion and ion-ion collisions, respectively:

$$\nu_{EPW,coll} = \frac{\nu_{ei}}{2}, \tag{2.96a}$$

$$\nu_{IAW,coll} = \frac{v_{Ti}^2 \nu_{ii}}{2c_s^2}. \tag{2.96b}$$

2.2.5 Kinetic formulation of electrostatic waves: Landau damping

In a warm, unmagnetized plasma, the temperature effects gave a set of waves that propagate in space. However, those results have been obtained with a multiple fluid description. In this Section we will describe the effects on the dispersion relation when kinetic effects are being considered, and in particular the appearance of a collisionless, purely kinetic damping term not observable in a multi-fluid description, which will be of fundamental importance in the context of hot electron generation.

An early result was obtained by Vlasov, by linearizing equation 2.39 with the collision term set to 0 (i.e. Vlasov equation), decomposing the distribution function in $f_j = f_{0j} + \tilde{f}_j$, f_{0j} being the distribution at equilibrium, and $\boldsymbol{E} = \tilde{\boldsymbol{E}} \exp(i\boldsymbol{k} \cdot \boldsymbol{r} - \omega t)$, where the tilde indicates a small perturbation. Taking the Fourier transform both in time and space of the resulting equation, and remembering that $\boldsymbol{J} = e \int \boldsymbol{v}(\tilde{f}_i - \tilde{f}_e) d^3v$, one finds an expression for the generalized Ohm's law, and thus a form for the conductivity tensor [118]. The resulting equation has a pole in $v_z = \omega/k$, which is undefined unless specifying an integration path that is always below or above the pole. Vlasov [119] assumed the pole to be always above the integration path ($\Im\omega$) and chose to take the principal part of the integral, the average of the two paths above and below the pole. Using the definition of most probable velocity $v_j^2 \equiv 2T_j/m_j$, one can find the transverse and longitudinal components for the conductivity as a function of $Z(\zeta)$ and its derivative $Z'(\zeta)$,

defined as the *plasma dispersion function*, or *Zeta function*, a function tabulated by Fried and Conte [120] of the form:

$$Z(\zeta) \equiv \frac{1}{\sqrt{\pi}} \int_{\infty}^{\infty} \frac{\exp\left(-\xi^2\right)}{\xi - \zeta} d\xi, \quad \Im\zeta > 0. \tag{2.97}$$

By deriving the permittivity from the expression of the conductivity, and setting it to zero, one can find the associated dispersion relation, with the corresponding solution being:

$$\omega \simeq \omega_{pe} \left[1 + \frac{3}{4} \left(\frac{v_{Te}}{v_{ph}} \right)^2 - i\sqrt{\pi} \left(\frac{v_{ph}}{v_{Te}} \right)^3 \exp\left(-\frac{v_{ph}^2}{v_{Te}^2} \right) \right], \tag{2.98}$$

which has an imaginary part $\Im(\omega) < 0$, in contradiction with the initial assumption. Therefore, the problem is not well posed.

Landau [121] found a solution by treating the problem as an initial value problem, by using on the Vlasov equation the Fourier transform in space, but the *Laplace transform* (and its inverse) in time, with its time derivative being:

$$\left(\frac{dX}{dt} \right)_p = pX_p + \left[X \exp\left(-pt\right) \right]_{t=0}^{t \to \infty}. \tag{2.99}$$

Applying these transforms to the Vlasov equation, by introducing the Laplace transform of the electrostatic potential $\tilde{\phi}_p$, we find the form of the potential in real space [118]:

$$\phi(z,t) = \int_{\sigma - i\infty}^{\sigma + i\infty} \frac{dp}{2\pi i} \int_{-\infty}^{+\infty} \frac{1}{2\pi} \tilde{\phi}_p(k,p) \exp\left(ikx + pt\right) dk. \tag{2.100}$$

In order to compute the integral, it is necessary to choose an integration path. Landau proposed to move the path to the left, but keeping the singularity to the right. This means that it is possible to compute the integral by evaluating the singularities through the *residue theorem*:

$$\tilde{\phi}(k,t) = \sum_n \exp\left(p_n t\right) [(p - p_n) \tilde{\phi}_p(k,p)]_{p=p_n}. \tag{2.101}$$

In the Vlasov model, the evaluation of $\tilde{\phi}_p$ was the issue; however, in the Landau approach this can by studied by using analytic continuation. Considering a function G with poles within, the *residue theorem* says that the function evaluated on a contour (1) below the singularity is the same as a path (2) above the singularity, with the addition of a term that evaluates the function within in the pole:

$$G\left(\frac{ip}{k} \right) = -4\pi i e k \int_{-\infty}^{+\infty} \frac{g(u) du}{u - ip/k}, \tag{2.102a}$$

$$G\left(\frac{ip}{k} \right)_{(1)} = G\left(\frac{ip}{k} \right)_{(2)} + 2\pi i [g(u)]_{u=ip/k}. \tag{2.102b}$$

Integrating under the pole and integrating over the singularities, we obtain a principal integral which gives as a result:

$$1 - \frac{\omega_{pe}^2}{\omega^2} \left[1 + \frac{3}{2} \left(k\lambda_{De} \right)^2 + ... \right] - i\epsilon_i \simeq 0, \tag{2.103a}$$

$$\epsilon_i = \frac{\pi \omega_{pe}^2}{k^2} \frac{df_0(u)}{du}\Big|_{u=\omega/k} = 0, \tag{2.103b}$$

where Eq. 2.103a is the general form of the Bohm-Gross frequency found in Section 2.2.4 (particularly, its real part). The difference now is the presence of a complex term in the expression

of ω. This term will subject the wave to damping. Assuming $\omega = \omega_r + i\gamma$ and that $\gamma \ll \omega_r$, we obtain that $\gamma = (1/2)\omega_r \epsilon_i$ and, taking a Maxwellian as the equilibrium distribution f_0, we find an expression for the *Landau damping* of an EPW:

$$\gamma_{Le} = -\sqrt{\pi}\frac{\omega_{pe}^2 \Re(\omega)^2}{k^3 v_{Te}^3} \exp\left(-\frac{\Re(\omega)^2}{k^2 v_{Te}^2}\right), \tag{2.104}$$

with a dispersion relation equivalent to:

$$1 - \frac{\omega_{pe}^2}{k^2 v_{Te}^2} Z'\left(\frac{\omega}{k v_{Te}}\right) = 0, \tag{2.105}$$

From analysis of Eq. 2.104, Landau damping becomes dominant when the term in the exponential $\omega^2/k^2 v_{Te}^2 = v_{ph}^2/v_{Te}^2$ becomes small [79], the EPWs are more resonant with the electron population, and Landau damping dominates. In practical terms, this happens when $v_{ph} \simeq 3 - 5 v_{Te}$. In the opposite case, when the EPW phase velocity is high enough for the electron thermal velocity to become negligible, $v_{ph} \gtrsim 10 v_{Te}$; this is called the *collisional regime*. In terms of the electron Debye length λ_{De}, considering the *fluid limit* $k_{EPW}\lambda_{De} \ll 1$, we can approximate Eq. 2.103a as $\omega_{EPW} \simeq \omega_{pe}$, thus obtaining that $v_{Te}/v_{ph} \sim |\boldsymbol{k}_{EPW}|\lambda_{De} \simeq 0.2 - 0.3$. In other words, wave numbers beyond $|\boldsymbol{k}_{EPW}| \sim (0.2 - 0.3)/\lambda_{De}$ are going to be strongly Landau damped.

From a physical point of view, Landau damping occurs when particles (in this case, electrons) have velocities v close to the wave phase velocity v_{ph}. In case $v \simeq v_{ph} - \delta v$ (with $\delta v \ll v_{ph}$), energy will be transferred from the wave to the electrons, and viceversa in case the electrons have velocities $v \simeq v_{ph} + \delta v$. From an energy point of view, if there is a net electron population slower than the wave, energy transfer from the wave to the electrons occurs, and thus the wave is being damped. This is an essential process in the context of Inertial Confinement Fusion. We will see in Section 2.3 the arising of laser-plasma instabilities in the system. Some of these instabilities will generate electron plasma waves as a result of their activity, which can be Landau damped by the plasma electron population. This leads to a significant Landau damping of the EPW, which can create a *suprathermal* (or *hot*) electron population, with an average kinetic energy higher than the rest of the plasma. These electrons can propagate and ultimately impact against the ICF target, posing preheat concerns. We will discuss about this in Section 2.3.
For the ion-acoustic waves (IAWs) the process is similar, but while in the electron case the ion motion had been neglected, in this case both electron and ion contributions must be taken into account. Thus, the dispersion relation for the IAWs becomes:

$$1 - \frac{\omega_{pe}^2}{k^2 v_{Te}^2} Z'\left(\frac{\omega}{k v_{Te}}\right) - \frac{\omega_{pi}^2}{k^2 v_{Ti}^2} Z'\left(\frac{\omega}{k v_{Ti}}\right) = 0, \tag{2.106}$$

which ultimately leads to the *IAW Landau damping*:

$$\frac{\gamma_{Li}}{\omega_r} = -\sqrt{\frac{\pi}{8}}\frac{1}{(1 + k^2\lambda_{De}^2)^{3/2}}\left[\sqrt{\frac{m_e}{m_i}} + \left(\frac{T_e}{T_i}\right)^{3/2} \exp\left(-\frac{T_e/T_i}{2(1 + k^2\lambda_{De}^2)}\right)\right]. \tag{2.107}$$

2.2.6 Ponderomotive force

Before discussing about the instabilities developing due to laser-plasma coupling, we want to consider the effects on the plasma particles of a propagating light wave on the particle populations. We consider the motion of an electron in the oscillating $\boldsymbol{E}$ and $\boldsymbol{B}$ fields of a wave, with fields of the form $\boldsymbol{E}_0 = \boldsymbol{E}_0(\boldsymbol{x}) \sin(\omega_0 t)$ and with $\omega_0 \gtrsim \omega_{pe} \gg \omega_{pi}$. We neglect the background component of the magnetic field $\boldsymbol{B_0}$. The Newton equation associated with said electron is:

$$m_e \frac{d\boldsymbol{v_e}}{dt} = -e\left[\boldsymbol{E}(\boldsymbol{r}) + \boldsymbol{v} \times \boldsymbol{B}(\boldsymbol{r})\right]. \tag{2.108}$$

At the first order, the $\boldsymbol{v_1} \times \boldsymbol{B_1}$ term in Eq. 2.108 must be neglected, since it is a second order term. Therefore, integrating twice the resulting equation $m\ddot{x} = qE_0$ for a particle along the x direction, we obtain the electron's first order motion [66, 122]:

$$x_1 = x_0 - \frac{qE_0}{m\omega_0^2}\cos(\omega_0 t) = x_0 - \frac{v_{osc}}{\omega_0}\cos(\omega_0 t), \tag{2.109}$$

where $v_{osc} \equiv qE_0/m_e\omega_0$ is defined as the *quiver (or oscillation) velocity* of the particle within the field. The motion is then a sinusoidal oscillation around the equilibrium position x_0. We now consider the second order contributions in Eq. 2.108. The product $\boldsymbol{v_1} \times \boldsymbol{B_1}$ must now be included, with $\boldsymbol{B_1}$ given by Eq. 2.1c, and therefore:

$$B_1 = -(1/\omega_0)\nabla \times \boldsymbol{E_0}\sin(\omega_0 t) \tag{2.110}$$

Therefore, the second order part of Eq. 2.108 is given by:

$$m_e\frac{d\boldsymbol{v_2}}{dt} = -e\left[((x_1 - x_0)\cdot\nabla)\boldsymbol{E} + \boldsymbol{v_1} \times \boldsymbol{B_1}\right] \tag{2.111}$$

Inserting Eqs. 2.109 and 2.110 into Eq. 2.111, applying an average over time through $\langle\cdot\rangle$, and remembering that, over a period T, the average of a sinusoidal function is $\langle\cos(\omega_0 t)\rangle_T = \langle\sin(\omega_0 t)\rangle_T = 1/2$:

$$m_e\left\langle\frac{d\boldsymbol{v_2}}{dt}\right\rangle = -\frac{e^2}{m_e\omega^2}\frac{1}{2}\left[(\boldsymbol{E_0}\cdot\nabla)\,\boldsymbol{E_0} + \boldsymbol{E_0} \times (\nabla \times \boldsymbol{E_0})\right]. \tag{2.112}$$

From the theory of operators, the double cross product gives a term $-(\boldsymbol{E_0}\cdot\nabla)\boldsymbol{E_0}$. Therefore, Eq. 2.112 becomes:

$$\boldsymbol{F}_p = -\frac{e^2}{4m_e\omega_0^2}\nabla\boldsymbol{E}_0^2(\boldsymbol{x}), \tag{2.113}$$

which depends on the square of the charge, and thus its direction is not affected by particles with different charge, and on the particle mass, which makes it more effective at moving electrons than ions. The particle is being accelerated in the opposite direction than the electric field gradient. Eq. 2.113 is called *ponderomotive force*, and it is a nonlinear force caused by the propagation of the laser wave within the plasma, which pushes the plasma away from regions of high laser intensity through a gradient in field pressure. For electrons, the ponderomotive force per unit volume reads, according to the result found by Landau and Lifshiz (1950s) [46]:

$$\boldsymbol{f}_{pe} = -\frac{n_e e^2}{4m_e\omega_0^2}\nabla\boldsymbol{E}_0^2 = -\frac{1}{16\pi}\left(\frac{\omega_{pe}}{\omega_0}\right)^2\nabla\boldsymbol{E}_0^2. \tag{2.114}$$

When $v_{osc} > v_{Te}$, the laser pushes the plasma away to the point of forming density depressions in its wake. This condition can be rewritten in terms of the laser intensity and wavelength $I_{laser}\lambda^2$. In the case of plasmas with temperature range of the order of $10^2 - 10^3\ eV$, this condition is [47]:

$$I_{laser}\lambda^2 \gtrsim 5 \times 10^{15} T_e, \tag{2.115}$$

where T_e is in keV, λ in μm and I_{laser} in W/cm^2. When this happens, there is formation of *light channels* and the formation of *filamentation instability*, in which the laser refracts within the channel because of the denser plasma at the channel border, in a process called *self-focusing*. The effect of the ponderomotive force on the dispersion relation is to add a force term into the fluid momentum equation 2.43b. By following the same procedure done in cold and warm plasmas (finding an expression for the continuity and momentum equations for small perturbations from equilibrium, then finding the conductivity by using the monochromatic solution / pass in

Fourier space), assuming a cold plasma in 1D, with ions fixed and a ponderomotive force F_p, we obtain [46]:

$$\omega_{\mathrm{R}} = \left(\omega_{\mathrm{p}}^2 + \frac{F_{\mathrm{p}}^2 k^2}{4 m_{\mathrm{e}}^2 \omega_{\mathrm{p}}^2} \right)^{1/2}, \tag{2.116a}$$

$$\omega_{\mathrm{I}} = \frac{F_{\mathrm{p}} k}{2 m_{\mathrm{e}} \omega_{\mathrm{R}}}. \tag{2.116b}$$

Eqs. 2.116 show that the modes do propagate even in the cold plasma case ($T_e = 0$) when considering the ponderomotive force, with velocities:

$$v_\phi = \frac{\omega}{k} = \sqrt{\frac{\omega_{\mathrm{p}}^2}{k^2} + \frac{\mathrm{i} f f}{m_{\mathrm{e}} k}}, \quad v_{\mathrm{g}} = \frac{\partial \omega}{\partial k} = \frac{\mathrm{i} f}{2 m_{\mathrm{e}}} \left(\omega_{\mathrm{p}}^2 + \frac{\mathrm{i} f k}{m_{\mathrm{e}}} \right)^{-1/2}. \tag{2.117}$$

2.3 Parametric instabilities

As mentioned in the previous sections, the laser light propagates within the plasma, until reaches the critical density n_c, at which point its wavenumber becomes zero and it is being reflected after losing a fraction of its energy. In inertial confinement fusion scenarios, it is paramount to maximize the energy absorbed close to n_c, since a greater laser energy absorbed results in a stronger pressure on the ICF target and an overall stronger laser-target coupling. This coupling becomes worse in the case of:

- Scattering of the light waves due to *laser-plasma instabilities* occurring at or below critical density, such as CBET, SRS and SBS.
- Anomalous absorption, in which a part of the laser light energy is converted into energy for the hot particles, especially the *hot electron* (HEs) population. These electrons, despite their low number, can pre-heat the ICF target central region, worsening the compression efficiency and thus the fusion yield.

The collisional absorption of a light wave happens via the process of inverse Bremmstrahlung discussed in Section 2.2.2.2. This mode of absorption appears mainly in the region of critical density and in long scale length plasmas. However, in the underdense region there is the possibility the laser-plasma interaction becomes strongly nonlinear, with a detrimental scaling in $I\lambda^2$. These interactions reduce the energy transfer from the laser and constitute the aforementioned *anomalous absorption*, one of which is Landau damping, discussed in Section 2.2.5.

In this section we will describe a category of instabilities, called *parametric instabilities*, which are capable of both scattering light and lose energy through anomalous absorption. Their main mechanism is the decay of a *pump or mother wave* into two *product or daughter waves*, following a set of *matching conditions* in both wave number and frequency, which reflect conservation of momentum and energy. The most notable parametric instabilities are *Stimulated Raman Scattering* (SRS), *Two Plasmon Decay* (TPD) and *Stimulated Brillouin Scattering* (SBS). These instabilities are classified as [79] *primary*, since their decay includes the laser light as the pump wave. Instabilities where the laser pump is not the mother wave are defined as *secondary* instabilities instead, some of the most notable ones being the *Langmuir Decay Instability* (LDI). Since all these instabilities couple the mother wave to the decay of two daughter waves, they are also defined as *three wave processes*. There also exist instabilities that do not follow a three-wave decay, which we will not focus on this work. These are the *filamentation instability*, which can be based on ponderomotive forces, thermal motion or relativistic effects and *resonance absorption* (RA).

From a practical point of view, all the instabilities listed play a role in the disruption of the implosion [5] in an ICF scenario. Most notably, SBS plays a role in scattering light from the plasma before it can propagate to higher intensities and be absorbed. Filamentation can lead to self-focusing of the laser drive, and the resulting intensity enhancement can induce other instabilities in regions where they normally would be below their instability threshold. Finally, the generation of Electron Plasma Waves (EPWs) from RA, LW collapse, SRS, TPD and LDI are generators of HEs and thus fuel pre-heat.

In the following sections, we will focus mainly on the parametric instabilities capable of generating HE at quarter critical density. Therefore, we will discuss about SRS, TPD and LDI. We will briefly evoke the SBS instability as well due to its importance, despite not being considered in this work. l

2.3.1 Introductory concepts on parametric instabilities

In a parametric instability decay process, a pump wave couples to product waves, characterized by an unstable growth, following a set of *matching conditions* in frequency and wave vector, derived from the Manley-Rowe relations [123]. Labeling with index "0" the pump wave and with "1" and "2" the product waves:

$$\omega_0 = \omega_1 + \omega_2, \tag{2.118a}$$

$$\boldsymbol{k}_0 = \boldsymbol{k}_1 + \boldsymbol{k}_2. \tag{2.118b}$$

These conditions express the conservation of energy and momentum within the three-wave system.

Early work [85, 124, 125, 126, 127] modeled the waves as two damped oscillators with an outside force (the pump wave) driving the motion. We consider a pump wave with $(\omega_0, \boldsymbol{k}_0)$ and two product waves with $(\omega_1, \boldsymbol{k}_1)$ and $(\omega_2, \boldsymbol{k}_2)$ respectively, within a continuous medium. Their *normalized electric field* assumes the general form $A_j(\boldsymbol{x}, t) = a_j(\boldsymbol{x}, t) \exp\left[i(\boldsymbol{k}_j \cdot \boldsymbol{x} - \omega_j(\boldsymbol{k}_j)t\right] + c.c.$, where "c.c." is the *complex conjugate* and $j = 0, 1, 2$. The equations for the two oscillators can be written with a coupling term within each one, depending on the other daughter wave and the pump. The result obtained [47, 79] is:

$$\left(\partial_t + \boldsymbol{v}_{g1} \cdot \partial_{\boldsymbol{x}} + \nu_1\right) a_1(\boldsymbol{x}, t) = M_1 a_0 a_2^*, \tag{2.119a}$$

$$\left(\partial_t + \boldsymbol{v}_{g2} \cdot \partial_{\boldsymbol{x}} + \nu_2\right) a_2(\boldsymbol{x}, t) = M_2 a_0 a_1^*, \tag{2.119b}$$

where the coefficients ν_1 and ν_2 are the respective wave dampings (sum of both collisional and Landau damping), and $\boldsymbol{v}_{g1}, \boldsymbol{v}_{g2}$ are the associated waves' group velocity. We define the square of the *coupling coefficient* as [79]:

$$\gamma_0^2 \equiv M_1 M_2^* |a_0|^2, \tag{2.120}$$

where the coupling is proportional to the ponderomotive force of the pump wave. Eqs. 2.119 describe an *unstable system* with a threshold:

$$\gamma_0^2(x) > \gamma_{0\ thr}^2 \equiv \nu_1(x)\nu_2(x), \tag{2.121}$$

condition obtained by combining the two equations in 2.119 after Fourier transforming both in time and space. The WKB theory and temporal SVEA discussed in Section 2.2.2.1 can be applied in the case of $\gamma_0 \ll \min(\omega_1, \omega_2)$ and $|v_{g1}| \ll |v_{g2}|$. In these conditions, the regime is called *weak coupling regime*, and is otherwise called *strong coupling regime* (which we will not focus our attention onto). Generally, the coupled system of Eqs. 2.119 describe an eigenvalue problem where:

- The system is *stable* when there are no unstable eigenmodes (i.e. with a negative imaginary part).

- The system is characterized by *convective instability* when the system is characterized by stable eigenmodes, but the initial perturbation can undergo spatial amplification along the propagation direction, and therefore the product waves grow exponentially $\propto \exp(Kx)$, with K being defined as an *amplification factor*.

- The system presents at least one unstable eigenmodes (i.e. imaginary part > 0), which is defined as being *absolutely unstable*. In this case the perturbation grows exponentially in time according to $\propto \exp(\gamma t)$, where γ is defined as the *temporal growth rate*.

2.3.1.1 Parametric instabilities in an homogeneous infinite medium

Considering an infinite homogeneous medium, Bers and Briggs [128, 129, 130] provided an instability analysis by studying the asymptotic behavior of the *Green function* $G_\infty(x,t)$. This function, also called *system response function*, is defined as the solution of the equation $\Delta(i\partial_t, -i\partial_x)G_\infty = \delta(t)\delta(x)$, where $\delta(t)$ and $\delta(x)$ are Dirac's deltas both in time and space, while satisfying the boundary conditions $G_\infty(\pm\infty, t) = 0$ for every time $t > 0$, and zero for $t < 0$. The operator $\Delta(i\partial_t, -i\partial_x)$ is a linear partial derivative operator where time and space do not explicitly appear.

The study of this function leads to the following conclusions when the system is unstable (i.e. when $\gamma_0^2 > (\nu_1\nu_2)^{1/2}$), and when the group velocities are unidirectional along x:

- The system is absolutely unstable if the two waves are propagating in opposite directions. In this case, the threshold condition is given by:

$$v_{g1}v_{g2} < 0, \tag{2.122a}$$

$$\gamma_0 > \gamma_{thr}^{abs} \equiv \frac{|v_{g1}v_{g2}|^{1/2}}{2}\left(\frac{\nu_1}{|v_{g1}|} + \frac{\nu_2}{|v_{g2}|}\right), \tag{2.122b}$$

- The system is convectively unstable if the threshold condition is satisfied, but not the absolute threshold one. Thus, in the case of counter-propagating waves $v_{g1}v_{g2} < 0$, the growth rate is: $\gamma_{0\ thr} < \gamma_0 < \gamma_{thr}^{abs}$, and it is defined as a *strong damping regime*. In the case of co-propagating waves, $v_{g1}v_{g2} > 0$, the instability is convective over the whole domain, and $\gamma_0 > \gamma_{thr}^{abs}$. This defines the *weak damping regime*.

2.3.1.2 Parametric instabilities in a finite homogeneous medium

Finite length effects play a role in a spatially limited interaction zone. Waves in this case can grow both in space and time. Moreover, under the Bers and Briggs stability analysis, it can be shown that the notions of stability valid in an infinite medium are applicable in a finite one as well. In particular, we can expect that if the finite system possesses at least one unstable eigenvalue, it will be close to the absolute growth rate γ_{abs} of the infinite system, and thus we can expect the associated eigenmode will behave similarly to the infinite case. On the other hand, in the case of the absence of absolutely unstable modes, we can expect a spatial amplification dictated by an initial perturbation, following a spatial amplification rate K similar to the infinite case.

The finite parametric system allows unstable modes if:

- We are in the absolute instability regime previously discussed: $v_{g1}v_{g2} < 0$ and $\gamma_0 > \gamma_{thr}^{abs}$.

- The length of the system L overcomes a critical length $L_{crit}(\gamma_0, \gamma_{thr}^{abs}/\gamma_0)$. However, after the condition $\gamma_0 \gg \gamma_{thr}^{abs}$ is satisfied, L_{crit} becomes equal to a value L_c independent on the damping rates:

$$L_c(\gamma_0) \equiv L_{crit}(\gamma_0 \gg \gamma_{thr}^{abs}+) = \frac{\pi}{2}\left(\frac{\gamma_0}{\sqrt{|v_{g1}v_{g2}|}}\right)^{-1} \tag{2.123}$$

These waves do not require a seeded amplitude at the boundaries, and thus the boundary conditions can be:

$$A_j(x=0)=0 \quad if \quad v_{gj}>0, \tag{2.124a}$$
$$A_j(x=L)=0 \quad if \quad v_{gj}<0. \tag{2.124b}$$

On the other hand, the convective instability regime in a parametric system arise with the following results:

- The length of the system L overcomes the characteristic length $L_{crit} \equiv K_{max}^{-1}$, where K_{max} is the amplification factor. This length is, in the weak damping regime ($\gamma_0 > \gamma_{thr}^{abs}$) and co-propagating waves $v_{g1}v_{g2}>0$):

$$L_{crit} = \frac{|v_{g1}v_{g2}|^{1/2}}{\gamma_0}, \tag{2.125}$$

  while in the strong damping regime for $\gamma_{0\ thr} < \gamma_0 < \gamma_{0\ thr}^{abs}$ and no matter the sign of $v_{g1}v_{g2}$, it is:

$$L_{crit} = \frac{|v_{g1}v_{g2}|\max\left(\nu_j/|v_{gj}|\right)}{\gamma_0^2-\nu_1\nu_2} \tag{2.126}$$

- The asymptotic spatial behavior within the interval $[0, L]$ is identical to the one of an infinite system, provided L surpasses the critacteristic length L_{crit}. The validity is limited by a lower value in length L_{lim}:

$$L_{lim} = \frac{v_{g2}}{\nu_2} \ll |K_{max}|^{-1} = L_{crit} \tag{2.127}$$

- The product waves' amplitudes spatially grow exponentially $\propto \exp\left[G(L)\right]$, where:

$$G(L) = |K_{max}|L = \frac{L}{L_{crit}}. \tag{2.128}$$

2.3.1.3 Effects on parametric instabilities in an infinite inhomogeneous plasma

In the case of an inhomogeneous plasma the matching conditions 2.118 for the wave number are only valid locally:

$$k_0(\omega_0,k) = k_1(\omega_1,k) + k_2(\omega_0-\omega_1,x), \tag{2.129}$$

which is an implicit equation for the variable ω_1, since ω_0 is fixed and given by the pump wave. We will use the term $D_j(\omega_j,k,x)$ as the dispersion relation for the associated j-th wave, where $j=0,1,2$, in the sense of Eq. 2.68. We denote $\omega_1^{(0)}$ as the solution of Eq. 2.129 given point x_0. We can write the functions $k_j(\omega_j^{(0)},x)$, solutions of the dispersion relations $D_j(\omega_j,k,x)=0$, as a spatially dependent quantity of the form:

$$k_j(\omega_j^{(0)},x) = k_j^{(0)} + \delta k_j(x), \tag{2.130}$$

where the couple $(\omega_j^{(0)}, k_j^{(0)})$ are the solutions to the matching conditions of Eq. 2.129 at $x=x_0$:

$$\omega_0^{(0)} \equiv \omega_0, \quad \omega_2^{(0)} \equiv \omega_0 - \omega_1^{(0)}, \quad k_j^{(0)} \equiv k_j(\omega_j^{(0)},x_0) \tag{2.131}$$

The quantities δk_j and the normalized fields a_j defined as $a_j \equiv E_j/E_0$, within the WKB theory and the envelope approximation described in Section 2.2.2.1:

$$\delta k_j \simeq \frac{D_j(\omega_j^{(0)},k_j^{(0)},x) - D_j(\omega_j^{(0)},k_j^{(0)},x_0)}{v_{gj}(\partial D_j/\partial\omega_j^{(0)})}, \tag{2.132a}$$
$$a_j = \tilde{a}_j \exp\left[i\int_{x_0}^{x}\delta k_j(x')dx'\right]. \tag{2.132b}$$

Using monochromatic propagating waves of the form $E_j(x,t) = \bar{E}_j(x,t)\exp\left(-i(\omega_j^{(0)}t - k_j^{(0)}x)\right) + c.c.$, we obtain from Eqs. 2.119 and the solution 2.132b (by replacing $\tilde{a}_j$ with a_j:

$$[\partial_t + \nu_1 + v_{g1}\partial_x]a_1 = -\gamma_0 a_2 \; exp\left[-i\int_{x_0}^{x}\Delta k(x')dx'\right], \tag{2.133a}$$

$$[\partial_t + \nu_2 + v_{g2}\partial_x]a_2 = -\gamma_0 a_1 \; exp\left[-i\int_{x_0}^{x}\Delta k(x')dx'\right], \tag{2.133b}$$

where $\Delta k(x)$ is defined as the *detuning function*:

$$\Delta k(x) \equiv \delta k_0(x) - \delta k_1(x) - \delta k_2(x) \tag{2.134}$$

The solution of the system 2.133 depends on this function's behavior. There are two main regimes depending on the approximation of the detuning function:

- A *linear profile*, where the detuning function is approximated by:

$$\Delta k(x) = \Delta k'_{x=0}x, \tag{2.135}$$

  where $(\bullet)'$ is the spatial derivative. The length over which resonance occurs is given by:

$$L \simeq \frac{4\gamma_0}{|\Delta k'_{x=0}||v_{g1}v_{g2}|^{1/2}} \qquad for\ \gamma_0 > \gamma_{thr}^{abs}, \tag{2.136a}$$

$$L \simeq \frac{2}{|\Delta k'_{x=0}|}\max\left(\frac{\nu_j}{|v_{gj}|}\right) \quad for\ \gamma_{0\ thr} < \gamma_0 < \gamma_{thr}^{abs}. \tag{2.136b}$$

  In these conditions, the results are what follows:

  - The system is stable in the sense that does not present any eigenmode that causes absolute instability, while convective instability is free to occur.
  - The parametric system presents a spatial amplification when the condition $\gamma_0 > \gamma_{0\ thr} = (\nu_1\nu_2)^{1/2}$ is satisfied. In particular, when $\gamma_0 \gg \gamma_{0\ thr}$, the spatial amplification assumes the form of the *Rosenbluth gain* [17]:

$$G_{Ros} \equiv \frac{\pi\gamma_0^2}{|v_{g1}v_{g2}\Delta k'_{x=0}|} \tag{2.137}$$

  - Above $\gamma_0 > \gamma_{0\ thr}$, the characteristic distance above which spatial amplification takes place is given by Eqs. 2.136a and 2.136b.

- A *parabolic regime*, where the detuning function is approximated by:

$$\Delta k(x) = \frac{1}{2}\Delta k''_{x=0}x^2. \tag{2.138}$$

  In this case, the resonance length is given by:

$$L_{res}^{inh} \simeq 4\left(\frac{\gamma_0}{|\Delta k''_{x=0}||v_{g1}v_{g2}|^{1/2}}\right)^{1/2} \qquad for\ \gamma_0 > \gamma_{thr}^{abs}, \tag{2.139a}$$

$$L_{res}^{inh} \simeq 2^{3/2}\left(\frac{\max\left(\nu_j/|v_{gj}|\right)}{|\Delta k''_{x=0}|}\right)^{1/2} \qquad for\ \gamma_{0\ thr} < \gamma_0 < \gamma_{thr}^{abs}, \tag{2.139b}$$

  and the following results can be listed [17, 131]:

– The parametric system is absolutely unstable if the following conditions are satisfied:

$$v_{g1}v_{g2} < 0, \tag{2.140a}$$

$$\gamma_0 \geq \max\left(\gamma_0^{inh}, \gamma_{thr}^{abs}\right) = \max\left[\left(\frac{|v_{g1}v_{g2}|^{1/2}|\Delta k''_{x=0}|^{1/3}}{4^{2/3}}\right), \gamma_{thr}^{abs}\right]. \tag{2.140b}$$

In this case, the resonance length is the one defined in Eq. 2.139a.

– The parametric system is stable in the sense of absolute instability in case the instability does not satisfy the conditions at the previous point.

In the case of $\gamma_0 > \gamma_{thr}^{abs}$ and $v_{g1}v_{g2} > 0$, there is spatial amplification of the product waves of the order of:

$$G \simeq \left(\frac{\gamma_0}{\gamma_0^{inh}}\right)^{\frac{3}{2}}, \tag{2.141}$$

with a characteristic distance from Eq. 2.139a.

In the case of $\gamma_{0\ thr} \ll \gamma_0 < \gamma_{thr}^{abs}$, whatever the sign of $v_{g1}v_{g2}$, a spatial amplification given by:

$$G = \left(\frac{\pi}{2^{5/2}}\right)\left(\frac{\gamma_0}{\gamma_0^{inh}}\right)^{\frac{3}{2}}\left(\frac{\gamma_0}{\gamma_{thr}^{abs}}\right)^{\frac{1}{2}} \tag{2.142}$$

is present, and the resonance length is given by 2.139b.

2.3.2 Stimulated Raman Scattering

We now consider the process of Stimulated Raman Scattering (SRS). This is a parametric instability where the pump wave is an incident light wave (i.e. a laser wave in ICF scenarios) and the daughter waves are an Electron Plasma Wave (EPW) and a scattered light wave (Raman wave), respectively. The matching conditions are:

$$\omega_0 = \omega_R + \omega_{EPW}, \tag{2.143a}$$

$$\boldsymbol{k}_0 = \boldsymbol{k}_R + \boldsymbol{k}_{EPW}. \tag{2.143b}$$

From a physical point of view, the pump wave can beat with the scattered light that is generated as noise in the perturbed plasma (*Raman wave*) with an amplitude $\boldsymbol{E}_R$. Provided the matching conditions are satisfied, the ponderomotive force from the two fields beating together ($\boldsymbol{F}_p \propto \nabla(\boldsymbol{E}_0 \cdot \boldsymbol{E}_R)$) excites an electron density perturbation ($\delta n/n_e$) in the plasma, therefore generating a transverse nonlinear current $\delta\boldsymbol{J} = -e\boldsymbol{v}_{osc}\delta n$, where $v_{osc} \equiv e\boldsymbol{E}_0/m_e\omega_0$ is the *quiver velocity* in the laser field discussed in Section 2.3. This current generates a stronger scattered electromagnetic field $\boldsymbol{E}_R$ which beats with the laser light and produces a bigger ponderomotive force which drives a bigger density fluctuation. Therefore, a positive feedback loop is established, giving origin to the SRS parametric instability [45, 132]. The scheme of the instability is illustrated in Fig. 2.5. The SRS instability can generate different scattering configurations, which are defined in reference to the emission of the scattered Raman wave: there exist a *forward scattering* configuration where the Raman wave is emitted parallel to the pump, a *backward scattering* one where the Raman wave is antiparallel to the pump, and a *sidescattering* one for Raman waves emitted with a perpendicular component to the pump.

The dispersion relations for the two electromagnetic waves (laser and Raman), as well as the EPW, are:

$$\omega_{0,R}^2 = \omega_{pe}^2 + k_{0,R}^2c^2, \tag{2.144a}$$

$$\omega_{EPW}^2 = \omega_{pe}^2 + 3k_{EPW}^2v_{Te}^2, \tag{2.144b}$$

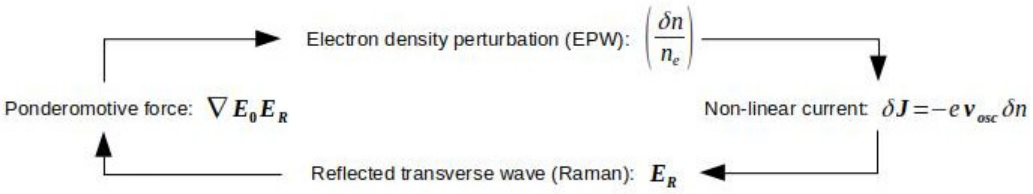

Figure 2.5: Schematic representation of the Stimulated Raman Scattering process.

where the subscripts "0" and "R" are referred to the laser and the Raman light, respectively. The minimum wave frequency for both the Raman wave and the EPW is the electron plasma frequency ω_{pe} in both cases. As such, we can approximate Eq. 2.143a as $\omega_0 \gtrsim 2\omega_{pe}$ and, recalling the definition of plasma frequency and critical density n_c, this implies $n_e \lesssim n_c/4$. As such, the SRS instability cannot develop at densities above $0.25 n_c$, also called *quarter critical density*. Both Eqs. 2.144a and 2.144b are at their minimum (i.e. at $n_c/4$) when $k_{R,EPW} = 0$; therefore, quarter critical density is the region where absolute SRS develops, while at lower densities (where $k_{R,EPW} \neq 0$) convective SRS can take place.

It must be noted that the following results are obtained in simple conditions (i.e. normal incidence, no sidescattered SRS, etc.). A more detailed analysis has been performed by [18, 21, 132].

2.3.2.1 Derivation of the EPW and Raman coupled equations

Let us consider the overall fields in the system $\boldsymbol{E}$ and $\boldsymbol{B}$ as functions of a vector and a scalar potential $\boldsymbol{A}$ and ϕ respectively. The two fields then assume the form:

$$\boldsymbol{E} = -\frac{1}{c}\frac{\partial \boldsymbol{A}}{\partial t} - \nabla\phi, \tag{2.145a}$$

$$\boldsymbol{B} = \nabla \times \boldsymbol{A}, . \tag{2.145b}$$

Choosing a *gauge fixing* for this system of the form $\nabla \cdot \boldsymbol{A}$ (*Coulomb gauge*), we can rewrite the Ampere's and Gauss' law in the Maxwell's equations as functions of $\boldsymbol{A}$ and ϕ. Including the *continuity equation* for the electric charge density ρ as well, and decomposing the current density into a longitudinal and a transverse component $\boldsymbol{J} = \boldsymbol{J}_l + \boldsymbol{J}_t$ and using $\nabla \cdot \boldsymbol{J}_t = 0$, we obtain:

$$\frac{\partial}{\partial t}\nabla\phi = 4\pi \boldsymbol{J}_l, \tag{2.146a}$$

$$\left(\frac{1}{c^2}\frac{\partial^2}{\partial t^2} - \nabla^2\right)\boldsymbol{A} = \frac{4\pi}{c}\boldsymbol{J}_t. \tag{2.146b}$$

Eq. 2.146a relates the longitudinal plasma behavior (i.e. $\boldsymbol{J}_l$) solely with the scalar part of the overall electromagnetic wave (ϕ), while Eq. 2.146b relates the transverse plasma behavior ($\boldsymbol{J}_t$) with the vector part of the electromagnetic wave ($\boldsymbol{A}$). In this last equation, we consider the case of the vector potential $\boldsymbol{A}$ being perpendicular to the density gradient of the inhomogeneous plasma, $\boldsymbol{A} \cdot \nabla n_e = 0$, leading to the condition $\boldsymbol{E}_t = -(1/c)\partial \boldsymbol{A}/\partial t$. In this case, the transverse current can be expressed as $\boldsymbol{J}_t = -n_e e \boldsymbol{u}_{osc}$, where $\boldsymbol{u}_{osc} \equiv e\boldsymbol{A}/m_e c$ is the expression of the oscillation velocity. Decomposing the overall vector potential into a large amplitude wave $\boldsymbol{A}_L$ and a perturbation $\tilde{\boldsymbol{A}}$ and the electron density as a background density n_b and a perturbation so that $n_e = n_b + \tilde{n}_e$, Eq. 2.146b for the perturbations becomes:

$$\left(\frac{\partial^2}{\partial t^2} - c^2\nabla^2 + \omega_{pe}^2\right)\tilde{\boldsymbol{A}} = -\frac{4\pi e^2}{m_e}\tilde{n}_e \boldsymbol{A}_L, \tag{2.147}$$

where we used the definition of the plasma frequency $\omega_{pe} = \sqrt{4\pi e^2 n_b/m_e}$ and the definition of the transverse current density $\boldsymbol{J}_t$. If we associate $\boldsymbol{A}_L$ with the laser light, according to Eq. 2.147

a field perturbation $\tilde{\boldsymbol{A}}$ (i.e. the scattered Raman light) is generated by the coupling between the laser light wave and the density perturbation $\tilde{n}_e$, which is here an EPW.

We now consider the continuity equation for the density, as well as the momentum equation:

$$\frac{\partial n_e}{\partial t} + \nabla \cdot (n_e \boldsymbol{u}_e) = 0, \tag{2.148a}$$

$$\frac{\partial \boldsymbol{u}_e}{\partial t} + \boldsymbol{u}_e \cdot \nabla \boldsymbol{u}_e = -\frac{e}{m_e}\left(\boldsymbol{E} + \frac{\boldsymbol{u}_e \times \boldsymbol{B}}{c}\right) - \frac{\nabla p_e}{n_e m_e}, \tag{2.148b}$$

where n_e, $\boldsymbol{u}_e$ and p_e are the electron density, velocity and pressure respectively. Considering the magnetic field as negligible, and separating the velocity in a longitudinal and a transverse component respectively, $\boldsymbol{u}_e = \tilde{\boldsymbol{u}} + e\boldsymbol{A}/m_e c$, Eq. 2.148b becomes an evolution equation for the longitudinal momentum:

$$\frac{\partial \tilde{\boldsymbol{u}}}{\partial t} = \frac{e}{m_e}\nabla\phi - \frac{1}{2}\nabla\left(\tilde{\boldsymbol{u}} + \frac{e\boldsymbol{A}}{m_e c}\right)^2 - \frac{\nabla p_e}{n_e m_e}. \tag{2.149}$$

Taking $n_e = n_0 + \tilde{n}_e$, $\boldsymbol{A} = \boldsymbol{A}_L + \tilde{\boldsymbol{A}}$ and $\phi = \tilde{\phi}$ and using the polytropic equation $p_e n_e^{-3} = const$, we can linearize Eqs. 2.148a and 2.149 for the perturbation quantities (indicated by the tilde). In particular, applying the time derivative of the linearized Eq. 2.148a and the divergence to the linearized Eq. 2.149, as well as the Poisson's equation for the perturbations ($\nabla^2\tilde{\phi} = 4\pi e\tilde{n}_e$), we obtain an equation for the density perturbations $\tilde{n}_e$:

$$\left(\frac{\partial^2}{\partial t^2} - 3v_{Te}^2\nabla^2 + \omega_{pe}^2\right)\tilde{n}_e = \frac{n_0 e^2}{m_e^2 c^2}\nabla^2\left(\boldsymbol{A}_L \cdot \tilde{\boldsymbol{A}}\right). \tag{2.150}$$

Similarly to Eq. 2.147, in this case an electron density perturbation (i.e. an EPW) is generated by the ponderomotive coupling between the laser light wave $\boldsymbol{A}_L$ and the Raman light $\tilde{\boldsymbol{A}}$. The results, as well as their derivation, can be found at [45].

Overall, Eqs. 2.147 and 2.150 describe the coupling between scattered Raman light waves and electrostatic waves (EPWs) in presence of a pump wave $\boldsymbol{A}_L$, given by the laser, and play an important role in the evolution and dispersion relation of the instability, as will be seen in the following section.

2.3.2.2 SRS dispersion relation and growth rate

We consider a laser field of the form $\boldsymbol{A}_L = \boldsymbol{A}_0 \cos(\boldsymbol{k}_0 \cdot \boldsymbol{x} - \omega_0 t)$, and analyze in Fourier space Eqs. 2.147 and 2.150. The resulting equations are:

$$\left(\omega^2 - k^2c^2 - \omega_{pe}\right)\tilde{\boldsymbol{A}}(\omega, \boldsymbol{k}) = \frac{4\pi e^2}{2m_e}\boldsymbol{A}_0\left[\tilde{n}_e(\omega - \omega_0, \boldsymbol{k} - \boldsymbol{k}_0) + \tilde{n}_e(\omega + \omega_0, \boldsymbol{k} + \boldsymbol{k}_0)\right], \tag{2.151a}$$

$$\left(\omega^2 - \omega_{EPW}^2\right)\tilde{n}_e(\omega, \boldsymbol{k}) = \frac{k^2 e^2 n_0}{2m_e^2 c^2}\boldsymbol{A}_0 \cdot \left[\tilde{\boldsymbol{A}}(\omega - \omega_0, \boldsymbol{k} - \boldsymbol{k}_0) + \tilde{\boldsymbol{A}}(\omega + \omega_0, \boldsymbol{k} + \boldsymbol{k}_0)\right], \tag{2.151b}$$

where ω_{EPW} is given by the Bohm-Gross frequency (Eq. 2.144b), and the quantities ω_0 and $\boldsymbol{k}_0$ relates to the laser light. We combine Eq. 2.151a and 2.151b to eliminate $\tilde{\boldsymbol{A}}$, and we neglect the terms $\tilde{n}_e(k - 2k_0, \omega - 2\omega_0)$ and $\tilde{n}_e(k + 2k_0, \omega + 2\omega_0)$ for being non-resonant. By doing so, we obtain a dispersion relation for the Raman scattered wave of the form:

$$\omega^2 - \omega_{EPW}^2 = \frac{\omega_{pe}^2 k^2 v_{osc}^2}{4}\left[\frac{1}{D(\omega - \omega_0, \boldsymbol{k} - \boldsymbol{k}_0)} + \frac{1}{D(\omega + \omega_0, \boldsymbol{k} + \boldsymbol{k}_0)}\right], \tag{2.152}$$

where $D(\boldsymbol{k}, \omega) \equiv \omega^2 - k^2c^2 - \omega_{pe}^2$ and v_{osc} is the quiver velocity in terms of the electric field (Sec. 2.3). If we consider backscattering or sidescattering, the *Anti-Stokes component* $D(\omega + \omega_0, \boldsymbol{k} + \boldsymbol{k}_0)$

can be neglected as out of resonance. Therefore [45]:

$$\left(\omega^2 - \omega_{EPW}^2\right)\left[(\omega-\omega_0)^2 - (\boldsymbol{k}-\boldsymbol{k}_0)^2 c^2 - \omega_{pe}^2\right] = \frac{\omega_{pe}^2 k^2 v_{osc}^2}{4}. \tag{2.153}$$

Taking $\omega = \omega_{EPW} + \delta\omega$, where $\delta\omega \ll \omega_{EPW}$ is a small perturbation from the EPW frequency, and $\boldsymbol{k} = \boldsymbol{k}_{EPW}$, we can work out Eq. 2.153 and separate its real and imaginary part. The imaginary part gives the dispersion relation for the backscattered Raman wave when the matching conditions $\omega_R = \omega_0 - \omega_{EPW}$ and $\boldsymbol{k}_R = \boldsymbol{k}_0 - \boldsymbol{k}_{EPW}$ are satisfied:

$$(\omega_{EPW} - \omega_0)^2 - (\boldsymbol{k}_{EPW} - \boldsymbol{k}_0)^2 c^2 - \omega_{pe}^2 = 0, \tag{2.154}$$

which, as expected, is equal to the propagation of a light wave in a plasma as in Eq. 2.144a. The real part of Eq. 2.153 gives the form of the *growth rate*:

$$\gamma = \frac{k_{EPW} v_{osc}}{4}\left[\frac{\omega_{pe}^2}{\omega_{EPW}(\omega_0 - \omega_{EPW})}\right]^{\frac{1}{2}}, \tag{2.155}$$

where k is determined by inverting Eq. 2.154 for k, giving $k_{EPW} = k_0 + (\omega_0/c)(1 - 2\omega_{pe}/\omega_0)^{1/2}$. From the form of k it can be shown that the maximum wave number for the SRS wave is $k_{EPW} = 2k_0$ for $n_e \ll n_c/4$, going down to $k_{EPW} = k_0$ when at quarter critical density. Eq. 2.155 is the maximum growth rate in the backscatter geometry. Any case with $\boldsymbol{A}\cdot\nabla n_e \neq 0$ will see a reduced growth rate, and the instability will vanish when the electric field and the Raman light are parallel ($\tilde{\boldsymbol{A}}\cdot\boldsymbol{A}_L = 0$). Therefore, sidescattering will occur preferentially out of the polarization plane.

For the case of forward scattering, the procedure is similar to the one presented, but now both $D(\omega-\omega_0, \boldsymbol{k}-\boldsymbol{k}_0)$ and $D(\omega+\omega_0, \boldsymbol{k}+\boldsymbol{k}_0)$ can be considered resonant. We can approximate both as $D(\omega\pm\omega_0, \boldsymbol{k}\pm\boldsymbol{k}_0) \simeq 2(\omega_{pe}\pm\omega_0)\delta\omega$, and choosing $k = \omega_{pe}/c$ and $\omega = \omega_{pe} + \delta\omega$, we obtain the following growth rate:

$$\gamma \simeq \frac{\omega_{pe}^2}{2\sqrt{2}\omega_0}\frac{v_{osc}}{c}. \tag{2.156}$$

2.3.2.3 SRS growth rates and intensity thresholds

Up until now we discussed the instability development as a positive feedback loop, which allows both EPWs and Raman light to grow indefinitely. However, wave damping (both collisional and Landau) can be strong enough to prevent the instability from developing. As such, a *threshold* must be reached for the instability to grow. This occurs when the instability condition seen in Section 2.3.1 is satisfied: $\gamma_0 > \sqrt{\nu_R \nu_{EPW}}$, with the coupling parameter γ_0 being [79]:

$$\gamma_0^{SRS} = \bar{\gamma}_0^{SRS} C\left(\frac{n_e}{n_c}\right), \tag{2.157a}$$

$$\frac{\bar{\gamma}_0^{SRS}}{\omega_0} \equiv 4.27\times10^{-3}\left(\frac{n_e}{n_c}\right)^{\frac{1}{4}}\left(I_{14}\lambda_0^2\right)^{\frac{1}{2}}, \tag{2.157b}$$

in the case of normal scattering of the daughter Raman wave. The pump wave intensity I_{14} is expressed in units of $10^{14}\ W/cm^2$, while λ_0^2 is the pump wavelength in μm. The term $C(n_e/n_c)$ is a function of the EPW and Raman wave. Its approximations can be, for backscattered light, $C(n_e/n_c) \simeq 1 + O(n_e/n_c)$ in the case of densities far below quarter critical ($n_e/n_c \ll 1/4$), or $C(n_e/n_c) = \sqrt{3/8}$ near quarter critical; for forward scattering, the only case where there is growth is at $n_e/n_c \ll 1/4$, with $C(n_e/n_c) = \sqrt{n_e/n_c}/2$.

With the expression of γ_0 and the definition of the damping rates as the sum between collisional and Landau damping for the EPWs, and a collisional damping for the Raman waves

(via inverse bremsstrahlung , Section 2.2.2.2), we can derive an expression for the laser intensity threshold for densities below quarter critical. Therefore, this threshold is for the *convective SRS instability* for backward and forward scattering. In the case of normal incidence and for plasmas where collisional damping is dominant with respect to Landau damping, we obtain:

$$(I_{14}\lambda^2)^{SRS,\ conv}_{thr,\ back} = 4.1\times10^{-5}\frac{\epsilon\ \ln(\Lambda_{IB})\ln(\Lambda_{ei})(Z_{\text{eff}}/\lambda_0)^2(n_e/n_c)^{\frac{5}{2}}}{T_e^3(1-\sqrt{n_e/n_c})^2}, \tag{2.158a}$$

$$(I_{14}\lambda^2)^{SRS,\ conv}_{thr,\ forw} = 1.61\times10^{-4}\frac{\epsilon\ \ln(\Lambda_{IB})\ln(\Lambda_{ei})(Z_{\text{eff}}/\lambda_0)(n_e/n_c)^{\frac{3}{2}}}{T_e^3}, \tag{2.158b}$$

where $\ln\Lambda_{IB}$ and $\ln\Lambda_{ei}$ are the Coulomb logarithms for inverse bremsstrahlung and electron-ion collisions, respectively, ϵ is the dielectric permittivity depending on the density profile (from the WKB theory), and $Z_{\text{eff}} = \langle Z^2\rangle/\langle Z\rangle$, defined in Section 2.1.5. The *absolute SRS instability* threshold is given, in the case of backscattering (since the instability cannot propagate beyond $n_c/4$) and in the same conditions as the convective instability, by:

$$(I_{14}\lambda^2)^{SRS,\ abs}_{thr} = 0.87\times10^{-3}\epsilon\left[\frac{(n_e/n_c)\ln(\Lambda_{ei})(Z_{\text{eff}}/\lambda_0)}{T_e^2}\right]^2\frac{8k_R(\omega_0/c)^2}{k_{EPW}}. \tag{2.159}$$

Eqs. 2.158a, 2.158b and 2.159 all refer to the ideal case of a homogeneous infinite plasma. However, as seen in Section 2.3.1, introducing changes to the system such as a inhomogeneous density profile, changes the thresholds accordingly:

In the case of plasma inhomogeneities, we can introduce a *density scale length*:

$$L_n = \left(\frac{1}{n_e}\frac{\partial n_e}{\partial x}\right)^{-1}, \tag{2.160}$$

which is defined as the characteristic length for changes to the density gradient normalized to the density profile itself. Using this quantity in presence of inhomogeneities, nearby $n_c/4$ (i.e. absolute instability), and by considering the angle of incidence θ as the angle between the incident wave vector and the density gradient, the result for the SRS threshold is obtained as [21]:

$$\left(\frac{v_{osc}}{c}\right)^2\left(\frac{\omega_0 L_n}{c}\right)^{\frac{4}{3}} \geq f(\omega_{pe},\theta), \tag{2.161}$$

where $f(\omega_{pe},\theta)$ is a function of the angle of the plasma frequency, the angle of incidence of the pump wave. Its shape depends on the *light polarization*, which can be either *s-polarized* of $\boldsymbol{E}\cdot\nabla n_e = 0$, or *p-polarized* otherwise. Therefore:

$$s-polarization: \quad f_s(\omega_{pe},\Theta) = \frac{(\omega_{pe}/\omega_0)^{2/3}}{[2-2\omega_{pe}/\omega_0-(\omega_{pe}/\omega_0)^2]\pm2(1-2\omega_{pe}/\omega_0)^{1/2}\sqrt{\epsilon}\sin\theta}, \tag{2.162a}$$

$$p-polarization: \quad f_p(\omega_{pe},\Theta) = \frac{(\omega_{pe}/\omega_0)^{2/3}}{[2-2\omega_{pe}/\omega_0-(\omega_{pe}/\omega_0)^2]}. \tag{2.162b}$$

These results account for all three scattering configurations (forward, backward and side-scattering), both in s and p polarization. In particular, for the purpose of our work, considering a p-polarized monochromatic laser pump wave in the $n_c/4$ region ($\omega_0 \simeq 2\omega_{pe}$), the threshold condition for absolute backscattered SRS becomes:

$$\left(\frac{v_{osc}}{c}\right)^2_{thr,SRS} = \frac{2^{4/3}}{3}\left(\frac{c}{\omega_0 L_n}\right)^{\frac{4}{3}}. \tag{2.163}$$

In terms of laser intensity I, knowing that the oscillation velocity is of the form $v_{osc} = \epsilon^{-1/4} e/(m_e \omega_0)\sqrt{8\pi I/c}$, where the term $\epsilon^{-1/4}$ comes from the propagation of a transverse wave in a plasma in the WKB theory, and $\epsilon = 0.75$ at $n_c/4$, Eq. 2.163 becomes (in W/cm^2) [133]:

$$I_{thr}^{SRS} = 10^{-7} \times \frac{2^{\frac{1}{3}}}{\sqrt{3}} \frac{m_e^2 \omega_0^2 c^3}{8\pi e^2} \left(\frac{c}{\omega_0 L_n}\right)^{\frac{4}{3}}. \tag{2.164}$$

To provide an example in typical ICF conditions, considering a Nd-YAG laser ($\lambda_0 = 0.351$ μm) and plasma conditions typical of the OMEGA facility (i.e. $L_n \simeq 125$ μm), the SRS threshold becomes $I_{thr}^{SRS} \simeq 2.76 \times 10^{14}$ W/cm^2 in vacuum.

2.3.2.4 SRS additional effects: broadband and multi-beam effects

The thresholds and growth rates represented here do not take into account of more sophisticated effects, such as a pump wave with a spectrum of frequencies (i.e. *broadband effects*) and the presence of *multiple laser beams* and *polarization smoothing* in the plasma density.

- We now consider the presence of *temporal incoherence* (also named *broadband effects*) on the SRS intensity threshold introduced by the laser. We will focus only on the backscattered case, but results for forward scattering can be found at [79] and [134]. In this case, a term $(\Delta\omega_0/\omega_0)$ appears in the intensity thresholds, where $\Delta\omega_0$ is the temporal incoherence, which works to suppress the instability by raising the intensity threshold [133, 135, 136]. The analytical result given by the works of Lu reads:

$$\left(\frac{v_{osc}}{c}\right)^2_{Lu} = 3^{\frac{1}{12}} 2^{\frac{7}{8}} \frac{1}{k_0 L_n} \left(\frac{\tau_0}{2\pi\tau_c}\right)^{\frac{1}{3}}, \quad \beta < 1, \tag{2.165a}$$

$$\left(\frac{v_{osc}}{c}\right)^2_{Lu} = \frac{1}{3} \frac{1}{k_0 L_n} \left(\frac{\tau_0}{2\pi\tau_c}\right), \quad \beta > 1, \tag{2.165b}$$

  where $\tau_0/2\pi\tau_c$ is a reformulation of the term $\Delta\omega/\omega_0$. $\tau_0 = 2\pi/\omega_0$ is the pump wave period and τ_c is the *coherence time*, which assumes the form of $2/\Delta\omega$, $\sqrt{8\pi \ln 2}/\Delta\omega$, $2\pi/\Delta\omega$ for a Lorentzian, Gaussian and a flat spectra for the pump wave respectively [133]. The parameter β is equivalent to: $\beta \equiv 2^{1/3} 3^{-1/3} (v_{osc}/c)^2 k_0 L_n (\tau_0/2\pi\tau_c)^{1/3}$.

- The previous results are all obtained in the presence of one single laser beam impinging on the plasma system. In the case of multiple beams incident on a plasma system and assuming identical angles of incidence, such as an ICF scenario where multiple laser beams arranged in a cone irradiate the ICF target, there can be sharing of a common daughter wave along the symmetry axis [55]. In the case the "shared wave" is the scattered Raman wave, the matching conditions can occur at any density, with absolute instability occurring around $n_c/4$. In the case of the EPW being the shared wave, the common EPW can drive a hot electron population at low angles of emission with respect to the ICF target, and aside convective SRS, absolute SRS can occur at densities below quarter critical [23, 137]. We will focus on this last case's results, as in [23]. Considering N laser beams in 2D , with an angle of incidence θ, each beam will undergo SRS, emitting a wave in a sphere centered in $\boldsymbol{k}_{0j}$ with radius $k_{Rj} = (\omega_0/c)[1 - 2/\sqrt{n_e/n_c}]^{1/2}$. Therefore, there will be a shared EPW only if the spheres of Raman emission all intersect in a region, identified as:

$$n_e \leq n_{lim}(\theta_v) \equiv \frac{n_c}{4} \cos^4(\theta_v), \tag{2.166}$$

  where $\sin(\theta_v) = \epsilon \sin(\theta)$ (Snell's law). In case $n_e < n_{lim}$, we have convective instability. The Rosenbluth gain can be expressed as:

$$G = \frac{\pi L_n \sum_j |a_{0j}|^2 \cos^2 \phi_j}{4} \frac{k_{EPW}^2}{k_{Rz}}, \tag{2.167}$$

where $k_{EPW} = k_0 \cos(\theta) + \sqrt{k_R^2 - k_0^2 \sin^2(\theta)}$ and $k_{Rz}^2 = k_R^2 - k_0^2 \sin^2(\theta)$. When $n_e \simeq n_{lim}$, the Rosenbluth analysis becomes invalid, and G tends to zero. Therefore, the instability becomes absolute in this region, which is below $n_c/4$ because of the $\cos^4(\theta_v)$ term. The general threshold intensity for a single beam in this case becomes:

$$\left(\frac{v_{osc}}{c}\right)^2 \cos^2(\phi) > \frac{(n_e/n_c)^{1/3}}{(k_{EPW}/k_0)^2(1 - n_e/n_c)} \left(\frac{c}{L_n \omega_0}\right)^{\frac{4}{3}}, \tag{2.168}$$

and for N beams of equal intensity, the threshold hold by making the substitution $(v_{osc}/c)^2 \rightarrow \sum_j (v_{osc}/c)_j^2 \cos^2(\phi)$. The term $\cos^2(\phi) \equiv (1 + \sin^2(\theta))/2$ is related to the radial polarization component in presence of *polarization smoothing* [5], where the beam obtains increased uniformity by breaking the field into two orthogonally polarized components, propagating in slightly different directions. This gives a factor of $1/\sqrt{2}$ of nonuniformity reduction. At $n_e = n_{lim}$, the instability becomes absolute, and k_{EPW} becomes equal to $k_0 \cos(\theta)$, and therefore the N-beam threshold becomes:

$$N(v_{osc}/c)^2 > f^{-1}(\theta_v) \left(\frac{\lambda_0}{\pi L_n}\right)^{\frac{4}{3}}, \tag{2.169}$$

where $f(\theta_v)$ is a function of the angle θ_v, approximating to $f \simeq 2 \pm 0.2$ in case θ_v belongs to the interval of $[20° - 60°]$. In these conditions, the threshold in practical units becomes, for a single beam:

$$(I_{14}\lambda_0^2) \geq 1.5 \times 10^3 \left(\frac{\lambda_0}{L_n}\right)^{\frac{4}{3}}, \tag{2.170}$$

for an interaction parameter of $I_{14}\lambda_0^2 \simeq 0.594\ 10^{14}\mathrm{W}\mu\mathrm{m}^2/\mathrm{cm}^2$ in OMEGA conditions ($L_n = 125\ \mu$m) and a Nd-YAG laser ($\lambda_0 = 0.351\ \mu$m).

2.3.3 Two Plasmon Decay

The Two Plasmon Decay (TPD) instability is given by the parametric decay of a laser pump wave in two EPWs. The matching conditions read:

$$\omega_0 = \omega_1 + \omega_2, \tag{2.171a}$$
$$\boldsymbol{k}_0 = \boldsymbol{k}_1 + \boldsymbol{k}_2, \tag{2.171b}$$

where $(\omega_0, \boldsymbol{k}_0)$ is related to the laser, and $(\omega_{1,2}, \boldsymbol{k}_{1,2})$ refer to the two EPWs. The dispersion relations for the waves are the ones at Eqs 2.144a and 2.144b. Similarly to the SRS case, the minimum frequency for each EPW is ω_{pe}. As such, the matching conditions give $\omega_0 \geq 2\omega_{pe}$, and therefore the instability takes place at densities $n_e \leq n_c/4$. Moreover, convective TPD modes are characterized by lower growth rates (and stronger damping) in the underdense plasma, and viceversa for the absolute modes [138]. Thus, the presence of absolute TPD is dominant over convective TPD. Moreover, we will see in the following sections that TPD is mostly a 2D effect. An in-depth analysis of the instability can be found in an extensive bibliography, some of which are: [19, 81, 138, 139, 140, 141].

2.3.3.1 TPD coupling equations

The procedure used to find the coupling equations for TPD is similar to the one applies for Eqs. 2.147 and 2.150. Treating ions as a fixed background, we can describe the electrons as a warm fluid. Therefore, we can decompose the electron density as $n_e = n_0 + \tilde{n}_e$ and the electron fluid velocity as $\boldsymbol{u}_e = \tilde{\boldsymbol{u}}_L + \boldsymbol{v}_{osc}$, where $\boldsymbol{v}_{osc}$ is the quiver velocity. Linearizing the fluid continuity

and momentum equations, we obtain two equations for the perturbed density $\tilde{n}_e$, longitudinal velocity $\tilde{\boldsymbol{u}}_L$ and potential $\tilde{\phi}$:

$$\frac{\partial \tilde{n}_e}{\partial t} + n_0 \nabla \cdot \tilde{\boldsymbol{u}}_L + \boldsymbol{v}_{osc} \cdot \nabla \tilde{n}_e = 0, \tag{2.172a}$$

$$\frac{\partial \tilde{\boldsymbol{u}}_L}{\partial t} = \frac{e}{m_e} \nabla \tilde{\phi} - \frac{3 v_{Te}^2}{n_0} \nabla \tilde{n}_e - \nabla (\boldsymbol{v}_{osc} \cdot \tilde{\boldsymbol{u}}_L). \tag{2.172b}$$

Following the same procedure of Section 2.3.2.1, taking the time derivative of Eq. 2.172a and the divergence of Eq. 2.172b, using the definition of the Poisson's equation and combining the two resulting equations, we obtain:

$$\left(\frac{\partial^2}{\partial t^2} + \left(\omega_{pe}^2 - 3 v_{Te}^2 \nabla^2 \right) + \frac{\partial (\boldsymbol{v}_{osc} \cdot \nabla)}{\partial t} \right) \tilde{n}_e = n_0 \nabla^2 (\boldsymbol{v}_{osc} \cdot \tilde{\boldsymbol{u}}_L). \tag{2.173}$$

Eq. 2.173 states that the coupling between the electron oscillatory motion due to a light pump wave and their average motion in the longitudinal direction (caused by an EPW) is a source term for the electron density perturbation.

2.3.3.2 TPD dispersion relation

Fourier transforming Eq. 2.173 in the 1D case, and representing the pump wave with the electron velocity so that $u_{osc} = u_{osc}[\exp(i\boldsymbol{k}_0 \cdot \boldsymbol{x} - i\omega_0 t) + \exp(-i\boldsymbol{k}_0 \cdot \boldsymbol{x} + i\omega_0 t)]/2$, we obtain a dispersion relation of the form:

$$\begin{aligned} (-\omega^2 + \omega_{EPW}) \tilde{n}_e(k,\omega) + \frac{\omega}{2} \boldsymbol{k} \cdot \boldsymbol{v}_{osc} \left[\tilde{n}_e(k - k_0, \omega - \omega_0) + \tilde{n}_e(k + k_0, \omega + \omega_0) \right] + \\ + \frac{n_0 k^2}{2} \boldsymbol{v}_{osc} \cdot \left[\tilde{\boldsymbol{u}}_L(k - k_0, \omega - \omega_0) + \tilde{\boldsymbol{u}}_L(k + k_0, \omega + \omega_0) \right] = 0. \end{aligned} \tag{2.174}$$

which can be decoupled for the first and second EPW by choosing either (k, ω) or replacing them for $(k - k_0, \omega - \omega_0)$ in Eq. 2.174. By choosing $\omega \sim \omega_{pe}$ and neglecting the terms $\omega + \omega_0$ and $\omega - 2\omega_0$ as off-resonant, we obtain two coupled equations for $\tilde{n}_e(k,\omega)$ (first EPW) and $\tilde{n}_e(k - k_0, \omega - \omega_0)$ (second EPW):

$$\begin{aligned} &(-\omega^2 + \omega_{EPW}^2) \tilde{n}_e(k,\omega) + \\ &\quad + \frac{\boldsymbol{v}_{osc}}{2} \cdot \left[\omega \boldsymbol{k} \tilde{n}_e(k - k_0, \omega - \omega_0) + n_0 k^2 \tilde{\boldsymbol{u}}_L(k - k_0, \omega - \omega_0) \right] = 0, \end{aligned} \tag{2.175a}$$

$$\begin{aligned} &\left[-(\omega - \omega_0)^2 + \omega_{EPW}(k - k_0) \right] \tilde{n}_e(k - k_0, \omega - \omega_0) + \\ &\quad + \frac{\boldsymbol{v}_{osc}}{2} \cdot \left[(\omega - \omega_0) \boldsymbol{k} \tilde{n}_e(k,\omega) + n_0 (\boldsymbol{k} - \boldsymbol{k}_0)^2 \tilde{\boldsymbol{u}}_L(k,\omega) \right] = 0, \end{aligned} \tag{2.175b}$$

where $\omega_{EPW}^2(k - k_0)$ is given by the Bhom-Gross frequency by applying the substitution $(k) \to (k - k_0)$. These equations describe the propagation of the two EPWs, respectively. Substituting Eq. 2.175b into Eq. 2.175a, we obtain the *dispersion relation* for TPD [45]:

$$(\omega^2 - \omega_{EPW}^2) \left[(\omega^2 - \omega_0^2) - \omega_{EPW}^2 (k - k_0) \right] = \left[\frac{\boldsymbol{k} \cdot \boldsymbol{v}_{osc} \omega_{pe} [(\boldsymbol{k} - \boldsymbol{k}_0)^2 - k^2]}{2k |\boldsymbol{k} - \boldsymbol{k}_0|} \right]^2 \tag{2.176}$$

2.3.3.3 TPD growth rate

As in the SRS case, the growth rate is found by substituting the $\omega = \omega_{EPW} + i\gamma$ in Eq. 2.176, remembering that $\boldsymbol{k}_0 \cdot \boldsymbol{v}_{osc} = 0$, and using the TPD matching conditions in Section 2.3.3. Denoting one EPW as $(\boldsymbol{k}, \omega)$ and the other one as $(\boldsymbol{k} - \boldsymbol{k}_0, \omega - \omega_0)$, we obtain:

$$\gamma_0^2 = \frac{(\boldsymbol{k}_2 \cdot \boldsymbol{v}_{osc})^2}{4} \left[\frac{k_1^2 - k_2^2}{k_2 k_1} \right]^2 = \frac{(\boldsymbol{k} \cdot \boldsymbol{v}_{osc})^2}{4} \left[\frac{(\boldsymbol{k} - \boldsymbol{k}_0)^2 - k^2}{k |\boldsymbol{k} - \boldsymbol{k}_0|} \right]^2. \tag{2.177}$$

The Bohm-Gross dispersion relation is a function with a weak dependence on $k = k_{EPW}$ when $k_{EPW}\lambda_{De} < 1$. It can therefore be verified that, in the region of $\omega_0/\omega_{pe} = 2$ (i.e. in the quarter critical region), there can be significant changes in $\boldsymbol{k}_{EPW,1}$ and $\boldsymbol{k}_{EPW,2}$. We change the form of Eq. 2.177 by using:

$$\boldsymbol{k}_1 = \boldsymbol{k_0}/2 + \boldsymbol{K} + k_y\boldsymbol{e}_0, \tag{2.178a}$$

$$\boldsymbol{k}_2 = \boldsymbol{k_0}/2 - \boldsymbol{K} + k_y\boldsymbol{e}_0, \tag{2.178b}$$

where $(\boldsymbol{k_0}/2 \pm \boldsymbol{K})$ is the orthogonal component to the polarization field vector $\boldsymbol{e}_0$ (i.e. the EPW x component) and $k_y\boldsymbol{e}_0$ is the parallel component (i.e. the y component). Therefore, considering the (k_1, k_2) form of Eq. 2.177, the growth rate becomes:

$$\gamma_0^2 = (k_y v_{osc})^2 \frac{(\boldsymbol{k}_0 \cdot \boldsymbol{k})^2}{\left[(\boldsymbol{k}_0/2 - \boldsymbol{K})^2 + k_y^2\right]\left[(\boldsymbol{k}_0/2 + \boldsymbol{K})^2 + k_y^2\right]} \tag{2.179}$$

The growth rate is maximum when $\boldsymbol{K}$ and $\boldsymbol{k}_0$ are co-linear, meaning that the EPWs wave numbers for which the instability grows the most is on the plane $(\boldsymbol{e}_0, \boldsymbol{k}_0)$. Therefore, TPD has a mainly 2D emission of EPWs, even in a 3D system, depending on the light polarization. In particular, γ_0 becomes maximum when $K^2 - k_y^2 = (k_0/2)^2$, resulting in:

$$k_y^2 = k_x(k_x - k_0), \tag{2.180}$$

where $k_x \equiv k_0/2 + K$. Eq. 2.180 describes an hyperbole in the 2D Fourier space for k, or *k-space*. The EPWs lying on the hyperbole are characterized by the maximum value of the growth rate given by Eq. 2.179, which reads [45]:

$$\gamma_0 = \frac{k_0 v_{osc}}{4} = \frac{1}{2}\epsilon(n_e/n_c)\left(\frac{\omega_0}{2}\right)\left(\frac{v_{osc}}{c}\right), \tag{2.181}$$

where $\epsilon(n_e/n_c)$ is the usual dielectric permittivity in a plasma. This value is obtained in the case $k_{1,2} \gg k_0$, the wave number components become $k_y = \pm k_x$, with the EPWs being emitted at $\sim 45°$ angles with respect to both k_0 and v_{osc}. However, this value is the same across the whole hyperbola, and results in the formation of four "lobes" in the region along the maximum growth, as will be seen in chapter 3.

Eq. 2.177 and 2.181 are *homogeneous convective growth rates*. If we were to consider inhomogeneities, Liu and Rosenbluth (1976) [19] consider the problem of the TPD instability in an inhomogeneous density profile, in more general conditions than the work of Lee and Kaw [138], and for wave vectors close to 0. The result they reached was that, for a parameter $\lambda \equiv 2v_{osc}\omega_{pe}/3k_{EPW,y}v_{Te}^2 > \lambda_1$, where λ_1 is of the order of unity, absolute instability can manifest, with a growth rate equal to Eq. 2.181 with a correction for inhomogeneities:

$$\gamma_{0,inh} = \frac{k_0 v_{osc}}{4} - \frac{3v_{Te}^2}{8v_{osc}L_n}, \tag{2.182}$$

where L_n is the density scale length.

2.3.3.4 TPD intensity threshold

The convective threshold for TPD is given, as usual, by $\gamma_0^2 > \nu_1\nu_2$, the subscripts "1,2" referring to the two daughter EPWs. Therefore for an homogeneous infinite medium, the threshold in practical units is [79]:

$$I_{14}\lambda^2 \simeq 1.4 \times 10^{-5}\left(\frac{\ln(\Lambda_{ei})Z_{\text{eff}}/\lambda_0}{T_e^{3/2}}\right)^2\left(1 + \frac{\nu_{1L}}{\nu_{1c}}\right)\left(1 + \frac{\nu_{2L}}{\nu_{2c}}\right), \tag{2.183}$$

where the last two terms disappear when in the collisional regime ($\nu_{jL} \ll \nu_{jc}$, $j = 1, 2$).

In presence of an inhomogeneous plasma, TPD analysis from A. Simon and R.W. Short [81] shows different absolute threshold regimes according to the parameters $\beta \equiv 9v_{Te}^4k_0^2/(|v_{osc}|^2\omega_0^2)$:

- $\beta \gg 1$, $(k_{jy}/k_0)^2 \ll 1$ $(j = 1, 2)$: the EPWs are characterized by the majority of TPD activity concentrated in the vicinity of $(k_x, k_y) \simeq (0, 0)$ and $(k_x, k_y) \simeq (k_0, 0)$. In such regime, the intensity threshold reads:

$$\frac{3}{4}\frac{\alpha}{\beta^{\frac{1}{2}}} = \left(\frac{v_{osc}}{v_{Te}}\right)^2 \frac{k_0 L_n}{4} > \zeta = 4.134, \tag{2.184}$$

where $\alpha \equiv (4k_0|v_{osc}|/\omega_0)k_0 L_n$. In practical units, $\beta \equiv 1.41 T_e^2/I_{14}\lambda^2$, where T_e is in keV and λ is in μm. The result presented in Eq. 2.184 is the corrected one for $v_{osc} \equiv eE/m_e\omega_0$. The minimum perpendicular wave number the product EPWs can assume are:

$$\left(\frac{k_y}{k_0}\right)^2 = 0.106 \left(\frac{I_{14}\lambda^2}{T_e}\right). \tag{2.185}$$

- $\beta \ll 1$, $k_y/k_0 \gg 1$: very much like previously, the EPWs are mainly focused around the center of the spectrum in k-space. The intensity threshold is:

$$\frac{3}{4}\frac{\alpha}{\beta^{\frac{1}{2}}} = \left(\frac{v_{osc}}{v_{Te}}\right)^2 \frac{k_0 L_n}{4} > \zeta = 3.094, \tag{2.186}$$

and the same intensity threshold Eq. 2.188 can be given with the new value of ζ. The minimum wave number is:

$$\left(\frac{k_y}{k_0}\right)^2 = 0.19 \left(\frac{I_{14}\lambda^2}{T_e}\right). \tag{2.187}$$

In both cases, the threshold reads [133]:

$$I_{thr}^{TPD} = 10^{-7} \times 4\zeta \frac{c^4 m_e \omega_0}{8\pi e^2 c^2} \frac{T_e}{L_n}, \tag{2.188}$$

where L_n is in μm as well, and T_e is in keV as above. The term 10^{-7} gives the threshold in W/cm^2. For typical OMEGA conditions (i.e. $L_n = 125$ μm and a plasma temperature of $T_e = 4$ keV, and a laser wavelength of $\lambda_0 = 0.351$ μm), the TPD threshold in vacuum becomes $I_{thr}^{TPD} \simeq 6.42 \times 10^{14}$ W/cm^2.

2.3.3.5 Effects of bandwidth and multiple beams on TPD

Similar to SRS, TPD is affected by more refined phenomena, such as the use of a broadband laser and the presence of multiple beams:

- Similarly to the SRS case, for TPD where the pump light wave is characterized by a broad bandwidth, the intensity threshold assumes the form [134, 135]:

$$\left(\frac{v_{osc}}{c}\right)^2_{Lu} = 4\sqrt{\frac{2}{3}} \frac{1}{k_0 L_n} \frac{v_{Te}}{c} \sqrt{\frac{\tau_0}{2\pi\tau_c}}, \tag{2.189}$$

therefore resulting in a suppression of the instability even for small bandwidths [133, 142] with the same definition as in Section 2.3.2.4.

- We saw in the SRS case that multiple beams can drive a common EPW and two backscattered waves. In the case of TPD, the effect is similar [143], with two backwards emitted EPWs and a forward common one. Dubois et al. [54, 137] showed that a set of N non-interacting beams gives a modified instability threshold condition of the form:

$$N\gamma_0^2 = \nu_1\nu_2, \tag{2.190}$$

and therefore the laser intensity threshold required to trigger TPD with N beams would become $I_{thr,\,j}^{TPD} = (1/N) I_{thr}^{TPD}$, where I_{thr}^{TPD} is from Eq. 2.188. However, experimental results [55] show that there is indeed interaction between the beams, exhibiting a dependence on the density scale length L_n.

2.3.4 Langmuir Decay Instability

Another important parametric instability is the *Langmuir Decay Instability* (LDI), where an EPW decays into another EPW and an Ion Acoustic Wave (IAW) [37, 38]:

$$\omega_{EPW,0} = \omega_{EPW,1} + \omega_{IAW}, \tag{2.191a}$$

$$\boldsymbol{k}_{EPW,0} = \boldsymbol{k}_{EPW,1} + \boldsymbol{k}_{IAW}, \tag{2.191b}$$

where the subscript "0" is used to describe the pump EPW and "1" the daughter one. This instability can be classified as a *secondary instability*, since its pump wave is not the incident wave light in the system, but an EPW. As such, it depends on EPW-generating instabilities (such as TPD and SRS) to be active. Moreover, LDI can be triggered by a daughter EPW of a previous LDI decay. Therefore, there can be a phenomenon of *LDI cascade* [37], until there is a truncation of the series due to the matching conditions no longer satisfied.

Finally, effects that modify the instability threshold such as laser broadband and multibeam effects, do not have any direct influence on the LDI decay, since its pump wave is an EPW. However, there is still an indirect influence on the instability through the modification of the primary instabilities. For this reason, we will treat any of these effects in this section.

Details on the theory of the instability can be found in the works of [24, 37, 38, 39, 79].

2.3.4.1 LDI dispersion relation

The dimensionless dispersion relation reads, according to [79] and considering $k\lambda_D \ll 1$ and $|k_{0,EPW}\lambda_D| \ll 1$:

$$\left(\Omega\left(\Omega + 2i\nu_2\right) - \kappa^2\right)\left(\left(\Omega + i\nu_1 - 2\kappa\kappa_0\right)^2 - \kappa^4\right) = \epsilon_0\kappa^4, \tag{2.192}$$

where the dimensionless quantities in Eq. 2.192 being defined as:

$$\Omega \equiv \frac{3}{2}\frac{(\omega/\omega_{pe})}{\mu(1+\tau_{i,\text{eff}})}, \tag{2.193a}$$

$$\kappa \equiv \frac{3}{2}\frac{k\lambda_D}{\left(\mu\left(1+\tau_{i,\text{eff}}\right)\right)^{1/2}}, \tag{2.193b}$$

$$\varepsilon_0^2 \equiv \frac{3}{2}\frac{\mu\left(v_{osc}/v_{Te}\right)^2\cos^2\alpha}{\left(\mu\left(1+\tau_{i,\text{eff}}\right)\right)^2}, \tag{2.193c}$$

describing the normalized quantities of wave frequency, vector and quiver velocity, respectively. Λ_D is the overall Debye length (with both electron and ion contributions), $\mu \equiv Z_{\text{eff}}m_e/m_i$, and $\tau_{i,\text{eff}} \equiv \gamma_i T_i/Z_{\text{eff}}T_e$, where $\gamma_i = 3$ if $|v_{ph,EPW}| \gg v_{Ti}$ and $\gamma_i = 1$ in the opposite case. The definition of $\tau_{i,\text{eff}}$ is given by the relation $C_{s,\text{eff}}^2/v_{Te}^2 \equiv (1/v_{Te}^2)(Z_{\text{eff}}T_e + T_i)/m_i \equiv \mu(1+\tau_{i,\text{eff}})$. Finally, m_i is the ion mass, and $\cos^2\alpha$ is the angle of emission of the daughter EPW with respect to the pump EPW. The quantity κ_0 is defined as $\kappa_0 \equiv \kappa(k\lambda_D \to k_{0,EPW}\lambda_D\cos\theta)$. The normalized damping rates are defined as:

$$\bar{\nu}_{1,2} = \frac{3}{2}\frac{1}{\mu\left(1+\tau_{i,\text{eff}}\right)}\frac{\nu_{EPW,IAW}}{\omega_{pe}}, \tag{2.194}$$

where the subscripts $1, 2$ refer to the daughter EPW and IAW, respectively. The wave numbers of the product EPW and IAW are [24, 39]:

$$k_{EPW}^2 = k_{0,EPW}^2 - 2\Delta k k_0\cos\theta + \Delta k^2, \tag{2.195a}$$

$$k_{IAW} = 2k_{0,EPW}\cos\theta - \Delta k, \tag{2.195b}$$

where $\Delta k \equiv (2/3)[C_{s,\text{eff}}/(v_{Te}\lambda_D)]$. We must remember that Eqs. 2.195a and 2.195b refer to one decay only, without considering the cascade. Therefore, to obtain the wave numbers of an EPW and an IAW at its n-th decay as a function of the original pump EPW (i.e. the 0-th one), we need to substitute both equations within themselves.

In the case of $\cos\theta = +1$, the daughter waves are aligned with the pump, and Eqs. 2.195a and 2.195b can be reduced to a more convenient form, and can be used to derive the EPW and IAW wave vectors' of the n-th iteration from the TPD daughter wave (0-th iteration) [39]:

$$k_{n,EPW} = k_{0,EPW} - (n-1)\Delta k, \tag{2.196a}$$

$$k_{n,IAW} = 2k_{0,EPW} - (2n-3)\Delta k. \tag{2.196b}$$

The group velocities of both the daughters EPW and IAW are given by:

$$\boldsymbol{v}_{g,EPW} = 3\frac{v_{Te}^2}{2\omega_{pe}}\boldsymbol{k}_{EPW}, \tag{2.197a}$$

$$\boldsymbol{v}_{g,IAW} = c_s\frac{\boldsymbol{k}_{IAW}}{|\boldsymbol{k}_{IAW}|}. \tag{2.197b}$$

The dependence of $\boldsymbol{v}_{g,EPW} \propto \boldsymbol{k}_{EPW}$ implies a lower group velocity for further daughter EPWs in the LDI cascade process, which will serve as an explanation in further discussions in Chapters 3 and 4.

2.3.4.2 LDI growth rate and threshold condition

The decay of an EPW into another EPW and an IAW can belong to either a *modulational instability*, or to a *parametric decay*. In the parametric decay regime, we can distinguish between two sub-regimes, the *standard* regime and the *modified* one. LDI is located in the parametric standard regime, which is defined by the condition:

$$\varepsilon_0 \leq \frac{1}{4}\left[\kappa_0 + \left(\kappa_0^2+2\right)^{\frac{1}{2}}\right]^{\frac{1}{2}}\left[3\kappa_0 - \left(\kappa_0^2+2\right)^{\frac{1}{2}}\right]^{\frac{3}{2}}, \tag{2.198}$$

where Eq. 2.198 describes the curve, as a function of κ_0, below which parametric decay is possible, instead of modulational instabilities; moreover, this equation implies that $\epsilon = 0$ if $\kappa_0 = 1/2$, which corresponds to very small wave vectors. The standard regime is located below Eq. 2.198 up until $\kappa_0 = 2$, after which there is a split between the parametric standard and the modified regime. Therefore, for $\kappa_0 > 2$ Eq. 2.198 assumes the form:

$$\varepsilon_0 < 2^{\frac{3}{2}}\left(\kappa_0 - \frac{1}{2}\right)^{\frac{1}{2}}. \tag{2.199}$$

In the parametric standard regime, where LDI is located, the maximum growth rate is given by:

$$\gamma_0^2 = \frac{1}{4}\mu^{\frac{1}{2}}\omega_{pe}^2 k_{max}\lambda_D\left(\frac{v_{osc}}{v_Te}\right)^2, \tag{2.200}$$

where k_{max} is the IAW wave vector that maximizes the growth rate, given by $\boldsymbol{k}_{max} \equiv (2k_0 - \Delta k)\boldsymbol{k}_0/|\boldsymbol{k}_0|$. Therefore, the maximum growth rate is achieved when $\cos\theta = 1$, and the daughter waves are emitted parallel to the pump wave vector $\boldsymbol{k}_0$.

The threshold condition reads, as usual, $\gamma_0^2 > \nu_1\nu_2$, where $nu_{1,2}$ refer to the EPW and IAW damping rates, respectively, in dimensional form. In the case of $2k_0 \gg \Delta k$, the threshold condition can be approximated by:

$$\left(\frac{v_{osc}}{v_{Te}}\right)^2 \geq 4\mu^{\frac{1}{2}}\left(1+\tau_{i,\text{eff}}\right)^{\frac{3}{2}} k_{max}\lambda_D. \tag{2.201}$$

In this case, $\tau_{i,\text{eff}}$ is defined as $\tau_{i,\text{eff}} = 3T_i/Z_{\text{eff}}T_e$.
Finally, we can also give an expression of the maximum growth rate (i.e. $\cos\theta$) as a function of the density perturbation $\delta n_e/n_0$, in case the condition $2k_0 \gg \Delta k$ is satisfied:

$$\gamma_0 \simeq \frac{\mu^{1/4}}{2^{1/2}}\omega_{pe}\frac{\delta n_e/n_0}{(k_0\lambda_D)^{1/2}}. \tag{2.202}$$

2.3.5 Stimulated Brillouin Scattering

We will now describe the Stimulated Brillouin Scattering (SBS) parametric instability. Because SBS does not produce EPWs (and therefore no hot electrons), and because its derivation is similar to SRS, we will provide a more condensed description of the instability. More details can be found in [19, 45, 79, 132].

SBS occurs when a pump light wave decays into a scattered wave and an *Ion Acoustic Wave* (IAW). The physics of the instability is the same as for SRS (Fig. 2.5). However, as it will be seen in the following section, the laser light drives an electron density perturbation $\delta n_e/n_0$ that is at a lower frequency than its SRS counterpart, thus describing IAW. Its matching conditions are therefore:

$$\omega_0 = \omega_B + \omega_{IAW}, \tag{2.203a}$$
$$\boldsymbol{k}_0 = \boldsymbol{k}_B + \boldsymbol{k}_{IAW}. \tag{2.203b}$$

The pump and Raman light waves in Eq. 2.203 have a frequency of the form Eq. 2.144a, as they are light waves propagating in a plasma, and the IAW follows the relation 2.91, which in a more general form assumes the form:

$$\omega_{IAW}^2 = \gamma_i k_{IAW}^2 v_{Ti}^2 + \frac{k_{IAW}^2\lambda_D^2\omega_{pi}^2}{1 + k_{IAW}^2\lambda_D^2}, \tag{2.204}$$

where λ_D is the total Debye legnth given by both the electron and ion contribution, and γ_i is the same as in Section 2.3.4.1. Eq. 2.204 also includes the effects of $k_{IAW}\lambda_D$. By approximating $k_{IAW}\lambda_D \ll 1$ and $\lambda_D \simeq \lambda_{De}$, Eq. 2.91 can be retrieved.

Therefore, $\omega_0 \geq \omega_B \simeq \omega_{pe}$, and the instability can develop throughout the entire plasma profile until reaching the critical density, $n_e \leq n_c$, similarly to SRS (which can develop up to $n_e \leq n_c/4$). Because the IAW has a much lower frequency than the scattered Brillouin wave, the laser energy gets transferred mainly to the scattered wave, making SBS an important concern for laser energy absorption and for potential disruption of the implosion symmetry, since the Brillouin wave changes the location at which the energy is absorbed.

2.3.5.1 Analysis of the instability

Similarly to SRS, SBS is characterized by a set of equations that couple the pump light wave to either an electron density fluctuation or the scattered Brillouin wave of the form:

$$\left(\frac{\partial^2}{\partial t^2} - c^2\nabla^2 + \omega_{pe}^2\right)\tilde{\boldsymbol{A}} = -\frac{4\pi e^2}{m_e}\tilde{n}_e\boldsymbol{A}_L, \tag{2.205}$$

where there are only electron related quantities because the ion response to the light wave electric field is lower than the electron response by a factor $Z_{\text{eff}}m_e/m_i$. However, for the Brillouin instability the quantity $\tilde{n}_e$ is associated to a low frequency electron density fluctuation, which describes an Ion Acoustic Wave (IAW). Therefore the equation for this density, resulting from the coupling between the laser light and the Brillouin scattered wave, will have to consider the ion motion as well. By following the same reasoning as in the SRS case, we consider the equation of motion, and splitting the fluid velocity $\boldsymbol{u}_e$ into a longitudinal component $\boldsymbol{u}_L$ and a

transverse one $e\boldsymbol{A}/m_e c$, we obtain once more Eq. 2.148b. However, we now neglect the electron inertia ($\partial \boldsymbol{u}_L/\partial t \to 0$), since we are focusing on a low frequency fluctuation. We can also apply the isothermal equation of state as well (i.e. $p_e = n_e T_e/k_B$, where T_e is in keV and k_B is the Boltzmann constant). splitting $n_e = n_0 + \tilde{n}_e$, $\boldsymbol{A} = \boldsymbol{A}_L + \tilde{\boldsymbol{A}}$ and $\phi = \tilde{\phi}$, Eq. 2.148b becomes:

$$\frac{e}{m_e}\nabla\tilde{\phi} = \frac{e^2}{m_e^2 c^2}\nabla\left(\boldsymbol{A}_L \cdot \tilde{\boldsymbol{A}}\right) + \frac{v_{Te}^2}{n_0}\nabla\tilde{n}_e. \tag{2.206}$$

Considering the continuity and momentum equation for the ion fluid characterized by a density $n_i = n_{0i} + \tilde{n}_i$, a fluid velocity $\boldsymbol{u}_i = \tilde{\boldsymbol{u}}_i$ and a potential $\phi = \tilde{\phi}$, and combining these two equations into a single one [45], we obtain:

$$\frac{\partial^2 \tilde{n}_i}{\partial t^2} - \frac{n_{0i} Z_{\text{eff}} e}{m_i}\nabla^2\tilde{\phi} = 0. \tag{2.207}$$

Using Eq. 2.206 to substitute $\nabla\tilde{\phi}$ into 2.207, and remembering the assumption of global charge neutrailty in a plasma ($N_{\text{eff}}\tilde{n}_i \simeq \tilde{n}_e$), we finally obtain an equation for the low frequency electron fluctuation $\tilde{n}_e$:

$$\left(\frac{\partial^2}{\partial t^2} - c_s^2\nabla^2\right)\tilde{n}_e = \frac{Z_{\text{eff}} n_0 e^2}{m_e m_i c^2}\nabla^2\left(\boldsymbol{A}_L \cdot \tilde{\boldsymbol{A}}\right), \tag{2.208}$$

where c_s is defined in Eq. 2.204. Eq. 2.208 couples the laser pump wave with the scattered Brillouin wave to give a low frequency density perturbation, an IAW, through ponderomotive force.

2.3.5.2 SBS dispersion relation

Considering a pump wave field of the form $\boldsymbol{A}_L \to \boldsymbol{A}_L \cos(\boldsymbol{k}_0 \cdot \boldsymbol{x} - \omega_0 t)$, and using a similar procedure to the SRS 1D case (i.e. Fourier analysis of Eqs. 2.205 and 2.208), we obtain two equations depending on $\tilde{n}_e(\omega \pm \omega_0, k \pm k_0)$ and $\tilde{\boldsymbol{A}}_L(\omega \pm \omega_0, k \pm k_0)$. Substituting one of these equations in the other, assuming $\omega \ll \omega_0$ and neglecting the nonresonant terms, we obtain the following dispersion relation:

$$\omega^2 - k^2 c_s^2 = \frac{k^2 v_{osc}^2}{4}\omega_{pi}^2\left[\frac{1}{D(\omega - \omega_0, \boldsymbol{k} - \boldsymbol{k}_0)} + \frac{1}{D(\omega + \omega_0, \boldsymbol{k} + \boldsymbol{k}_0)}\right], \tag{2.209}$$

where $D(\omega, k) \equiv \omega^2 - k^2 c^2 - \omega_{pe}^2$, and $\omega_{pi} = \omega_{pe}(Z_{\text{eff}} m_e//m_i)^{1/2}$ is the ion plasma frequency. A more general form can be found at [79], where damping and $k_{IAW}\lambda_D$ contributions are included. Eq. 2.209 form allows to derive the growth rates and thresholds in the following section.

2.3.5.3 SBS growth rates and instability thresholds

As presented in section 2.3.1, the instability develops when $\gamma_0^2 > \nu_1\nu_2$. Here ν_1 corresponds to the scattered Brillouin wave damping, poportional to the Inverse Bremsstrahlung Coulomb logarithm $\ln(\Lambda_{IB})$, and ν_2 to the IAW, composed by IAW Landau damping and a term proportional to the ion-ion collisional damping. In the following, we will consider only the SBS backscatter growth rates and thresholds:

- In the *convective regime*, the dimensionless SBS growth rate is:

$$\frac{\gamma_{0,conv}}{\omega_{IAW}} = \frac{\bar{\gamma_0}}{\omega_{IAW}}\frac{|\sin\alpha|}{|\cos\theta|^{\frac{1}{2}}(c_{s,\text{eff}}/c_s)^{\frac{3}{2}}(1 + k_{IAW}^2\lambda_D^2)^{\frac{1}{4}}}, \tag{2.210a}$$

$$\frac{\bar{\gamma_0}}{\omega_{IAW}} \equiv 1.06\frac{(I_{14}\lambda^2)^{\frac{1}{2}}(n_e/n_c)^{\frac{1}{2}}(A_{\text{eff}}/Z_{\text{eff}})^{\frac{1}{4}}}{(T_e(1 - \tau_{i,\text{eff}}))^{\frac{3}{4}}\epsilon^{\frac{1}{4}}}, \tag{2.210b}$$

where $\epsilon \equiv 1 - n_e/n_c$ is the dielectric permittivity, and α and θ are the angles between the scattered Brillouin and the IAW, respectively, and the pump wave. The ratio $c_{s,\text{eff}}/c_s \equiv \sqrt{(3T_i(1+k_{IAW}^2\lambda_D^2)+Z_{\text{eff}}T_e)/(3T_i+Z_{\text{eff}}T_e)}$ accounts for effects from $k_{IAW}\lambda_D$, and it is 1 if $k_{IAW}\lambda_D \ll 1$. The corresponding instability threshold for the intensity reads:

$$(I_{14}\lambda^2)_{conv} = 1.5\left(\frac{(T_e(1+\tau_{i,\text{eff}}))^{\frac{3}{2}}\epsilon^{\frac{1}{2}}(Z_{\text{eff}}/A_{\text{eff}})^{\frac{1}{2}}}{n_e/n_c}\right)\frac{|\cos\theta|(c_{s,\text{eff}}/c_s)^3(1+k_{IAW}^2\lambda_D^2)^{\frac{1}{2}}}{|\sin^2\alpha|}. \tag{2.211}$$

- In the *absolute regime*, the instability growth rate assumes the form:

$$\frac{\gamma_{0,abs}}{\omega_{IAW}} = 0.683\times10^{-1}\frac{(n_e/n_c)^{\frac{1}{2}}(I_{14}\lambda^2)^{\frac{1}{2}}}{[T_e(1+\tau_{i,\text{eff}})]^{\frac{1}{2}}\epsilon^{\frac{1}{2}}}\frac{\sin\alpha}{(1+k_{IAW}^2\lambda_D^2)}, \tag{2.212}$$

and an intensity threshold of:

$$(I_{14}\lambda^2)_{abs} = 2.14\times10^2\frac{(\nu_{IAW}/\omega_{IAW})^2T_e(1+\tau_{i,\text{eff}})\epsilon}{n_e/n_c}\frac{(1+k_{IAW}^2\lambda_D^2)^2}{\sin^2\alpha}. \tag{2.213}$$

2.3.5.4 Effects on SBS of an inhomogeneous density profile and broadband

The SBS instability is weakly sensitive to an inhomogeneous density profile. Therefore, the daughter waves' dispersion relation is similar to their homogeneous case. This assumption is valid if the flow velocity of the plasma expansion of the ICF target can be considered negligible. In the case this velocity is not negligible, if we consider the underdense domain ($n_e/n_c \ll 1$), so that $k_{IAW}^2\lambda_D \ll 1$, the IAW will see a plasma with an expansion velocity v_{exp} in the opposite direction of the laser light. Considering backscattering in a simple 1D case (i.e. expansion antiparallel to the laser propagation), the product waves' frequencies will experience a blue shift due to Doppler effect, with their velocity terms shifted by a factor v_{exp}:

$$\omega_{IAW} = |k_{IAW}|(c_s - v_{exp}), \tag{2.214a}$$

$$\omega_B = \omega_0\left(1 - 2(1-n_e/n_c)^{\frac{1}{2}}\frac{c_{s,\text{eff}} - v_{exp}}{c_s}\right). \tag{2.214b}$$

The existence of an expansion velocity does not change the convective threshold. However, the absolute threshold is modified, in the case of subsonic flow, by a factor of $1/(1-M)$, where $M \equiv v_{exp}/c_s$ is the *Mach number*, while in the supersonic regime, there can be no absolute instability. The Rosenbluth gain for backscattered SBS in this case is given by:

$$G_{Ros}^{SBS} = 0.92\times10^{-1}\frac{I_{14}\lambda^2}{T_e(1+\tau_{i,\text{eff}})}\frac{L}{\lambda_0}\frac{n_e}{n_c}, \tag{2.215}$$

where $L \equiv [(1/\omega_{IAW}^2)(\partial\omega_{IAW}^2/\partial x)]^{-1}$.
In the case of the presence of a temporal incoherence, similarly to SRS, a term $\Delta\omega/\omega_0$ appears in the expression of the intensity threshold. The threshold condition, in the case of backscattering, is given by:

$$I_{14}\lambda^2 \leq \frac{3\times10^5}{\cos\theta}\left(\frac{\Delta\omega}{\omega_0}\right)^2\frac{(T_e(1+\tau_{i,\text{eff}}))^{\frac{1}{2}}}{(2Z_{\text{eff}}/A_{\text{eff}})^{\frac{1}{2}})(n_e/n_c)\epsilon}\left(1+k_{IAW}^2\lambda_D^2\right)^{\frac{3}{2}}. \tag{2.216}$$

2.4 Conclusions

We have presented the basic theory of electromagnetism of waves in plasmas. The waves propagate in a plasma according to their dispersion relation, and considering a kinetic plasma description, the effect of Landau damping comes to light. Moreover, we considered the important consequence for a plasma when a wave propagates within, generating a ponderomotive force that pushes the plasma away from high field pressure regions. This is key to the formation of a specific class of laser-plasma instabilities called parametric couplings, where a pump wave decays into two daughter waves according to a set of matching conditions both in frequency and wave vector: from a physical point of view, the pump wave excites an electron density perturbation (generating a longitudinal wave in the plasma), which drives a nonlinear current that couples with the pump wave via ponderomotive force, therefore establishing a positive feedback loop by driving an even stronger density perturbation, which continues the cycle as long as the energy provided by the pump wave overcomes the wave dampings (both collisional and Landau) of the daughter waves in the plasma. On this regard, particular emphasis has been put on the theory of parametric instabilities, from general considerations about their domain of existence in different plasma conditions: from an infinite homogeneous plasma to a finite inhomogeneous one, introducing effects such as amplification gain and density scale lengths. Moreover, a brief compendium of the relevant instabilities for this work has been provided, determining growth rates and pump intensity thresholds, which will translate, in an ICF scenario, in constraints for the laser intensity for the parametric instabilities (and therefore hot electron generation). This chapter lays the framework for the discussion of the physical result that will be presented in the following chapters, both from a simulation and an experimental point of view.

Chapter 3

Introduction to the LPSE code: simulations of SRS, TPD and HE generation

As we discussed in the previous chapter, laser-plasma couplings in the system generate parametric instabilities, which grows either because of spatial amplification as the wave travels within the plasma, or in time because the instability is contained in a localized region, and the eigenvalue system has at least an unstable solution. The problem is then to accurately model the instabilities within the plasma system.

Particle In Cell (PIC) codes are one way to solve this problem. They resolve the system of equations composed by the Maxwell equations for the fields, and the kinetic evolution of the particles in the plasma. In a PIC code, the simulation domain is specified by a matrix of *nodes*, with the area included between each node constituting a *cell*. Within a cell, the behavior of a population of *virtual or macro-particles* each constituting an ensemble of electrons is simulated. The code computes the electromagnetic field at each node through the solution of the Maxwell equations, and uses said field to solve the macro-particles' trajectories (*push-up step*). The particles' motion generates an electromagnetic field that is averaged at each node through the solution of the Boltzmann equation, which is then plugged into the Maxwell's system of equation at the next time step. This constitutes a feedback between the particles and the field. Due to this feedback, PIC codes are very precise in their solution. However, they are computationally expensive. Considering characteristic dimensions of an ICF target in a 2D simulation (i.e. a grid of $\sim 10^{-3} \times 10^{-3}$ m $\times$ m) and for each cell (i.e. $\sim 10^{-8}$ m per dimension), assuming each cell contains $\sim 10^2$ particles, the memory allocation for one single quantity (i.e. the particle velocity in the 2D space), assuming it would take 1 byte, would be ~ 1 TB for each time step. It is clear therefore that PIC codes are a very useful at microscopic and mesoscopic scales, but rapidly become computationally burdensome for increasing scales. Moreover, PIC codes consider the entire Fourier spectrum when computing the electromagnetic fields at each node, which further increases the duration of each simulation.

These two aspects are an issue when required to investigate a wide array of laser-plasma condition. A possible solution is given through the hybrid code *Laser Plasma Simulation Environment* (LPSE) [62]. The main approximation this code uses is the *Zakharov model*, whose assumption is to employ enveloped fields averaged over "fast times" as solution of the field equations. This significantly speeds up the computation by solving field equations instead of considering the entire Fourier spectrum for each wave. Moreover, the code can solve the kinetic evolution of a population of macro-particles in the plasma, with the difference that particles from LPSE do not generate their own field during the push-up step. They therefore evolve according to the field solution at each time step, but they can only provide feedback to the field solver through the calculation of the Landau damping evolution in time. These two approx-

imation (enveloped field and non interacting particles) allow for shorter simulation times and less computational resources, while investigating at the same scales PIC codes are capable of in a wider array of laser plasma conditions. Moreover, the code allows to choose the physics within the simulation, allowing an analysis of the effects singular physical phenomena have on the plasma. The downsides of this simplified formulation is that, due to the enveloped fields, the Zakharov model does not accurately predict phenomena such as convective SRS. Moreover, the code lacks a nonlinear saturation model for IAWs. LPSE history of investigating laser plasma instabilities ranges from inferring their mitigation using multilayered targets [144], including broadband [133, 142] and multibeam effects [55, 145], to the analysis of laser-plasma induced anomalous absorption [28] and spatiotemporal smoothing [146], as well as *Cross Beam Energy Transfer* (CBET) studies [62, 147] as shown in chapter 1.

In this chapter we describe the LPSE code field solver, giving the fundamental principles of the Zakharov model and the field equations used in LPSE, as well as the code validation on the threshold for SRS and TPD. Moreover, we give some fundamentals of the hot electron generation mechanisms considered, mainly from parametric instabilities and turbulence, and the kinetic model used by LPSE to simulate their generation.

3.1 LPSE field solver

The Laser Plasma Simulation Environment (LPSE) is a wave code computing a discrete approximation of the 3D wave equations for the laser light, the scattered (Raman or Brillouin) light, the Langmuir Waves (EPWs) and the Ion Acoustic Waves (IAW) [62, 133]. These equations are coupled through a linearized plasma response in the LW and IAW equations for small perturbations relative to the background density n_0. In the following sections the core field equations used in the code are presented. We describe the Zakharov model, upon which LPSE builds the field equations to be solved, which make the code require less resources for the simulations to occur. Finally, we discuss the derivation of the system itself.

3.1.1 Zakharov model

We now introduce the *Zakharov model* [25, 27, 40, 143, 148, 149]. In this description, we consider a plasma in the condition of $k\lambda_D \ll 1$. The motions in a plasma are decoupled into a high-frequency oscillatory motion, and a low-frequency one. Therefore, we can decouple the electron density profile in a background density n_0, while the perturbation is characterized by a low frequency component n_{el} and a high frequency one n_{eh}: $n_e = n_0 + n_{el} + n_{eh}$. The high and low frequency components are representative for the EPWs and the IAWs, respectively. The same can be done for the electron velocity, so that $u_e = v_{osc} + u_{el} + u_{eh}$. Moreover, the electric fields of the laser and the EPW can be written as $\boldsymbol{E_{las}} = 1/2\boldsymbol{E_0}(\boldsymbol{r})\exp(-i\omega_0 t) + \text{c.c.}$ and $\boldsymbol{E} = 1/2\boldsymbol{E_{EPW}}(\boldsymbol{r})\exp(-i\omega_{pe}t) + \text{c.c.}$, where ω_0 and ω_{pe} are the laser and plasma frequencies, respectively. The equation for the electron velocity is therefore given by [150]:

$$\begin{aligned} -i\omega_{pe}\boldsymbol{u}_e = &-\frac{e}{m_e}\boldsymbol{E} - \frac{e}{i\omega_{pe}m_e}\frac{\partial \boldsymbol{E}}{\partial t} + \frac{3T_e}{4\pi e n_0 m_e}\nabla(\nabla\cdot\boldsymbol{E}) + \\ &-\frac{e^2}{2m_e^2\omega_0\omega_{pe}}\left[(\boldsymbol{E}_0\nabla)\,\boldsymbol{E}^{\text{c.c.}} + (\boldsymbol{E}^{\text{c.c.}}\nabla)\,\boldsymbol{E}_0\right]\exp(-i\Omega t), \end{aligned} \tag{3.1}$$

where $\Omega = \omega_0 - 2\omega_{pe}$. Another equation that can be found is the equation for the high-frequency electron density:

$$-i\omega_{pe}n_{eh} + \frac{\partial n_{eh}}{\partial t} + \nabla\cdot\left[(n_0 + n_{el})\,\boldsymbol{u}_e\right] - \frac{n_0 e^2\exp(-i\Omega t)}{2im_e^2\omega_{pe}^2\omega_0}\nabla\cdot(\boldsymbol{E}_0\nabla\cdot\boldsymbol{E}^{\text{c.c.}}) = 0. \tag{3.2}$$

Combining Eqs. 3.1 and 3.2 in order to get rid of the electron velocity $\boldsymbol{u}_e$, simplifying the nonlinear term that appears through the identity $\nabla \times [a \times b] = a\nabla \cdot b - b\nabla \cdot a + (b\nabla)a - (a\nabla)b$, and finally taking into account the presence of collisionless (Landau) damping, one obtains an equation for the EPW electric field $\boldsymbol{E}$:

$$\nabla \cdot \left[\frac{2}{i\omega_{pe}} \left(\frac{\partial \boldsymbol{E}}{\partial t} + \hat{\Gamma}\boldsymbol{E} \right) - \frac{3T_e}{m_e\omega_{pe}^2} \nabla(\nabla \cdot \boldsymbol{E}) + \frac{n_{el}}{2n_0}\boldsymbol{E} + \frac{e}{2m_e\omega_0\omega_{pe}} (\boldsymbol{E} \cdot \nabla)\, \boldsymbol{E}_0 \exp(-i\Omega t) \right] = 0, \tag{3.3}$$

where the term $\hat{\Gamma}\boldsymbol{E}$ is a convolution operator applied to the electric field, and describes the Landau damping effects through:

$$\hat{\Gamma}\boldsymbol{E} = \int \Gamma(\boldsymbol{r} - \boldsymbol{r'})\boldsymbol{E}(t, \boldsymbol{r'})d\boldsymbol{r'}, \tag{3.4}$$

where the function Γ is the Fourier transform of the Landau damping coefficients $\Gamma_{\boldsymbol{k}}$ each depending on a wave number $\boldsymbol{k}$: $\Gamma(\boldsymbol{r}) \equiv [1/(2\pi)^3] \int \Gamma_{\boldsymbol{k}} \exp(i\boldsymbol{k} \cdot \boldsymbol{r})d\boldsymbol{k}$. In the case of a Maxwell-Boltzmann electron distribution, each coefficient $\Gamma_{\boldsymbol{k}}$ assumes the form of Eq. 2.104.

For the low-frequency density perturbation of the electrons (IAWs), with a similar procedure [150] one finds:

$$\frac{\partial^2 n_{el}}{\partial t^2} + \hat{\gamma}\frac{\partial n_{el}}{\partial t} - \frac{T_e + T_i}{m_i}\nabla^2 n_{el} = \frac{1}{16\pi m_i}\nabla^2|E|^2, \tag{3.5}$$

with the term $\hat{\gamma}$ being a convolution operator for n_{el}, following the same behavior as $\hat{\Gamma}$ (Eq. 3.4). The resulting coefficients $\gamma_{\boldsymbol{k}}$ are given by Eq. 2.107.

Eqs. 3.3 and 3.5 describe a coupled system of equations between EPWs and IAWs, respectively, in the plasma system. However, these equations consider the entire Fourier spectrum for both EPWs and IAWs, and require significant computational resources. In this context, Zakharov [40] proposed a simplified version of these equations, without resorting to a kinetic description for the coupled waves. The main idea of the *Zakharov model* (ZAK) is to introduce a representative frequency ω_{p0} in Eq. 3.4, rather than the entire Fourier spectrum of frequencies, therefore averaging over fast times $\tau = 1/\omega_{p0}$. This allows to simplify the problem by removing the time dependence from the high frequency component, which become of the form:

$$u_{eh} = \Re[\bar{u}_{eh}(x, t) \exp(-i\omega_{p0}t)], \tag{3.6}$$

where ω_{p0} is the *envelope frequency*, and it is usually set to the electron plasma frequency $\omega_{p0} = \omega_{pe}$ or its half $\omega_{p0} = \omega_{pe}/2$, according to the density at which the considered phenomenon occurs (either at critical or quarter critical density). We can therefore write down the *Zakharov equations*, which are similar to Eqs. 3.3 and 3.5 but with simply one frequency (ω_{p0}) in the Landau damping operator. These equations are derived in the absence of collisional damping ($\nu_{e,i} = 0$). The Zakharov model is used to describe both three and four wave interactions (the latter not discussed here), and is useful for the study of strongly turbulent systems [151] and is the model implemented in LPSE [62].

3.1.2 Field equations

As we discussed in the introduction, the LPSE code solves a set of coupled equations for the laser light, Raman light, Langmuir Waves and IAWs, where the LW and IAW equations are linearized for small perturbations relative to the background density n_0. The fields of the laser and Raman light, as well as the LW/EPW are using the Zakharov model, therefore being enveloped in time. This allows a faster computation, since the code does not have to solve fields

that have frequencies along the entire Fourier spectrum, but with the shortcoming that the code needs two separate equations for the laser and the scattered Raman light, respectively:

$$\tilde{\boldsymbol{E}}_j(\boldsymbol{x},t) = \Re[\boldsymbol{E}_j(\boldsymbol{x},t)\exp(-i\omega_j t)], \tag{3.7a}$$

$$\tilde{\boldsymbol{E}}_h(\boldsymbol{x},t) = \Re[\boldsymbol{E}_h(\boldsymbol{x},t)\exp(-i\omega_{p0} t)], \tag{3.7b}$$

where ω_{p0} is the envelope frequency, corresponding to the electron plasma frequency at the chosen density n_0, and ω_j ($j = 0, 1$) is the frequency of the envelope for the laser ("0"), the Raman wave ("1") or the EPWs ("h").

The density profile is defined as $n_e = n_0 + \delta N(\boldsymbol{x}) + \delta n_l(\boldsymbol{x},t) + \delta n_h(\boldsymbol{x},t)$, where n_0 is the background density and δN is a user imposed density profile, while the evolution in both time and space of the density is represented by a low-frequency component δn_l and a high-frequency one δn_h. These last two terms represent the IAWs and the EPWs' contributions, respectively.

3.1.2.1 Laser pump wave

The equation for the laser (pump) wave is given by:

$$\begin{aligned}\frac{\partial}{\partial t}\boldsymbol{E}_0 =& \frac{ic^2}{2\omega_0}\left[\nabla^2\boldsymbol{E}_0 - \nabla(\nabla\cdot\boldsymbol{E}_0)\right] + \frac{i\omega_0}{2}\left[1 - \frac{\omega_{p0}^2}{\omega_0^2}\left(1 + \frac{\delta N}{n_0} + \frac{\delta n_l}{n_0}\right)\right]\boldsymbol{E}_0 + \\ &- \frac{\omega_{p0}^2}{2\omega_0^2}\left(1 + \frac{\delta N}{n_0}\right)\nu_{ei,0}\boldsymbol{E}_0 + \\ &+ \frac{ie}{4m_e\omega_1}\boldsymbol{E}_1\nabla\cdot\boldsymbol{E}_h + \frac{ie}{4m_e\omega_{p0}}(\boldsymbol{E}_h\nabla\cdot\boldsymbol{E}_h)_T\exp[-i(\omega_0 - 2\omega_{p0})t],\end{aligned} \tag{3.8}$$

where the ω_0 is the pump light frequency in vacuum, $\nu_{ei,0}$ the collisional damping for the pump wave, and ω_{p0} the envelope frequency. Eq. 3.8 describes the evolution of the pump wave electric field in time. It is characterized by its propagation in the plasma (first line), which depends on the plasma envelope frequency ω_{p0} and the imposed density profile δN. The feedback of a laser wave propagating in plasma and in turn generating an ion perturbation is also included in this term through the presence of δn_l. The second line of Eq. 3.8 includes damping effects through collisions. The code approximates these collisions of being only between electrons and ions. Finally, the last line describes the daughter wave couplings, both for SRS (first term) between the Raman scattered wave and EPW, and TPD (second term) between two EPWs, respectively, and represents the presence of laser pump depletion in the system.

3.1.2.2 Raman scattered wave

The equation for the Raman light is similar in form to the laser one:

$$\begin{aligned}\frac{\partial}{\partial t}\boldsymbol{E}_1 =& \frac{ic^2}{2\omega_1}\left[\nabla^2\boldsymbol{E}_1 - \nabla(\nabla\cdot\boldsymbol{E}_1)\right] + \frac{i\omega_1}{2}\left[1 - \frac{\omega_{p0}^2}{\omega_1^2}\left(1 + \frac{\delta N}{n_0} + \frac{\delta n_l}{n_0}\right)\right]\boldsymbol{E}_1 + \\ &- \frac{\omega_{p0}^2}{2\omega_1^2}\left(1 + \frac{\delta N}{n_0}\right)\nu_{ei,1}\boldsymbol{E}_1 + \frac{ie}{4m_e\omega_0}\boldsymbol{E}_0\nabla\cdot\boldsymbol{E}_h^{c.c.},\end{aligned} \tag{3.9}$$

where the propagation of the Raman scattered wave of frequency ω_1 is given by the first line of Eq. 3.9 (where δn_l, indicator of the IAW presence, gives its SBS contribution), and its damping by the first term in the second line (with a damping rate coefficient of $\nu_{ei,1}$). The last term in the second line is similar to Eq. 3.8, and describes the coupling between a laser wave and an EPW, to give rise to the scattered Raman wave. This describes the SRS parametric instability. The field $\boldsymbol{E}_h^{c.c.}$ is the complex conjugate of the Langmuir field.

3.1.2.3 High-frequency plasma response: Langmuir Waves

The field equation for the EPWs describes the wave propagation and damping, but since the wave is a plasma wave, there are some additional interactions with both the plasma and the waves. The equation reads:

$$\begin{aligned}\nabla\cdot\left[i\left(\frac{\partial}{\partial t}+\nu_e\circ\right)+\frac{3v_{Te}^2}{2\omega_{p0}}\nabla^2-\frac{\omega_{p0}}{2}\frac{\delta N}{n_0}\right]\boldsymbol{E}_h=\\ =\frac{\omega_{p0}}{2}\nabla\cdot\left(\frac{\delta n_l}{n_0}\boldsymbol{E}_h\right)+\frac{e\omega_{p0}}{4m_e\omega_0\omega_1}\left(1+\frac{\delta N}{n_0}\right)\nabla^2\left(\boldsymbol{E}_0\cdot\boldsymbol{E}_1^{c.c.}\right)+\\ +\frac{e}{8\omega_{p0}m_e}\nabla\cdot\left[\nabla\left(\boldsymbol{E}_0\cdot\boldsymbol{E}_h^{c.c.}\right)-\boldsymbol{E}_0\nabla\cdot\boldsymbol{E}_h^{c.c.}\right]\exp\left[-i(\omega_0-2\omega_{p0})t\right]+S_h.\end{aligned}\tag{3.10}$$

The first line describes the EPW propagation in space and time with an envelope frequency of $2\omega_{p0}$, following the Bohm-Gross relation (Eq. 2.90). Moreover, the term ν_e describes the EPW damping, both collisional (between electrons and ions) and Landau. The operator "$\circ$" is a convolution operator between the damping and the EPW field $\boldsymbol{E}_h$. The first term at the second line of Eq. 3.10 couples the EPW field and the low-frequency electron density perturbation δn_l. Therefore, this term is the source of the Langmuir Decay Instability. The following term is a coupling term between the laser and Raman scattered light. This gives the ponderomotive force driving the electron density perturbation into an EPW, and it is therefore a term for the Stimulated Raman Scattering parametric instability. At the third line, the first term in square brackets describes a similar coupling to the SRS one, but between a laser wave and an EPW. This generates a ponderomotive force that drives another EPW, and it is the source term for TPD.

This equation therefore describes the high-frequency plasma behavior in relation to the low-frequency perturbations (IAW), the laser light and the Raman light, as well as the EPW field itself. In order for the Langmuir Waves to grow, Eq. 3.10 needs a source term S_h, representing noise in the EPW field due to preexisting density perturbations. This is necessary to seed the laser-plasma instabilities in the simulation domain.

3.1.2.4 Low-frequency plasma response: Ion Acoustic Waves

Finally, the low frequency plasma response, indicator of IAW presence, is included in the system as well. Instead of using a wave equation for the field, a fluid description is used for the low frequency density and velocity perturbations δn_l and $\delta\boldsymbol{u}_l$. The two equations used are the continuity and momentum equations:

$$\left[\frac{\partial}{\partial t}+\boldsymbol{u}_0(\boldsymbol{x})\cdot\nabla\right]\left(\frac{\delta n_l}{n_0}\right)=-\mathcal{W}_l,\tag{3.11a}$$

$$\left[\frac{\partial}{\partial t}+\boldsymbol{u}_0(\boldsymbol{x})\cdot\nabla+2\gamma_i(\boldsymbol{k})\circ\right]\mathcal{W}_l=-\nabla^2\left[c_s^2\left(\frac{\delta n_l}{n_0}\right)+\frac{Z_{eff}e^2}{4m_em_i}\left(\left|\frac{\boldsymbol{E}_h}{\omega_{p0}}\right|^2+\left|\frac{\boldsymbol{E}_0}{\omega_0}\right|^2+\left|\frac{\boldsymbol{E}_1}{\omega_1}\right|^2\right)\right],\tag{3.11b}$$

where $\boldsymbol{u}_0$ is the background flow velocity, $\mathcal{W}_l\equiv\nabla\cdot\delta\boldsymbol{u}_l$, γ_i is the IAW Landau damping coefficient, depending on $\boldsymbol{k}$ and multiplying $\mathcal{W}_l$ in Fourier space, and c_s and Z_{eff} being the acoustic ion velocity ($c_s^2\equiv(Z_{eff}T_e+3T_i)/m_i$) and the effective charge, respectively. In particular, Eq. 3.11b has a source term depending not only on the electron low-frequency perturbation in density, but also on the fields influencing the low-frequency electron motion, from the EPW ($\boldsymbol{E}_h$), the laser ($\boldsymbol{E}_0$) and the Raman wave ($\boldsymbol{E}_1$).

3.1.2.5 CFL condition and code convergence

These simulations had been done in a 1D spatial domain with density profile approximated as linear, where $[n_{min},n_{max}]=[0.18n_c,0.3n_c]$ in our particular case, and L_{sim} is the length of the

simulation domain (x-axis). Therefore, increasing the density scale length means choosing a bigger simulation domain in order to keep the density extremes fixed. This imposes a condition on the number of simulation nodes in each dimension. Save for particular situations, the code requires ~ 15 wavelengths per single cell in order to converge, requiring cell sizes of $\gtrsim 5.265$ μm. Therefore, in order to maintain the same cell length, given by $L_{cell} = L_{sim}/(N_{nodes} - 1)$, the number of nodes must increase as well, increasing the computation time by $\mathcal{O}(n^d)$, where d is the dimension of the system. In our case, the simulations went from $L_{sim} = 57.6$ μm, with ~ 2400 nodes in the case of $L_n = 60$ μm, to $L_{sim} = 288$ μm and ~ 12000 nodes in the case of $L_n = 600$ μm. This is caused by the *CFL condition* (from Courant-Friedrichs-Lewy):

$$\frac{u\Delta t}{\Delta x} < C_{lim}, \tag{3.12}$$

where the ratio between the velocity u at which the physical phenomenon propagates and the velocity of the phenomenon computed by the simulation $\Delta x/\Delta t$ must be below a limit constant C_{lim}, whose value depends on the type of equation that must be solved and its approximation scheme. Therefore, in order for the simulation to converge, if the spatial grid is reduced, the time interval must be reduced in order to keep the same converging solution. In addition to that, the more the simulations were closer to threshold, the longer simulation time they required, since the instability growth rate is the inverse of the characteristic growth time $t \sim \gamma^{-1}$, with the theoretical requirement of an infinite time for the instability to develop when the system is exactly at the instability threshold. Therefore, the simulation time has been adjusted to $t = 250$ ps.

3.2 Code validation and first simulations

In this section, we describe the first simulations in LPSE to observe the output quantities for simple cases, such as 1D SRS and TPD in 2D. Moreover, we conduct a small validation work of the code for the absolute intensity threshold for SRS, as well as the comparison of the TPD growth rate with the theory, the presence of TPD pump depletion and the effect of the ion contribution on the instabilities, in particular the development of turbulence from LDI and cavitation.

3.2.1 1D SRS

We first present an illustrative comparison of the calculations of the 1D SRS growth rate against the theory, in order to provide a first validation of LPSE's algorithm. The simulations are performed both in absence and presence of laser pump depletion, considering a linear density profile. The density interval is $[0.2n_c, 0.28n_c]$ for a CH plasma at 50% of fraction of both carbon and hydrogen ($Z_{eff} = 3.5$, $m_i/m_e \simeq 11952.42$), with an electron and ion plasma temperature of $T_e = 4$ keV and $T_i = 3$ keV respectively. The laser incident on the system is a plane wave with intensity $I = 2.415 \times 10^{14}$ W/cm^2 and $\lambda_0 = 0.351$ μm. The simulation domain has a length of $L_{sim} = 60$ μm. By the definition of density scale length (Eq. 2.160), in case of a linear profile and evaluated at quarter critical density, its form is $L_n = (L_{sim}/4)[n_c/(n_{max} - n_{min})]$, where n_{min} and n_{max} are the density extremes of the considered profile. Therefore, the associated density scale length with these parameters is $L_n = 187.5$ μm. The simulation grid has been chosen with 1440 nodes, setting a number of cells per wavelength (essential for the field solver convergence, as will be seen in the following section) of $\simeq 7$. While the lowest errors can be achieved at $\simeq 15 - 20$ cells per wavelength, this value has been chosen as compromise between having a reasonable error and computational cost for later 2D simulations.

Figure 3.1a shows the 1D evolution both in both space (x axis) and time (y axis) on the 1D Raman electromagnetic field. The region with the strongest fields is the one localized around $n_c/4$, coherently with the theory of absolute SRS. The instability starts appearing at $t \sim 2$ ps

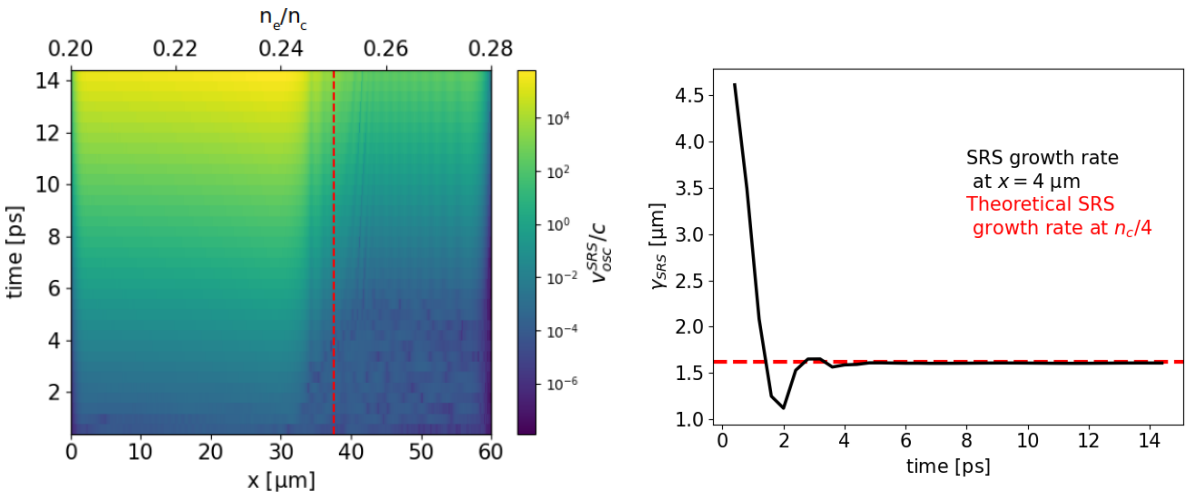

(a) (b)

Figure 3.1: a) Raman 1D electric field evolution both in space and time. The upper x axis shows the density interval. The red line is the location of the quarter critical density. b) Growth rate for 1D SRS, as a function of time, compared to the theory.

and grows not only at the quarter critical region ($n_e \sim 0.245$), but also at lower densities. This is caused both by the propagation of the Raman waves in space from $n_c/4$, but also from the generation of convective SRS, which spatially amplifies both the laser wave and the backscattered SRS Raman waves. There is a small signature of SRS forward scatter as well, as shown by the fields beyond $n_c/4$, but it can be considered negligible due to its amplitude being $2-3$ orders of magnitude lower than the region below $n_c/4$. Therefore, the primary decay in Fig. 3.1a is SRS backscattering.

3.2.1.1 1D SRS growth rate validation

The growth rate evolution in time can be extracted by the Raman scattered field under the assumption that $E_{SRS} = E_0(x,t)\exp(\gamma_{SRS}t)$, where $E_0(x,t) = E_0(x)\exp(-i\omega t)$ is the propagating field. Therefore, the growth rate can be extracted from the Raman field with:

$$\gamma_{SRS}(x) \simeq \frac{\partial[\log|E_{SRS}|]}{\partial t}, \tag{3.13}$$

where $|E_{SRS}|$ is the SRS field absolute value. Figure 3.1b shows the growth rate for absolute 1D SRS, taken at $x = 4$ μm in order to consider SRS backscattered light only. After an initial time period needed for the code to reach a steady state, the growth rate establishes itself at a constant value of $\gamma_{SRS} \simeq 1.59$ ps^{-1}. This growth rate is bound to infinitely grow at constant γ_{SRS} due to the absence of saturation mechanisms nor collisionless damping, as well as a fixed ion background. For this reason, this is called *linear growth regime*, characterized by an exponential field growth (linear growth if we consider $\log(E_{SRS})$). The theoretical value for the growth rate is given as well in Fig. 3.1b, reaching a value of $\gamma_{SRS}^{theo} = 1.62$ ps^{-1}, calculated at $n_c/4$ (Eq. 2.155). Therefore, the comparison between the theoretical growth rate at quarter critical, and the measured one from the backscattered Raman field (under the assumption to be originated at $n_c/4$), give an error of less than 2%.

These results, were useful to obtain a first grasp of the use of the code, and the physical phenomena involved and to progress to more complex simulation scenarios.

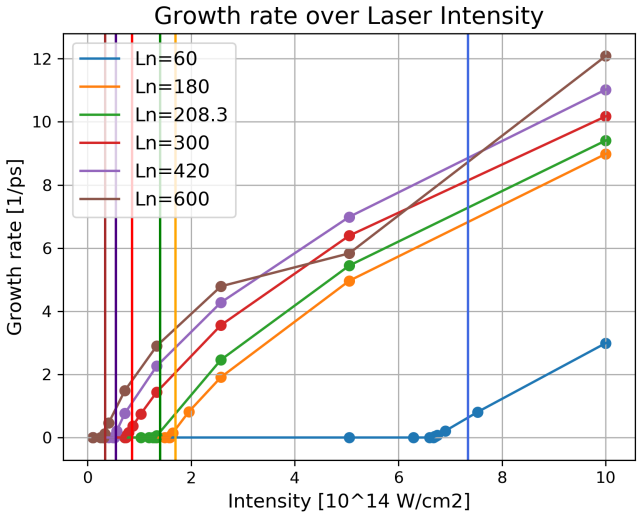

Figure 3.2: 1D absolute SRS growth rate depending on the input laser intensity. The vertical lines are the theoretical threshold from Eq. 2.164. The SRS threshold found by LPSE is at the point where the SRS growth rate becomes nonzero. The different colors in the legend are for simulations with different density scale lengths L_n, matching their theoretical intensity threshold.

3.2.1.2 1D SRS threshold validation setup

We then look at validation of the 1D SRS threshold. As described in Section 2.3.2, the absolute nature of the SRS instability takes place at quarter critical density, with an intensity threshold given by Eq. 2.164. The instability threshold depends on the density gradient given by the density scale length L_n. A range of $L_n = [60, 600]$ μm has been chosen, to represent operating conditions from PALS ($L_n \sim 60$ μm), OMEGA ($L_n \sim 120 - 240$ μm) and NIF ($L_n \sim 400 - 600$ μm). The laser intensities used to test the presence of instability were chosen between the boundary values of $I = 10^{13}$ to 10^{15} W/cm^2, and λ_0 is kept at 0.351 μm.

From the LPSE simulations at these two extremes, the profile of the SRS growth rate γ_{SRS} in time has been extracted by considering the gradient of the backscattered Raman light at 4 μm from the light injection boundary, as previously explained in section 3.2.1. In order to compare to the theory, ions are fixed (no IAWs) and laser pump depletion is not accounted for. The simulation has been deemed to present absolute SRS instability in the case it would overcome a field threshold value of $v_{osc}/c = 10^{-3}$. These simulations had an input laser intensity whose value was determined from a bisection method, in order to identify and progressively restrict the intensity interval between which there was SRS activity on the right side of the interval, and no SRS activity on its left, iterating the process until an uncertainty $\leq 5\%$ has been reached.

The growth rates are summarized in Fig. 3.2, where they are being compared to their corresponding theoretical threshold, given by Eq. 2.164 (same color). This comparison has been done for different density scale lengths, for a total of ~ 80 simulations. The electron and ion temperatures have been kept equal for simplicity ($T_e = T_i = 2$ keV), considering a CH plasma at 50% for both species.

3.2.1.3 Results for the 1D SRS threshold validation

In Fig. 3.2, we report that the code's solution converges towards the theoretical threshold but, in contrast with the results of [133], we find that it always underestimates the theoretical threshold.

The discrepancies between the calculated and theoretical threshold are shown in Fig. 3.3a and 3.3b. The error has been calculated as the difference between the theoretical threshold I_{theo}

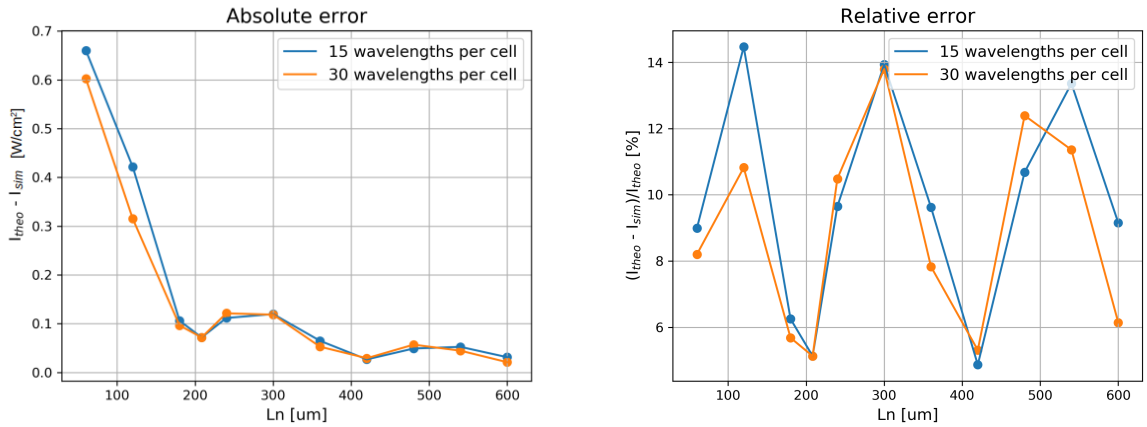

(a) (b)

Figure 3.3: a) Absolute and b) relative error between the theoretical laser intensity threshold for SRS I_{theo} and the LPSE simulation one I_{sim} as a function of the density scale length L_n.

and the one given by the simulations analysis I_{sim}. These have been done for the density scale lengths considered in Fig. 3.2. While the absolute discrepancy between theory and simulation threshold decreases for higher values of L_n, the relative error oscillates between $4\% - 15\%$ from the theoretical threshold, quantitatively in agreement with [133]. This error does not change much in case the number of cells per wavelengths is doubled to 30 (requiring double the number of nodes in the same simulation length interval), meaning that the code has converged even with 15 wavelengths. Nevertheless, the accuracy compared to the theory is there deemed acceptable.

3.2.2 2D TPD

We now consider simulations of Two Plasmon Decay in 2D. Since TPD activity is predominantly planar (Sec. 2.3.3), the simulations have been implemented in a 2D grid of 90×18 μm, with electron and ion temperatures of $T_e = 5$ keV and $T_i = 2.5$ keV, respectively. The chosen grid was of 4320×864 nodes, with a number of cells per wavelength of ~ 17. Therefore, the density scale length calculated in the domain is $L_n = 187.5$ μm. The density profile is linear, with extremes $[0.18n_c, 0.3n_c]$, with an incident plane wave in p-polarization, with a laser intensity of $I = 8.03 \times 10^{14}$ and $\lambda_0 = 0.351$ μm.

Results of the development of the TPD instability are illustrated in Fig. 3.4a and 3.4b. This simulation has been chosen in absence of saturation such as laser pump depletion and collisionless Landau damping, and in a fixed ion background to prevent secondary instabilities (i.e. LDI) and turbulence to develop. Therefore, the instability was allowed to grow indefinitely, remaining in the linear growth regime. The colorbar represents the absolute normalized electrostatic potential of the electrons $|e\phi/m_e c^2|$, and it is an indication of EPW field activity caused by the high frequency component of the electron density oscillations. The snapshot time $t = 1.6$ ps has been chosen as an initial point of the appearance of significant TPD activity in the simulation domain. Fig. 3.4a represents the EPW evolution in real space. We indicate the electron density as well on the top x axis, with a red dashed line indicating the quarter critical density. Development of absolute TPD in the linear growth phase can be observed, close to $n_e \simeq 0.24 n_c$. Fig. 3.4b represents the same time snapshot in Fourier space. At this snapshot, the produced EPWs follow the maximum growth rate hyperbola (Eq. 2.180), represented by the black curve with a maximum growth rate of:

$$\gamma_{TPD,max} = \frac{k_0 v_{osc}}{4}. \tag{3.14}$$

This gives the instability a distinct "lobed" shape, where the values far from $(k_\parallel, k_\perp) \simeq (0, 0)$ are

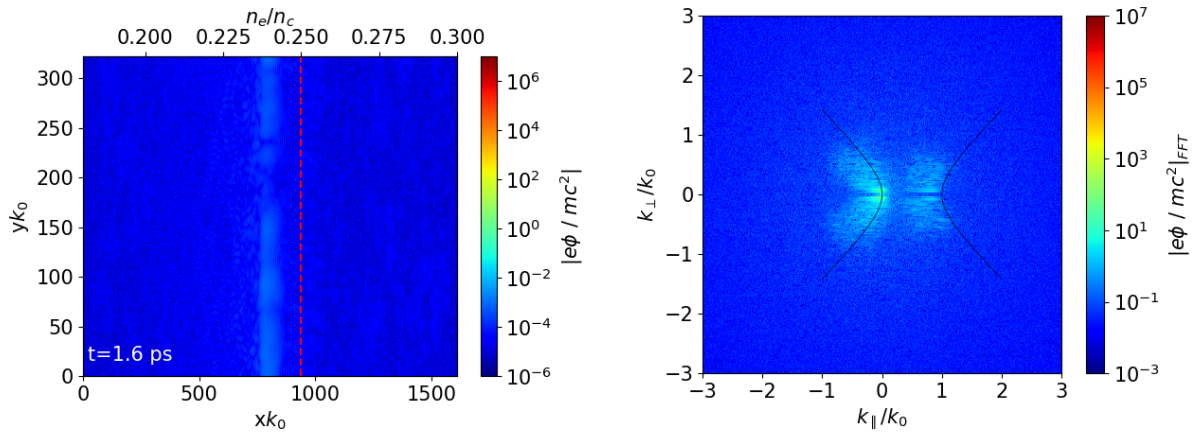

(a) (b)

Figure 3.4: Snapshot of the Two Plasmon Decay normalized electrostatic potential both in a) real and b) Fourier space at $t = 1.6$ ps. Both axes, corresponding to the parallel ($k_\parallel$) and perpendicular ($k_\perp$) components of the EPWs, are normalized to the laser wave vector in vacuum k_0.

developing convectively unstable modes, undergoing spatial amplification while passing through the critical region and propagating in space. Close to $(k_\parallel, k_\perp) \simeq (0, 0)$, there is the appearance of four high-field structures, where absolute TPD is located. These modes grow temporally around the quarter critical region, with a phase velocity almost vanishing because of their associated wave vector being $k_{EPW} \simeq 0$.

Fig. 3.5a and 3.5b show the same plots as Fig. 3.4a and 3.4b, but for a different time snapshot at $t = 4.8$ ps. In this case, the instability is far more developed, with a clear high-field region of absolute activity at quarter critical density. The fields close to this region present a lower but significant activity, either caused by convective TPD modes evolving, or by EPW advection in the domain. This would explains why there is EPW activity even beyond the $n_c/4$ region. In Fourier space (Fig. 3.5b), the EPW modes undergo convective saturation, spreading in k-space away form the maximum growth rate hyperbola. This spread is asymmetrical towards the left side of the plot, and it is caused by the inhomogeneous density profile causing the wave vector to decrease for higher densities. The intensity of the absolute modes at this time has greatly increased. In particular, at $k_\perp \simeq 0$ we register EPWs corresponding to TPD daughter waves in which one has a wave vector similar to the laser wave vector k_0 (in this plot, $k_\parallel/k_0 \simeq 1$) and the other is characterized by $k_\parallel/k_0 \simeq 0$. These waves grow the most, in particular the ones close to $(k_\parallel/k_0, k_\perp/k_0) \simeq (0, 0)$ because waves emitted at these wave numbers do not have a high enough phase velocity to leave the quarter critical region and advect their energy to lower densities. The result is these waves are going to be further amplified and grow to large field values. On the $k_\perp/k_0$ axis, there is a region between the four main absolute instability modes where there is no absolute growth. This is caused by the existence of a minimum wave number found by A. Simon and R.W. Short [81] to be:

$$k_\perp = \pm k_0 \sqrt{0.106 \frac{I_{14}\lambda_{0,\mu}^2}{T_{e,keV}^2}}, \tag{3.15}$$

where I_{14} is the laser intensity in vacuum in 10^{14} W/cm^2 and $\lambda_{0,\mu}$ is the laser wavelength in μm. In this case, the calculated wave vector threshold is $k_{\perp,min}/k_0 \simeq 0.0647$, close to the observed four main absolute instability structures, located in the region of $k_\perp/k_0 \sim \pm 0.05$.

We must note that the simulation in real space in Fig. 3.5a contains the presence of periodic structures along the y axis. These represent three wavelengths of the dominant growing mode,

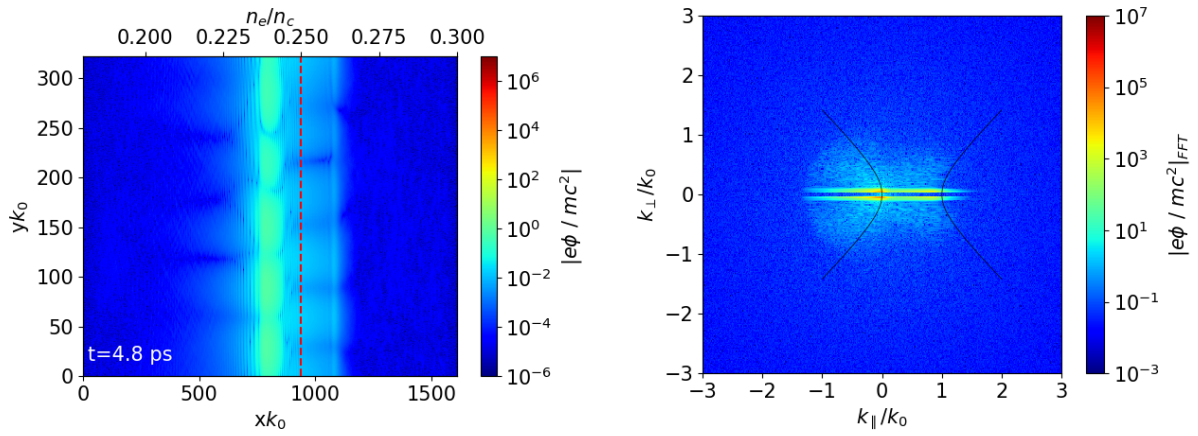

(a) (b)

Figure 3.5: Snapshot of the Two Plasmon Decay normalized electrostatic potential both in a) real and b) Fourier space at $t = 4.8$ ps.

which is constrained by the limited periodic boundaries along the y axis. These periodic lobes in real space correspond to the peaks at the Simon threshold for the minimum allowed $k_\perp \simeq \pm 0.0647 k_0$. Their presence is tied to the choice of the simulation domain, and therefore an artifact of the simulation, as has been proven by disrupting the boundary periodicity by using a different box length. This is not a concern for the hot electron scaling analysis that will be presented in the following chapter 4, where we will mainly focus in the so called *quasi-stationary regime*, where plasma turbulence and laser pump depletion have been already set in and the periodic structure disappears.

3.2.2.1 2D TPD growth rate verification

A simple growth rate verification has been conducted for a single TPD simulation as well. The growth rate for 2D TPD in absence of saturation nor anomalous absorption has been calculated from the developed EPW potential in Fourier space, in the same conditions as in the previous section ($T_e = 5$ keV, $L_n = 187.5$ μm, and $I = 8.03 \times 10^{14}$ W/cm^2). As seen in the previous section, the black curve in Fig. 3.5a shows the hyperbola in k-space where the TPD growth rate is maximum, given by the inhomogeneous absolute growth rate [19]: $k_0 v_{osc}/4 - \omega_{pe}/(8 k_{\perp,EPW} L_n)$ (Eq. 2.181). The calculated maximum growth rate, taking into account inhomogeneities, results in $\gamma_{max,theo} \simeq 12.87$ ps^{-1} for these laser-plasma conditions. In order to compare it with the simulations, we identified the coordinates in k-space of the associated maximum EPW field, which correspond to $\boldsymbol{k}_{EPW} =\simeq [-0.0195 k_0, -0.0585 k_0]$. We therefore calculated the more general formula:

$$\gamma_{TPD,sim} = \frac{(\boldsymbol{k}_{sim} \cdot \boldsymbol{v}_{osc})^2}{4} \left[\frac{(\boldsymbol{k}_{sim} - \boldsymbol{k}_0)^2 - k_{sim}^2}{k_{sim} |\boldsymbol{k}_{sim} - \boldsymbol{k}_0|} \right]^2 - \frac{\omega_{pe}}{8 k_{\perp,EPW} L_n}, \tag{3.16}$$

by using the wave vector sampled from the simulation, $\boldsymbol{k}_{sim}$. The calculated TPD growth rate results in $\gamma_{TPD,sim} \simeq 13.535$ ps^{-1}, with an overestimation of the simulation of $\sim 4.2\%$ compared to the theory.

3.2.2.2 2D TPD threshold verification

While not having verified the TPD threshold with the same extent of the SRS one, in part since this had already been done in the works of R.K. Follett [133], a limited verification of the TPD intensity threshold has been conducted as well. The simulations considered have the

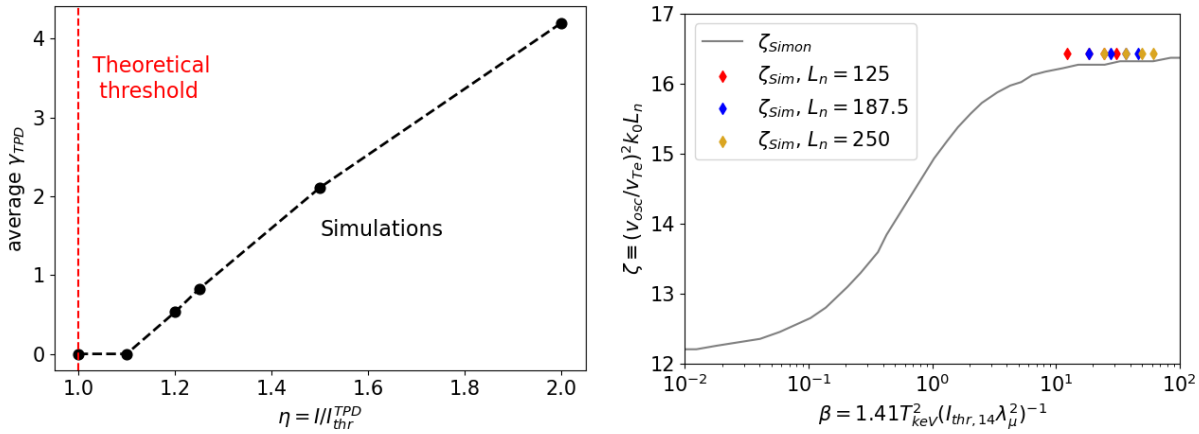

(a) (b)

Figure 3.6: a) Comparison between simulation growth rate (black curve) and calculated one (red curve) as a function of the drive strength $\eta = I_{laser}/I_{thr}^{TPD}$. b) ζ value as a function of β, where $\zeta \equiv (v_{osc}/v_{Te})^2 k_0 L_n$. The grey line is the theoretical behavior as found in [81], while the diamonds are the simulation data for different density scale lengths.

same parameters of section 3.2.2. The verification has been done by considering the growth rate γ_{TPD} starting from the averaged EPW energy ϵ_{EPW} over the whole spatial domain. Since this quantity is proportional to the square of the EPW field, it is therefore possible to extract the growth rate as in Eq. 3.13 by substituting $\sqrt{\epsilon_{EPW}}$ in the logarithm.

The verification was done by observing the TPD growth rate γ_{TPD} from the TPD energy, this time as a function of the *laser drive strength*, defined as $\eta \equiv I_{laser}/I_{thr}^{TPD}$, where I_{laser} is the incident laser light intensity, and I_{thr}^{TPD} is the absolute TPD intensity threshold described in Eq. 2.188. The threshold has been observed to lie between $\eta = 1.0$ and $\eta = 1.2$, predicting an error between theory and simulations in the interval of $\simeq 10 - 20\%$, where the simulations consistently overestimate the threshold even for different laser-plasma conditions. However, increasing simulation time from $t = 20$ ps to longer times can decrease the error.

As seen in section 2.3.3.4, the TPD absolute intensity threshold in Eq. 2.188 depends on the quantity ζ [81], which differs in value according to the parameter $\beta \equiv 9 v_{Te}^4 k_0^2 / (|v_{osc}|^2 \omega_0^2)$ defined in [81]. A feedback loop has been implemented in order to match the correct value of β with the intensity threshold. As initial hypothesis, we considered a value of $\zeta = 4.134$ in the case of $\beta \geq 10$ and $\zeta = 3.094$ for $\beta \leq 0.1$. This hypothesis is valid by considering Fig. 3.6b (grey curve), where the dependence on the value ζ, given by Eq. 2.184 [81] is being plotted as a function of β. An iterative procedure has been set up calculating the intensity threshold assuming an initial β value of 10, and then calculating a new value of β using the obtained iteration. If both β values belong in the same regime (i.e. $\beta \geq 10$ or $\beta \leq 0.1$), the threshold can be calculated with an established value for ζ. Fig. 3.6b also shows a verification of a set of simulations at $L_n = 187.5$ and $\lambda_0 = 0.351$ μm, for different electron plasma temperature values of $T_e = [2.5, 3, 4, 5]$ keV. All values are in the high-β case, with an error from the theoretical value of ζ of $\simeq 4\%$. Therefore, the TPD threshold in Eq. 2.188 has been verified to be $\zeta = 4.134$ in all cases of the simulation scaling, as hypothesized in [133].

3.2.2.3 Laser pump depletion effect on 2D TPD

Instability growth implies an energy transfer from the pump wave to the daughter wave; as such, there will come a regime in which the pump wave does not have any more energy to provide to the daughter wave to grow, because of energy conservation. This process is called *laser pump depletion* [79], and its result is an overall decrease in the pump wave's amplitude, when the

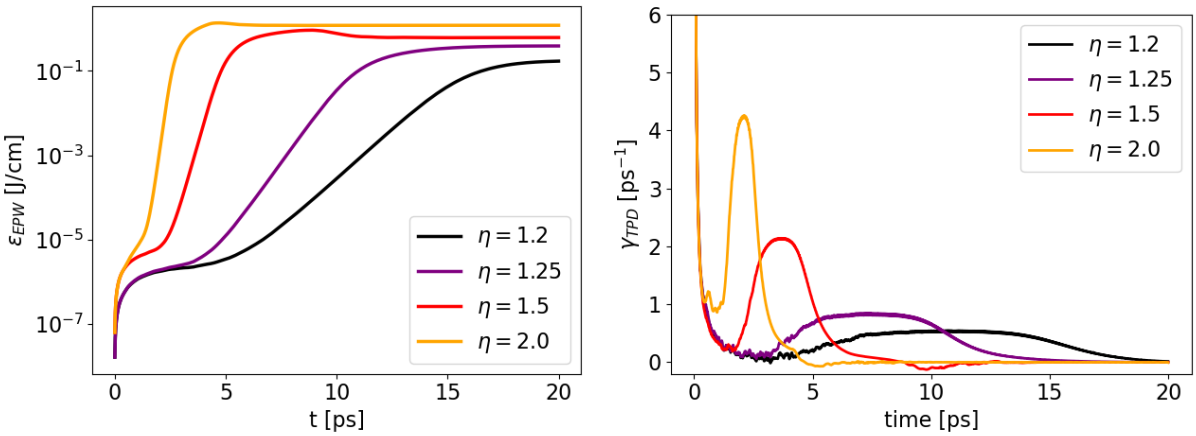

(a) (b)

Figure 3.7: a) EPW energy ε_{EPW} and b) the integrated TPD growth rate in space as a function of time in presence of laser pump depletion, for fixed $L_n = 187.5$ μm and $T_e = 5$ keV and different drive strength η values. The EPW energy has been plotted in logarithmic scale to show the beginning of the linear growth regime.

product wave grows, eventually to the point where the instability stops growing and becomes increasingly weaker, allowing the pump to grow in amplitude again. This cycle continues until reaching equilibrium between the pump and daughter wave.

The LPSE field solver allows enabling laser pump depletion in the laser equation, therefore enabling a feedback between the daughter waves and the laser pump. However, this makes the simulations computationally more expensive.

Fig. 3.7a shows the average EPW energy (ε_{EPW}) behavior as a function of time. Since the simulation is in 2D, the quantity reported by the virtual diagnostic is given in $[erg/cm]$. The simulations start in the linear growth regime, growing exponentially in time until the laser light amplitude starts diminishing. This is accompanied by a stabilization of the EPW energy onto a constant level after an intermediate period in which fluctuations of the EPWs and laser pump wave occur, reaching a quasi-stationary regime.

The same behavior can be seen in Fig. 3.7b, where after an initial growth in which the instability reaches a constant level during the linear regime, the growth rate becomes zero once both the pump and daughter ave amplitudes reach equilibrium. Each curve in both Fig. 3.7a and 3.7b are for different drive strength values, with a shorter time for establishing stationary conditions due to pump depletion for increasing intensities. The reason of this can be seen in the growth rate in Fig. 3.7b. Remembering that the growth rate depends on the field oscillation velocity, which in turn depends on the incident pump wave intensity, at constant TPD intensity threshold the growth is enhanced for increasing $\eta = I/I_{thr}^{TPD}$, and therefore TPD will grow in a shorter time since $t_{TPD} = \gamma_{TPD}^{-1}$.

Considering laser pump depletion in the simulations allows for energy balance considerations, calculating quantities such as the *laser transmittivity*, defined as the laser power leaving the simulation boundary opposite to the laser injection, normalized to the injected laser power. It is an indicator of the laser energy fraction propagating outside of the quarter critical region and towards the ICF target. Fig. 3.8 shows a plot for the laser transmittivity in the same conditions as Fig. 3.7a and 3.7b (i.e. $T_e = 5$ keV and $L_n = 187.5$ μm). After a period of exponential decrease in transmittivity, coincident with the TPD linear growth regime, the transmittivity stops at a quasi-stationary level. This can go down to 20% (for the highest laser intensities) of laser energy propagated from the absolute region towards higher densities. It must be noted that a TPD related absorption of laser light for $\sim 80\%$ of its injected energy is only obtained in

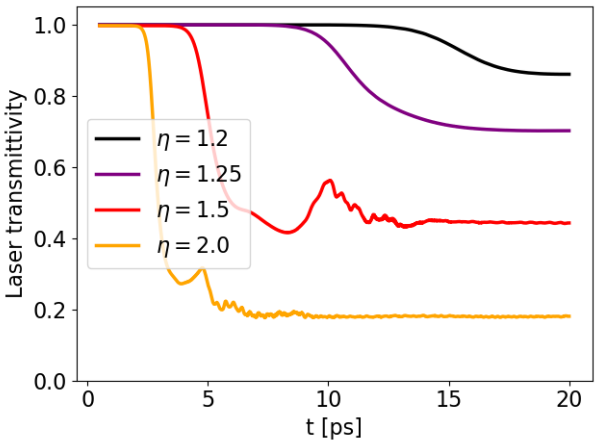

Figure 3.8: Laser transmittivity as a function of time, for different drive strength values and at fixed electron plasma temperature ($T_e = 5$ keV) and density scale length ($L_n = 187.5$ μm).

simplified cases where plasma turbulence and Landau damping are not present, as well as more refined phenomena such as broadband effects and laser speckles dynamics.

3.3 Hot electron generation: Landau damping

As we previously discussed, propagating electromagnetic fields generate plasma density perturbations, which in turn generate plasma waves and currents. These plasma waves influence the particle motion, due to Coulomb forces. As stated in Chapter 2, when the phase velocity of a plasma wave, particularly an EPW, is very high with respect to the electrons' thermal velocity (i.e. $v_{ph} \gg v_{Te}$), the influence of such a fast varying field can be considered negligible on the electron motion. In such a scenario, the electrons mainly dissipate energy via collisions. However, when the EPW phase velocity is comparable to the thermal electron velocity, $v_{ph} \simeq v_{Te}$, the electrons see a near constant field. According to the slope of the electron velocity distribution function $\partial f(v_{ph})/\partial v$ (Eq. 2.103b), a transfer of energy from the wave to the electrons in case $v_{el} \simeq v_{ph} - \delta v$ can occur, and viceversa in the case of $v_{el} \simeq v_{ph} + \delta v$. In the case of wave-to-electron energy transfer, the wave diminishes in amplitude, with a damping rate equivalent to the *Landau damping* of an EPW (Eq. 2.104) and the energy of the wave is transferred to the electrons. Eq. 2.104 is a particular case derived for a Maxwellian distribution. In a more general case, Landau damping is given by integration of the velocity distribution function, which will be the approach used for the kinetic module of LPSE. Through progressive resonance processes with EPWs at increasingly high phase velocities and densities (in a phenomenon called *multi-stage acceleration* [152]), the electrons may acquire energies considerably higher than the rest of the plasma electrons, from some tens of keV up until the order of 10^2 keV for laser intensities of the order of $I\lambda_0^2 \sim 10^{13} - 10^{16}$ Wμm^2/cm^2. In case of the IAWs, the phase velocity domain is between $v_{Te} \gg v_{ph,IAW} \gg v_{Ti}$, and therefore the IAWs cannot start energy transfer processes from the wave to the electrons that bring them to as high energies as EPWs do.

A high-energy electron population is labeled as *hot electrons* (HEs). Because of their high v_{Te}, they are less affected by collisions (since the Braginskii electron-ion collisional damping ν_{ei} depends on v_{Te}^{-3}, Eq. 2.35b), and therefore are allowed to propagate to longer distances. These particles can reach and deposit their energy into the ICF target which, as seen in Chapter 1, can have beneficial [42, 44] or detrimental effects [57, 153] on the ignition dynamics.

Hot electron generation is therefore tied to the presence of EPWs in the system. Laser plasma instabilities producing EPWs, such as SRS, TPD and LDI, are then the main contributors to such generation. Another contribution is due to *plasma turbulence*. LDI is already a process

that can emit EPWs in an array of directions (due to their secondary instability nature), and it is tied to *weak turbulence*. A stronger nonlinear turbulence is tied to the formation of *cavitons* within the plasma, which can act as resonators for trapped EPWs, and then collapse if the EPW gets weakened enough by Landau damping. This process is called *Langmuir wave collapse*, or *cavitation*, as it will be shown in the following sections.

3.3.1 Weak plasma turbulence

Nonlinear effects are given by coupling between different oscillation modes such as parametric instabilities. When these waves parametrically couple between each other, they generate plasma longitudinal waves by perturbing the electron and ion plasma density, as previously illustrated. These perturbations generate *turbulence* within the plasma.

In case the nonlinear wave interactions' characteristic times are sufficiently larger than their periods and one can consider the oscillations to be locally linear with slowly varying parameters, it is possible to develop a *Weak Turbulence Theory* [83, 154, 155, 156].

As in previous analyses, the plasma motion can be decoupled in a high-frequency and a low-frequency part, indicative of EPWs and IAWs, respectively. The condition of wavelengths larger than the Debye length (i.e. $k\lambda_{De} \ll 1$) still applies, which means that $\omega_{EPW} \simeq \omega_{pe}$ by the Bohm-Gross relation even for large variations of EPW wavelength. Neglecting interaction between high-frequency oscillations, we can describe such oscillations by using the continuity and momentum fluid equations, as well as the EPW wave equation:

$$\frac{\partial n_e}{\partial t} + \nabla \cdot (n_0 + \delta n_{el})\boldsymbol{v}_e = 0, \tag{3.17a}$$

$$\frac{\partial \boldsymbol{v}_e}{\partial t} + 3v_{Te}^2 \nabla \left(\frac{\delta n_{eh}}{n_0} \right) = -\frac{e\boldsymbol{E}}{m_e}, \tag{3.17b}$$

$$\frac{\partial^2 \boldsymbol{E}}{\partial t^2} + c^2 \nabla \times \nabla \times \boldsymbol{E} - 4\pi e(n_0 + \delta n_{el}) \frac{\partial \boldsymbol{v}_e}{\partial t}, \tag{3.17c}$$

with an electron density in the form:

$$n_e = n_0 + \delta n_{eh} + \delta n_{el}, \quad \delta n_{eh}, \delta n_{el} \ll n_0, \tag{3.18}$$

where n_0 is the background density, and δn_{eh} and δn_{el} are the high and low density perturbation for the electrons, respectively. The system 3.17 can be treated by using an electric field of the form $\boldsymbol{E} = \tilde{\boldsymbol{E}} \exp(-i\omega t) + c.c.$, where $\tilde{\boldsymbol{E}}$ is a slowly varying quantity in time, so that $\partial \tilde{\boldsymbol{E}}/\partial t \ll \omega_{pe}\tilde{\boldsymbol{E}}$. Assuming that $\boldsymbol{E} = -\nabla\varphi$, φ being the electrostatic potential, the system of equations 3.17 can be manipulated to give:

$$\nabla^2 \left(i\frac{\partial}{\partial t} + \frac{3}{2}\frac{v_{Te}^2}{\omega_{pe}}\nabla^2 \right) \varphi = \frac{\omega_{pe}}{2} \nabla \cdot \left(\frac{\delta n_{el}}{n_0} \nabla\varphi \right), \tag{3.19}$$

where the integral $I = K \int |\nabla\varphi|^2$ is conserved K being a constant. However, Eq. 3.19 is not closed, needing a connection between δn_{el} and $\tilde{\boldsymbol{E}}$. This is given, in the case of the absence of an external magnetic field, by:

$$\overline{\boldsymbol{v}_e \nabla \boldsymbol{v}_e} = \frac{e}{m_e}\nabla\varphi_{el} - \frac{T_e}{m_e}\frac{\nabla n_e}{n_0}, \tag{3.20}$$

where the bar means an average over time, and φ_{el} is the low frequency component of the electrostatic potential. The term $\overline{\boldsymbol{v}_e \nabla \boldsymbol{v}_e}$ is proportional to the ponderomotive force (see section 2.3) $\nabla|\tilde{\boldsymbol{E}}|^2$, where the weak varying plasma wave of amplitude $\tilde{\boldsymbol{E}}$ pushes away the electrons from the wave field localization. This force is noticeably stronger on electrons than on ions, due to the presence of an m_e/m_i factor. Overall, this term is the one responsible for weak turbulence in the system.

3.3.2 Strong plasma turbulence

The parametric instabilities of SRS, TPD and LDI tend to produce product waves with downshifted frequency, long wavelengths and higher phase velocity [40]. If there is no energy dissipation mechanism (such as collisional damping), the wave energy would then accumulate within waves at long wavelengths. When $(k\lambda_{De})^2 \ll E^2/4\pi n_e T_e \sim v_{ph}^2/v_{Te}^2$, then nonlinear effects in the wave dispersion relation overcome the thermal plasma behavior. Therefore, the weak turbulence theory briefly illustrated in the previous section, where density perturbations such as δn_e are small, no longer applies; when this happens, a *strong turbulence* regime appears, which brings the waves back to short wavelengths and low phase velocities, allowing the energy to be advected from the the wave through Landau damping. The Zakharov model described in section 3.1.1, and used by the LPSE code field solver, was born to provide a framework for treating such strong turbulence regime [40, 41].

The accumulation of long wavelength (small k) plasma waves gives rise to very localized regions of high electric fields, resulting in the formation of ion density depressions in the plasma profile. These depressions are referred to as *cavities / cavitons*, which trap and resonate EPWs, whose field will sustain the cavity. When an electron with a thermal velocity resonant with the wave phase velocity traverses the cavity, there will be an energy transfer to the electron. This contributes to the HE generation within the system, and therefore weakening the EPW field through Landau damping. This process continues until the field is not able to sustain the cavity anymore, which "collapses". This collapse is characterized by a shock wave caused by the plasma returning to its equilibrium configuration, emitting IAWs from the cavity's location, which is the source of the strong turbulence in this regime.

Unlike the weak turbulent regime, the *LW collapse* has an amplitude threshold that depends on the EPWs' spectral distribution. This process would imply to consider the entire Fourier spectrum of frequency to determine which EPW can generate cavities. To simplify the problem, Zakharov in [40], proposed a model by averaging the EPWs over fast times of frequency "$1/\omega_{pe}$". The result is to use an equation for the EPW evolution, which closely resembles Eq. 3.19, but where the electric potential φ can be decomposed in:

$$\varphi \equiv \frac{1}{2}\left(\psi \exp\left(-i\omega_{pe}t\right) + \psi^* \exp\left(i\omega_{pe}t\right)\right), \tag{3.21}$$

where ψ is a slowly varying potential, and φ in Eq. 3.19 can be substituted by ψ. Considering a Maxwell-Boltzmann distribution, the overall density perturbation for both ions and electrons is:

$$\delta n = n_0 \left[\exp\left(-\frac{U}{T_e + T_i}\right) - 1\right] \sim \frac{n_0 U}{T_i + T_e}, \tag{3.22}$$

where $U \equiv e^2|\nabla\psi|^2/4m_e\omega_{pe}^2$ is the potential energy of an electron oscillating in the EPW field. With these observations, Eq. 3.19 can be rewritten as:

$$\nabla^2\left(\frac{\partial}{\partial t} + \frac{3}{2}\frac{v_{Te}^2}{\omega_{pe}}\nabla^2\right)\psi = -\frac{e^2 q}{4m_e\omega_{pe}T_e}\nabla\cdot\left(|\nabla\psi|^2\nabla\psi\right), \tag{3.23}$$

with $q \equiv T_e/(T_e+T_i)$. We define $w \equiv W/n_e T_e$, where W is the average energy of the electrostatic field, and $\mu \equiv m_e/m_i$. In the case of $(k\lambda_{De})^2 > \mu/3$ and at small amplitudes so that $w \ll \mu^{1/2}k\lambda_{De}$ and $T_i \ll T_e$, there is IAW production, with a growth rate of the form:

$$\gamma_{LW} = \frac{\omega_{pe}}{2}\mu^{\frac{1}{4}}w^{\frac{1}{2}}(k\lambda_{De})^{\frac{1}{2}}\frac{|[k_{EPW}, k_{EPW}-k]|^2}{|k_{EPW}||k_{EPW}-k|}, \tag{3.24}$$

where the term $[k_{EPW}, k_{EPW}-k]$ indicates the wave vectors k around a reference monochromatic Langmuir wave k_{EPW}. The maximum increment occurs at $k \simeq 2k_{EPW}$, and the growth rate in Eq. 3.24 assuming the form:

$$\gamma_{LW} \simeq \frac{1}{2}\omega_{pe}\mu^{\frac{1}{4}}(2k_{EPW}\lambda_{De})^{\frac{1}{2}}w^{\frac{1}{2}}. \tag{3.25}$$

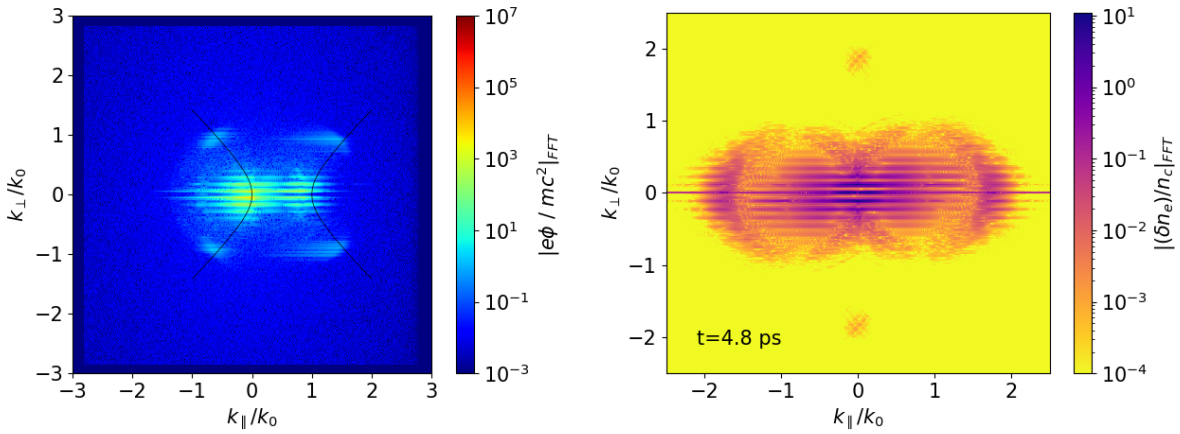

(a) (b)

Figure 3.9: a) EPW potential and b) IAW density perturbation for $t = 4.8$ ps in Fourier space.

In the case of $w \gg \mu^{1/2} k \lambda_{De}$, there is a modified decay instability with a maximum growth rate at $k \simeq 2k_{EPW}$ of the form:

$$\gamma_{LW} \simeq \omega_{pe} \left(\frac{W k^2}{m_i n_0 \omega_{pe}^2} \right)^{\frac{1}{3}}. \tag{3.26}$$

In these cases, the generated Langmuir waves are close to $\boldsymbol{k} \simeq -\boldsymbol{k}_{EPW}$, with a filling of a frequency region corresponding on a sphere of radius $\omega = \omega_{EPW}$. The growth of the instability leads to the formation of a density depression, a *cavity*, with a growing EPW within. The EPW field pushes away electrons from the cavity, due to ponderomotive pressure [40]. The characteristic dimension of the central area of the cavity is of the order of $L \sim \lambda_{De} \mu^{-1/2}$, and the estimated energy within the cavity is $\Delta\epsilon \simeq n_e T_e \lambda_{De}^3 \mu^{-1/2}$, where $T_i \ll T_e$. The EPW field will continue to sustain the cavity until a population of electrons passing through the cavity are resonant for EPW energy transfer to occur, at which point the EPW field undergoes Landau damping until the cavity collapses by the ion acoustic shock wave that fills the cavity and restores an homogeneous density profile. The upper bound for the electrons leaving the cavern has been estimated to be of the order $\epsilon < T_e \mu^{-1/2}$. The characteristic cavern developement time is of the order of $\tau \simeq (\omega_{pe} w)^{-1}$, after which the caviton collapse takes place.

3.3.3 Turbulence effects on the 2D TPD simulations

After introducing the concept of plasma turbulence, we now discuss about the development of turbulence when introducing IAWs in LPSE simulations. A test simulation at $T_e = 5$ keV, $L_n = 187.5$ μm has been performed, in the presence of laser pump depletion. T_i has been set as well, since turbulence depends on the ion temperature as well through IAW Landau damping, as well as for development of LDI and strong Langmuir turbulence (i.e. Eq. 3.22), to $T_i = 2.5$ keV.

Figure 3.9a shows the normalized EPW potential behavior at the snapshot $t = 4.8$ ps, while Fig. 3.9b shows the electron density perturbation at low frequency normalized to the background density at equilibrium $\delta n_e/n_0$, indicative of IAWs. While at $t < 4.8$ ps the instability grows in real space similarly to the TPD only case, beyond $t = 4.8$ ps in Fourier space there is the appearance of a high field region around $(k_\parallel/k_0, k_\perp/k_0) \simeq (0, 0)$. There is also the presence of four anomalous lobes at $(k_\parallel/k_0, k_\perp/k_0) \simeq (\pm 1, \pm 1)$, lying on the maximum growth hyperbola, which have been identified as numerical artifacts given by the combined effects of neglecting Landau damping and of the growth of high-wavenumber modes in the simulation domain, which disappear when Landau damping is being considered. The horizontal periodic lines in Fig.

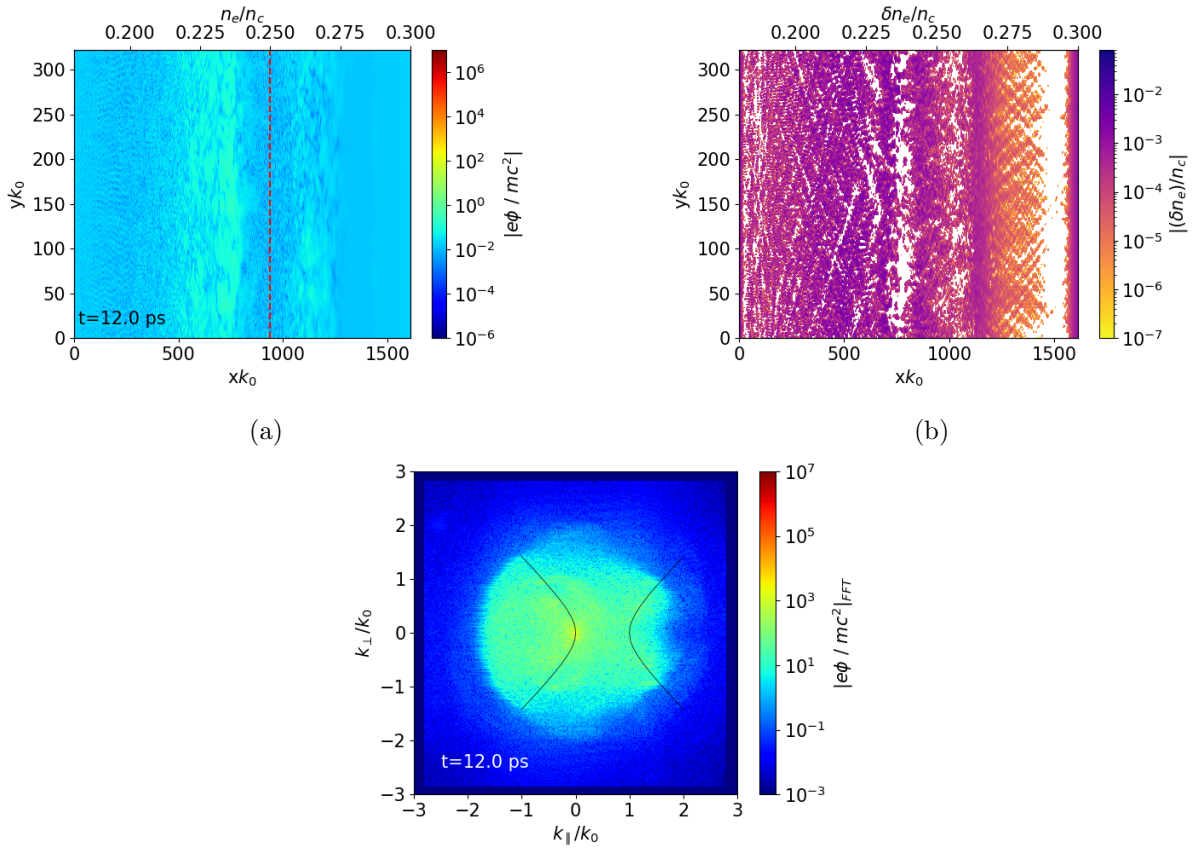

Figure 3.10: a) EPW potential and b) IAW density perturbation in real space for $t = 12$ ps. c) EPW potential in Fourier space for $t = 12$ ps for a TPD simulation in the presence of Ion Acoustic Waves.

3.9a are harmonics of the fastest growing mode, which undergo LDI cascade [37] (Sec. 2.3.4) following the relation between the mother EPW from TPD and the daughter one given by Eq. 2.195a [39]. The fastest growing modes are in the condition of $\theta \sim 0$, where θ is the angle between the mother EPW and the daughter IAW. Therefore, the daughter EPWs' wave vectors can be approximated in the form of Eq. 2.196a, with a co-propagating daughter IAW and a counter-propagating daughter EPW with respect to the mother EPW. The cascade produces EPWs with progressively lower wave vectors, increasing the EPW potential in the region close to the origin in k-space (long wavelengths), even beyond the Simon threshold given by Eq. 3.15. The associated modes are characterized by a low phase velocity (Eq. 2.197a), which becomes the seeding process for caviton formation and subsequent Langmuir Wave collapse, developing in strong turbulence. Fig. 3.9b shows the Fourier spectrum of the IAWs, exhibiting a similar periodic structure with two main "lobes" of IAW activity. The activity region where high fields are concentrated have been estimated to be double in amplitude compared to the EPW spectrum in Fig. 3.9a.

After a period of weak turbulence, strong turbulence appears in the system after the low-k EPW field is intense enough for cavitons to form and collapse in the plasma. In Figs. 3.10a, 3.10b and 3.10c, we illustrate the behavior of the EPW potential and the IAW behavior when TPD, plasma turbulence and laser pump depletion have fully developed, establishing a quasi-stationary regime. In Fig. 3.10c, the EPW Fourier spectrum shows waves being emitted in every direction, despite conserving some weakly distinguishable features of growth along the TPD hyperbola (at $(k_\parallel/k_0, k_\perp/k_0) \sim (\pm 1.5, \pm 1)$). This uniform EPW emission is not only

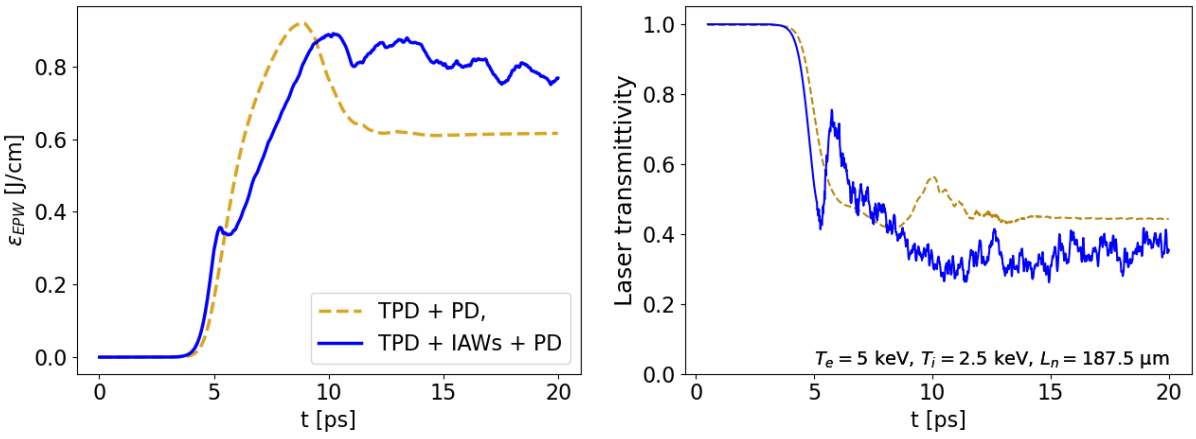

(a) (b)

Figure 3.11: Comparison in a) EPW energy and b) laser transmittivity as a function of time between 2D TPD simulation in presence of low-frequency electron contributions (black curve) and without (orange curve). Both simulations have laser pump depletion enabled, and at fixed $T_e = 5$ keV, $T_i = 2.5$ keV, $L_n = 187.5$ μm and $\eta = 1.5$.

related to weak turbulence due to LDI cascade and strong turbulence from caviton formation within the plasma, but also to daughter EPWs generated by TPD in the forward direction, and subsequently refracted backwards after encountering the quarter critical region. As far as turbulence is concerned, cavitation releases the trapped EPWs with no preferential direction at the moment of collapse, and emit IAWs because of the collapsing cavity [40]. Fig. 3.10a shows the same quasi-stationary regime, but in real space. The region of most activity is located around $n_e/n_c \sim [0.215 - 0.245]$ (i.e. $xk_0 \sim [500 - 850]$). This corresponds to a weak low frequency perturbation density in Fig. 3.10b, where the IAW potential is plotted in real space. A region characterized by several density depression can be identified, and they have been attributed to caviton formation (further supported by the $k_{\perp,IAW} \sim 2k_{EPW}$ seeding in Fig. 3.9a [26]).

The presence of IAWs and turbulence in the system affects the energy in the EPWs, as well as the laser energy propagating from the resonance region. Figs. 3.11a and 3.11b show the change in EPW energy and laser transmission by comparing simulations in absence and presence of IAWs. One main characteristic is that the signal is characterized by a more noisy behavior with the introduction of IAWs, especially in the quasi stationary regime, as expected by the establishment of weak and strong turbulence, leading to a more irregular EPW emission. Moreover, the EPW energy in presence of IAWs and turbulence stops at a higher quasi-stationary level than the case without IAWs, while the laser fraction being transmitted beyond the resonance region is lower. Quantitatively, the changes for this particular simulation are $\sim 33\%$ higher and $\sim 18\%$ lower for the EPW energy ε_{EPW} and the laser transmittivity, respectively.

3.3.4 LPSE: Hybrid Particle Evolution kinetic module

LPSE's has been widely used to solve enveloped fields propagating in a limited domain, allowing to study parametric instabilities' evolution and modification due to more sophisticated effects such as multibeam and broadband effects [55, 133, 142, 157], as well as CBET analysis [62]. The code also includes a kinetic module called *Hybrid Particle Evolution* (HPE), which allows the calculation of the collisionless Landau damping coefficient in time by evolving a population of "virtual" macroparticles in the simulation domain.

At the first time step, the HPE module generates the virtual particles' (referred from now on as "test electrons" or, more conveniently, "electrons") population within the simulation domain, and they are sampled by a Maxwell-Boltzmann distribution in 3D with the plasma temperature

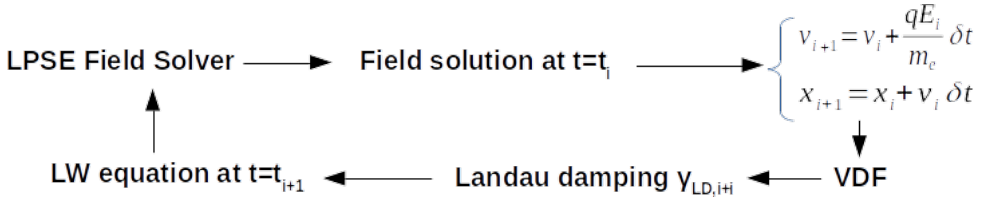

Figure 3.12: Interaction between the LPSE field solver and HPE module.

as its average. These particles represent an ensemble of real particles (i.e. electrons), responding to the calculated fields for each time step. Moreover, they are "test" particles in the sense that they do not interact with each other through collisions, nor do generate feedback with the wave solver. As such, they do not directly modify the field solution in the LPSE solver at the successive time step, with the only exception being the Landau damping coefficient.

In the following time steps, the LPSE solver transmits a field solution to the HPE module, which evolves the particles accordingly to the high-frequency electrostatic field in real space. If the particles reach the simulation boundaries, they are either re-emitted as thermalized particles from the same location, or emitted from the opposite side of the domain with their original velocity. The probability of these events can be controlled in the code to simulate a thermal bath. The velocities and locations are updated according to their value at the previous step, by considering:

$$\boldsymbol{v}_{i+i} = \boldsymbol{v}_i + (qE_i/m_e)\delta t, \tag{3.27a}$$

$$\boldsymbol{x}_{i+1} = \boldsymbol{x}_i + \boldsymbol{v}_i \delta t \tag{3.27b}$$

where the subscript "i" refers to the i-th time step of duration δt. Therefore, the particle velocities are evolved by adding the Coulomb force given the field solution given by the LPSE field solver at the i-th time step, E_i. This allows to find a *Velocity Distribution Function* (VDF) in real space, by obtaining a multi-dimensional array of velocities in real space. The Landau damping coefficient is calculated by using the kinetic formulation:

$$\gamma_{LD} = \frac{\pi\omega_{p0}^2}{k^2} \int \frac{\partial \langle F_e \rangle(\boldsymbol{v}, t)}{\partial \boldsymbol{v}} \delta(\omega_{p0} - \boldsymbol{k} \cdot \boldsymbol{v}) d\boldsymbol{v}, \tag{3.28}$$

where ω_{p0} is the envelope frequency and $\langle F_e \rangle(\boldsymbol{v}, t)$ is the VDF in real space, estimated at the envelope frequency ω_{p0} through the presence of the Dirac's delta $\delta(\omega_{p0} - \boldsymbol{k} \cdot \boldsymbol{v})$. In case $\langle F_e \rangle(\boldsymbol{v}, t)$ is a Maxwell-Boltzmann distribution, the quantity γ_{LD} assumes the form of Eq. 2.104. The Landau damping for the i + 1 time step is then plugged into the Langmuir equation 3.10 for the field solution at the next time step.

3.3.5 TPD simulations with HPE

We discussed up to now about the presence of laser pump depletion, IAWs and turbulence in a system characterized by TPD activity. In light of the theory in Sec. 3.3, we now consider the effects of introducing an electron population. Note that the electron trajectory computation and the feedback between the LPSE kinetic module and field solver increase the computational cost of each simulation significantly.

Figs. 3.13a and 3.13b show, as in previous sections, the EPW energy and the laser transmittivity in the plasma, but this time in the presence of feedback between fields and particles given by collisionless Landau damping. Both diagnostics for the EPW energy and laser transmission are characterized by a noisy signal, much likely to the IAW case (Section 3.3.3), caused by turbulence from the moving particles, which reflects to the electron plasma waves in noise on the Landau damping term. For both of the density scale length values considered ($L_n = 125.0$ μm

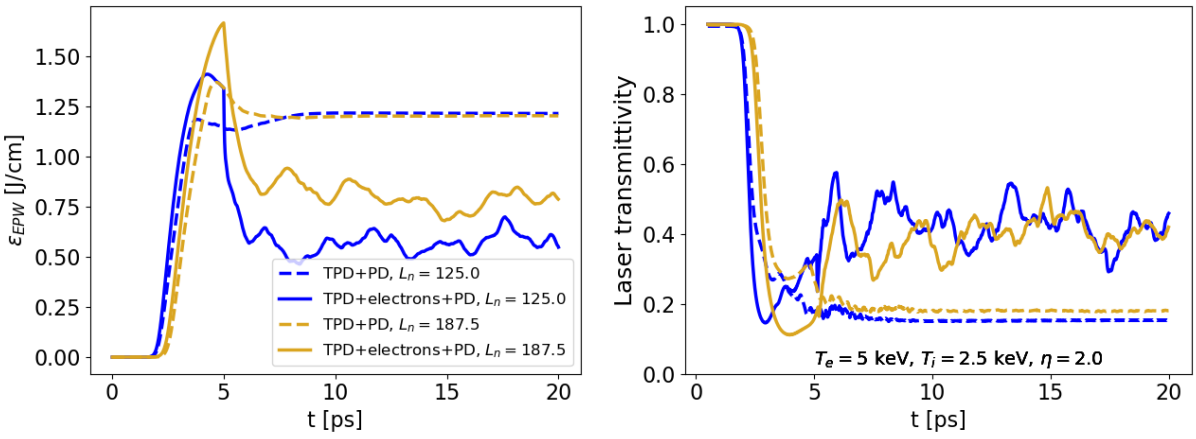

(a) (b)

Figure 3.13: Comparison in a) EPW energy and b) laser transmittivity as a function of time between 2D TPD simulation in presence of electrons (solid line) and without (dashed line), for different density scale lengths at $L_n = 125.0$ and 187.5 μm (blue and orange curves, respectively). Simulations have fixed $T_e = 5$ keV, $T_i = 2.5$ keV, and $\eta = 2.0$, and include laser pump depletion.

for the blue curves, $L_n = 187.5$ μm for the orange ones) the average quasi-stationary behavior is the same, with the simulations with the electron tracker enabled possessing a lower EPW average energy due to Landau damping decreasing the amplitude of the overall EPW field. This translates into a higher laser energy fraction advecting away from $n_c/4$.

Fig. 3.14a shows the fraction of laser power absorbed by EPW Landau damping behavior in time. This diagnostic gives a rough estimation of the degree of hot electron generation by the plasma instabilities. At early times, there is no Landau damping activity, since the HPE module can specify an injection time for the particles, which is recommended to be large enough to allow the laser plasma instabilities to fully establish themselves and converge. In this case, the particle injection time has been set to $t \sim 5$ ps, coherent with the sudden rise in Landau damping activity. Immediately after $t \sim 5$ ps, the injected electrons (sampled from a Maxwell-Boltzmann distribution) see a region of strong fields, resulting in an abrupt energy transfer from the waves to the electrons that translates in a peak of Landau activity; we must note that this effect is not physical, but a reaction of the injection of particles to the field system at an arbitrary instant of time. After $t \simeq 7.5$ ps, the system stabilizes itself to quasi stationary regime with an average absorption level of about $\simeq 20\%$.

A verification of the energy conservation in this case has been conducted in Fig.3.14b. The plot compares the laser power in TW/cm injected (dashed orange line) in the system versus the sum of the laser power losses (continuous blue line), either due to laser light and EPWs leaving the simulation boundaries, or because of EPW collisional and anomalous (Landau) absorption. After a period of exponential field growth ($t < 5$ ps) and an initial period of pump depletion setting in ($t \leq 5$ ps), the electrons are injected in the system ($t = 5$ ps), with a non-physical peak in energy absorbed caused by Landau damping absorption after the injection and the setup of a quasi-stationary regime at $t \simeq 7.5$ ps, where the TPD instability, laser pump depletion and collsionless Landau damping are in equilibrium. The dashed red line represents the average value of the power losses signal from $t > 10$ ps. This level reaches a power $P_{loss,avg} \simeq 1.854$ TW/cm which, compared to the initial injected power of $P_{in} \simeq 1.924$ TW/cm, gives a discrepancy of $\sim 3.5\% - 4\%$ for this particular case.

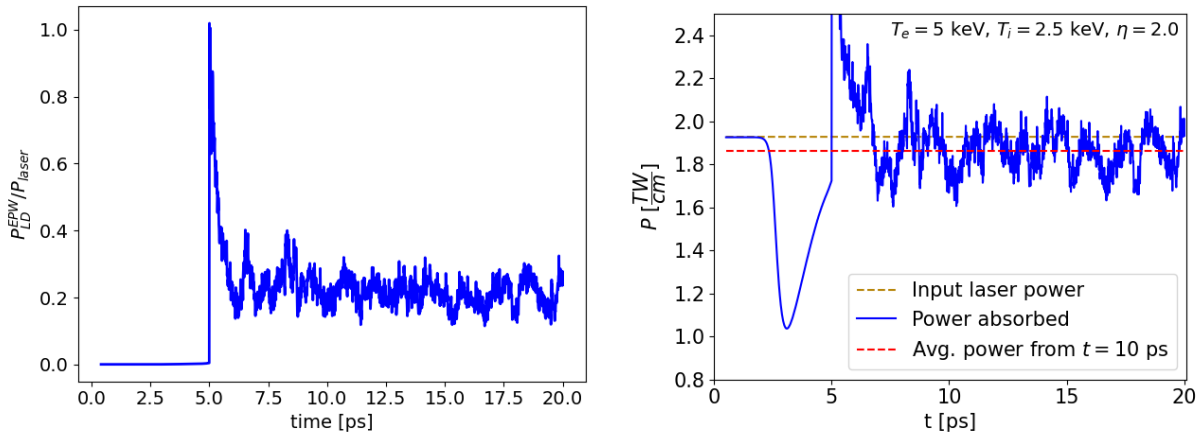

(a) (b)

Figure 3.14: a) Fraction of power absorbed by Landau damping (in TW/cm) as a function of time. b) Power injected (dashed orange line) by the laser compared to the absorbed power (continuous blue line). The red dashed line is the average absorbed power from $t \simeq 10$ ps.

3.4 Conclusions

In this chapter, we presented the hybrid code (LPSE) used in this work. We first described the theoretical model upon which the code is based on, the Zakharov model. We then proceeded to illustrate the equations LPSE solves, a set of linearly coupled wave propagation equations for the laser and scattered light, as well as the Langmuir waves, and two hydrodynamic equations for the low frequency electron response, representing the Ion Acoustic Waves (IAW). We provided examples of code usage for simple physical systems. A simple simulation of 1D SRS in absence of saturation has been verified to follow its expected theoretical behavior; moreover, we verified the code determination of the instability thresholds by using a bisection method on the growth rate, between the simulation and theory between 4% and 15%, while for TPD we made a simple validation by considering only one simulation, obtaining $\sim 3.5\%$ of discrepancy with the theoretical threshold. A verification on the TPD intensity threshold has been conducted as well, with an error between $10 - 20\%$ between simulation and theory caused by not accounting for Landau damping in the threshold calculation. We finally proceeded to describe the effects of saturation such as laser pump depletion on the 2D TPD system.

We then illustrated the concept of hot electron (HE) generation, which is mainly caused through energy transfer from the EPWs to the electron population, resulting in Landau damping of the EPW field amplitude and an acceleration of the electrons in a multi-stage acceleration process when propagating at higher densities. Moreover, a few theoretical notions about weak turbulence caused by LDI cascade and strong turbulence given by Langmuir wave collapse have been discussed, especially in the optics of EPW production and therefore contributing as a HE generation source. The effect of turbulence in the simulations has been discussed thereafter, with the arising of a quasi-stationary, chaotic regime in k-space after a few picoseconds after the linear growth regime has taken place.

We discussed about the kinetic module of the LPSE code, which evolves electrons in the simulation domain, allowing to compute the Landau damping evolution in time through the collection of the Velocity Distribution Function (VDF) for each time step, allowing the collection of HE related results. Finally, we have shown a simulation with the HPE module on, and discussed the changes with the rest of the simulations, as well as doing a verification on the energy conservation of the simulation, about which we report a difference of $\sim 3.5\% - 4\%$ between the laser power injected and the total of the power dissipated by the plasma (either through EPW

collisional and Landau damping) plus the power transmitted through the resonance region.

We must note that the quantities shown such as the TPD and LDI growth rates as well as the TPD threshold, have been calculated to provide insight on the average errors that is expected by the code, and can vary from simulation to simulation. More details about LPSE verification, as well as the inclusion of more sophisticated phenomena, can be found in the work of R.K. Follett [133, 133, 142].

In the following chapter, we will set up a scaling analysis for HE generation for a 2D TPD system, in presence of turbulence, saturation and kinetic particle evolution, with particular care in choosing the laser-plasma parameters necessary for the scaling setup and the extraction of HE quantities from the simulations.

Chapter 4

HE scaling analysis of Two Plasmon Decay and Stimulated Raman Scattering

In the previous chapters we discussed about the theory of parametric instabilities, as well as the effects of turbulence and HE generation. We discussed about the hybrid code LPSE and the Zakharov model it uses to solve a set of linearly coupled field propagation equations for the laser light, scattered light and EPWs, and a hydrodynamic model for IAWs. Moreover, we discussed about the kinetic aspect of the code, which evolves virtual particles (representing an electron ensemble) in space according to the fields given by the field solver, therefore allowing to compute a Landau damping time behavior globally applied to the simulation domain.

After having performed some preliminary code validation in the simulations shown in Chapter 3, we now present a more complete work where SRS and TPD have been considered as the driving parametric instabilities for HE generation. In particular, the physics involved in this problem depends on a set of key laser-plasma conditions, from which the phenomena involved are influenced, mainly through damping and growth rates. For each combination of these input parameters, it is possible to extract the HE energy flux, conversion fraction and average temperature, which constitutes the *scaling analysis* presented in this work.

Section 4.1 explains the LPSE equations used for the purposes of this scaling, the general simulation setup and boundary conditions, the calculated damping rates and the HPE module parameters, and finally the definition of the laser-plasma conditions used as input parameters for the database. In section 4.2 the analysis of a single 2D simulation for a system where TPD, LDI and LW collapse are present. In this case, no SRS is present. Of particular note is the study on the electron energy flux to fit the data and derive the HE quantities of relevance, as well as a study on the electron emission through the velocity distribution function (or VDF), and the observation of the electron trajectories and their energy acquisition. After this, a first database is presented in section 4.3, for the 2D TPD system without SRS. The results of this scaling analysis have then been used to provide a physical explanation of the HE quantities' behavior depending on the variations of each input parameter, and to infer preliminary scaling laws to explain the data behaviors. Moreover, the changes in HE quantities when passing from 2D to 3D simulations has been carried out by comparing a limited set of 3D simulations (with and without laser pump depletion) to the 2D database. In section 4.4, the HE database for a physical system where SRS and TPD coexist is being presented. Similarly to section 4.3, an analysis for a single simulation has been carried out, albeit with the focus on pointing out the differences from the TPD only scaling. After that, the HE database is being presented, explaining the differences (and similarities) in HE generation between the TPD and SRS+TPD cases. Moreover, a preliminary work on a multi-variable scaling law have been presented in this section. Both the TPD and SRS+TPD HE databases mainly refer to plasma conditions similar

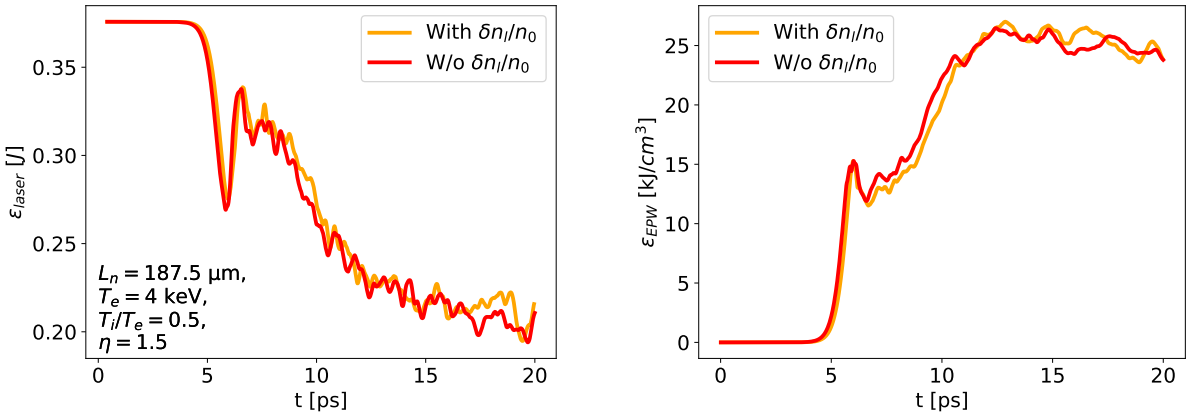

(a) (b)

Figure 4.1: a) Laser energy and b) EPW energy density time evolution with (orange) and without (red) density profile steepening in a typical TPD simulation in 2D.

to the OMEGA facility; in the SRS+TPD scaling however, a reduced scaling for laser-plasma conditions referring to the NIF facility has been presented as well, in order to draw comparisons between the OMEGA and NIF HE results in the light of the setup presented in this scaling. Finally, LPSE has been compared to the PIC code SMILEI in order to assess the HE results from LPSE, as well as other simulation and experimental results available in the literature.

4.1 Definition of the simulation setup and the input parameters

In this section, we first describe the stup of LPSE for TPD simulations of the scaling. Then, we will discuss the considered physics and their influence on growth instability and HE production, from which we derive the input parameters of the scaling.

4.1.1 LPSE equations for a pure TPD scaling

This first scaling only includes TPD as the driving parametric instability. After a period of exponential field growth, characterized by high-frequency perturbation of the electron density, the EPW field couples with a low-frequency electron density perturbation to give a secondary EPW and an IAW. Provided the matching conditions are satisfied, this decay can occur for the secondary EPW as well, and can continue in a decay process of *LDI cascade*, discussed in section 2.3.4 and 3.3.3. LDI is considered a secondary instability (i.e. the incident laser light is not the pump wave), generating a *weak turbulent* regime in the system. Due to the cascade's matching conditions for the EPWs and IAWs' wave vectors (Eqs. 2.196a and 2.196b) the instability generates waves with decreasing wave vectors, leading to a condensation towards low-k values (long wavelengths). This low-k electrostatic field is able to couple with the low-frequency component of the electrons, "pushing" away the plasma ions until a density depression, a *cavity*, is formed, acting as a resonator for the trapped EPW [64]. The *caviton* is then sustained by the EPW field until the electron population crossing the cavity resonates with the EPW field, resulting in an energy transfer from the wave to the electron that decreases the EPW amplitude through Landau damping. This process continues until the EPW field is weak enough for the cavity to collapse, leading to an ion shock wave and a consequent generation of IAWs and the generation of a *strong turbulent* regime within the system. The presence of *laser pump depletion* (PD) for the TPD instability ensures energy conservation.

In this setup, we neglect feedback on the low frequency electron density perturbation on the laser field evolution. This is governed by $\delta n_l/n_0$ in Eq. 3.8, where n_0 is the envelope

density from the Zakharov model, and its effects on the physics of the system is to include Stimulated Brillouin Scattering (SBS) and also the influence of density profile steepening on the laser. Moreover, plasma flow has not been enabled (i.e. the term $\boldsymbol{u}_0(\boldsymbol{x})$ has been neglected), therefore neglecting plasma expansion and development of SBS around quarter critical density. This leaves the term $\delta n_l/n_0$ to control profile steepening only. Fig. 4.1 shows the effects of the term $\delta n_l/n_0$ on the average laser energy, as well as on the average EPW energy density as a function of time for a typical TPD simulation in 2D. The profile show no significant change; therefore, while density profile steepening is present in the plasma, it does not significantly affect its laser evolution and propagation.

After these assumptions, the equations used to simulate the system are a subset of Eqs. 3.8, 3.9, 3.10, 3.11a and 3.11b. As discussed in previous chapters, LPSE allows several options to simplify the set of equations solved by the code. Since the scaling analysis presented in this chapter does not include the presence of Stimulated Raman Scattering (SRS), Eq. 3.9 has been removed from the system altogether, as well as the influence of SRS in Eq. 3.10 (depending on $\boldsymbol{E}_0 \cdot \boldsymbol{E}_1^{c.c.}$). As said before, the influence of the IAWs on the laser propagation has been removed as well. Finally, the electron-ion collisional damping for the laser light (inverse bremsstrahlung) has been set to zero for simplicity, which removes the term depending on $\nu_{ei,0}$, and the noise signal used to seed the EPW field has been taken as 10^{-5} V/m. The end result is a simplified system of field equations that simulates the evolution of TPD, LDI and cavitation in presence of laser pump depletion. The equation for Stimulated Raman Scattering (SRS), as well as terms that include SRS in the laser, EPW and IAW equations have been included as well in blue. While not relevant for the TPD scaling, they are relevant for the SRS+TPD scaling, which we We will discuss about in section 4.4:

$$\frac{\partial}{\partial t}\vec{E}_0 = \frac{ic^2}{2\omega_0}\left[\nabla^2\vec{E}_0 - \nabla(\nabla\cdot\vec{E}_0)\right] + \frac{i\omega_0}{2}\left[1 - \frac{\omega_{p0}^2}{\omega_0^2}\left(1+\frac{\delta N}{n_0}\right)\right]\vec{E}_0 + \\ + \frac{ie}{4m_e\omega_1}(\vec{E}_1\nabla\cdot\vec{E}_{EPW}) + \frac{ie}{4m_e\omega_{p0}}(\vec{E}_{EPW}\nabla\cdot\vec{E}_{EPW})^T e^{-(\omega_0-2\omega_{p0})t}, \tag{4.1}$$

$$\frac{\partial}{\partial t}\vec{E}_1 = -\frac{\omega_{p0}^2}{2\omega_1}\left(1+\frac{\delta N}{n_0}\right)\nu_{ei,1}\vec{E}_1 + \frac{ic^2}{2\omega_1}\left[\nabla^2\vec{E}_1 - \nabla(\nabla\cdot\vec{E}_1)\right] + \\ + \frac{i\omega_1}{2}\left[1 - \frac{\omega_{p0}^2}{\omega_1^2}\left(1+\frac{\delta N}{n_0}+\frac{\delta n_l}{n_0}\right)\right]\vec{E}_0 + \frac{ie}{4m_e\omega_0}\vec{E}_0\nabla\cdot\vec{E}_h^{c.c.}, \tag{4.2}$$

$$\nabla\cdot\left[i\left(\frac{\partial}{\partial t}+\nu_e\circ\right) + \frac{3\mathrm{v}_{Te}^2}{2\omega_{p0}}\nabla^2 - \frac{\omega_{p0}}{2}\frac{\delta N}{n_0}\right]\vec{E}_{EPW} = \frac{\omega_{p0}}{2}\nabla\cdot\left(\frac{\delta n_l}{n_0}\vec{E}_{EPW}\right) + \\ + \frac{e\omega_{p0}}{4m_e\omega_0\omega_1}\left(1+\frac{\delta N}{n_0}\right)\nabla^2(\vec{E}_0\cdot\vec{E}_1^{c.c.}) + \\ + \frac{e}{8\omega_{p0}m_e}\nabla\cdot\left[\nabla(\vec{E}_0\cdot\vec{E}_{EPW}^{c.c.} - \vec{E}_0\nabla\cdot\vec{E}_{EPW}^{c.c.})\right]e^{-i(\omega_0-2\omega_{p0})t} + S_{EPW}, \tag{4.3}$$

$$\left[\frac{\partial}{\partial t}\right]\left(\frac{\delta n_l}{n_0}\right) = -\mathcal{W}_l, \tag{4.4}$$

$$\left[\frac{\partial}{\partial t} + 2\nu_{Landau,i}(\vec{k})\circ\right]\mathcal{W}_l = -\nabla^2\left[c_s^2\frac{\delta n_l}{n_0} + \frac{Ze^2}{4m_em_i}\left(\left|\frac{\vec{E}_{EPW}}{\omega_{p0}}\right|^2 + \left|\frac{\vec{E}_0}{\omega_0}\right|^2 + \left|\frac{\vec{E}_1}{\omega_1}\right|^2\right)\right]. \tag{4.5}$$

4.1.2 General simulation setup

We now describe the general simulation setup for the simulations in the scaling.

The simulations have been performed in 2D. The number of cells per wavelength is set to $\simeq 7.0$ for all simulations to ensure a good convergence and a reasonable total computational cost. The transversal boundary conditions are set to be periodic, while the longitudinal ones as

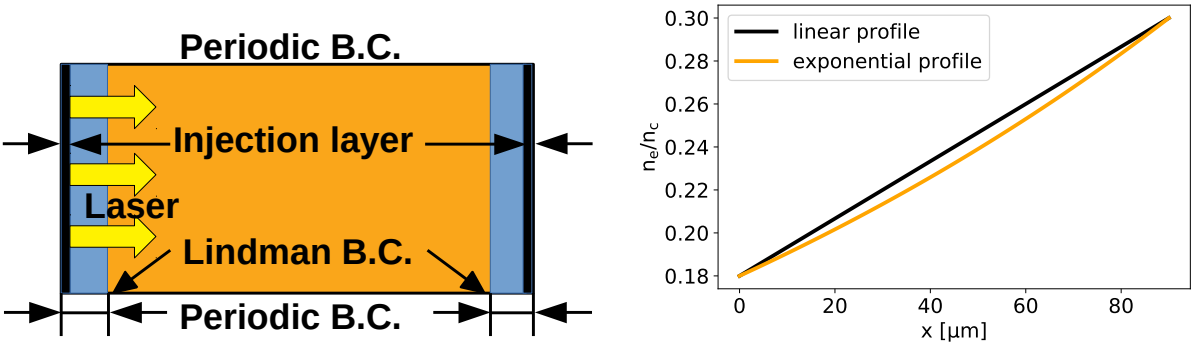

(a) (b)

Figure 4.2: a) Simulation boundary conditions and b) simulation density profile.

absorbing boundary conditions, also called *Lindman boundary conditions*, within which the fields decay exponentially when entering the *absorbing boundary layer*. These boundary conditions are valid for both the laser and the EPW fields, but the width of the absorbing boundary layer has been set to different values for the two, respectively 3 and 2.5 μm for the laser and EPWs from the simulation boundaries. Moreover, an *injection layer* has been set up where the laser light is injected, at 1 μm from the simulation boundaries. These boundaries have been marked in Fig. 4.2a.

The considered plasma is limited close to the region of quarter critical density, in the interval $n_e/n_c = [0.18 - 0.3]$, located at $x = 0$ and $x = L_{box}$ respectively. The density profile has been considered linear for simplicity, with a small deviation from a more realistic exponential profile (Fig. 4.2b). The envelope density n_0 required for the Zakharov model has been set to 0.24; its corresponding envelope frequency is given by $\omega_{p0} = \omega_0\sqrt{n_0/n_c}$, where ω_0 is the laser frequency and n_c the corresponding critical density. The simulations consider a CH plasma with 50% in ion species distribution, for an average charge number of $\langle Z\rangle \equiv \sum_i f_i Z_i = 3.5$, where f_i is the ion fraction ($f_i = 0.5$ for both C and H ions). This has been taken due to its common use in ICF implosions [43, 144]. The ion-over-electron mass ratio has been set to $m_i/m_e \equiv \sum_i (f_i A_i) m_p/m_e = 11952.43$, where A_i is the mass number of the i-th ion species and m_p the proton mass.

The incident laser pulse is a single normally incident, p-polarized plane wave. The laser wavelength is $\lambda_0 = 0.351$ μm, corresponding to the frequency-tripled pulse of a Nd-glass laser, such as in the OMEGA facility [158].

Finally, a simulation time of $t_{sim} = 20$ ps has been chosen in order to balance the computational cost and a reasonable time for which the instability has fully set in a *quasi stationary* regime, where the effects of TPD, LDI cascade, cavitation and laser pump depletion have reached an equilibrium configuration. We chose this regime in order to obtain simple and stable conditions for HE production, which could then be implemented into the steady-state ray-tracing models of hydrodynamic codes.

4.1.3 Damping rates

The EPWs and IAWs' evolution is going to be controlled by their associated wave damping rates. In particular, while the EPW Landau damping is being calculated by the HPE module (discussed in section 3.3.4 and whose settings will be discussed in the following section), the EPW collisional damping and the IAW dampings (both collisional and Landau) need to be manually entered as parameters.

The collisional damping given by the laser, leading to inverse bremsstrahlung (IB) 2.2.2.2, has been set to zero for simplicity, while the ion-ion collisional damping rate has been considered

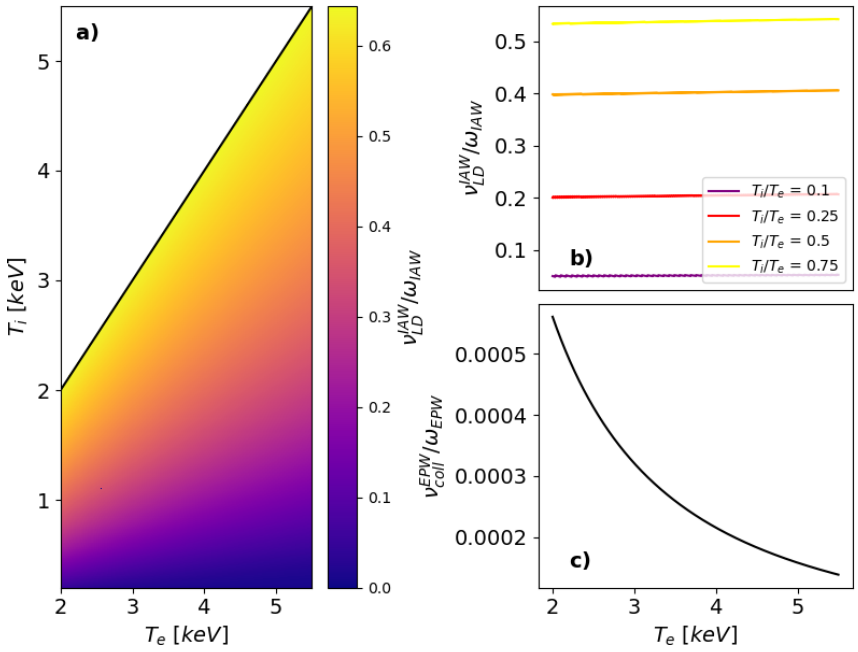

Figure 4.3: (a) IAW Landau damping rate ν_{LD}^{IAW} as a function of T_e and T_i , (b) IAW Landau damping rate as a function of T_e only (at fixed values of T_i/T_e), and (c) EPW collisional damping rate ν_{coll}^{EPW} , as a function of the electron temperature T_e. The black line in (a) is the condition $T_e = T_i$. All damping rates have been evaluated at quarter critical density, and normalized with respect to $\omega_{IAW} \equiv k_0 c$ and $\omega_{EPW} \equiv \omega_0/2$, where ω_0 and k_0 refer to the laser light. The real part of the IAW frequency, ω_{IAW}, has been obtained from the roots of the dielectric function ε.

negligible with respect to the IAW Landau damping rate.

The IAW Landau damping is calculated by using the kinetic approach discussed in section 2.2.5, using the tabulated derivative of the *plasma dispersion function* $Z'(\omega/k\sqrt{2}\mathrm{v}_{Ti})$ to find the roots of the ion dielectric permittivity given by $\varepsilon = 1 + \sum_j \chi_j$ or, as in Eq. 2.105, to find the root frequencies so that the dispersion relation:

$$\varepsilon = 1 - \frac{\omega_{pi}^2}{k^2 2\mathrm{v}_{Ti}^2} Z'\left(\frac{\omega}{k\sqrt{2}\mathrm{v}_{Ti}}\right) - \frac{\omega_{pe}^2}{k^2 2\mathrm{v}_{Te}^2} Z'\left(\frac{\omega}{k\sqrt{2}\mathrm{v}_{Te}}\right) = 0 \tag{4.6}$$

is satisfied [118]. The IAW Landau damping is the imaginary part of the frequency minimizing the dielectric permittivity ε so that $\nu_{LD}^{IAW} = \Im(\omega_{IAW})$. Figs. 4.3a and 4.3b show the behavior of the IAW Landau damping rate. It strongly depends on T_i/T_e, reaching values of the order of $\mathcal{O}(10^{-1})$ for increasing T_i/T_e. There is also a dependency on T_e, shown in Fig. 4.3b, but it can be considered negligible.

Fig. 4.3c shows EPW collisional damping rate. It depends inversely on the electron temperature through T_e or, conversely, through v_{Te} (from Eq. 2.35b), while it does not depend on the ion temperature T_i.

Finally we must note that, despite LPSE approximating the plasma as a single ion species, the IAW damping results have been calculated taking into account a multi-species (CH) plasma. Therefore, the ion contribution of the IAW Landau damping calculation in Eq. 4.6 must be separately calculated for each ion species, namely:

$$\frac{\omega_{pi}^2}{k^2 2\mathrm{v}_{Ti}^2} Z'\left(\frac{\omega}{k\sqrt{2}\mathrm{v}_{Ti}}\right) = \sum_j \frac{\omega_{pj}^2}{k^2 2\mathrm{v}_{Tj}^2} Z'\left(\frac{\omega}{k\sqrt{2}\mathrm{v}_{Tj}}\right), \tag{4.7}$$

where the subscript "j" indicates the ion species. This approach is more accurate than calculate an average ion contribution, since the damping would be underestimated by an order of magnitude.

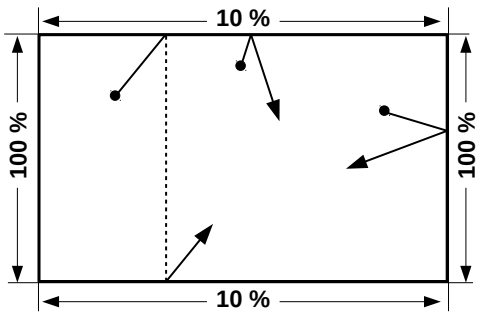

Figure 4.4: HPE boundary conditions. The numbers indicate the thermalization probability for a particle reaching that boundary.

4.1.4 HPE module parameters

In this scaling analysis the HPE module of LPSE has been used to determine the kinetic evolution of the electron particle population. The module injects a number of virtual (or macro-) particles in the domain. As discussed in section 3.3.4, these particles interact with the solution passed by the field solver, but they do not generate fields on their own nor do they interact with each other. The only feedback they provide to the field solver is through the EPW Landau damping within the overall electron damping ν_e in Eq. 4.3 and 3.10. The number of these virtual particles is set to $N_{part} = 10^6$, considered to be a sufficient number of particles for 2D simulations. Each virtual particle accounts for 1.559×10^{10} electrons, and represents the average behavior of each electron in the ensemble. Therefore, we will use the terms "particle" and "electron" interchangeably in what follows. The electrons are injected with a random velocity sampled from a Maxwell-Boltzmann distribution at the average plasma temperature T_e, while their position has been sampled from an uniform distribution. The particles are injected at $t = 5$ ps from the start of the simulation. This is done to allow the instability to reach a steady growth regime. After injection, the particles evolve according to 3.3.4, where their velocity and position are updated at each time step following the electric field passed by the field solver. The particles in the plasma are subjected to a set of boundary conditions representing the continuation of the plasma beyond the simulation domain. Moreover, the particles collected at the boundaries give the energy flux and power needed to extract the HE quantities.

The boundary conditions for these particles are *thermalization probabilities*. The forward and backward boundaries have been set to have a thermalization probability of 100% 4.4. Therefore, every particle that crosses these boundaries are being counted in the diagnostics, and then re-injected within the simulation domain from the same position with a velocity randomly chosen from the bulk Maxwell-Boltzmann distribution. On the lower and upper boundaries, the particles have a 10% probability to thermalize. If so, they follow the same steps as for the forward and backward boundaries. If they do not thermalize, the particles are re-injected at the same x position, but at the opposite boundary, with the same velocity and direction.

In order to extract HE quantities, the HPE module can have several virtual diagnostics set up. One such diagnostics recovers the average electron energy flux after specifying the energy intervals at which the data have to be binned, for a total of 50 energy intervals. In these simulations, the electron flux data are collected from the temperature T_e up to the energy of 500 keV. Since the electron statistic is higher for lower energies, the bins are taken with a logarithmic spacing instead of a linear one. Moreover, the HPE module can record the trajectories and velocities of a number of particles sampled from the population. This increases the simulation computational cost considerably. However, it gives a useful tool to describe the behavior of individual (virtual) particles within the domain, and their response to the fields.

Table 4.1: Simulation dimensions and grid for different L_n values.

L_n	125.0 μm	187.5 μm	250.0 μm
Grid $[\mu m \times \mu m]$	60×12	90×18	120×24
Nodes	1440×288	2160×432	2880×576

4.1.5 Laser-plasma conditions: database entries

The physics processes involved in the simulation are TPD, LDI and cavitation / LW collapse. On the kinetic part, HE generation takes place as well. These phenomena are governed by their respective damping rates. Moreover, the appearance of the primary instability (TPD) and the system's energy balance are important as well. Therefore, the construction of a relevant dataset of laser-plasma conditions must take into account these aspects. These conditions are identified in four general quantities, namely:

- The density scale length L_n, previously defined in Eq. 2.160, is a measure of the density profile gradient. It appears in the definition of the laser intensity threshold for absolute TPD (Eq. 2.188), and it enlarges the activity region around quarter critical density. The values used for this parameter scan have been chosen to represent OMEGA-like conditions [57], taken at $L_n = 125, 187.5$ and 250 μm respectively. The choice of this value also affects the simulation dimensions and grid, in order to keep the simulation with the same degree of convergence from the code (7.0 cells per wavelength), as shown in Table 4.1.

- The average electron temperature in the plasma T_e, around which the Maxwell-Boltzmann distribution for the plasma is centered. It influences the instability threshold for which TPD manifests [133], as well as the threshold for LDI [79]. Moreover, it influences the development time of density cavities and the amount of energy stored within it, as well as its energy damping when said cavity collapses [40]. It is featured in the majority of damping rates such as the EPW collisional damping, the EPW Landau damping and the IAW Landau damping as well. The temperature values chosen for the parameter scan range from $T_e = 2.5$ keV to $T_e = 5$ keV.

- The ion-electron temperature ratio T_i/T_e. It is a quantity representing the more common $\langle Z \rangle T_e/3T_i$ quantity, which is a parameter governing the existence of IAWs in the plasma, according to their frequency ω_{IAW} (Eq. 2.91), solution of the dispersion relation for longitudinal modes in a warm plasma. As a consequence, this term majorly influences any process involving IAWs, such as the Langmuir Decay Instability, as seen in the LDI threshold (Eq. 2.200 and 2.201), and the IAW Landau damping rate. We chose values of T_i/T_e ranging from 0.1 to 0.75.

- The laser drive strength, defined as the ratio between the laser intensity and the TPD intensity threshold $\eta \equiv I_{laser}/I_{thr}^{TPD}$. It is a parameter that represents how much above threshold the laser is (while keeping T_e and L_n constant). It is chosen to range from $\eta = 1.0$, at threshold, up to 2.0.

These four parameters constitute the basic input parameters of laser-plasma conditions from which the HE scaling is then extracted, for a total of 240 simulations per scaling. Table 4.2 shows the overall range of values for the dataset.

4.2 Analysis of a LPSE simulation for 2D TPD

In the previous chapter, we discussed the general setup of the LPSE simulations, and the dataset of laser-plasma conditions used to perform the parameter scan. We now focus on the analysis

Table 4.2: Input laser plasma parameter for the HE database

L_n $[\mu m]$	T_e $[keV]$	T_i/T_e	η
125.0	2.5	0.1	1.0
187.5	3.0	0.25	1.2
250.0	4.0	0.5	1.25
	5.0	0.75	1.5
			2.0

of a single representative LPSE simulation, from the development of the EPW potential and the IAW density perturbation to the analysis of the electron energy flux spectrum, and the extraction of hot electron related data.

The laser-plasma conditions we choose for this simulation are $L_n = 187.5$ μm, $T_e = 4$ keV, $T_i/T_e = 0.5$ and $\eta = 1.5$.

With respect of the cases we presented in chapter 3, the system in this section is characterized by the presence of TPD, LDI, LW collapse (cavitation / caviton collapse) and laser pump depletion, with the injection of virtual particles in the system at $t = 5$ ps through the HPE module form LPSE. These phenomena dictate the evolution of the EPW potential.

4.2.1 EPW potential

We first analyze the EPW potential (Fig. 4.5) for different time frames.

At t = 1.6 ps, the instability is starting to appear around the region of quarter critical density, at about $xk_0 \simeq 800 - 850$ (Fig. 4.5a). The instability is in the *linear growth regime* where the EPW field grows exponentially (and its growth rate increases linearly). The Fourier picture (Fig. 4.5b) shows there is predominantly TPD activity, due to the field growing along the TPD maximum growth rate (Eq. 2.179) and following the corresponding hyperbola (red curve) in k-space (Eq. 2.180), showing its characteristic lobed structure. There is no major distinction between the absolute modes' field, in the region around $(k_\parallel, k_\perp) \simeq (0, 0)$, and the convective modes' field, which are located in the lobes of the hyperbola.

At further times (t = 4.4 ps), the instability continues growing in the linear regime, mainly in the region of quarter critical density and in particular around $xk_0 \simeq 800$, with some of the field propagating outwards both in the forward and backward directions. These are convective modes propagating away from the resonance region. The fields in the resonance region and the ones propagating away from it differ between each other by about one order of magnitude. Moreover, the EPW field sharply decreases at $xk_0 \simeq 1050$ as the TPD instability is unable to exist beyond $n_c/4$, save for plasma local inhomogeneities which slightly extend the quarter critical region to higher densities. In Fourier space (Fig. 4.5d), the distinction between absolute and convective modes becomes clearer, with the appearance of four peaks at $(k_\parallel, k_\perp) \simeq (0, 0)$ and $(k_\parallel, k_\perp) \simeq (1, 0)$, which belong to the same TPD decay. These peaks are separated along $k_\perp$ by a distance corresponding to the Simon critical wave number, defined by Eq. 2.185, which in the laser-plasma conditions specified above becomes $k_\perp \equiv \pm k_0 \sqrt{0.106(I_{14}\lambda^2_{0,\mu}/T^2_{e,keV})} \simeq \pm 0.058 k_0$. Moreover, the modes that have been deemed as "absolute" smear horizontally because of their low propagation velocity. While these modes grow absolutely in time due to their low phase velocity, they eventually advect out of the resonance region and propagate in space, contributing to the high field region around it. The convective modes follow the maximum growth hyperbola and are also "smeared" in k-space.

At t = 5.2 ps, the instability further develops. The fields grow even more in the quarter critical region (Fig. 4.5e), with an overall increase in the fields in the entire domain. Overall, the qualitative features looks similar to the ones in Fig. 4.5c. However, the Fourier spectrum (Fig. 4.5f) presents a different picture. The convective modes are spread in almost every direction,

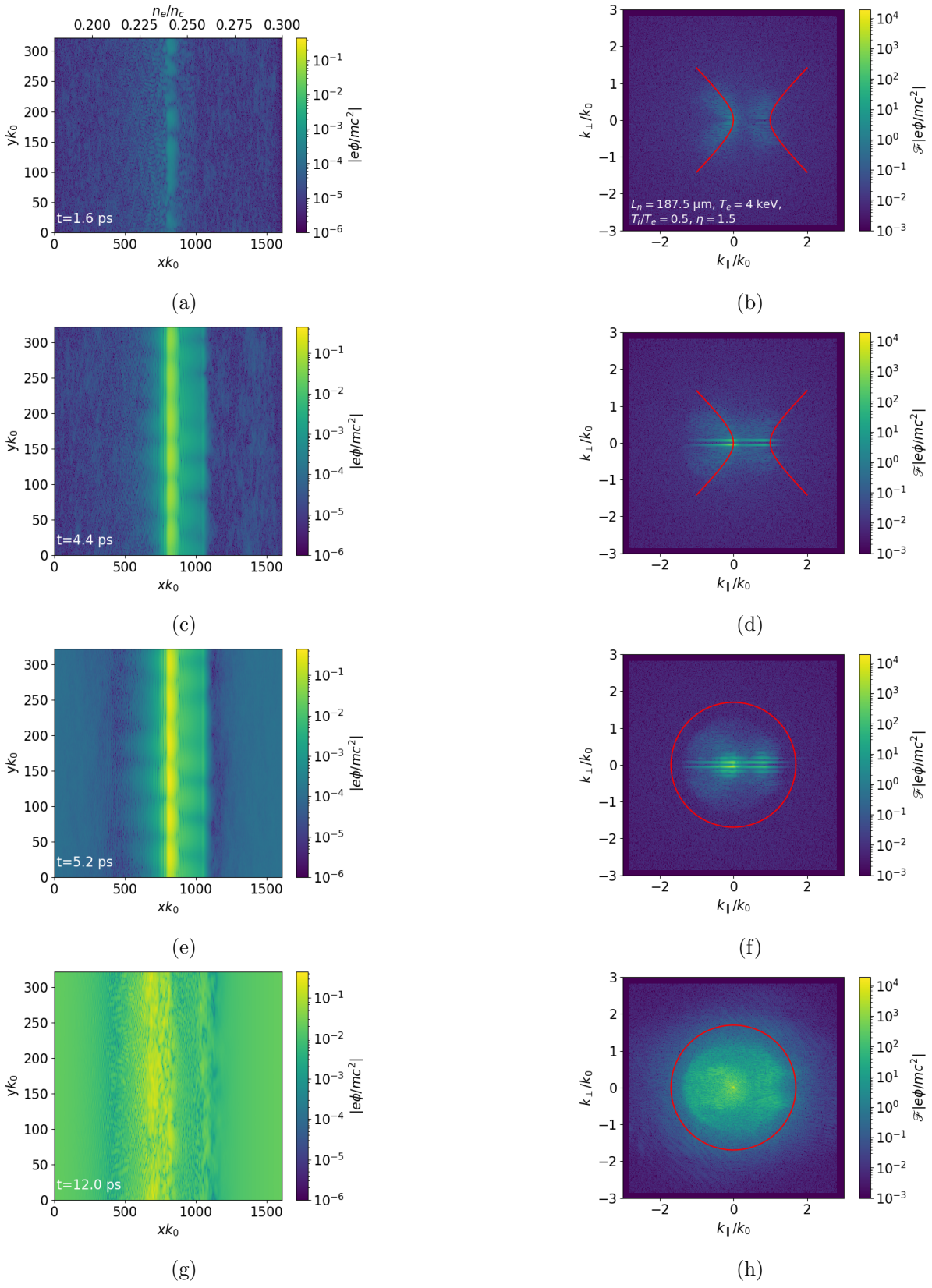

Figure 4.5: EPW potential in a)-c)-e)-g) real space and b)-d)-f)-h) Fourier space. The left column is the normalized EPW potential's absolute value in real space $|e\phi/m_e c^2|$, while the right one is its Fast Fourier transform (FFT) $\mathscr{F}|e\phi/m_e c^2|$ in the corresponding Fourier space. The axes both in real and Fourier space have been normalized to the laser wave vector $k_0 \equiv 2\pi c/\lambda_0$, where λ_0 is the laser wavelength.

and the maximum growth hyperbola is difficult to identify. The modes' wave numbers appear to be limited in a circular region around $(k_\parallel, k_\perp) \simeq (0, 0)$, with a radius of about $k/k_0 \simeq 1.5$. This circumference corresponds to the *Landau damping cutoff*, beyond which the EPWs are heavily Landau damped. This limit is in the region of $k_{EPW}\lambda_{De} \simeq 0.2 - 0.3$ (red circle in Fig. 4.5f reports $k_{EPW}\lambda_{De} = 0.3$).

Finally, after t $\sim$ 6 ps, about 1 ps from the particle injection from the HPE module, the plasma is characterized by a regime of strong turbulence. Fig. 4.5g shows a snapshot of such turbulent regime at t = 12 ps. The average EPW potential is considerably higher, with a resonance region shifted towards lower densities in the range of $xk_0 \simeq 650 - 800$. The Fourier spectrum (Fig. 4.5h) follows such turbulent regime, where the maximum growth rate hyperbola is not visible. There is still an absolute activity region close to the center in k-space, but now the waves are free to propagate below the Simon threshold. This suggests the modes do not belong to TPD, and their high values in EPW potential suggest it is not given by LDI cascade neither. The waves are also noticeably Landau damped beyond the cutoff (red circle). Overall, the plasma system in this snapshot has reached so-called *quasi-stationary conditions*, where the physical phenomena within are in a steady-state regime. This regime persists for several picoseconds [84] is where we extracted the HE quantities constituting our scaling analysis.

4.2.2 IAW profile: LDI and cavitation

The IAW field, since it is mainly driven from LDI (and successively from the collapse of the density cavities in the plasma), follows the EPW potential's behavior discussed in the previous section.

Fig. 4.6 illustrates the corresponding low frequency electron density perturbation δn_l, solution of Eq. 4.4 and 4.5, normalized to the critical density n_c at different time frames, following the frames in Fig. 4.5. This quantity represents the evolution in time of the low frequency response field to the pump wave, and it is therefore indicative of the presence of IAWs in the plasma.

At t = 4.4 ps, different regions start appearing around $n_c/4$, where the density perturbation profile is modified by the EPW fields, showing regions where the perturbation gives concentrations and depressions in density in a periodic pattern. Their periodicity stems from the periodic boundary conditions, allowing the dominant mode and its harmonics to grow faster than the rest (the highest activity region in Fig. 4.5c is a factor of $\simeq$ 10 higher). While this is an unphysical feature, it still illustrates the correct qualitative growth of the instability, and when quasi-stationary conditions are reached, the periodic pattern disappears. In Fourier space (Fig. 4.6b), there is the appearance of two circles joining at $(k_\parallel, k_\perp) \simeq (0, 0)$ and several horizontal lines along k-space. These lines are a product of the harmonic growth previously suggested. The shape of the IAW modes is caused by the TPD modes' growth. Since the strongest EPW modes grow along the hyperbole of maximum growth rate in Fourier space (Fig. 4.5b), the LDI decays of these EPW modes from TPD generate IAWs following the matching condition given by Eq. 2.195b, resulting in the two circles observed for the IAWs in Fourier space.

At t = 5.2 ps, the transverse density oscillations in real space further develop, growing in amplitude (Fig. 4.6c). In particular, the regions where $\delta n_l/n_c$ is the highest around $n_c/4$ correspond to the highest EPW potential regions (Fig. 4.5e), implying a longitudinal ion acoustic wave generation due to LDI cascade and their successive propagation towards higher densities. The perturbation is still very weak, with a low-density variation from critical density of $\simeq 10^{-3}$ at its maximum, and $\simeq 10^{-5}$ as minimum. The Fourier representation (Fig. 4.6d) remains qualitatively unchanged compared to 4.6b, with waves filling the associated region of existence through the matching conditions. Moreover, the IAW spectrum's longitudinal component is about double in size than the EPW one, implying not only that Eq. 2.196b is satisfied, but also that the IAWs tend to propagate along the direction of laser propagation.

Finally, at t = 12 ps a turbulent plasma state is achieved, in line with the EPW potential

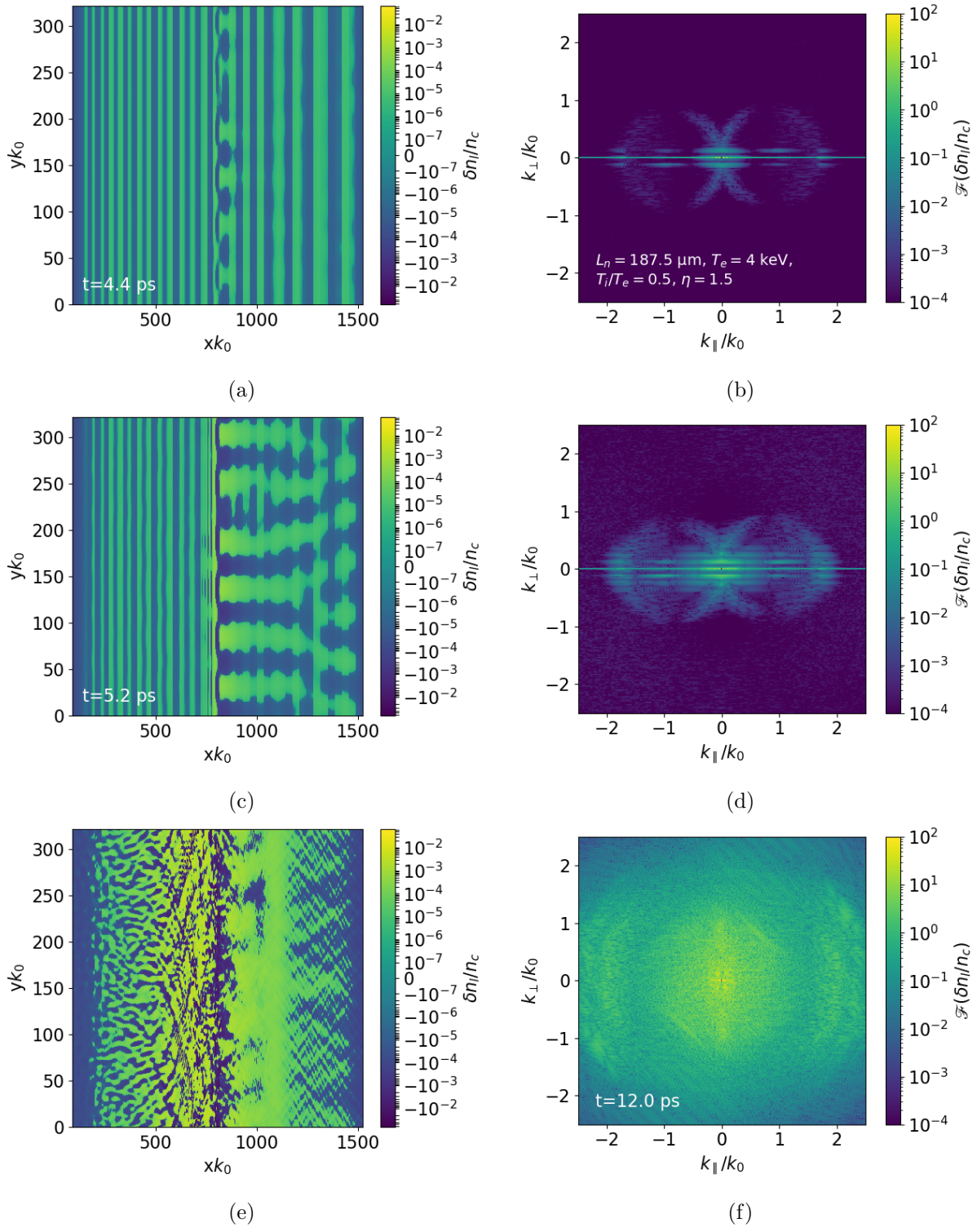

Figure 4.6: Low-frequency electron density perturbation δn_l, normalized to the critical density n_c, in a)-c)-e) real space and b)-d)-f) Fourier space.

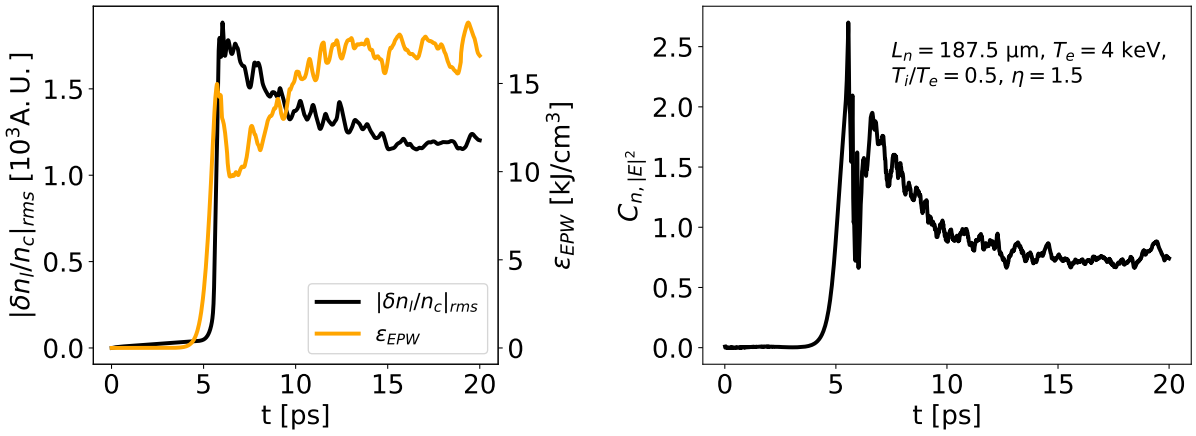

(a) (b)

Figure 4.7: a) Behavior of the root mean square of the space-averaged $|\delta n_l/n_c|$ (black curve), the EPW energy density (orange curve), and the b) caviton correlator, as a function of time.

behavior. Fig. 4.6e shows the turbulent regime in real space, with the EPW field pushing the plasma away in the resonance region at $xk_0 \simeq 800$, followed by a region of high IAW activity. The regions from lower densities up to quarter critical show the presence of localized density depressions, caused by the EPWs propagating in the backwards direction. These are cavitons forming due to the intense EPW field (dark blue spots), which subsequently collapse generating IAWs (yellow regions). In Fourier space (Fig. 4.6f), the IAWs are distributed across the entire spectrum, with no characteristic behaviors.

Fig. 4.7a shows the evolution of the absolute value of the root mean square of $\delta n_l/n_c$ as a function of time. The IAW generation (black curve) follows closely the EPW linear growth (orange curve) with a delay of a few fractions of ps. After the linear growth has taken place and both the EPWs and LDI cascade has set in, the electron population injected at t = 5 ps starts evolving the PW damping rate, as well as strong turbulence / cavitation setting in after a time delay (at $\simeq 5.6$ ps). After a period of stabilization, both the EPW energy and the IAW signature enter in a quasi-stationary regime, at a time t $\simeq 12.5$ ps. The overall cavitation / caviton formation / LW collapse activity in the simulation plasma as a function of time is expressed by the *caviton correlator* [25, 27]:

$$C_{n,|E|^2} = \frac{\langle n_e |E|^2 \rangle}{\langle n_e^2 \rangle^{\frac{1}{2}} \langle |E|^2 \rangle}, \tag{4.8}$$

which correlates the peaks in Langmuir wave field to the density depressions trapping the field. A value of 0.5 and above denotes strong cavitation activity. After a period of strong turbulent regime (and the correlator reaching values up to 2.5), the system reaches equilibrium at $C_{n,|E|^2} \simeq 0.75$, signifying that, in quasi-stationary conditions, strong cavitation activity is in steady state with the TPD instability and LDI cascade.

4.2.3 HE energy spectrum

The HPE module collects the energy flux as one of its virtual diagnostics, as introduced in section 4.1.4. They give the average electron energy flux (in W/cm^2) for each separate boundary in the simulation domain (i.e. $\pm$x, $\pm$y and $\pm$z, where +x refers to the forward x boundary, $-$x the backward one, and so on) for each energy bin specified in the diagnostic and at each time frame the diagnostic has been collected. The flux is averaged over the number of collisions with the boundaries the virtual particles had, and it does not account for the thermalization boundary

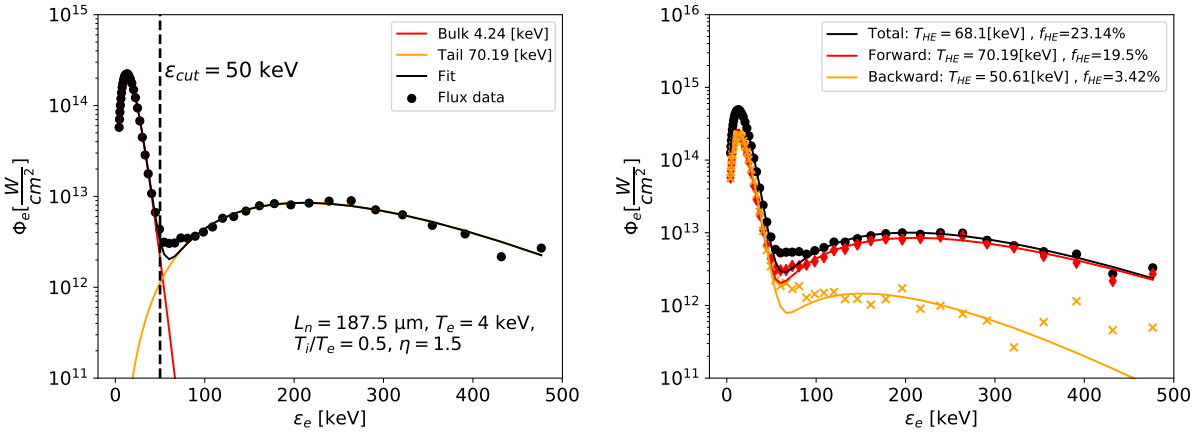

(a) (b)

Figure 4.8: a) Electron energy flux in the forward direction as a function of the electron energy ε_e (in keV) (black data points), and their fitting functions for the bulk (red curve), HE tail (Orange curve) and the overall fit (black curve). b) Electron energy flux as a function of the electron energy ε_e (in keV), for the total flux incident on all boundaries (black), on the forward boundary only (red) and on the backward one (orange). The electron flux is in units of W/cm^2 because it is binned in energy.

conditions. Therefore, the data collected must be multiplied by their respective thermalization probability: $\Phi_e = \sum_s (\Phi_{+s} + \Phi_{-s}) \mathrm{P}_s^{th}$, where $s = x, y, z$ and P_s^{th} is the thermalization probability for the s-component of the flux. For the purpose of this scaling, as said in section 4.1.4, the thermalization probability has been set to $\mathrm{P}^{th} = [1, 0.1, 0.1]$.

An assumption made in this scaling analysis is to consider the quasi-stationary plasma regime, and thus the energy flux profile has first been averaged over the time interval in which such regime occurs. The quasi-stationary regime sets at different times following the instability growth rate $\gamma_{TPD} \equiv v_{osc} k_0/4 \propto \eta I_{thr}^{TPD} k_0/4$, with its strongest dependence being from the drive strength η. Therefore, the simulations' quasi stationary conditions have been selected at different times, most notably at $\mathrm{t}_{q.s.} = (17.5, 17.5, 15, 12.5, 10)$ ps for $\eta = (1.0, 1.2, 1.25, 1.5, 2.0)$, respectively. For the simulation here discussed this time has been set to $\mathrm{t}_{q.s.} = 12.5$ ps.

The electron energy flux Φ_e is shown in Fig. 4.8a, for the electrons collected at the forward boundary $(+x)$ as a function of the electron energy bin, constituting the simulation's energy spectrum. The main feature of this profile is the appearance of two main plasma populations. The first region is located at low energies (up to $\simeq 50-60$ keV), constituting the majority of the plasma (reaching values of $\Phi_e \simeq 10^{15}$ units). Therefore, it will be referred to as *bulk plasma*. The data at energies higher than $\simeq 50 - 60$ keV belong to a much smaller population ($\Phi_e \simeq 10^{13}$), and can reach energies of 500 keV (the energy limit set in the virtual diagnostic) and beyond. This region gives the hot electron population emitted, and therefore it will be referred to as the plasma's *hot electron (HE) tail*.

In order to fit these data points, a suitable distribution was Maxwell-Boltzmann. This distribution is conventionally used for the plasma bulk, due to their low energy (compared to the HE population) and isotropic emission. However, the HE tail, as we will be discussed further, is highly directional, and it violates the requirement of an isotropic plasma population. Despite this, it is a popular choice in literature [53, 57, 84, 159] due to its simplicity. The fitting procedure uses the Maxwell-Boltzmann energy distribution (in keV^{-1}cm^{-3}) of Eq. 2.21 as hypothesis function for both the plasma bulk and HE tail:

$$f(x, \varepsilon) = \sqrt{\frac{2}{\pi}} N_j \frac{\sqrt{\varepsilon}}{T_j^{3/2}} \exp\left(-\frac{\varepsilon}{T_j}\right), \tag{4.9}$$

where N_j and T_j are the fitting density and temperature, respectively, for the bulk and the HE tail (subscript "j"), and ε is the particle energy. In order to obtain the energy flux for each bin, the third moment of the distribution has been integrated for each energy bin:

$$\Phi_{\varepsilon_i} = \int_{\varepsilon_i}^{\varepsilon_{i+1}} \varepsilon \sqrt{\frac{2\varepsilon}{m_e}} f(x,\varepsilon) d\varepsilon, \tag{4.10}$$

where $\varepsilon_i, \varepsilon_{i+1}$ are the energy bin's energy bounds. The curve given by Φ_{ε_i} for all energy bins is the function being fit with an analytical solution given by:

$$\begin{aligned}\Phi_{\varepsilon_i} = &-2\sqrt{\frac{2}{\pi m_e}} \frac{N_{ji}}{\sqrt{T_{ji}}} \Bigg\{ \left[\varepsilon^2 \exp\left(-\frac{\varepsilon}{T_{ji}}\right)\right]_{\varepsilon_i}^{\varepsilon_{i+1}} + \left[2T_{ji}\ \varepsilon\ \exp\left(-\frac{\varepsilon}{T_{ji}}\right)\right]_{\varepsilon_i}^{\varepsilon_{i+1}} + \\ &+ \left[2T_{ji}^2 \exp\left(-\frac{\varepsilon}{T_{ji}}\right)\right]_{\varepsilon_i}^{\varepsilon_{i+1}} \Bigg\},\end{aligned} \tag{4.11}$$

where N_{ji} and T_{ji} are the fitting density and temperature for either the plasma bulk or the HE tail (subscript "j") for the corresponding energy bin (subscript "i"). Such a fit has been done for the plasma bulk first, by imposing a limit on the cut-off energy between bulk and HE tail (= 50 keV). After obtaining the fit, the data points corresponding to the bulk are removed up to the cutoff energy ε_{cut}, where the tolerance between the data points and the bulk fit exceeds $\gtrsim 99\%$. The rest of the points are fit as the HE tail. The overall fit is the sum of both profiles, as shown in Fig. 4.8a.

The main features of the HE tail can therefore be determined by the fitting parameters, therefore finding the average *HE temperature* T_{HE} and the *HE energy flux* Φ_{HE}, given by the sum of the energy fluxes $\Phi_{HE,i}$ belonging to the HE tail. From the HE energy flux, it is possible to extract an average *HE conversion fraction*, which is the ratio between Φ_{HE} and I_{laser}: $\mathrm{f}_{HE} \equiv \Phi_{HE}/I_{laser}$. This is an important quantity widely used in literature [33, 53, 57, 133, 160] for describing the laser energy absorbed by the HEs, factoring in the system's energy balance. For these laser plasma conditions, the fitting parameters were for the bulk $N_{bulk} \simeq 8.02 \times 10^{20}$ cm^{-3} and $T_{bulk} \simeq 4.24$ keV, about $\simeq 5\%$ of difference from the electron plasma temperature specified, $T_e = 4$ keV. For the HE tail, these were $N_{HE} \simeq 4.57 \times 10^{17}$ cm^{-3}, with a HE temperature of $T_{HE} \simeq 70.19$ keV, for a resulting HE flux of $\Phi_{HE} \simeq 1.25 \times 10^{14}$ W/cm^2 and an overall HE fraction of $\mathrm{f}_{HE} \simeq 19.5\%$ in quasi-stationary conditions.

Figure 4.8b shows the electron energy flux data (and fits) for the flux virtual diagnostic in the forward (red curve) and the backward (orange curve) direction (i.e., the flux collecting at the $+x$ and $-x$ boundary, respectively), as well as the total energy flux (i.e. collected at both $\pm x$ and $\pm y$), in black. The forward HE data are the same as in Fig. 4.8a, while the ones in the backward direction are a smaller HE temperature $T_{HE} \simeq 50.61$ keV, a flux of $\Phi_{HE} \simeq 2.2 \times 10^{13}$ W/cm^2, and a significantly smaller HE fraction, at $\mathrm{f}_{HE} \simeq 3.42\%$. The total HE quantities are in contrast similar to the forward one, with $T_{HE} \simeq 68.1$ keV, $\Phi_{HE} \simeq 1.49 \times 10^{14}$ W/cm^2 and $\mathrm{f}_{HE} \simeq 23.14\%$. The difference between the sum of forward and backward HE fraction and the total HE one is given by the electron flux collected at the transversal boundaries ($\pm y$). Therefore, the most significant HE flux, the one emitted in the forward direction, constitutes the majority of the produced HE population, and it can be used for the purpose of the parameter scan as the most significant HE energy diagnostic, due to the HE emission towards the target being the most important for ICF implosions.

4.2.4 HE emission: Velocity distribution function and angular emission

The HE flux direction of emission is investigated through the *Velocity Distribution Function (VDF)* collected by the HPE module (Fig. 4.9). It is normalized so that the integral over relativistic momentum is one, $\int mv\ f_{VDF}(v)\ dv = 1$ (therefore in $[\mathrm{g} \times (\mathrm{m/s})]^{-1}$).

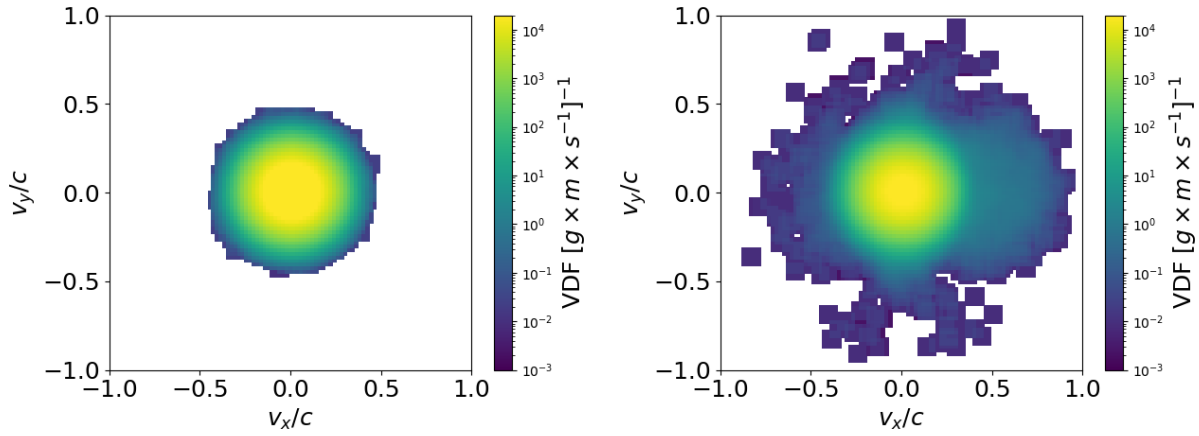

Figure 4.9: Evolution of the average electron VDF in quasi-stationary conditions as a function of the velocity components normalized to the speed of light c, in a) the presence and b) absence of laser-plasma instabilities.

The VDF is plot in velocity-space (normalized to the speed of light c) in absence of laser-plasma instabilities in Fig 4.9a. It has the shape of a Maxwell-Boltzmann distribution in two dimensions, characterized by isotropic emission in the velocity space, verifying the assumption for the plasma bulk of the electron population. The distribution starts from $(v_x/c, v_y/c) = (0, 0)$ and ends at $(v_x/c, v_y/c) \simeq (\pm 0.5, \pm 0.5)$, corresponding to an energy of $T_e \simeq 214$ keV, which corresponds to the tail of the bulk plasma.

Fig. 4.9b shows the effects of the laser-plasma instabilities (TPD, LDI) on the VDF. The Maxwellian shape of the bulk plasma is conserved, but there is a wider spread in the velocity space domain. A significant region of forward emitted particles, reaching energies up to $T_e \simeq 1.2$ MeV at low statistic, and more reasonably ($\simeq 10^1 - 10^2$ [g(m/s)]$^{-1}$) at energies in the range of $T_e \simeq 10^2$ keV. There is an expansion in the backward direction as well, but it is not as significant as the forward one, and the same can be said for transverse emission. We therefore conclude that the majority of the HE emission is in the forward direction, confirming the energy spectrum analysis in the previous section.

Moreover, the emission angle can be estimated from Fig. 4.9b. Assuming a cut-off energy of 50 keV (i.e. $(v_x^2 + v_y^2)^{1/2/c} \simeq 0.3$), the estimated angle of emission at this point is between $\alpha_{end-bulk} \simeq (-65°, +65°)$, while for high energies this angle becomes lower, at about $\alpha_{HE} \simeq (-30°, +30°)$. Moreover, upon changing to different laser plasma conditions, the angle of emission remains mostly unchanged.

4.2.5 Particle trajectories

Another way to observe features of electron emission, as well as their acceleration, is through the analysis of the individual particle trajectories. In these laser-plasma conditions, the individual trajectories of a sample population have been recorded by the particle tracker in the HPE module. A sample of 4000 virtual particles are recorded out of 10^6 injected. Out of there, only a few particles that reached HE energies (~ 20) are recorded. Both the positions and the trajectories of the chosen electrons are recorded at each time step, significantly extending the computation time. Therefore, this simulation has been used as representation of the simulations in the whole parameter scan.

Fig. 4.10 shows the particle behavior for the population of electrons that ends their trajectory at $\varepsilon \simeq 25$ keV. The plots of Figs. 4.10a and 4.10b record the particles' trajectories in real space (normalized to the laser wave number k_0) for the forward and backward emission. Due to their

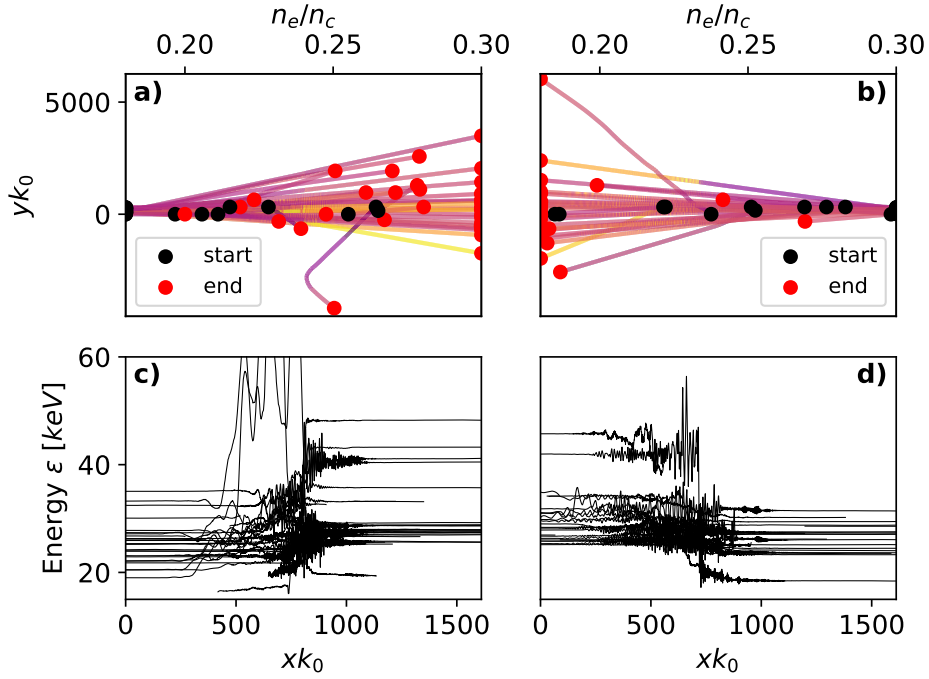

Figure 4.10: Electron trajectories with final energies at the end of the bulk region ($\simeq$ 25 keV) in a) the forward and b) the backward direction. The black points signify the starting point of the trajectories, and the red point its ending. The energy of each particle is the color of the trajectory, from low energies (darker) to high ones (brighter). The energy acquisition along the x axis for each particle has also been recorded, in c) the forward and d) the backward direction.

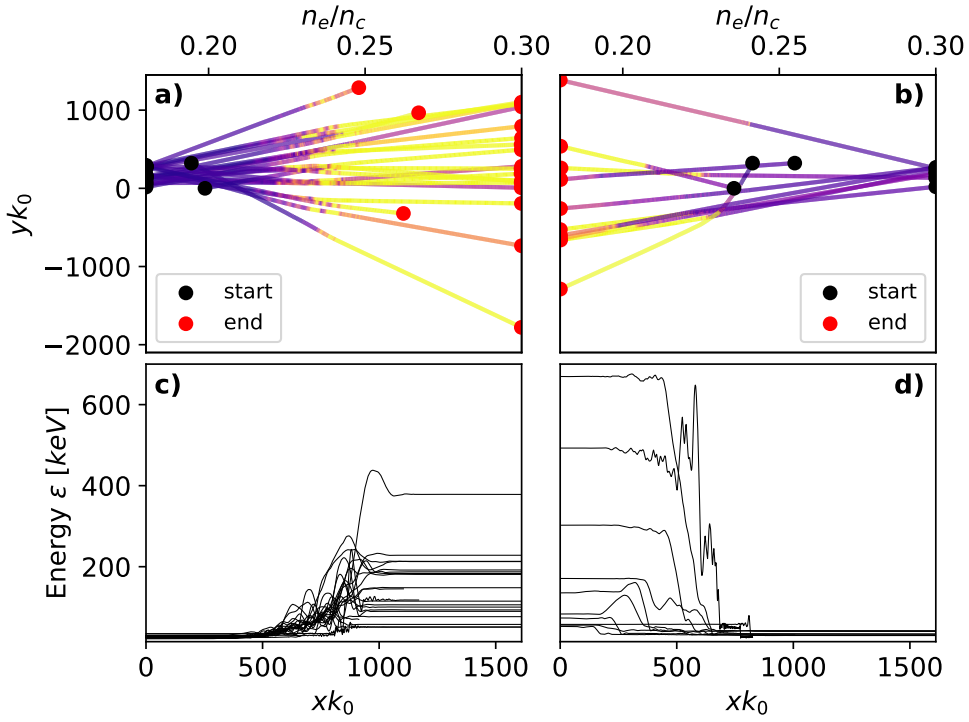

Figure 4.11: Electron trajectories reaching HE energies (beyond 50 keV) in a) the forward and b) the backward direction. The plots' representation is identical to Fig. 4.10. The same applies for the energy acquisition along the x axis, in both c) the forward and d) the backward direction.

trajectories crossing the periodic boundary conditions, the particles in these plots propagate in the plasma beyond the initial simulation boundaries in the y direction. Both directions of emission have a similar number of particles, emitted in a cone in agreement with the VDF (Fig. 4.9b). The particle trajectories appear to be almost unaffected, with the greatest deviations happening in the region where the EPW field is strongest, in the region of quarter critical density. Moreover, while the majority of particles do not acquire much energy (as can be seen from the lines' change from darker to brighter colors), some show clear signs of acceleration. The cone of emission can be estimated to be $\alpha_{end-bulk} \simeq \tan^{-1}(yk_0/xk_0) \simeq 65°$ at its maximum (neglecting the few particles undergoing strong deviations), coherent with the VDF data in the previous section. Fig. 4.10c and 4.10d show the energy acquisition of the particle along the x direction in the forward and backward direction, respectively. It can be noticed that the particles propagate with almost no change in energy until they reach the region around $xk_0 \simeq 450$ up to $xk_0 \simeq 950$, where there is EPW field activity. After a period of oscillatory behavior, the particle ends its trajectory with an energy higher than before, therefore indicating an energy transfer from the EPWs in the region to the particles. The most notable feature is that all the particles in these plots have a starting energy in the interval of $20 - 35$ keV, a high value compared to the rest of the Maxwell-Boltzmann distribution of the bulk plasma. Conversely, we registered no particle below this interval that acquired energy up to ~ 25 keV. Moreover, particles in the range of $20 - 35$ keV correspond to a velocity range of $v_e \simeq 0.28\text{c} - 0.37\text{c}$. The EPW phase velocity corresponding to the Landau cut-off $k_{EPW}\lambda_{De} \simeq 0.3$, for a 4 keV plasma, reaches similar values at $v_{ph,c.o.} \simeq 0.296\text{c}$. Therefore, we infer that particles in the $20 - 35$ keV energy range are a good match with the EPW phase velocity close to the Landau cut-off, with a stronger resonance and therefore energy transfer (and strong Landau damping of these EPWs as a consequence) from the EPWs to the particles.

We now analyze the particle trajectories with final energies belonging to the HE tail region with $\varepsilon \geq 50$ keV (Figs. 4.11a and 4.11. The trajectories share some features with the ones shown previously to reach $\varepsilon \sim 25$ keV (i.e. their trajectories are almost unchanged until they cross the resonance region). However, the backwards trajectories are notably less in number than the forward ones, in accordance with the VDF plot of section 4.2.4. Moreover, their energy acquisition is more pronounced, as shown by the greater trajectory color gradient. Their cone of emission is consistent with the VDF results, with an angle of emission in the range of $\alpha_{HE} \simeq \pm 50°$ at maximum and $\alpha_{HE} \simeq \pm 30°$ on average. it can be clearly seen that the region where the forward emitted particles acquire energy is close to the quarter critical region, while for the backwards emitted ones, the region is wider, from $xk_0 \simeq 250$ to $xk_0 \simeq 750$, and towards lower densities. Moreover, the acceleration occurs in a wide region in space, a feature not clearly visible at lower energies. In the backwards direction (Fig. 4.11d), the HEs acquire energy in a wider region and at lower densities, which we assume is due to resonance with EPWs propagating at low densities, characterized by lower phase velocities ($\omega/k \sim \omega/(k_0\sqrt{\epsilon})$). The energy acquisition along the forward x direction (Fig. 4.11c) show a similar behavior, with an acceleration around $n_c/4$ ($xk_0 \simeq 500 - 1000$) and final energies of the order of hundreds of keV. This is also evidenced in Fig. 4.11a in the trajectory color gradient. We infer that this is caused by *staged acceleration* [152], where the particles are accelerated by successive resonance interactions with waves at progressively higher phase velocities (which increase with the plasma density). Similarly to Fig. 4.10, the electrons that resonate with the EPWs possess initial energies in the range of $20 - 35$ keV, further reinforcing the hypothesis that particles below this range do not interact often with the waves.

4.2.6 Energy balance

We now consider the overall energy balance in the simulations through the LPSE energy metric.

The energy metrics of each simulation are recorded by LPSE through the field solver. These are integrated in space to get a spatially average profile evolving in time. Fig. 4.12 shows the

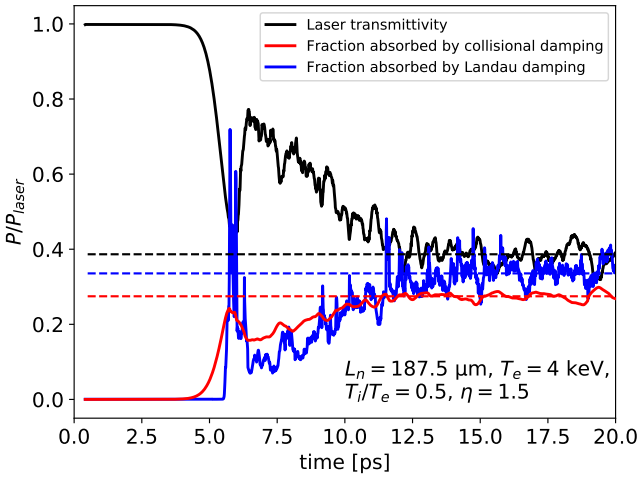

Figure 4.12: Time evolution of the laser transmittivity (black curve), EPW power absorbed by Landau damping (blue curve) and EPW power absorbed by collisional damping (red curve), normalized to the laser input power. The corresponding dashed lines belong to the time averaged values in quasi-stationary conditions (after t = 12.5 ps for this simulation).

power that leaves the simulation region (and therefore escapes the quarter critical region) as a black curve, normalized to the laser power injected into the system, measuring the *laser transmission* (or *transmittivity*) evolution in time. Fig. 4.12 also shows the power fraction absorbed by the plasma through EPW collisional damping and Landau damping. These constitute the totality of the absorption, since the inverse bremsstrahlung collision coefficient has been set to zero.

At a time t $\simeq$ 3.75 ps, TPD grows significantly, and the laser transmission starts decreasing. At the same time the EPW power absorbed by collisional damping starts increasing. After t $\simeq$ 5 ps, the electrons are injected into the plasma. Therefore, after a short delay due to their propagation, the EPW power absorbed by Landau damping also increases, characterized by a period of strong turbulence. The steady-state regime is reached around t $\simeq$ 12 ps. The average level of these power fractions across the quasi-stationary regime is given by the dashed lines in Fig. 4.12. The laser transmission settles at $P_{out}^{laser}/P_{in}^{laser} \simeq 38.56$ %, while the EPW power absorbed by collisional damping at $P_{CD}^{EPW}/P_{in}^{laser} \simeq 27.25$ % (consistent with previous work at similar conditions [28]) and the Landau one at $P_{LD}^{EPW}/P_{in}^{laser} \simeq 33.32$ % of the total input laser power. In particular, $P_{LD}^{EPW}/P_{in}^{laser}$ can be split into the average HE conversion fraction $f_{HE}^{tot} \simeq 23.14\%$ discussed in section 4.2.3, and a remaining $\simeq 9\%$ belonging to particles that did not reach HE energies above $\simeq$ 50 keV and therefore are not counted as HEs.

4.3 TPD scaling analysis

We now focus on the parameter scan of simulations of 2D TPD The laser-plasma conditions are the ones in Table 4.2. In particular, the laser intensity ($I_{laser} \simeq 10^{14} - 10^{15}$ W/cm^2) and the density scale length ($L_n = 125 - 250$ μm) have been chosen to be in similar conditions to the OMEGA laser facility [57].

4.3.1 HE quantities scaling

The HE results obtained through the energy spectrum fitting have been collected in a set of plots and tabulated. The HE quantities in these plots have been taken in quasi-stationary conditions averaging from t = (17.5, 17.5, 15, 12.5, 10) to 20 ps for the corresponding $\eta = (1, 1.2, 1.25, 1.5, 2)$.

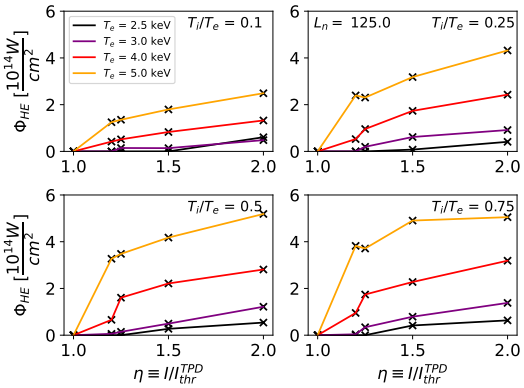

(a) Φ_{HE}, $L_n = 125$ μm

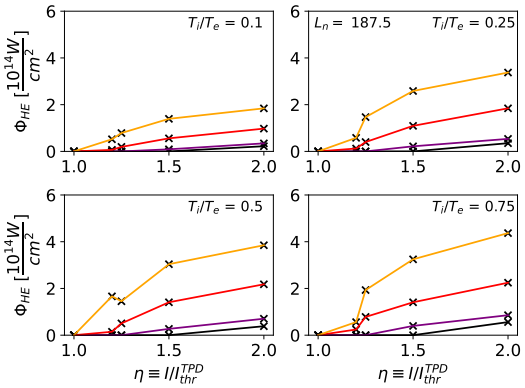

(b) Φ_{HE}, $L_n = 187.5$ μm

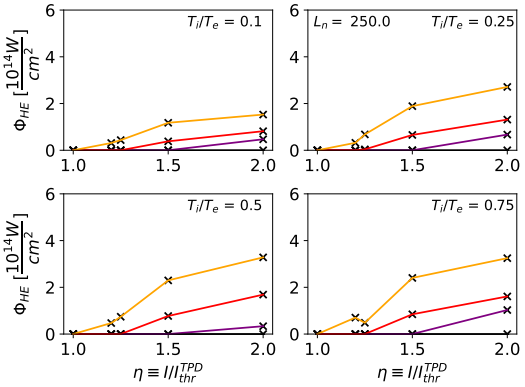

(c) Φ_{HE}, $L_n = 250$ μm

Figure 4.13: Parameter scan of the HE energy flux for 2D TPD with LDI, cavitation and pump depletion. The different curves (from black to orange) refer to increasingly high electron plasma temperature (T_e) values, while each different subplot within each figure corresponds to a different T_i/T_e ratio.

The scaling involves HE quantities taken in the forward direction only.

The results of this scaling are shown in Fig. 4.13 for the HE energy flux Φ_{HE}, and Fig. 4.14 for both the HE conversion fraction (f_{HE}) and the average HE temperature T_{HE}, as a function of the laser drive strength η.

The HE flux across the scan reaches values in the range of $\Phi_{HE} \simeq (0.5 - 5.5) \times 10^{14}$ W/cm^2, as shown in Fig. 4.13. After overcoming the TPD threshold, the HE flux grows with the drive strength η. Each curve within a single subplot increases its values with increasing T_e, and the same occurs for the same curve evaluated for increasing T_i/T_e. The opposite behavior is observed for the density scale length, with Φ_{HE} becoming lower for higher L_n. Moreover, the low statistic of the HE tail at high L_n artificially shifts the appearance of the instability towards higher drive strength values.

The HE conversion fraction (Figs. 4.14a, 4.14c and 4.14e) is a product of the flux through the relation $f_{HE} = \sum_i \Phi_{HE}(\varepsilon_i)/I_{laser}$, where ε_i is the i-th energy bin in the spectrum. The normalization allows to understand the fraction of laser energy absorbed by the HE production, as well as readily compare it with other energy fractions. After crossing the laser threshold, f_{HE} reaches a stable "plateau". There is an increase in T_e similar to Φ_{HE}, and the same can be said for T_i/T_e. Moreover, the HE fraction appears to remain almost unchanged for increasing L_n. It reaches values, in these laser-plasma conditions, up to 40%.

Finally, the average HE temperature T_{HE} (Figs. 4.14b, 4.14d and 4.14f) has a more noisy behavior, with high values for low η, and decreasing for high η. The behavior of T_{HE} for

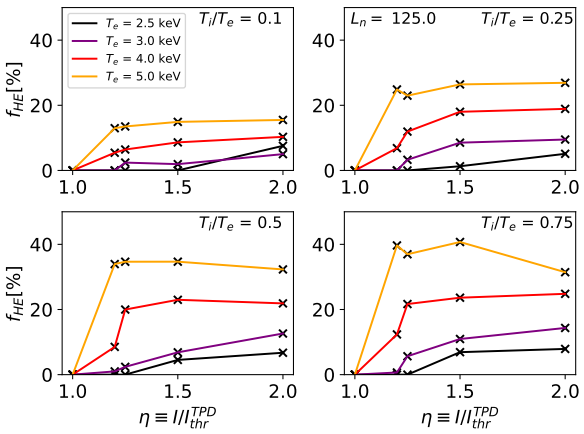

(a) f_{HE}, $L_n = 125$ μm

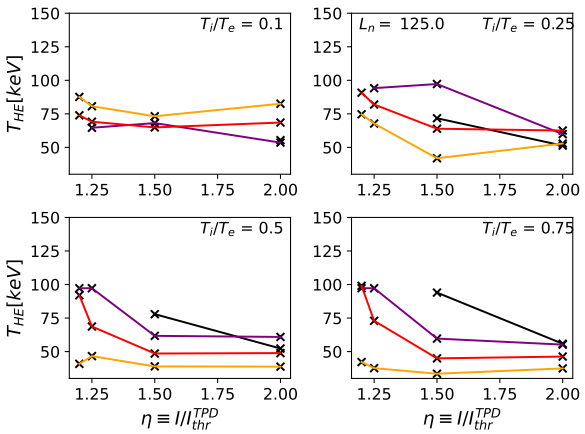

(b) T_{HE}, $L_n = 125$ μm

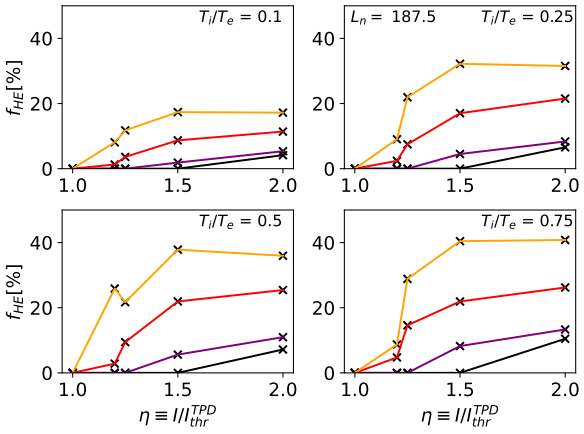

(c) f_{HE}, $L_n = 187.5$ μm

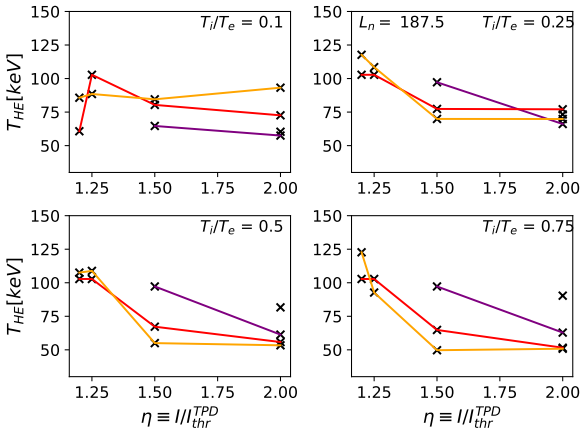

(d) T_{HE}, $L_n = 187.5$ μm

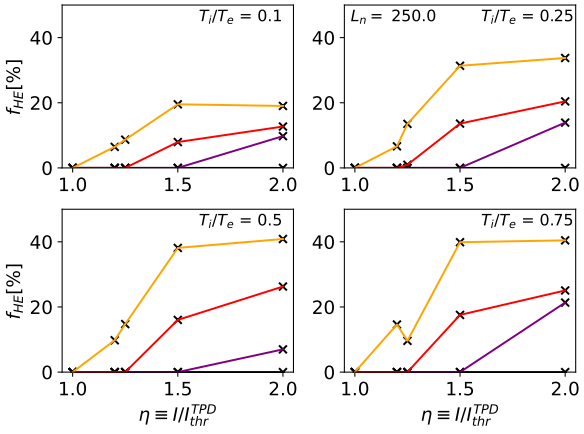

(e) f_{HE}, $L_n = 250$ μm

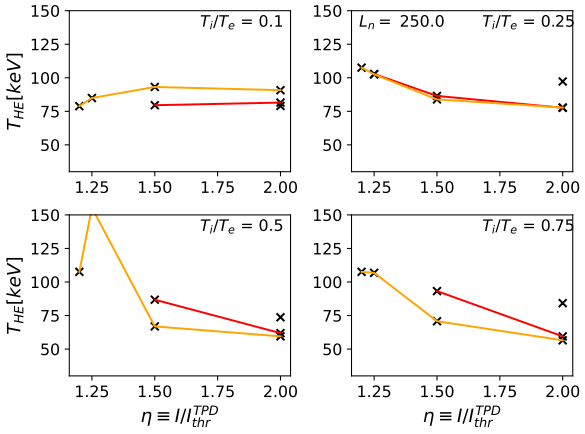

(f) T_{HE}, $L_n = 250$ μm

Figure 4.14: Parameter scan of the HE a)-c)-e) conversion fraction and b)-d)-f) average temperature scaling for 2D TPD with LDI, cavitation and pump depletion. The different curves (from black to orange) refer to increasingly high electron plasma temperature (T_e) values, while each different subplot within each figure corresponds to a different T_i/T_e ratio.

different values of T_e shows no clear trend. However, an observation that can be done is the energy interval in which these simulations fall, especially at high drive strength values, where the HE tail statistic is more significant. With this, the HE average temperature falls into the range of $T_{HE} = 50 - 100$ keV, while for $L_n = 125$ μm it is in the range of $T_{HE} = 35 - 75$ keV.

The angular emission for the hot electrons, as said in section 4.2.4 and 4.2.5, remains in a cone at $\alpha_{HE} \simeq \pm 30^\circ$ across the entire parameter scan. As far as the average laser transmission is concerned, the values range from $T \simeq [30\% - 60\%]$, while the EPW power fraction absorbed by collisional damping ranges within $P_{coll}^{EPW} \simeq [15\% - 35\%]$.

We must note that one of the main assumptions of the scaling analysis is taking the HE quantities in quasi-stationary conditions, when there is equilibrium between the instabilities. However, a number of simulations at low drive strength η, low electron plasma temperature T_e and high density scale length L_n did not manage to reach quasi-stationary conditions. This is because the instability takes a time $\propto \gamma_0^{-1}$ to develop, such that simulation at low γ_0 requires more than 20 ps as simulation time. Since γ_0 depends on the electron oscillation velocity v_{osc} (whose maximum is given by Eq. 2.181), which in turn depends on the drive strength η, the TPD development time depends on both I_{laser} and I_{thr}^{TPD}. In particular, I_{thr}^{TPD} is a function of T_e and L_n^{-1} (Eq. 2.188); therefore changes in the growth rate due to these two quantities is expected.

4.3.2 Scaling analysis: drive strength parameter scan

We now analyze the physical behavior of HE scaling analysis as a function of the laser drive strength η. In particular, we will analyze the energy metrics, such as laser fraction transmitted and absorbed, in order to infer general behaviors for the plasma instabilities at play. We also investigate the IAW and cavitation activity through the low-frequency electron density perturbation $\delta n_l / n_c$ and the caviton correlator $C_{n,|E|^2}$, to observe the role of turbulence in the system.

4.3.2.1 Saturation of laser transmission

A preliminary observation of the *laser transmittivity* (i.e. the ratio between the laser power exiting the simulation and the injected laser power $P_{laser}^{out}/P_{laser}^{in}$) is made as a function of η.

Fig. 4.15 shows the laser transmission evolution in time as a function of different physical processes considered within the simulation. Particularly, the parameter scan for the drive strength from low η (black) to high η (yellow) illustrated in Figs. 4.15g and 4.15h shows that a saturation in laser transmittivity is reached at a level of $\simeq 25\% - 40\%$ for the $L_n = 125.0$ μm case, and $\simeq 40\% - 50\%$ for the $L_n = 187.5$ μm one.

In order to investigate this saturation, we performed the same parameter scan in η in different conditions. Particularly, the main physics processes are progressively added in each of the scans, in order to observe the effects on the laser transmission given by each of them. [1]

Figs. 4.15a and 4.15b show simulations with laser pump depletion (PD) only and without EPW Landau damping. At initial times, the TPD instability growth is almost negligible, therefore allowing the entirety of the laser energy to advect outside the simulation region (transmittivity of $\simeq 100\%$). After the TPD linear growth regime sets in, the EPW field grows exponentially, and therefore the laser transmission sharply decreases. After a period of few picoseconds of linear growth, the laser energy depletes and the EPW field stops growing, leading to an oscillatory behavior (mainly visible in Fig. 4.15a, $\eta = 1.2 - 1.25$), that stabilizes towards a saturation level. This is *laser pump depletion*. The laser transmission reaches lower saturation levels for increasing η due to the stronger TPD activity (through γ_{TPD}) for higher laser intensities, which

[1] Moreover, no simulation at $\eta = 2.5$ has been performed because high-η simulations present numerical instabilities tied to the CFL condition, therefore having to resort to a smaller time step and increasing the computation time to significant levels

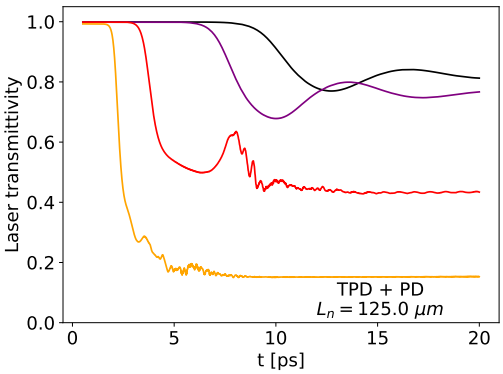

(a) $L_n = 125\ \mu$m, TPD+PD

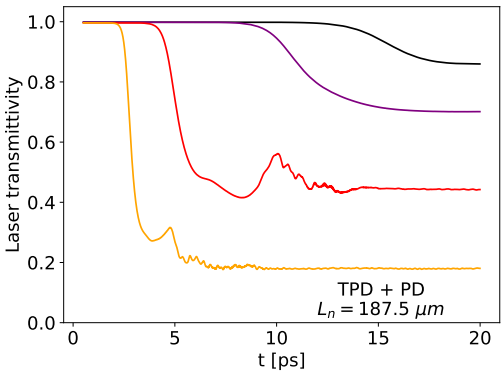

(b) $L_n = 187.5\ \mu$m, TPD+PD

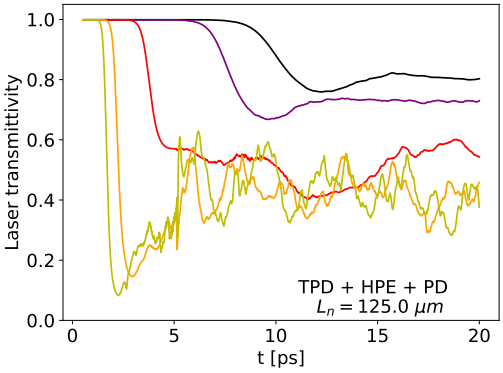

(c) $L_n = 125\ \mu$m, TPD+HPE+PD

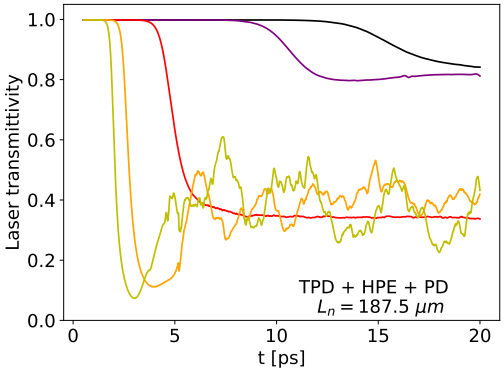

(d) $L_n = 187.5\ \mu$m, TPD+HPE+PD

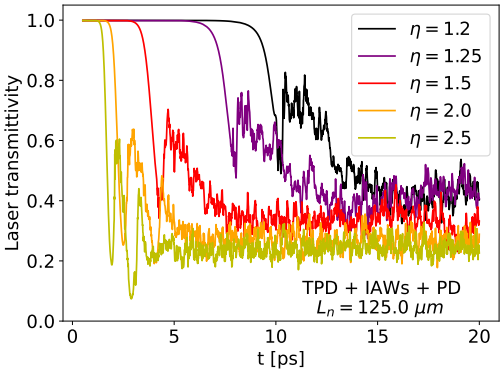

(e) $L_n = 125\ \mu$m, TPD+IAWs+PD

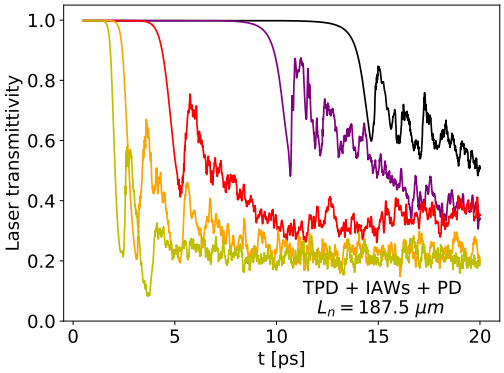

(f) $L_n = 187.5\ \mu$m, TPD+IAWs+PD

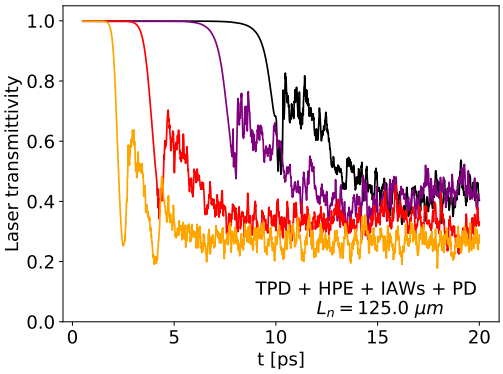

(g) $L_n = 125\ \mu$m, TPD+HPE+IAWs+PD

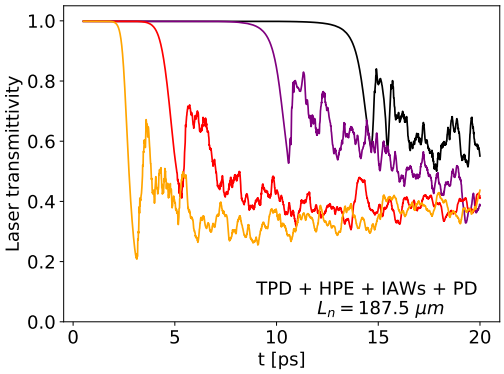

(h) $L_n = 187.5\ \mu$m, TPD+HPE+IAWs+PD

Figure 4.15: Laser transmission as a function of time for $T_e = 5$ keV, $T_i/T_e = 0.5$ and $L_n = 125$ and 187.5 μm. The color scale is for different drive strengths η.

leads to higher EPW fields and therefore a higher EPW global energy, which leads to higher energies absorbed by EPW collisional damping even though the collisional damping rate ν_{ei} (Eq. 2.35b) does not depend on η. In such conditions, the laser transmission at saturation reaches values below $\simeq 20\%$. There is no significant change to the saturation level between $L_n = 125$ μm and $L_n = 187.5$ μm. However, the instability develops at later times for increasing L_n, because I_{thr}^{TPD} is lower for longer L_n when η is constant.

We now include a time-evolving Landau damping coefficient in the Langmuir Wave equation (Eq. 4.3) computed from the HPE solver. After the initial period of linear growth, where the laser transmission sharply decreases from 100%, the signal becomes very noisy after $t \simeq 5$ ps, the time at which there is particle injection. The simulations at $\eta = 2.0 - 2.5$ for both $L_n = 125$ and 187.5 μm have a noisy signal even before this time, because of the Landau damping computed by the code previous to injection. The transmission signal becomes noisier at higher values of η, which corresponds to a higher energy absorbed by Landau damping, and therefore a higher HE generation. The simulations at the highest η (2.0 and 2.5) reach a similar value in both laser transmission and power absorbed by EPW Landau damping, suggesting a lower limit in laser transmission given by EPW Landau damping and HE generation. Finally, it can be seen that the simulations at low $\eta = 1.2 - 1.25$ and $L_n = 187.5$ μm do not reach a quasi-stationary regime. Overall, the simulations at high drive strength values reach a transmission around $\simeq 40\%$.

Adding IAWs to the TPD + PD system, the transmission follows the same behavior as before, until a noisy signal occurs and a saturation level is reached. We attribute the strongly oscillatory behavior to the seeding of LDI cascade, as well as cavitation activity, resulting into a noisy, turbulent laser transmission. There are significant differences between simulations with only the HPE module and the ones which only include IAWs. Most notably, lower transmission levels are reached by introducing IAWs instead of using the HPE solver. Ar low η values the transmission reaches $\simeq 40\%$ in the $L_n = 125$ μm case. On the other hand, the high-η simulations decrease their saturation level to $\simeq 20\%$, a similar value for both the values of L_n considered. We infer that the presence of LDI cascade and cavitation/caviton activity imposes a lower limit to the transmission saturation level by saturating and restricting wave amplitudes at high η, while at low η it imposes an upper limit due to the broadening of the activity region at $n_c/4$, allowing the convective modes to grow thanks to the turbulence adding to the noise seed.

Finally, the complete system used in the scaling is shown in Figs. 4.15g and 4.15h.

4.3.2.2 Power absorbed by EPW collisional and Landau damping

Fig. 4.16a and 4.16b show the EPW collisional damping for the same η parameter scan for $L_n = 125$ and 187.5 μm. This power follows the same behavior as the EPW field growth, with more EPW power absorbed due to the higher TPD activity, and then saturating at a quasi-stationary level when there is equilibrium between TPD activity, turbulence (i.e. LDI cascade and cavitation) and depletion of the laser pump energy. With the exception of the low η simulations at $L_n = 187.5$ μm that did not reach quasi-stationary conditions, the behavior of each simulation appears to be similar. There is an absorption of EPW energy through collisional damping that is originally negligible when TPD activity is weak, only to grow exponentially in the linear growth regime, at different times due to different growth rates. Comparing the cases of TPD+PD and the TPD+HPE+IAWs+PD systems, significant differences are observed for the steady state. Particularly, while the EPWs start growing at the same times, the saturation level of the power fraction absorbed by collisional damping does not increase with η anymore, due to a stronger turbulence in the system, which increases both LDI activity and caviton formation and redistributes laser energy towards these processes. Overall, in this particular parameter scan (with T_e and T_i/T_e fixed) the power absorbed by collisional damping is in the range of $P_{coll}^{EPW}/P_{laser}^{in} \simeq (7\% - 13\%)$ for $L_n = 125$ μm, while it is between $P_{coll}^{EPW}/P_{laser}^{in} \simeq (15\% - 20\%)$ for $L_n = 187.5$ μm. While there are no significant changes for different T_e and T_i/T_e, changes to the density scale length L_n increase the saturation level reached by $P_{coll}^{EPW}/P_{laser}^{in}$, as will be

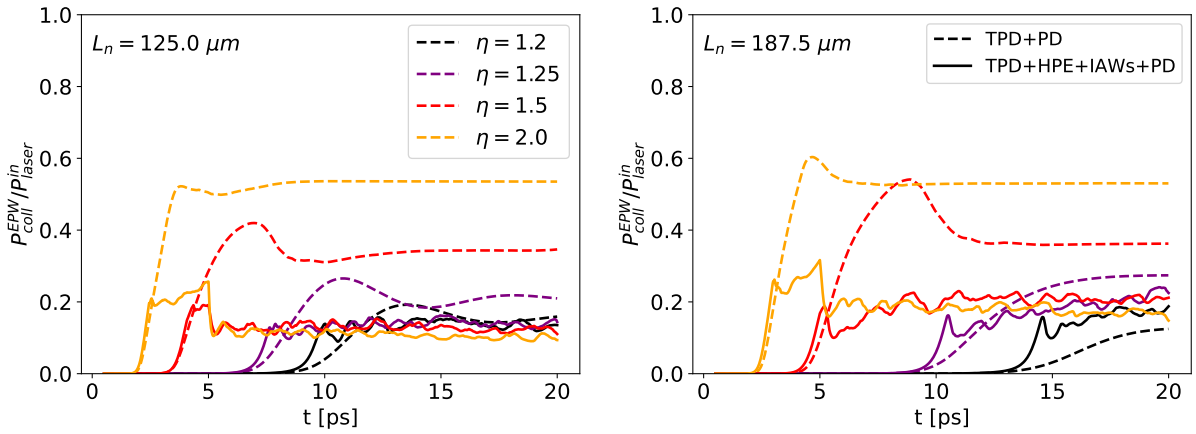

(a) (b)

Figure 4.16: EPW power absorbed by collisional damping, normalized to the laser input power P_{laser}^{in}, as a function of time, for $T_e = 5$ keV, $T_i/T_e = 0.5$ and a) $L_n = 125$ μm and b) $L_n = 187.5$ μm. The different color scale is for increasing drive strength values η (from black to yellow).

seen in the L_n parameter scan.

Finally, Fig. 4.17 illustrates the power fraction absorbed by Landau damping as a function of η. The particle population is injected by the HPE module at $t = 5$ ps; however, the code calculates the Landau damping coefficient without using a kinetic approach before those times, when the HPE module is enabled. While the Landau damping starts to be significant at different times, it grows to significantly higher values than the EPW absorption, meaning that Landau damping is the dominant damping term for the EPWs, but only by a factor of ~ 2. Moreover, there are significant differences in the parameter scan of η between simulations in absence (Figs. 4.17a and 4.17b) and presence (Figs. 4.17c and 4.17d) of IAWs, with $P_{LD}^{EPW}/P_{laser}^{in}$ increasing in value when IAWs are considered. The saturation effect generated from turbulence, regroups the range of EPW power fractions absorbed by Landau damping, in the range of $P_{LD}^{EPW}/P_{laser}^{in} \simeq (30\% - 40\%)$ for $L_n = 125$ μm and $\simeq (37\% - 46\%)$ for $L_n = 187.5$ μm (excluding the simulations at $\eta = 1.2 - 1.25$).

Therefore, there is no significant change to the overall power fractions absorbed either by collisional and Landau damping as far as a scan in laser drive strength η is concerned in the conditions of our scaling (i.e. TPD + HPE + IAWs + PD), a feature mainly due to turbulence caused by LDI cascade and cavitation, while there seems to be changes for different values in density scale length L_n. This will be discussed further in the L_n parameter scan (section 4.3.5).

4.3.2.3 IAW activity and cavitation

We now briefly consider the effect of η on the IAW and turbulence activity measured through $\delta n_l/n_c$ and the presence of cavitation in the system (Fig. 4.18).

The IAWs start appearing a few fractions of picoseconds after TPD growth, peaking at different times depending on the TPD growth rate. The maximum peak depends on the laser drive strength η. After the peak is reached, the IAW activity appears to decrease towards a saturation interval around $\delta n_l/n_c \simeq 0.002$, independently on the value of η. Correspondingly, the caviton correlator (Fig. 4.8) follows a similar trend. After the peaks of cavitation roughly coincide in time to the peaks in $\delta n_l/n_c$, the caviton correlator reaches around $\simeq 1.0$ in steady state, denoting strong cavitation activity. The IAW field grows until the low-k EPW field, generated through LDI cascade, becomes large enough for cavitons to form within the plasma. We therefore infer that the IAW generation becomes larger with η due to the stronger TPD activity for higher laser intensities. At that point, while the cavities can generate IAWs through

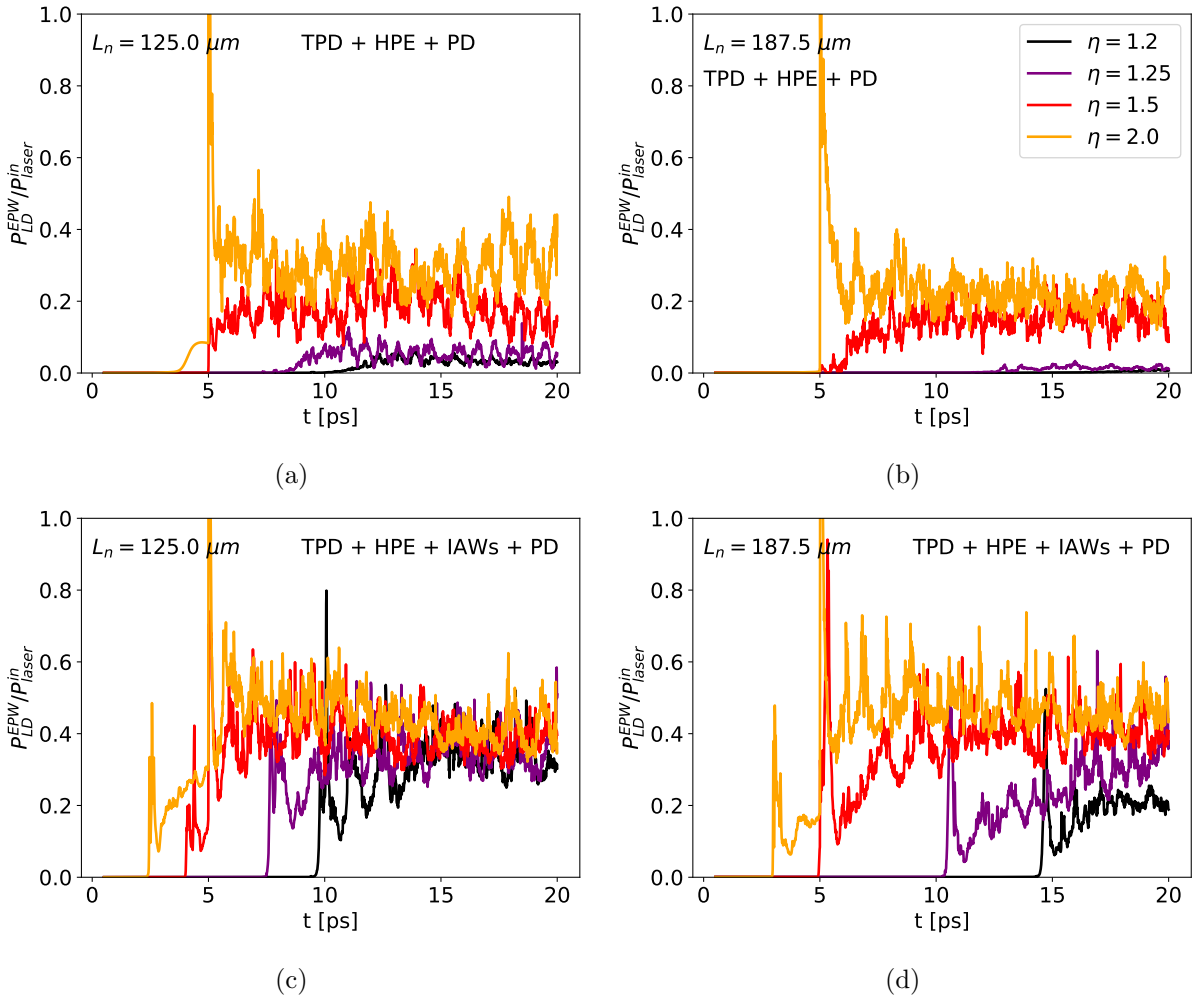

Figure 4.17: EPW power fraction absorbed by Landau damping as a function of time, for $T_e = 5$ keV, $T_i/T_e = 0.5$ and a) $L_n = 125$ μm and b) $L_n = 187.5$ μm. The different color scale is for increasing drive strength values η (from black to yellow).

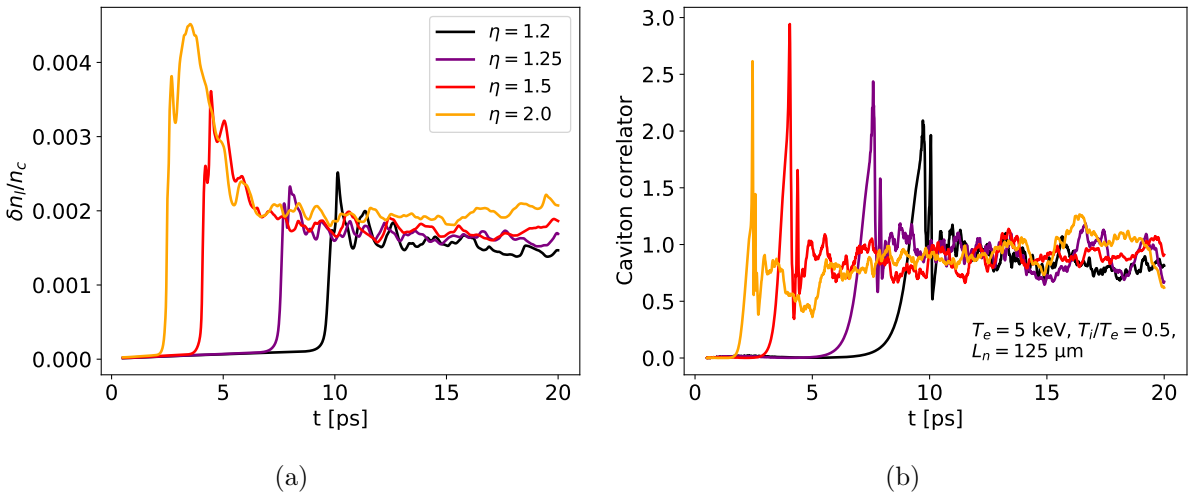

Figure 4.18: a) Low frequency electron density perturbation and b) caviton correlator behavior in time, for a parameter scan in η.

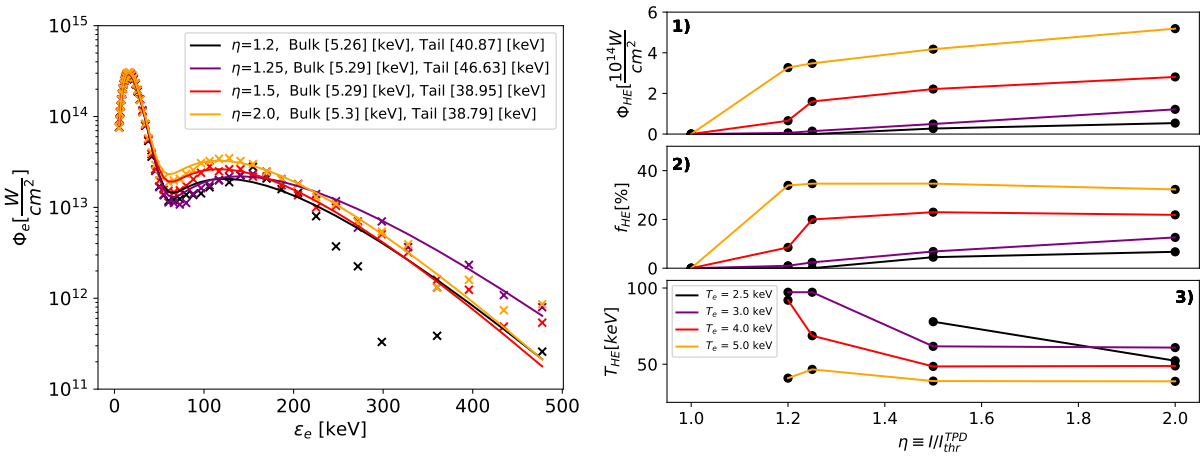

(a) (b)

Figure 4.19: a) Electron energy flux data fit for a parameter scan in η, with $T_e = 5$ keV, $T_i/T_e = 0.5$ and $L_n = 125$ μm. b) HE quantities scaling as a function of η, as well as T_e (from black to orange lines), for the hot electron b1) energy flux, b2) conversion fraction and and b3) average temperature, for $T_i/T_e = 0.5$ and $L_n = 125$ μm.

their collapse, LDI activity is reduced, resulting into a diminishing of IAWs in the system towards an equilibrium level where TPD, LDI and cavitons coexist independently from the laser drive strength applied.

4.3.2.4 Electron energy flux and hot electron quantities

The electron energy fluxes taken for the η parameter scan are given in Fig. 4.19a. These are averaged over time intervals where quasi-stationary conditions have been considered. All the simulations exhibit a population following a Maxwell-Boltzmann distribution around $T_e = 5$ keV, with a discrepancy of $\simeq 5\% - 6\%$. This is a common occurrence across the entire parameter scan for different values of T_e and T_i/T_e and may be due to fit accuracy. The energy flux reaches values up to $\Phi_e \simeq 2.5 - 3 \times 10^{14}$ W/cm^2 in this region.

The tail however presents several differences for increasing values of η. In the region between $\simeq 50 - 150$ keV, the electron energy flux increases with η, which is expected due to the stronger TPD growth for higher laser intensities, reaching values between $\Phi_e \simeq 2 - 4 \times 10^{13}$ W/cm^2. At the same time, the end part of the HE tail at energies $\gtrsim 150$ keV decreases. There is therefore an overall shift of the hot electron population towards lower energies, which will consequently increase the HE energy flux.

Fig. 4.19b shows the HE quantities derived from the electron energy flux data. A common feature is that there is no HE production at the laser intensity threshold for the instability ($\eta = 1$), which is consistent with the TPD developing time to be theoretically infinite when the laser intensity is exactly at threshold. At higher values of drive strength, starting from $\eta = 1.2 - 1.25$, the TPD instability starts growing, therefore generating LDI, cavitation and HE production.

The HE energy flux Φ_{HE} tends to increase for stronger drive strength values after the instabilities start growing. After $\eta = 1$, the HE energy flux (Fig. 4.19b1) reaches values up to $\Phi_{HE} \simeq 3.5 - 4 \times 10^{14}$ W/cm^2 at $\eta = 1.2$, for the corresponding scaling in Fig. 4.19a (orange line), and then increases for increasing drive strength up to $\Phi_{HE} \simeq 5.5 \times 10^{14}$ W/cm^2 for $\eta = 2.0$. This is consistent with the claim that a higher drive strength raises the TPD activity, which in turn drives a larger HE population.

However, the analysis of the HE fraction (Fig. 4.19b2) is almost insensible to changes in η after TPD activity starts growing, consistent with the constant EPW power absorbed by Landau

damping (Fig. 4.17c). Note that simulations at low laser drive strengths presents a very low statistic tail (e.g. $\eta = 1.2$ in Fig. 4.19a), such that T_{HE}, Φ_{HE} and f_{HE} are less well defined and fluctuate. The HE conversion fractions in the particular scaling of Fig. 4.19b range from a few percent to $f_{HE} \simeq 38\% - 40\%$. We attribute the absence of changes for η to the corresponding increase in turbulence in the system for higher η values discussed in the previous sections.

The HE average temperature (Fig. 4.19b3) decreases for increasing η, converging to a value ranging from 40 to 60 keV.

Overall, the HE generation compared to increasingly high values of drive strength η reflect the physics of the system, where for stronger laser drive strengths the TPD growth is stronger (and therefore generates more EPWs), which implies a higher population of HEs through an increase in HE energy flux Φ_{HE}. At the same time secondary processes such as LDI cascade and cavitation are more active in the presence of stronger EPW fields, either because of a higher probability to undergo a secondary decay (in the case of LDI) or because the EPW fields generate density depressions in the plasma (for cavitation). Both are supported by the $\delta n_l/n_c$, which generates a larger perturbation (and therefore stronger IAW fields) for higher η, and a caviton correlator activity reaching $\simeq 1$ in the plasma. At the same time, while the HE population increases, the fraction of laser energy converted into HEs f_{HE} almost does not change after the TPD threshold is crossed, which is caused by the equilibrium between the instabilities at quasi-stationary conditions. This is supported by the EPW power fraction $P_{LD}^{EPW}/P_{laser}^{in}$ in Fig. 4.17, which remains at a similar saturation level independent of the η applied.

We can compare the results of the HE fraction behavior with previous work from H.X. Vu, D.F. DuBois et al. [53], in which a Particle In Cell (PIC) code has been used. The conditions they used ($T_e = 2$ keV, $T_i/T_e = 0.5$ and $L_n \simeq 128$ μm) are similar to some simulations within our work. However, at such parameters LPSE generates a very low statistic of HEs in the tail, that produces difficulties to perform the fit at low η. We therefore attempted to use a modified version of the scaling law proposed in [53] in different laser-plasma conditions. Assuming the scaling law of the form:

$$f_{HE} = a\Big\{1 - \exp\Big[-(\eta - \eta_{thr}^{TPD})^b\Big]\Big\}, \tag{4.12}$$

where a and b are free parameters, and η_{thr}^{TPD} is the laser drive strength at which LPSE starts producing a HE tail. These parameters tend to change according to the laser plasma conditions considered. In the case of $T_e = 4$ keV, $T_i/T_e = 0.5$ and $L_n = 125$ μm, the coefficients are given by $\eta_{thr}^{TPD} = 1.2$, $a = 0.354$ and $b = 0.037$, while for $T_e = 5$ keV (shown in Fig. 4.20), the scaling gives $\eta_{thr}^{TPD} = 1$, $a = 0.563$ and $b = 0.095$. Considering a drive strength of $\eta = 2$, this leads to a HE conversion fraction of $\simeq 22.3\%$ and $\simeq 35.6\%$, respectively. For [53], the coefficients in Eq. 4.12 are $a = 2.6 \times 10^{-2}$, $\eta_{thr}^{TPD} = 1$ and $b = 0.5$, leading to a $f_{HE} \simeq 16.4\%$ in the case of $\eta = 2.0$. However, [53] considers two overlapped laser beams, so that $f_{HE} \equiv \Phi_{HE}/2I_{laser}$.

4.3.3 Scaling analysis: electron temperature parameter scan

We now examine the variation of HE quantities as the function of the electron plasma temperature T_e. The methods used are similar to those used for η. The IAW activity is similar to the scan in η, with a similar behavior and quantities. The caviton correlator reaching the same quasi-stationary values signifies a similar activity as well.

4.3.3.1 Electron temperature scan: energy metrics

We first consider the effect of T_e on the laser transmittivity in time (Fig. 4.21). Similarly to the η scan, simulations at high temperatures evolve faster than the low temperature ones: an increase in T_e means a higher TPD laser intensity threshold I_{thr}^{TPD}, such that I_{laser} (and γ_{TPD}) must be increased to keep η constant. It can be seen in Figs. 4.21a, 4.21b and 4.21d that there are some simulations that do not reach quasi-stationary conditions. These are all at the low

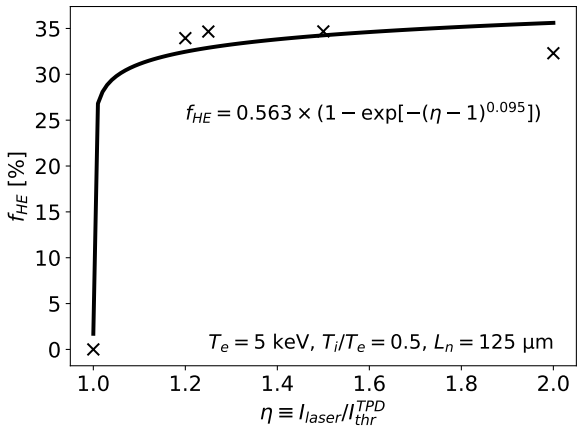

Figure 4.20: Tentative scaling law of the hot electron fraction f_{HE} as a function of η, for $T_e = 5$ keV, $T_i/T_e = 0.5$ and $L_n = 125$ μm, following the form proposed in Ref. [53].

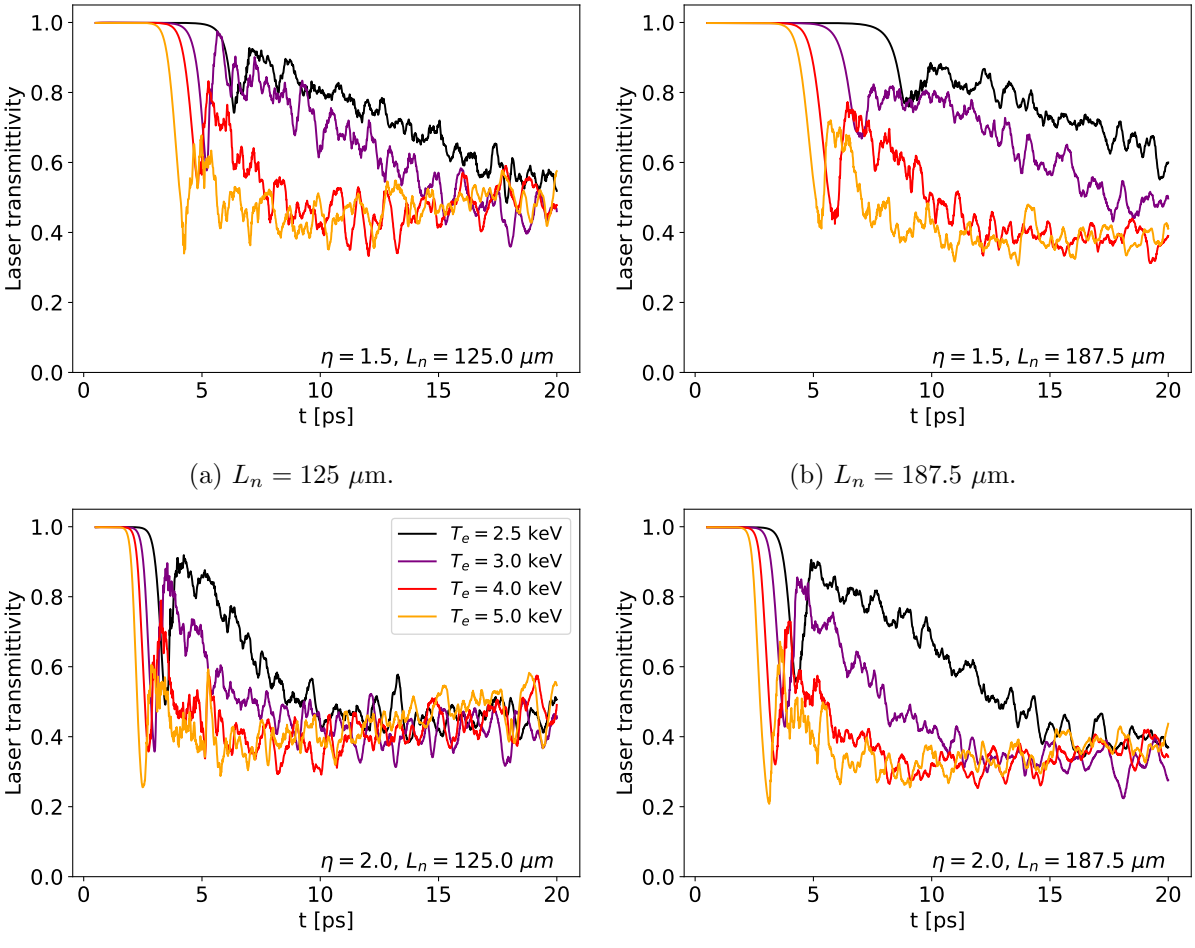

(a) $L_n = 125$ μm.

(b) $L_n = 187.5$ μm.

(c) $L_n = 125$ μm.

(d) $L_n = 187.5$ μm.

Figure 4.21: Laser transmission as a function of time for $T_i/T_e = 0.5$, for a)-c) $L_n = 125$ μm and b)-d) $L_n = 187.5$ μm, and for a)-b) $\eta = 1.5$ and c)-d) $\eta = 2.0$. The color scale is for different electron plasma temperatures T_e.

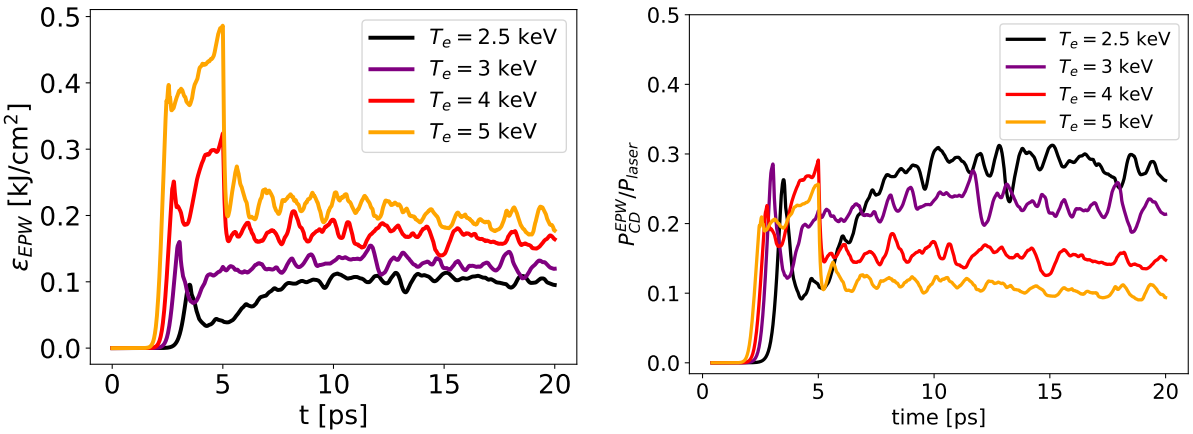

(a) (b)

Figure 4.22: a) EPW energy fluence and b) EPW power absorbed by collisional damping, normalized to the input laser power, as functions of time. The parameter scan is for the electron plasma temperature T_e (color scale), for $T_i/T_e = 0.5$, $\eta = 2.0$ and $L_n = 125.0$ μm.

temperatures of $T_e = 2.5, 3.0$ keV, as expected from the previous considerations on the growth rate, and they either do not generate hot electrons, or they generate a weak, statistically low population. At quasi-stationary conditions, the system reaches an equilibrium level once more, which is independent on the electron temperature T_e as well. Similarly to the parameter scan in η, there seems to be a regrouping of the interval of laser transmittivities reached, because of a combination of saturation from HE generation and turbulence. However, the EPW energy and power absorbed by collisional damping, as well as the power absorbed by Landau damping, will give additional motives to reaching such saturation level. The saturation levels reached are, in these conditions, similar to the ones in the η scan, with a laser transmittivity of $\simeq 40\% - 50\%$ for simulations at L_n simulations, while for $L_n = 187.5$ μm the laser transmission slightly drops at $\simeq 30\% - 40\%$, despite having less simulations that reach quasi-stationariety. Different drive strength values do not seem to affect the scan in T_e, reaching the same saturation levels.

We now consider the power absorbed within the plasma. Fig. 4.22a describes the behavior in time of the space-integrated EPW energy over the simulation domain, normalized to the transverse width. A normalization is applied over the transverse dimensions for non-3D simulations, which allows the direct comparison between energies and powers between simulations with different dimensions (notably important for L_n). For simplicity, we refer to ε_{EPW} simply as "EPW energy". The behavior of ε_{EPW} in time follows the usual linear growth regime for TPD at initial times, after which turbulence through both LDI cascade and cavitation takes place, as well as HE production after $t = 5$ ps. In the particular laser-plasma conditions of Fig. 4.22a, each simulation of the T_e scan reach quasi-stationary conditions after $t \simeq 10$ ps, with equilibrium levels of $\varepsilon_{EPW} \simeq 0.1 - 0.25$ J/cm. A noticeable feature is that there is a steady increase in EPW energy for plasmas with higher T_e, which has been consistently observed for different laser-plasma conditions as well. This increase in EPW energy with the electron plasma temperature is consistent with the rise in EPW activity in the system due to the increased growth rate.

Fig. 4.22b shows the behavior in time of $P_{coll}^{EPW}/P_{laser}^{in}$. The behavior is inverted with respect to, with less power absorbed for higher temperature plasmas, ε_{EPW} because the collision rate $\nu_{ei} \propto T_e^{-3}$. The power fractions absorbed decrease from $\simeq 30\%$ from the low electron temperature of $T_e = 2.5$ keV down to $\simeq 10\%$ to the highest temperature of our scaling, $T_e = 5$ keV.

The EPW power absorbed by Landau damping (and partially converted into hot electrons)

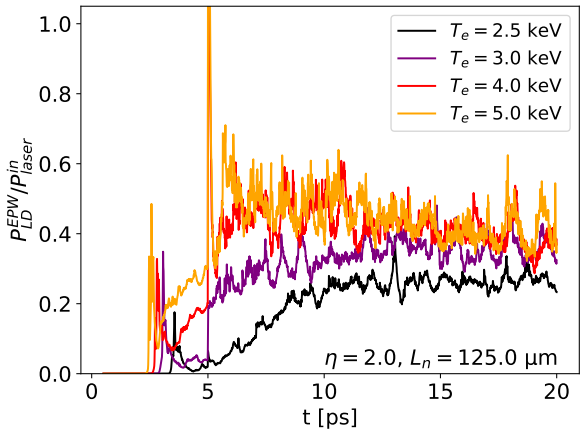

Figure 4.23: EPW power fraction absorbed by Landau damping and (partially converted into HEs) as a function of time, for a scan in electron temperature T_e, for $T_i/T_e = 0.5$, $\eta = 2.0$ and $L_n = 125$ μm.

is represented in Fig. 4.23. At the growth of TPD, the Landau damping reaches a peak, only to be decreased by IAW generation immediately afterwards. After the HPE module has injected virtual particles in the domain, the Landau damping can then be evolved in time. The average level in quasi-stationary conditions ranges from $\simeq 25\%$ to $\simeq 40\%$, and contrary to the η parameter scan, an increase in T_e shows an increase in Landau damping power. This increase is in part caused by the diminishing EPW power absorbed by collisional damping, such that the overall laser transmittivities for different values of T_e remain unchanged.

4.3.3.2 Electron energy flux and hot electron quantities

We now observe the changes in the energy spectrum (Fig. 4.25a). The electron energy flux belonging to the plasma bulk becomes higher for hotter plasmas, consistently with the higher EPW average energy in Fig. 4.22a. The energy flux in the HE tail increases significantly with the temperature, from peak fluxes of $\simeq 3 \times 10^{12}$ to $\simeq 2 \times 10^{14}$ W/cm^2 for the case in Fig. 4.25a. Similarly to the scan in η, plasmas at higher average T_e see their flux increase towards the beginning of the HE tail, while the HE population at high energies tends to become less significant. This contributes to lowering the average temperature of the tail's Maxwell-Boltzmann distribution.

The electron energy flux overall increase with T_e can be justified by:

- A stronger growth of TPD within the plasma at high electron temperatures and constant η, resulting into a larger available EPW energy in steady-state (Fig. 4.22a).
- More high energy bulk electrons available for staged acceleration by EPW modes with a phase velocity that is similar to the electrons' thermal velocity. In order to investigate the changes in the bulk maxwellian population as function of T_e only, a comparison between two simulations with the same growth rate and prescribing the same damping rates on both simulations has been carried out (Fig. 4.24a). The observed profile consistently shifts towards higher energies, with a higher HE fraction for increasing T_e.
- An insufficient LDI growth that does not compensate the TPD increase. Fig. 4.24b shows the average IAW field represented by the low-frequency electron density perturbation as a function of T_e. After a peak slightly increasing with T_e during the linear growth of the instability, the IAW signal reaches a quasi-stationary level at $|\delta n_l/n_c| \sim 0.2\%$ and is independent on T_e. We then conclude that LDI activity does not depend on the electron temperature.

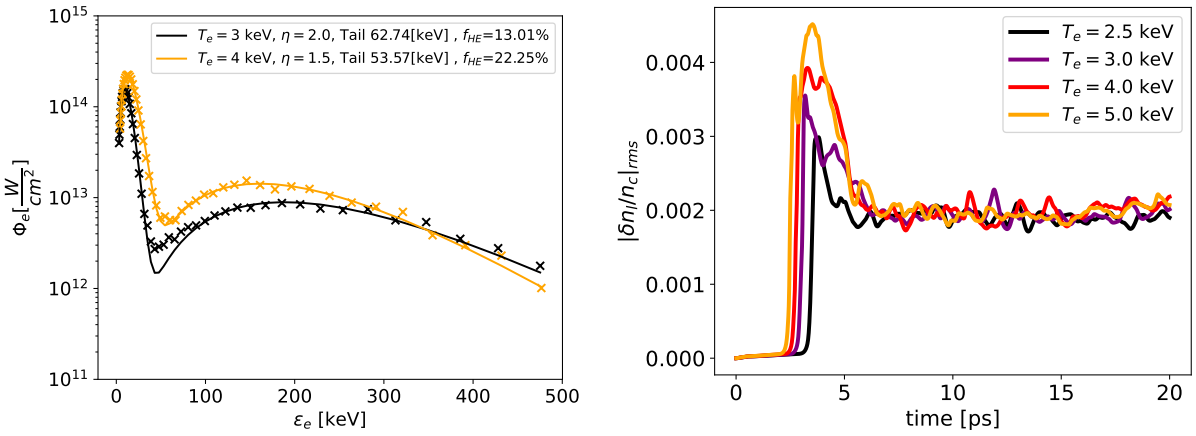

(a) (b)

Figure 4.24: a) Electron energy flux comparison between two simulations with $T_e = 3, 4$ keV and $\eta = 1.5, 2.0$ respectively. $L_n = 125$ μm and $T_i/T_e = 0.5$ have been kept constant. ν_{coll}^{EPW} and ν_{LD}^{IAW} are set to be the same value for both simulations. b) Low-frequency electron density perturbation as a function of T_e.

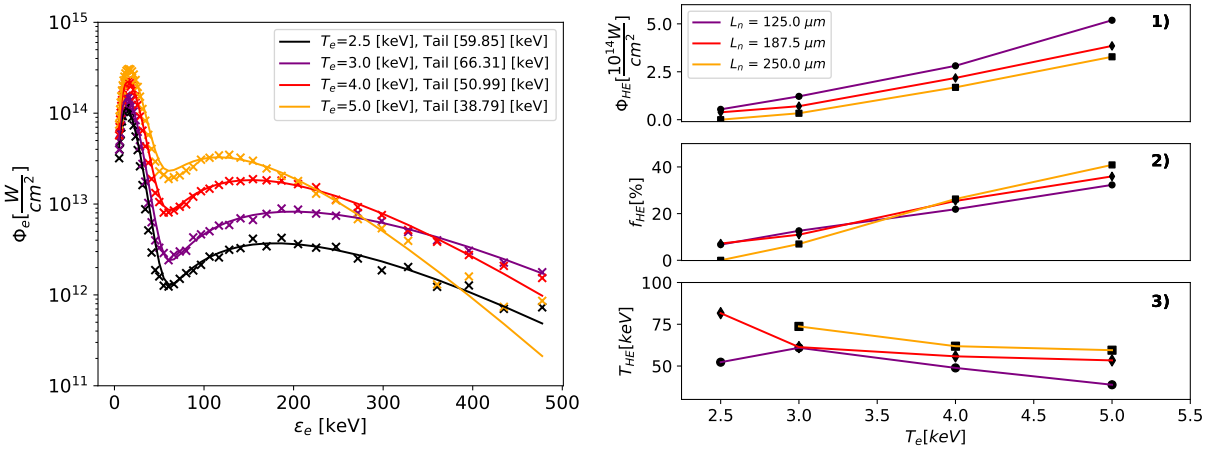

(a) (b)

Figure 4.25: a) Electron energy flux (in W/cm^2) energy spectrum for a parameter scan in electron plasma temperature T_e. b) HE scaling parameters as a function of T_e, for b1) HE energy flux, b2) HE conversion fraction and b3) HE average temperature. The different lines in b) correspond to different density sale lengths. Both figures have been taken for $T_i/T_e = 0.5$ and $\eta = 2.0$. While a) refers to the scaling for $L_n = 125.0$ μm only, b) is taken for all the L_n considered in the scaling analysis.

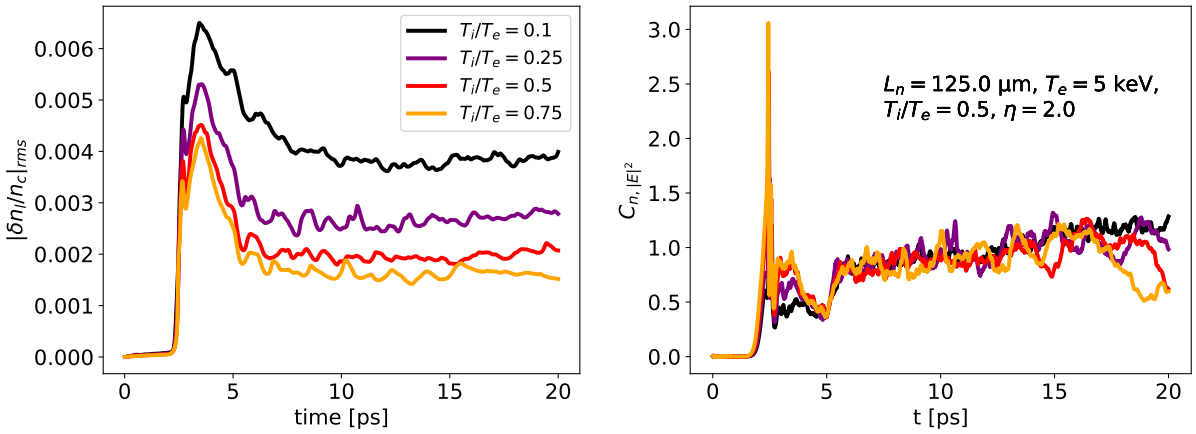

(a) (b)

Figure 4.26: a) IAW activity (through the low-frequency electron response of the plasma) and b) caviton correlator behaviors as a function of time. Both figures are for a parameter scan in T_i/T_e, at fixed $L_n = 125$ μm, $T_e = 5$ keV and $\eta = 2.0$.

Fig. 4.25b shows the increase in HE production for a scaling in T_e with $T_i/T_e = 0.5$ and $\eta = 2.0$. The different curves belong to different density scale lengths. Particularly, the HE energy flux (Fig. 4.25b1) becomes higher for increasing T_e, with an increase resembling a quadratic behavior. The maximum fluxes reached in this scaling are $\Phi_{HE} \simeq 5 \times 10^{14}$ W/cm^2 in this particular parameters and, as shown in Fig. 4.13, up to $\Phi_{HE} \simeq 5.8 \times 10^{14}$ W/cm^2 for the complete scaling analysis.

The HE conversion fraction f_{HE} (Fig. 4.25b2) increases linearly with respect to higher values of T_e. Since $f_{HE} \equiv \Phi_{HE}/I_{laser}$, this implies the HE production is greater than the increase in laser power injected, and since in this scaling $I_{laser} = \eta I_{thr}^{TPD} \propto \eta T_e$, then a quadratic increase for Φ_{HE} for T_e justifies the conversion fraction linear increase. The maximum levels of f_{HE} correspond to $\simeq 40\%$ of the laser energy entering the plasma. Hypothesizing a linear relation of the simplest form, $f_{HE} = \mathrm{a} \times T_e + \mathrm{b}$, the range of the two parameters across the whole scaling is in the range of $\mathrm{a} \sim (0.04, 0.12)$ and $\mathrm{b} \sim (-0.04, -0.22)$.

Finally, the average HE temperature in Fig. 4.25b3 verifies the observations of the energy spectrum in Fig. 4.25a, with an initial high value in HE temperature, which decreases for hotter plasmas. The values reached in quasi-stationary conditions remain confined within the range of $50 - 100$ keV.

4.3.4 Scaling analysis: ion-electron temperature ratio parameter scan

The third parameter considered in our analysis was the ion-electron temperature ratio T_i/T_e, which is mainly responsible for the secondary processes of LDI cascade and Langmuir Wave collapse.

4.3.4.1 Energy metrics, IAW activity and cavitation

The IAW activity shows significant change for different values of ion-electron temperature ratios, as illustrated in Fig. 4.26a. $\delta n_l/n_c$ reaches different saturation values, from 0.4% for $T_i/T_e = 0.1$ to $\simeq 0.15\%$ for $T_i/T_e = 0.75$ in this particular case, with a lower IAW generation for a higher ion-electron temperature ratio. This is caused by two factors. First, the IAW Landau damping increases for increasing T_i/T_e, as shown in Fig. 4.3a and 4.3b. The stronger IAW Landau damping means that LDI activity is reduced. Second, the LDI threshold increases with T_i/T_e (Eq. 2.201). In the end, a lower LDI activity implies more energy available for TPD and

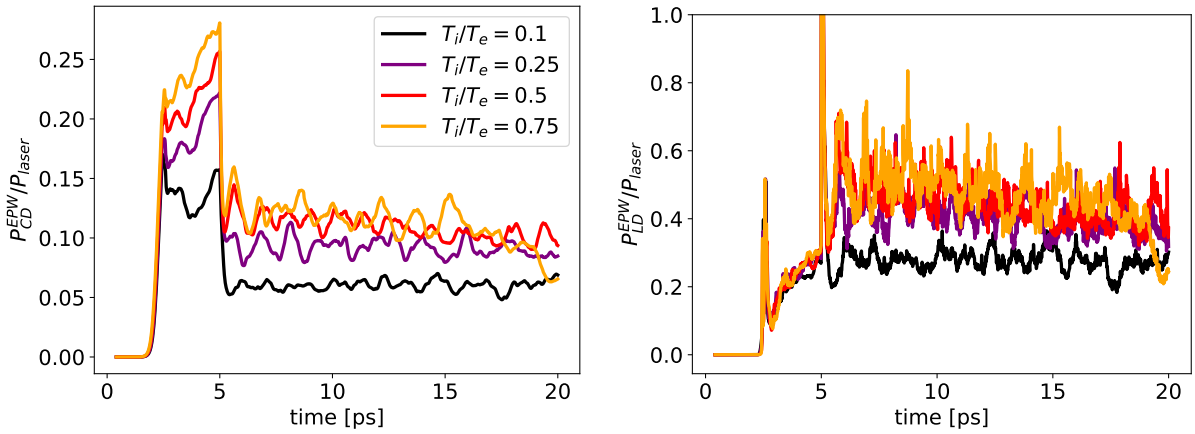

(a) (b)

Figure 4.27: a) EPW power fraction absorbed by collisional damping, b) converted into HEs by Landau damping across the simulation domain as functions of time for a parameter scan in T_i/T_e. The scan has been taken for $T_e = 5$ keV, $\eta = 2.0$ and $L_n = 125$ μm.

LW collapse / cavitation to occur, which tend to not dissipate their energy towards longer wavelengths and shorter frequencies.

Correspondingly, cavitation activity increases in the beginning of the instability and after the linear growth regime after the peak at $t \simeq 2.5$ ps, indicating, for a brief time interval, a change in LW collapse/cavitation activity. After a few picoseconds, laser pump depletion sets in (Fig. 4.26b), forcing all simulations to assume the same level of $C_{n,|E|^2}$ in quasi-stationary conditions, reaching values of strong caviton activity ($C_{n,|E|^2} \simeq 1$). We therefore conclude that, while cavitation activity is strong in all simulations in a scan in T_i/T_e, in the quasi-stationary regime there are no appreciable changes in the caviton activity. A possible explanation of this is that, while the evolution of cavities depends on both the electron and the ion temperatures through the parameter q is Eq. 3.23, the caviton growth rate in Eq. 3.26 mainly depends on the electron plasma temperature T_e.

Changes in the ion-electron temperature ratio may affect the energy balance within the system as well. Particularly, since the electron-ion collision frequency does not depend on the ion temperature, and T_e is fixed, a scan in T_i/T_e does not affect the EPW collision damping rate, and therefore it will possess the same behavior in time as the EPW energy. However, since the LDI activity is lower, more energy is available for TPD which raises the overall EPW energy, and consequently the EPW power fraction absorbed by collisional damping. These results are illustrated in Fig. 4.27a. Compared to Fig. 4.22b from the scan in T_e, these changes are more modest, with an increase from $\simeq 5\%$ to $\simeq 9\% - 10\%$. This further reinforces the assumption that modification of the ion plasma temperature (or T_i/T_e at fixed T_e) are secondary in nature compared to changes in other quantities such as T_e. The higher EPW fields due to the TPD instability favors an enhanced HE production, which are therefore more Landau damped, with a subsequent increase in power fraction converted into HEs through Landau damping (Fig. 4.27b. Values of the Landau damping at quasi-stationary conditions are larger than the ones for collisional damping by a factor of 2, reaching values from $\simeq 20\%$ to $\simeq 40\%$. The laser transmittivity reaches values starting from $\simeq 65\%$ for $T_i/T_e = 0.1$ down to $\simeq 40\%$ for $T_i/T_e = 0.75$, consistently with the overall energy conservation within the system.

4.3.4.2 Electron energy flux and HE results analysis

We now observe the changes in the electron energy spectrum for a scan in T_i/T_e at fixed $T_e = 5$ keV, $\eta = 2.0$ and $L_n = 125$ μm, as illustrated in Fig. 4.28a. The general shape of the spectrum

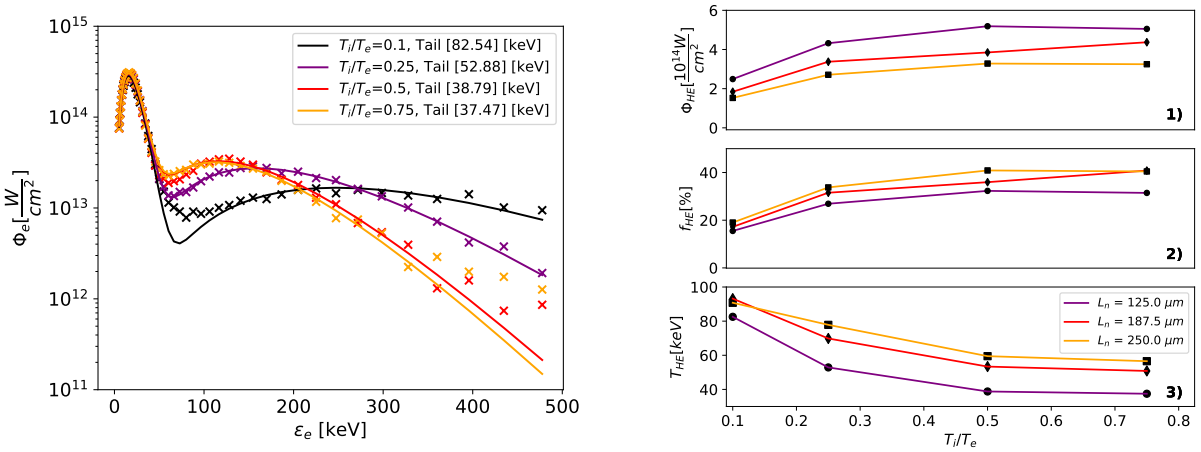

(a) (b)

Figure 4.28: a) Energy spectrum of the electron energy flux in the forward direction for $L_n = 125$ μm and b) HE quantities as function of the T_i/T_e parameter scan. All the figures have been taken for $T_e = 5$ keV and $\eta = 2.0$.

is similar to the previous scans in η and T_e. In this case, the plasma bulk is the same across the scan, with a Maxwell-Boltzmann distribution representing the plasma at an average temperature of $T_e = 5$ keV. The HE tail begins at similar energies, with no appreciable change similar to the T_e scan. The energy region corresponding to $50 - 200$ keV shows an electron population increase of the order from $\Phi_e \simeq 2 \times 10^{13}$ W/cm^2 to $\simeq 3 - 4 \times 10^{13}$ W/cm^2. In this energy interval, the peak of the Maxwell-Boltzmann distribution belonging to the HE tail shifts towards lower energies similar to the other parameter scans (see Fig. 4.19a and 4.25a) for increasingly higher T_i/T_e, indicating less electrons reach higher energies through staged acceleration.

The scaling analysis of the HE results for a parameter scan in T_i/T_e are illustrated in Fig. 4.28b, similarly to Fig. 4.25b. The HE energy flux Φ_{HE} becomes higher at higher T_i/T_e (Fig. 4.28b1). The fluxes grow with a root-like dependency from $T_i/T_e = 0.1$, and they reach a plateau at high T_i/T_e, particularly at $0.5 - 0.75$. The fluxes tend to plateau to a region around $\Phi_{HE} = 4 - 6 \times 10^{14}$ W/cm^2, the closer T_i is to T_e. This is consistent with the electron flux behavior of Fig. 4.28a, where a higher T_i/T_e allows a stronger IAW Landau damping, which suppresses the LDI cascade and increases the EPW energy available from TPD. This does not stop the formation of cavitation in the system, as shown in section 4.3.4.1. The HE conversion fraction f_{HE} in Fig. 4.28b2 follows a similar behavior, with values going from $f_{HE} \simeq 20\%$ to $\simeq 40\%$ for the highest T_i/T_e in the scan.

Finally, the hot electron average temperature in Fig. 4.28b3 reflects the behavior of the HE tail in Fig. 4.28a, with a reduction in T_{HE} for higher values of T_i/T_e, from $\simeq 80 - 100$ keV to a plateau at $\simeq 40 - 60$ keV. This behavior is similar across the whole scaling (Fig. 4.14). The reduction in HE average temperature would imply that the reduction in weak turbulence is connected to staged acceleration. The LDI cascade process produces low-k EPW modes which are characterized by overall higher phase velocities; therefore, a lower LDI activity means less high v_{ph} EPWs able to stage-accelerate electrons to the end energies of the HE tail, and consequently a lower overall T_{HE}.

In conclusion, the influence of T_i/T_e weakens the LDI instability activity through an increased Landau damping, promoting a higher EPW energy given by the TPD instability. This results into a root-like behavior of the HE flux Φ_{HE} and conversion fraction f_{HE}, with an increase in these quantities upon reaching a plateau level for increasing T_i/T_e, and a decreased T_{HE} due to less high phase velocity EPWs that accelerate electrons to high energies. A scaling law proposed

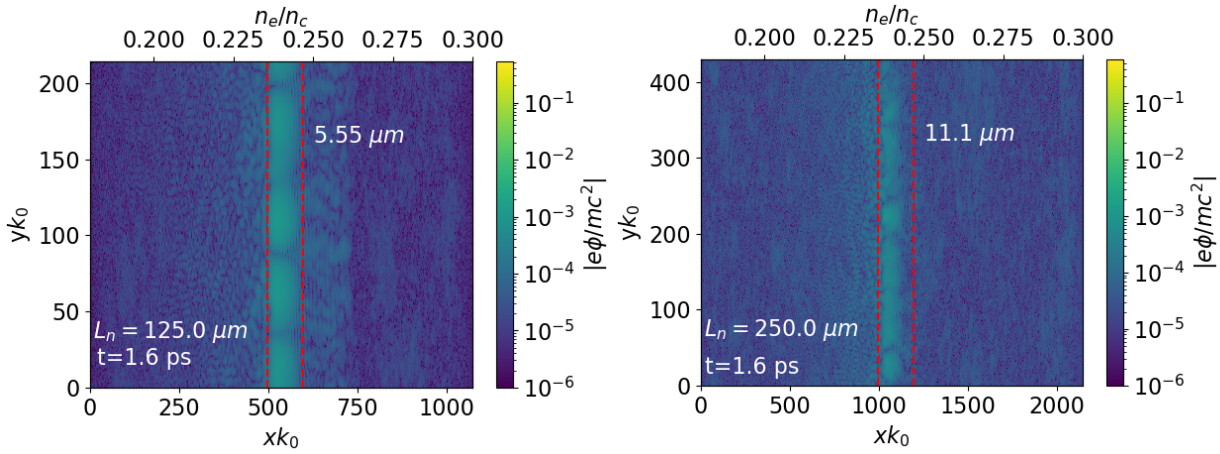

(a) (b)

Figure 4.29: Comparison of the resonance region width of the EPW potential for a) $L_n = 125$ and b) $L_n = 250$ ps. Both simulations have been taken at t = 1.6 ps, for $T_e = 5$ keV, $T_i/T_e = 0.5$ and $\eta = 2.0$.

for the HE conversion fraction is a simple power law of the form:

$$f_{HE} = a\left[\frac{T_i}{T_e} - \left(\frac{T_i}{T_e}\right)_{thr}\right]^b, \tag{4.13}$$

where $(T_i/T_e)_{thr}$ is a threshold value chosen at $T_i/T_e = 0.1$. The parameters of this scaling law for T_i/T_e scans at different values of L_n give the parameters a $\simeq 0.36 - 0.46$ and b $\simeq 0.17 - 0.2$.

4.3.5 Scaling analysis: density scale length parameter scan

The last parameter for which the scan has been carried out is the density scale length L_n. This parameter conserves many of the features of the previous scans in η, T_e and T_i/T_e. Particularly, changes in the HE quantities are already illustrated in Figs. 4.25b and 4.28b, which will be referred to when discussing about such quantities.

Changes in L_n have as a consequence a change in several of the diagnostics presented up to now. First of all, the laser intensity threshold for TPD directly depends on the density scale length according to Eq. 2.188 in the form of $I_{thr}^{TPD} \propto L_n^{-1}$. Therefore, it is theoretically easier for the TPD instability to appear in the plasma system, followed by LDI cascade and LW collapse. However, in the conditions of this scaling analysis at fixed η and T_e, the laser intensity is an input depending on $I_{laser} = \eta I_{thr}^{TPD}$. Therefore, if I_{thr}^{TPD} becomes weaker for higher values of density scale length, the laser intensity injected is lower as well to keep η constant.

As shown in section 4.1.2, the LPSE simulations have all been constrained with a linear density profile, with density extremes at $n_e/n_c = [0.18 - 0.3]$. This implies a change in simulation dimensions for different density scale lengths, and therefore an enlargement of the interaction region towards the longitudinal dimension. Fig. 4.29 shows a comparison between the EPW potential of two simulations at $L_n = 125$ μm (Fig. 4.29a) and $L_n = 250$ μm (Fig. 4.29b) for the fixed parameters $T_e = 5$ keV, $T_i/T_e = 0.5$, $\eta = 2.0$. In order to carry over a comparison between resonance region width, the focus has been over the linear growth regime, at t = 1.6 ps, when the TPD instability is dominant over the secondary instabilities, and turbulence does not influence the activity around $n_c/4$. The estimated density interval of the resonance region that has been considered for both simulations goes from $\simeq 0.2356$ to $\simeq 0.2467$. The resulting width in real space for the two density length has been calculated to be $\Delta x \simeq 5.55$ μm for $L_n = 125$ μm and $\Delta x \simeq 11.1$ μm for $L_n = 250$ μm, confirming the doubling in size of the resonance region for double the density scale length. Moreover, the lower EPW potential of the instability at

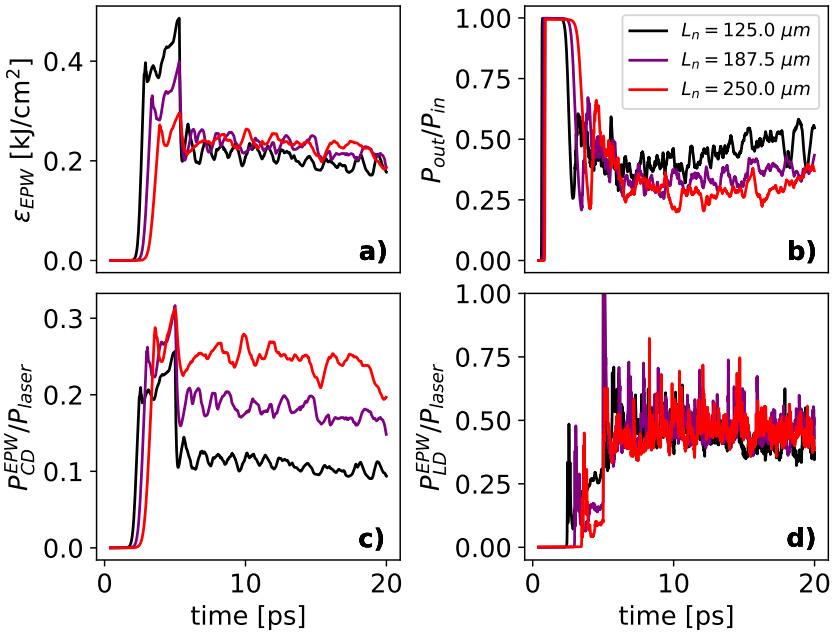

Figure 4.30: a) EPW energy fluence, b) laser transmission, c) fractional power absorbed by collisional and d) Landau damping for a scan in L_n, where $T_e = 5$ keV, $T_i/T_e = 0.5$ and $\eta = 2.0$.

quarter critical for the high L_n case confirms a slower development of the TPD instability in the same time frame, and therefore a lower overall maximum growth rate (due to keeping η constant).

The effects of a lower TPD threshold, lower input laser intensity, and a larger activity region result in an EPW energy flux ε_{EPW} (in J/cm^2) that remains unchanged across the L_n parameter scan. The larger region enhances the local EPW collisional absorption behavior at higher density scale lengths. This is due to the larger distance an electron has to cross in order to reach the boundaries, therefore increasing the probability of collisions despite the collision rate ν_{ei} and the particle mean free path remaining constant (Fig. 4.30c). For a particular scan in L_n with fixed parameters $T_e = 5$ keV, $T_i/T_e = 0.5$ and $\eta = 2.0$, the quasi-stationary power absorbed by collisional damping ranges from $\simeq 12\%$ at $L_n = 125$ μm to $\simeq 25\%$ for $L_n = 250$ μm. This does not affect the EPW fractional power absorbed by Landau damping, which remains almost unchanged for the entire scan in density scale length (Fig. 4.30d). The average fractional power absorbed by Landau damping is at $\simeq 40\% - 45\%$. The laser transmittivity therefore decreases according to the strengthening of the EPW fractional power absorbed by collisional damping (Fig. 4.30b).

The electron energy spectrum in Fig. 4.31a shows a different behavior than the previous graphs in Fig. 4.19a, 4.25a and 4.28a. While there is no change in the bulk flux for the L_n scan, the tail shifts its average temperature towards higher energies, with a repartition of the electron energy flux Φ_e towards higher energies and a decrease in the HE tail Maxwellian peak flux. The lower overall HE flux is attributed to the weaker available laser energy.

With respect to the scans in η, T_e and T_i/T_e, the density scale length scan is characterized by a higher average HE temperature for increasing values of L_n. This is consistent with the longer resonance region, which raises the occurrence of energy transfer between multiple EPW modes and an electron through the staged acceleration process discussed in section 4.2.5.

Finally, the HE conversion fraction behavior depends on the changes in Φ_{HE} related to the laser intensity I_{laser}. Since both quantities decrease, f_{HE} does not present a strong trend. While the T_e scan in Fig. 4.25b shows the f_{HE} curves with similar values across the density scale lengths considered, the one in T_i/T_e (Fig. 4.28b) shows an increasing trend. Fig. 4.31b shows another such scan for T_i/T_e, this time at fixed $T_e = 4$ keV and $\eta = 2.0$, and the f_{HE}

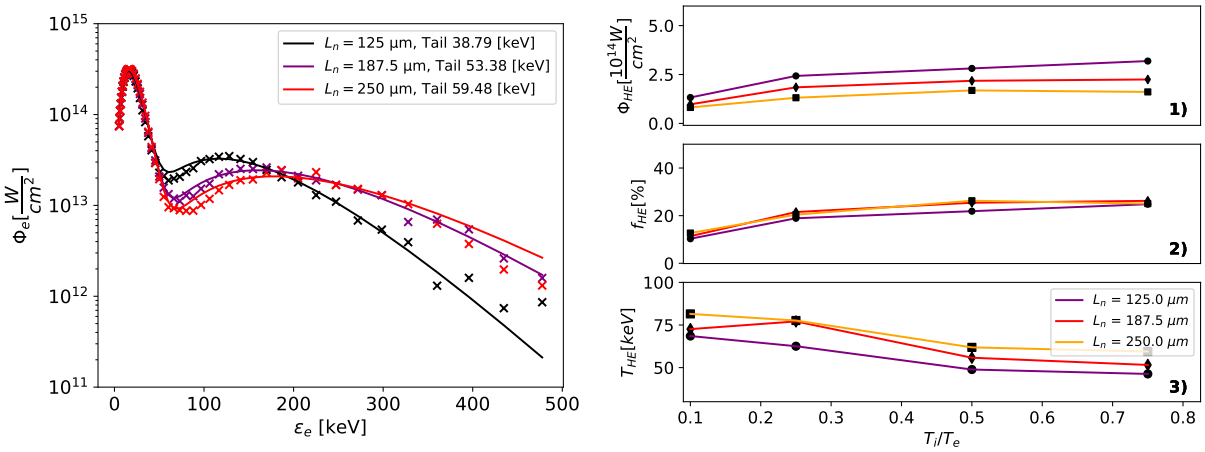

(a) (b)

Figure 4.31: a) Energy spectrum of the electron energy flux in the forward direction for an L_n scan, taken for $T_e = 5$ keV, $T_i/T_e - 0.5$ and $\eta = 2.0$. b) T_i/T_e and L_n scan for $T_e = 4$ keV and $\eta = 2.0$.

curves are almost overlapped. We therefore conclude that there is a compensation between the weaker HE energy flux and the decreasing laser intensity, which normalizes the curves to f_{HE} values close to each other. This is consistent with the saturation levels of the EPW fractional power absorbed by Landau damping discussed in the previous paragraph. However, the number of points for a single L_n scan are limited, and therefore additional data are required to give a more precise conclusion on the HE conversion fraction for longer L_n.

It is then difficult to infer a precise scaling law for the L_n scan. According to the theoretical TPD intensity threshold, doubling L_n implies halving I_{thr}^{TPD} at constant η. Assuming a simple linear relation between the data points, of the form $f_{HE} = a \times L_{n,\mu m} + b$, where $L_{n,\mu m}$ is in μm, we find $a \propto 10^{-4} \propto 10^{-1}$.

4.3.6 Scaling analysis: comparison of 2D vs 3D simulations of TPD without pump depletion

In this section we discuss the effects of considering a full 3D simulation domain, and discuss the changes with the 2D geometry.

The simulations are performed with a reduced scaling where only one density scale length, $L_n = 187.5$ μm, is considered. The density profile is linear in the longitudinal direction, but the density extremes are limited to $n_e/n_c = (0.2 - 0.28)$. Therefore, in order to keep the same density scale length, the simulation length and width have been set to $L = 60$ and $W = 12$ μm, respectively. This allows the use of a reduced grid, which reduces the CPU cost. The other parameters are $T_e = 3, 4, 5$ keV, $T_i/T_e = 0.1, 0.25, 0.5, 0.75$ and $\eta = 1.0, 1.2, 1.25, 1.5$.

The same laser conditions as the 2D scaling are considered, with a single p-polarized plane wave, with $\lambda_0 = 0.351$ μm, propagating along the x direction (the polarization vector being in the z direction).

Firstly, to observe more quantitative changes, a direct comparison between a 2D and 3D simulation with laser pump depletion is proposed in section 4.3.6.1, 4.3.6.2 and 4.3.6.3. Secondly, the HE scaling is carried out in section 4.3.6.4, without laser pump depletion in order to keep the computational cost manageable. This implies that the laser injected does not lose energy, and therefore the instabilities are not limited by pump depletion. The LDI cascade, as shown in chapter 3, does not present growth rates strong enough to act as a strong saturation mechanism for TPD, and in the most energetic simulations (i.e. high T_e and/or η), this is reflected in high values of the HE results (mainly conversion fractions). With this scaling analysis we will

therefore focus on the qualitative differences between the 3D scaling and an equivalent 2D one, performed without laser pump depletion as well.

4.3.6.1 EPW potential for 3D TPD

We now analyse the behavior of the EPW potential in Fourier space for the 3D TPD case. This simulation includes laser pump depletion, and the parameters $L_n = 187.5$ μm, $T_e = 4$ keV, $T_i/T_e = 0.75$ and $\eta = 1.5$.

Fig. 4.32a shows the EPW Fourier spectrum on the x-y plane for the 3D TPD simulation. The system has been taken in its linear growth phase, at a time of t = 4.8 ps, and similarly to the 2D case there is maximum growth on a hyperbole characterized by $k_y^2 = k_x(k_x - k_0)$. The two peaks at $(k_x, k_y) \simeq (0, 0)$ correspond, similarly to the 2D case, to the peaks of absolute TPD instability, which propagate towards higher $|k_x|$ and $|k_y| \simeq k_{Sim}$ due to advection of the absolute TPD modes outside of the resonance region. We remind that k_{Sim} is the Simon threshold for the wave vector [81], $k_{Sim} = k_y = \pm k_0\sqrt{0.106 I_{14}\lambda_{0,\mu}^2/T_{e,keV}^2}$ (see section 3.2.2). The simulation in Fig. 4.32b shows the occurrence of turbulence through LDI cascade and LW collapse, and the establishment of quasi-stationary conditions, which correspond to the same behavior of the 2D case, with the majority of TPD activity within the Landau damping cutoff $k_{EPW}\lambda_{De} \simeq 0.2-0.3$.

Figs. 4.32c and 4.32d show the 3D EPW potential in the same time frames, but seen from the y-z plane. There are two regions of activity close to the k origin at $k_z = 0$, and $k_y/k_0 = \pm k_{Sim}/k_0$, with a few waves propagating towards higher $|k_y|$ values. There is no significant EPW generation for $|k_y| \simeq 0$ towards the z direction. At t = 11.6 ps, the quasi-stationary conditions of the simulation become more turbulent, with EPW generation in every direction. However, the EPW modes are more localized in the y-z case, with normalized EPW potentials with amplitudes of $\mathscr{F}|e\varphi/mc^2| \geq 10^0$ at $(k_y/k_0, k_z/k_0) = (\pm 2, \pm 2)$. Moreover, the fields are overall weaker than the x-y projection.

Finally, Fig. 4.32e and 4.32f shows the x-z projection. It can be seen that the instability is flat at t = 4.8 ps, with the same peaks at the center of the spectrum, and faint TPD activity around it towards the z direction. The modes in t = 11.6 ps follow a more turbulent behavior, but they are more localized even than the y-z projection, with fields localized around $(k_x/k_0, k_z/k_0) \simeq (\pm 1, \pm 1)$, and the strongest fields at the center.

These simulations clearly show that, while the simulation is in 3D, the Two Plasmon Decay instability is an inherent 2D phenomenon, and that the majority of the waves that come from TPD are generated mainly in the x-y plane. After the turbulence is fully developed, LDI cascade and LW collapse are able to generate waves in every direction, with however retaining some limitations in EPW generation compared to the plane of TPD activity (in this case, the x-y plane). This has important repercussions on the HE production in the 3D case.

4.3.6.2 IAW activity and cavitation for 3D TPD

The IAW behavior for the 3D TPD case is presented in Fig. 4.33 at t = 11.6 ps (The laser-plasma conditions are the same as in Fig. 4.32). Fig. 4.33a shows a similar trend to the one presented in the 2D TPD case, with the development of laser-plasma turbulence around the region around $n_e/n_c \simeq 0.24$ up to $n_c/4$. The formation of depressions in the slow plasma response can be observed, indicating the presence of cavitons (and therefore LW collapse), particularly in the resonance region, while the fields outside of it are weak compared to $n_c/4$, becoming lower by a factor of $\simeq 10^{-1} - 10^{-2}$.

The projection of the same system along the y-z plane is shown in Fig. 4.33c and shows the plasma system from the front. $\delta n_l/n_c$ presents high fields across the entire domain, which is to be expected since the plot is being taken with an x component in the middle of the resonance region. The IAWs follow the EPWs' behavior, with the formation of vertical regions due to the modes' interference between each other. This is a feature that has been observed in the EPW

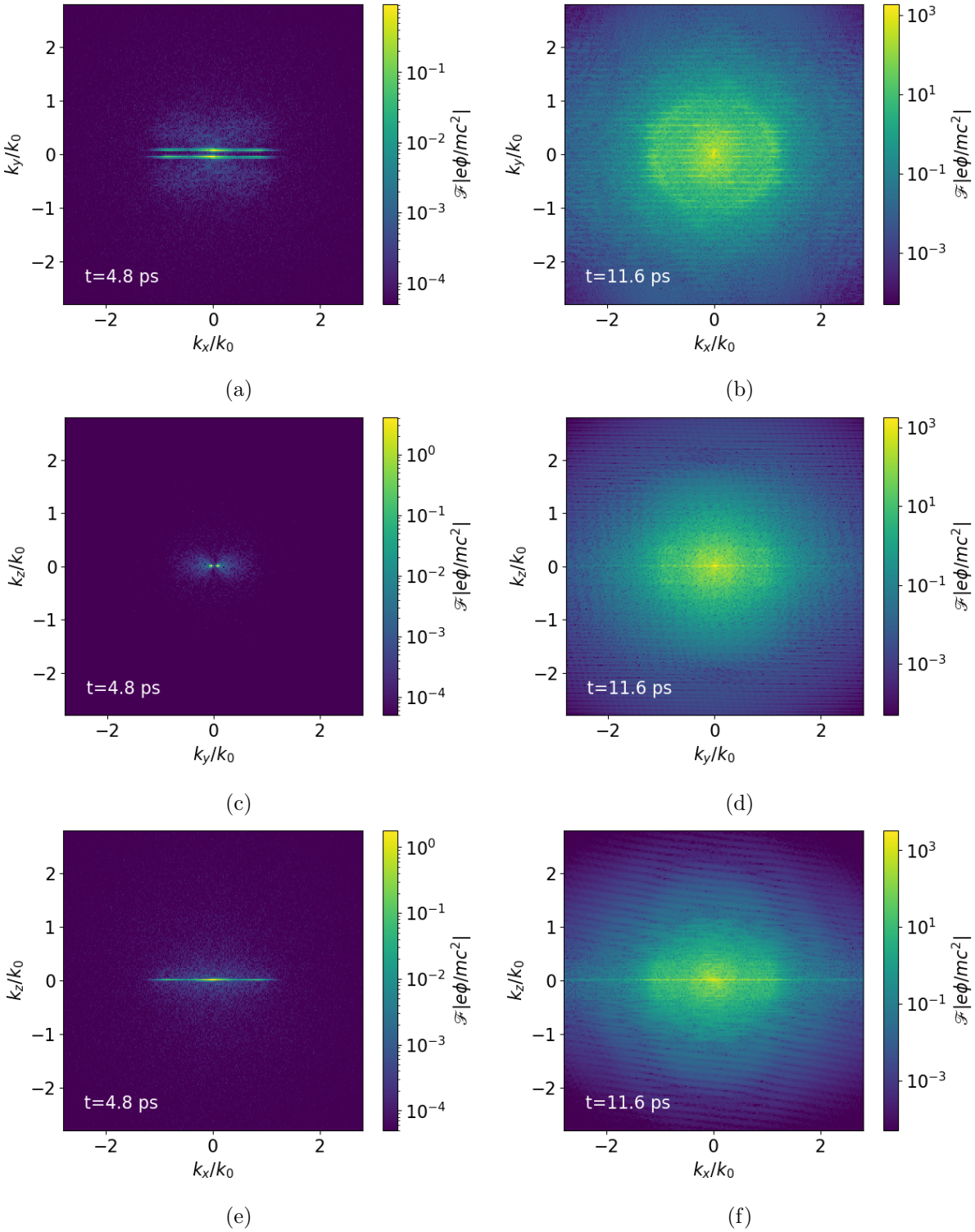

Figure 4.32: EPW potential in Fourier spectrum for the 3D TPD system, for a)-b) the x-y plane, c)-d) the y-z plane and e)-f) the x-z plane. The left and right image columns refer to the simulation time of t = 4.8 and 11.6 ps, respectively.

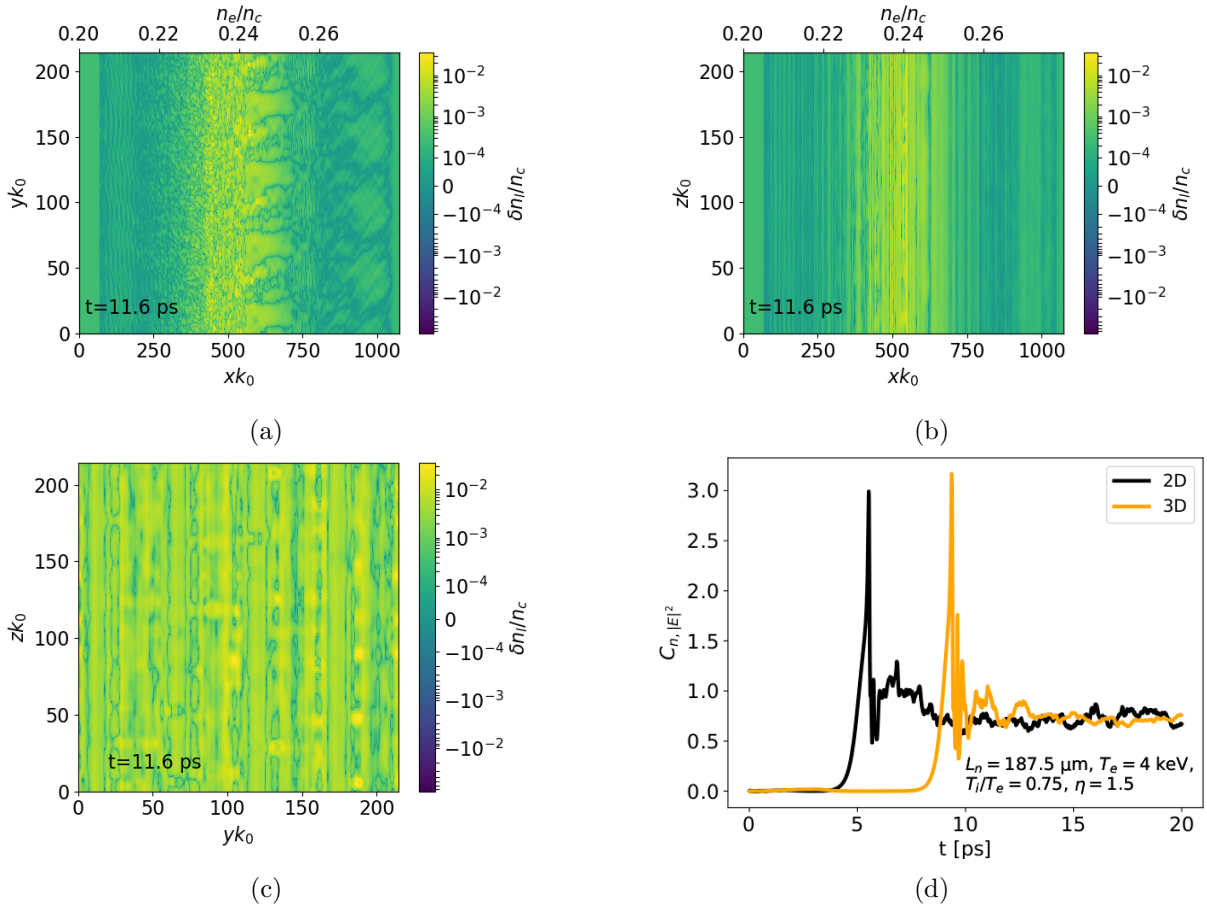

Figure 4.33: Low-frequency electron plasma response for the time frame t = 11.6 ps, for a) the x-y, b) the x-z and c) the y-z projection. The laser-plasma conditions are the same as in Fig. 4.32. d) Comparison between 2D and 3D simulations of the caviton correlator $C_{n,|E|^2}$ behavior in time, for $L_n = 187.5$ μm, $T_e = 4$ keV, $T_i/T_e = 0.75$ and $\eta = 1.5$.

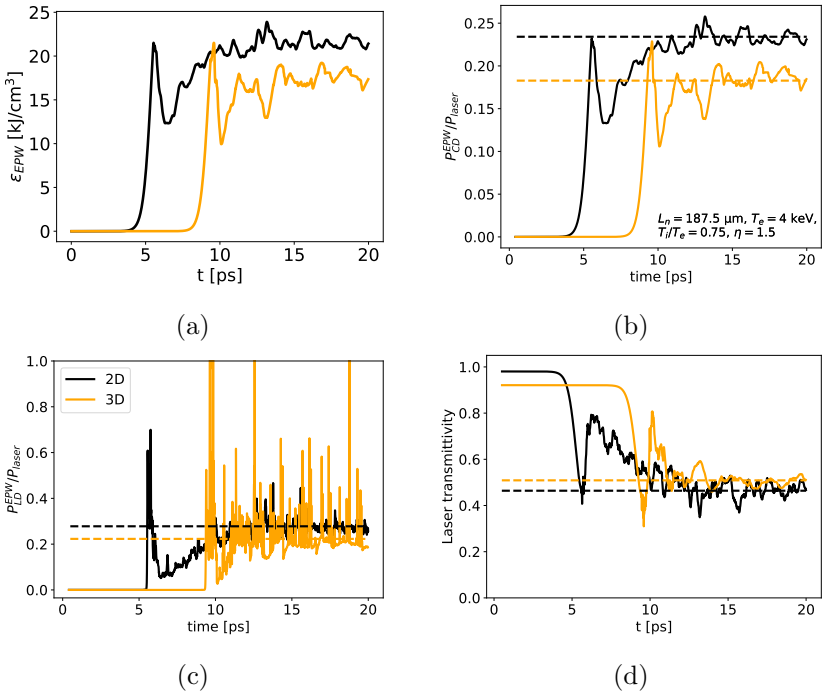

Figure 4.34: Energy metrics evolution in time of a) the EPW global energy density, as well as the fractional power absorbed by b) EPW collisional and b) Landau damping, as well as c) the laser transmittivity. The two curves refer to the 2D-3D comparison between simulations with pump depletion on and $L_n = 187.5$ μm, $T_e = 4$ keV, $T_i/T_e = 0.75$ and $\eta = 1.5$.

field in real space as well. Moreover, the formation of cavitons is shown in this figure, with regions of low field appearing across the whole space.

The projection of the x-z component in Fig. 4.33b shows the existence of the IAW modes in the z directions in a clearer way. While in the activity region some density depressions can be seen, they do not appear to be particularly developed along this region.

Overall, the presence of LDI cascade is ubiquitous in all three plots, and while not reported here, their corresponding spectrum in Fourier space indicates the emission of IAWs in every direction in a similar fashion to Figs. 4.32b, 4.32d and 4.32f, with a main activity region in Fourier space that is approximately double the one in all planes $(k_x/k_0, k_y/k_0, k_z/k_0) \simeq (\pm 2, \pm 2, \pm 2)$ and maximum fields about one order of magnitude less than the EPW ones, consistent with the LDI cascade emission for IAWs (Eq. 2.196b). Moreover, the density cavities produces IAWs at the time of their collapse, resulting in their homogeneous emission in Fourier space as well.

The comparison between 2D and 3D simulations of the caviton correlator behavior in time is shown in Fig. 4.33d. One of the main features is that the caviton correlator does not change problem's dimensions, meaning that cavitation activity, set at $C_{n,|E|^2} \simeq 0.75$, is strongly present within the system.

In conclusion, while the TPD instability mainly evolves in a 2D plane, both the EPW Fourier spectrum and the IAW behavior both in real and Fourier space imply that the secondary instabilities of LDI cascade and LW collapse developing in the system in quasi-stationary conditions are responsible for the majority of the homogeneous EPW emission.

4.3.6.3 EPW energy metrics and electron energy spectrum

We now study the changes in the energy metrics when considering a 3D system instead of a 2D one.

Fig. 4.34 illustrates the comparison between the energy metrics presented in section 4.3.2.2

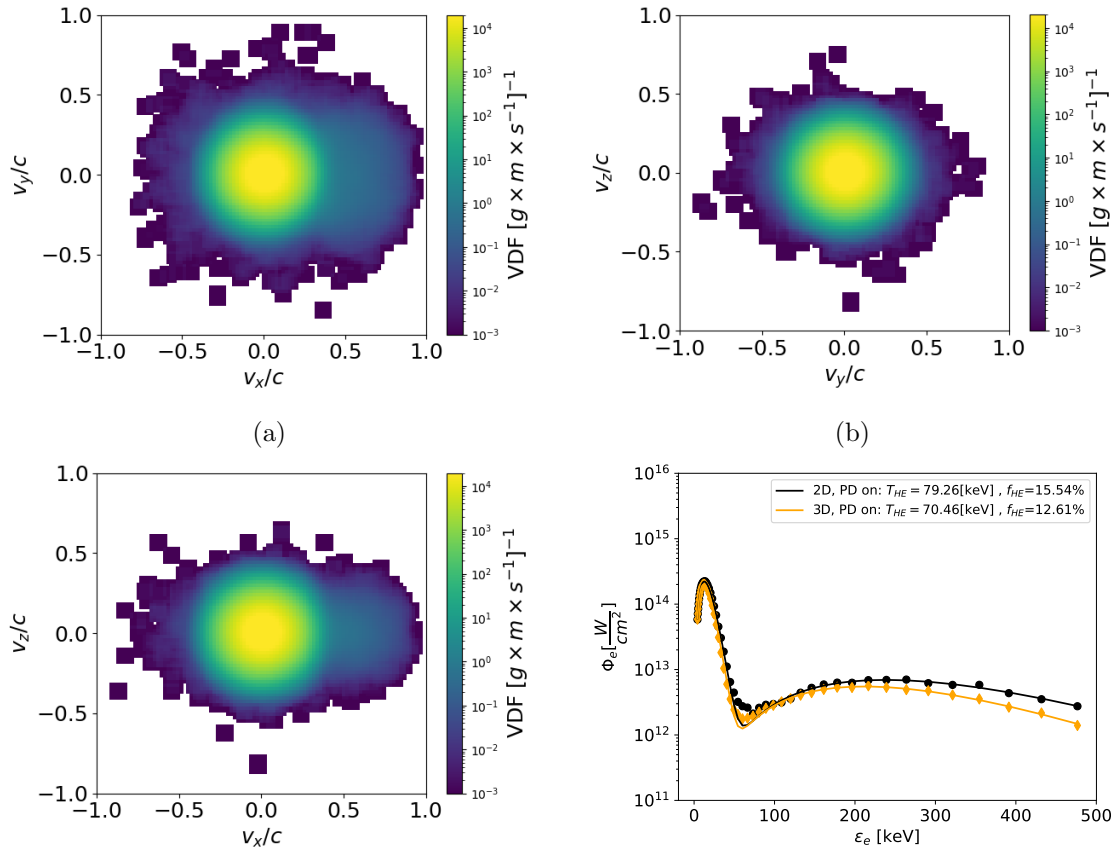

Figure 4.35: 3D VDF in a) the x-y, b) the y-z and c) the x-z plane. d) Electron energy flux in the forward direction for a 2D (black curve / data points) and a 3D (orange curve / data points) TPD systems.

of 2D and 3D TPD. The EPW energy density (Fig. 4.34a) reaches a lower quasi-stationary level in the 3D case, at about $\epsilon_{EPW,J/cm^3} \simeq 17.5$ kJ/cm^3 compared to the $\simeq 22.5$ kJ/cm^3 in the 2D case, for a decrease of $\sim 20\%$. An explanation of this effect is that, in the 3D case, waves that travel with a significant $k_z \neq 0$ can no longer produce TPD, and therefore the overall TPD activity is weakened.

The increase in phase space for an instability mainly developing in 2D reflects on the fractional powers absorbed both by collisional and Landau damping (Figs. 4.34b and 4.34c), which become lower in the 3D case. Due to the slightly lower EPW energy density, the fractional power absorbed by collisional damping is reduced from $\simeq 23\%$ in the 2D case to $\simeq 18\%$ in the 3D one ($\sim 21\%$ reduction). The Landau damping fractional power slightly decreases as well, from $\simeq 27.5\%$ to $\simeq 21\%$ when passing from 2D to 3D ($\sim 23\%$ reduction), because the EPWs that resonate with the electron population are mainly emitted in the forward direction. Finally, due to the decrease in fractional EPW collisional and Landau damping powers, the laser light transmitted through the resonance region and out of the simulation domain (Fig. 4.34d) increases to maintain the energy conservation, increasing from $\simeq 46\%$ to $\simeq 51\%$ ($\sim 10\%$ reduction) for the laser-plasma conditions chosen in this analysis. Overall, due to TPD developing mostly on a plane, we expect a HE production that reflects such decrease in the energy diagnostics.

4.3.6.4 2D vs 3D hot electron generation

We now focus on the differences in HE production between the 2D and 3D TPD cases. The comparison shown in Fig. 4.35d is carried over the electron energy flux Φ_e. The maxwellian constituting the bulk plasma is centered around $T_e = 4$ keV in both cases, with an almost overlapping profile between the two. Starting from electron energies of $T_e \simeq 50$ keV, the flux profiles begin to present differences between the 2D and 3D cases. Particularly, the 3D tail is lower than the 2D one for the HE emission in the forward direction. Following the VDF projections in 3D space in Fig. 4.35a, 4.35b and 4.35c, HE emission mainly occurs in a cone of $\sim \pm 30°$ of aperture in the forward direction. Therefore emission is not entirely confined to the 2D plane mentioned in the previous section, with HEs accelerated also with a small component. HE production is weakened as well, albeit slightly. The HE conversion fraction diminishes from $f_{HE,2D} \simeq 15.54\%$ to $f_{HE} \simeq 12.61\%$, a relative decrease of $\sim 20\%$, consistent with the decreases in EPW energy and fractional collisional and Landau powers. The average HE temperatures between the two cases also decreases, from $T_{HE,2D} \simeq 79.26$ keV to $T_{HE,3D} \simeq 70.5$ keV. Given that HEs are free to gain non-zero z components, where there are less EPWs with the right k-vectors, the stage acceleration decreases slightly, explaining the small decrease in temperature.

Comparisons between a reduced HE scaling analysis in 2D and 3D have been carried out within the limited laser-plasma conditions of $L_n = 187.5$ μm, $T_e = 3, 4, 5$ keV, $T_i/T_e = 0.1, 0.5, 0.75$ and $\eta = 1.0, 1.2, 1.25, 1.5, 2.0$. Fig. 4.36 shows such a comparison for $T_i/T_e = 0.1$ and 0.5 for the HE conversion fraction and HE average temperature. As previously stated, this scaling analysis is carried out without laser pump depletion, such that energy is not conserved. The assumption made was that the LDI cascade and the LW collapse could saturate the TPD instability at the given laser drive strengths, preventing it from growing indefinitely. However, while it is possible for LDI cascade and cavitation to saturate TPD at low IAW Landau damping rates, at high values of η, T_e and T_i/T_e the LDI growth rate does not manage to saturate the TPD instability. This results in occurrences where the HE conversion fraction reaches values above 100%. Nevertheless, it is instructive to compare the 2D and 3D cases for the simulations that reach a steady state.

Particularly, the HE conversion fraction at low ion-electron temperature ratio in Fig. 4.36a is similar both in the 2D and 3D case. At these laser-plasma conditions, the effects of LDI cascade and cavitation turbulence manage to saturate TPD growth, with a behavior similar to the one in Fig. 4.14. The profiles of f_{HE} are similar both in the 2D and 3D cases, reaching values of $f_{HE} \simeq 20\%$ at the highest T_e and η. The average 3D HE temperature (Fig. 4.36c) is smaller than the 2D one as well, consistently with our previous comparison. When the ion-electron ratio increases, the 2D simulations diverge due to the weaker LDI saturation of TPD, resulting in HE conversion fractions above 100%. However, the 3D f_{HE} values are similar to the $T_i/T_e = 0.1$ case, and do not diverge. The spread of EPWs out of the TPD plane acts to prevent divergence of the instability.

In conclusion, the comparison of a 3D HE scaling analysis versus 2D is mainly influenced by the nature of the TPD instability, which produces HEs mainly on a plane. This results in a moderate decrease in HE conversion fraction and temperature, which depends on the chosen laser-plasma conditions.

4.4 TPD and SRS scaling analysis

In this section we expand the physics in the system by adding the Stimulated Raman Scattering (SRS) parametric instability. However, we must note that this is a preliminary analysis that requires further investigation.

We follow the structure of analysis used in the TPD scenario. First, we give a brief discussion about the changes in the LPSE equations used for the simulation analysis, as well as defining

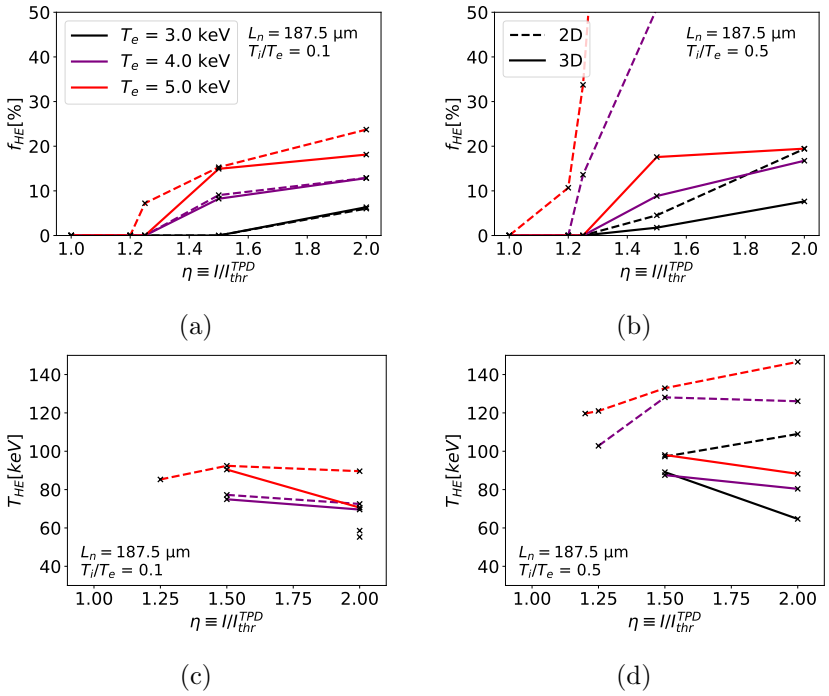

Figure 4.36: Scaling of the a)-b) HE conversion fraction and c)-d) average HE temperature as a function of the laser drive strength η. The scaling compares 2D simulations (dashed line) with 3D ones (full lines), for different T_e (curves' color scale from black to red) T_i/T_e values (different plots). Contrary to the previous results, in this simulation scaling the laser pump depletion has been turned off. The density scale length has been fixed to $L_n = 187.5$ μm.

the variables of the laser-plasma conditions. Particularly, a new scaling that is more relevant up to NIF conditions is being proposed.

After that, comparisons between the TPD and SRS+TPD case for a single simulation are presented. We discuss the differences between the EPW potentials and IAW fields through $\delta n_l/n_c$, as well as the electron emission through the VDF. A comparison at the energy balance with respect to the TPD case is also presented. Finally, the energy flux is discussed.

After considering the effects of the fields on a single simulation, the HE scaling is being presented. Again, the focus is to highlight the differences the SRS+TPD scenario possess with respect to the pure TPD case, noting possible changes when varying different laser-plasma conditions in the dataset.

In addition, a comparison between HE quantities found between LPSE and the PIC code SMILEI is presented, in an attempt to assess the validity of the LPSE results.

4.4.1 LPSE equations and parameter setup

The physics included in this scaling analysis is similar to the one employed in the TPD case. Accounting for Stimulated Raman Scattering in the equations implies the addition of several terms to the system of equations presented in 4.1.1.

The most important addition is the scattered light equation (Eq. 3.9), which computes the evolution of the scattered light field. Following the Zakharov model [40, 62] (section 3.1.1), the equation is a time-enveloped field for the scattered Raman light, with a representative envelope frequency of $\omega_1 \equiv \omega_0 - \omega_{p0}$, where ω_0 is the laser frequency and ω_{p0} is the plasma frequency calculated from the specified input of envelope density n_0 (sec. 4.1.1). The equation is similar in form to the laser equation, and describes the propagation of the wave through space (term proportional to c^2/ω_1) in the presence of density perturbations. Moreover, the IAW contribution

to the Raman scattered field has been enabled as well. The new system of equations is given considering the SRS equation and terms in the laser, EPW, and IAW equations in section 4.1.1 (Eqs. 4.1, 4.2, 4.3, 4.4 and 4.5).

The simulations have been performed in similar conditions to the TPD only scaling analysis. They involve a system where TPD and SRS compete for the laser energy, with the presence of secondary processes such as LDI and LW collapse / cavitation, which generate turbulence within the plasma. Laser pump depletion has been enabled. The simulations have been carried out in 2D to alleviate computational costs. The laser conditions are the same as in the TPD case, with a laser wavelength of $\lambda_0 = 0.351$ μm, and a p-polarized, plane wave configuration for simplicity. The plasma has a linear density profile in the direction of propagation of the laser, with extremes within $n_e/n_c = [0.18 - 0.3]$, as in the TPD case. The envelope density used in the LPSE field solver has been set to $n_0/n_c = 0.24$. The plasma used is a single ion species of CH at 50% fraction for both components, giving an average $\langle Z \rangle = 3.5$, and an ion-electron mass ratio of $m_i/m_e \simeq 11952.44$. No ion flow has been specified, and therefore the plasma ion background is not expanding. As far as the HPE module is concerned, the input conditions are the same as in the 2D TPD case, with an injection time starting at t = 5 ps for 10^6 virtual particles, and thermalization probabilities at the boundaries P_{th} of 100% in the forward and backward boundaries (Lindman conditions), and 10% for the side boundaries. Finally, to keep the same assumption of quasi-stationary conditions, the simulation time t_{sim} is also set to 20 ps.

The dataset of laser plasma conditions for the TPD + SRS scaling is the same as the TPD one (Table 4.2) and with the same simulation dimensions and number of nodes (Table 4.1). However, the scaling in η has been reduced to $\eta = 1.2, 1.25, 1.5, 2.0$. We must note that, while in the analysis of the TPD only system η was referring to the TPD laser intensity threshold only, in this case the definition is more ambiguous, because of the presence of SRS, which has its own intensity threshold (Eq. 2.159). In order to relate it to the previous scaling, the definition of η has been kept in relation to the TPD intensity threshold $\eta \equiv I_{laser}/I_{thr}^{TPD}$. Moreover, all simulations in the scaling have TPD intensity threshold higher than the SRS one. Therefore, the choice of I_{thr}^{TPD} in the definition of η allows to always have both SRS and TPD activity present.

Moreover, the TPD + SRS scaling includes one additional parameter scan done for the density scale length $L_n = 500$ μm, to simulate NIF-like in addition to OMEGA-like conditions. For this density scale length, a reduced scaling has been performed with $T_e = 4, 5, 6$ keV, $T_i/T_e = 0.1, 0.25, 0.5$, and $\eta = 1.25, 1.5, 2.0, 4.0$. The simulation dimensions had to be changed accordingly, with a size of 240×48 mum $\times$ mum over 4320×864 nodes which lowers the number of cells per wavelength to $\simeq 6$.

4.4.2 Comparison of EPW, IAW and Raman fields for the SRS+TPD case

We now consider the evolution of the TPD + SRS system. Comparisons are made with the TPD only case for the EPW potential and the IAW perturbation. The simulation considered is at $T_e = 4$ keV, $T_i/T_e = 0.5$, $L_n = 125.0$ μm and $\eta = 1.5$.

The laser plasma instabilities develop earlier in the SRS+TPD case, reaching quasi-stationary conditions at shorter times. This is because the absolute intensity threshold for SRS is lower than the TPD one across the entire scaling. Here, these thresholds have values of $I_{SRS}^{thr} \simeq 2.756 \times 10^{14}$ W/cm^2 and $I_{TPD}^{thr} \simeq 6.424 \times 10^{14}$ W/cm^2, respectively. Since the scaling analysis is related to the TPD drive strength, the equivalent η_{SRS} for SRS in this simulation is well beyond threshold, at $\eta_{SRS} \simeq 3.5$. When quasi-stationary conditions occur at t = 12 ps, the two systems are characterized by strong turbulence, with the highest values of EPW potential around the quarter critical region. Moreover, we observe a reduction in the width of the resonance region in real space, going from $xk_0 \simeq 200 - 750$ (corresponding to about 25 μm) for TPD only, to $xk_0 \simeq 300 - 750$, about 20 μm in the SRS+TPD case. In Fourier space (Figs. 4.37c and 4.37d), the two spectra for the EPW potential are similar to each other, with homogeneous emission due to the presence of turbulence through LDI cascade and LW collapse. Both EPW spectra

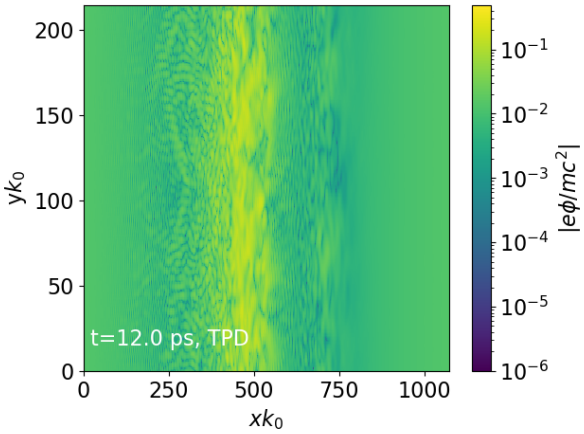

(a) t = 12 ps, TPD

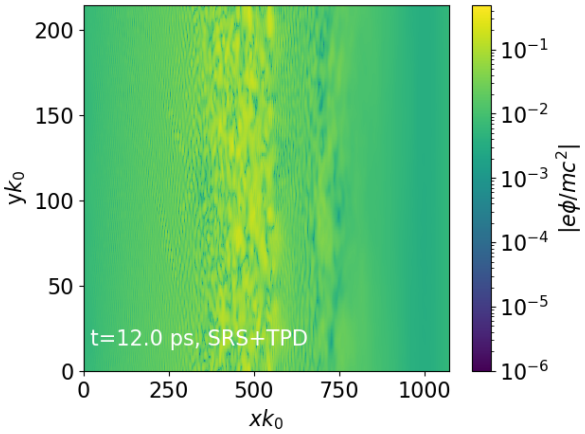

(b) t = 12 ps, TPD+SRS

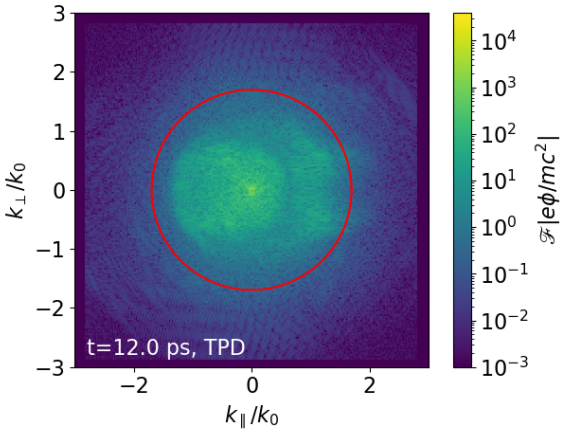

(c) t = 12 ps, TPD

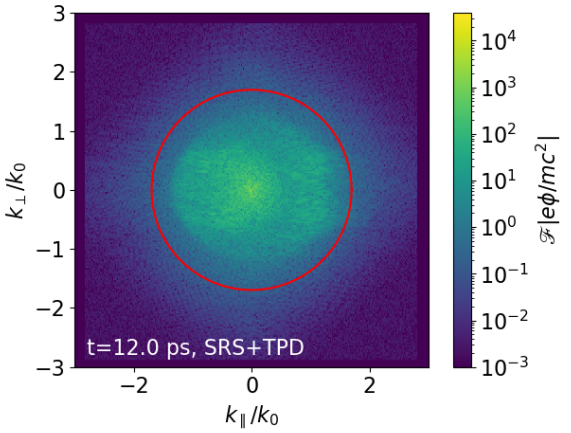

(d) t = 12 ps, TPD+SRS

Figure 4.37: Comparison between the EPW potential at t = 12 ps a)-b) in real space and c)-d) in Fourier space, for the TPD only (left column) and SRS+TPD (right column) cases. The red circle in Figs. 4.37c and 4.37d represent the Landau cutoff.

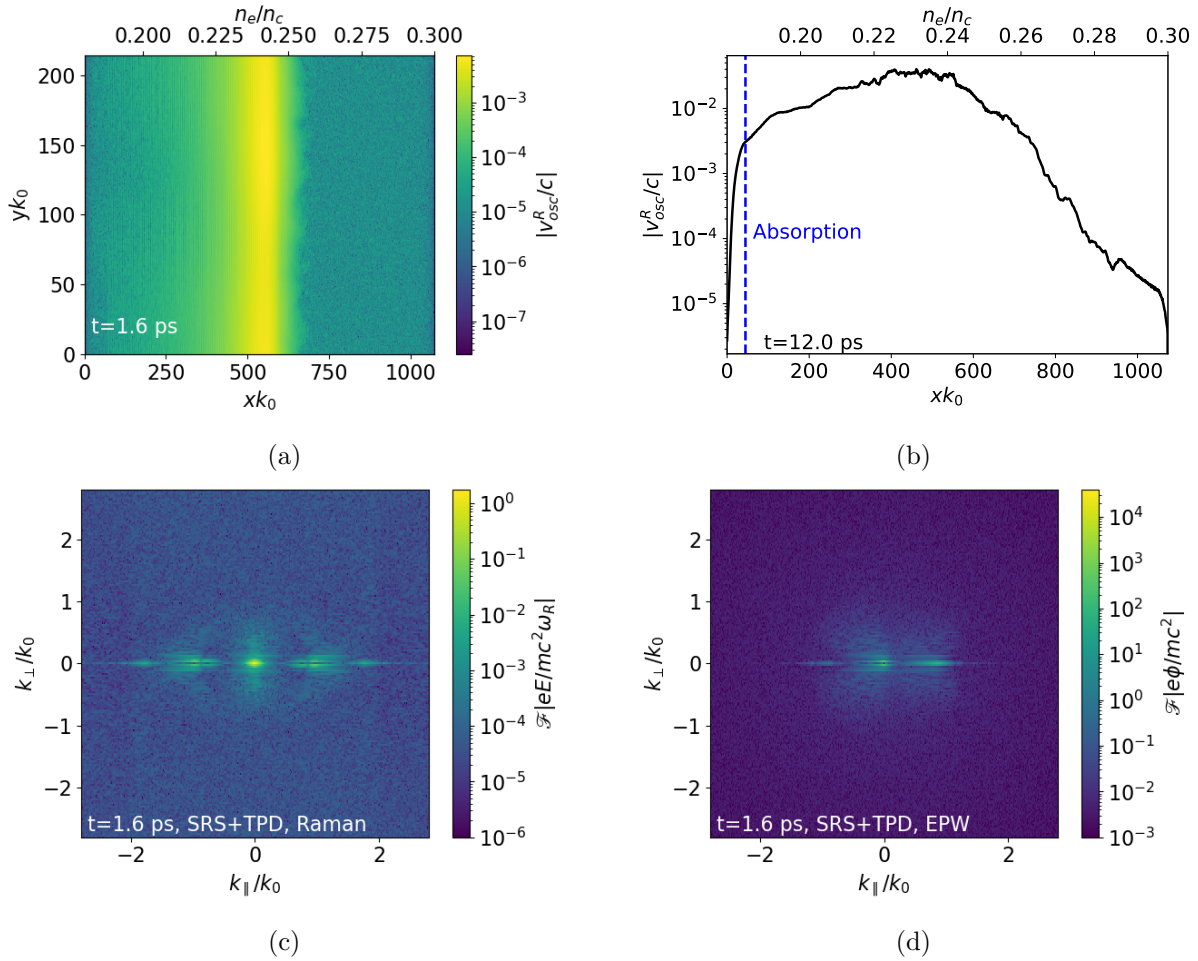

Figure 4.38: Time evolution of a) the Raman scattered light field (absolute value) in real space for t = 1.6 and b) for the averaged Raman field over y at 12 ps. Both are in units of $[v^R_{osc}/c]$. c) Fourier spectrum of the Raman field (in units of $[eE/mc\omega_R]$) and d) the EPW potential (in units of $[e\varphi/mc^2]$), at the time t = 1.6 ps. The blue line in b) represents the limit to the absorbing boundary layer.

have their strongest fields at low-k confined within the Landau cutoff at $k_{EPW}\lambda_{De} \simeq 0.2 - 0.3$, as identified by the red circles. Moreover, the maximum EPW potential increases from the TPD to the SRS+TPD case, with $e\varphi/m_e c^2 \simeq 0.408$ and $\simeq 0.487$ respectively. This is reflected in Fourier space, where the low-k fields appear to be stronger in the SRS+TPD case by a factor of $\simeq 1.5-2$. However, despite the stronger fields, the SRS+TPD case appears to present an overall weaker EPW field at larger wave numbers, beyond the Landau cutoff. Overall, the comparison of the EPW potential both in real and Fourier space leads to the conclusion that a regrouping of EPWs towards longer wavelengths occurs for SRS+TPD with respect to the TPD only case, which will reflect on the HE generation (as we will see in the following sections).

Fig. 4.38a shows a snapshot of the scattered Raman light evolution at t = 1.6. The scattered light field mainly grows around the resonance region, with a clear cutoff beyond $n_c/4$, consistent with the theory for SRS, where the scattered Raman waves reach their critical density and are reflected.

Figs. 4.38c and 4.38c show a snapshot at t = 1.6 ps for the Fourier spectrum of both the Raman field and the EPW potential. A peak of SRS activity is present at $(k_\parallel, k_\perp) \simeq (0, 0)$ in the Raman spectrum, with a corresponding peak at $k_\parallel \simeq k_0$ in the EPW one according to the expression of the wave vector in section 2.3.2.2. This is a signature of absolute SRS in the system,

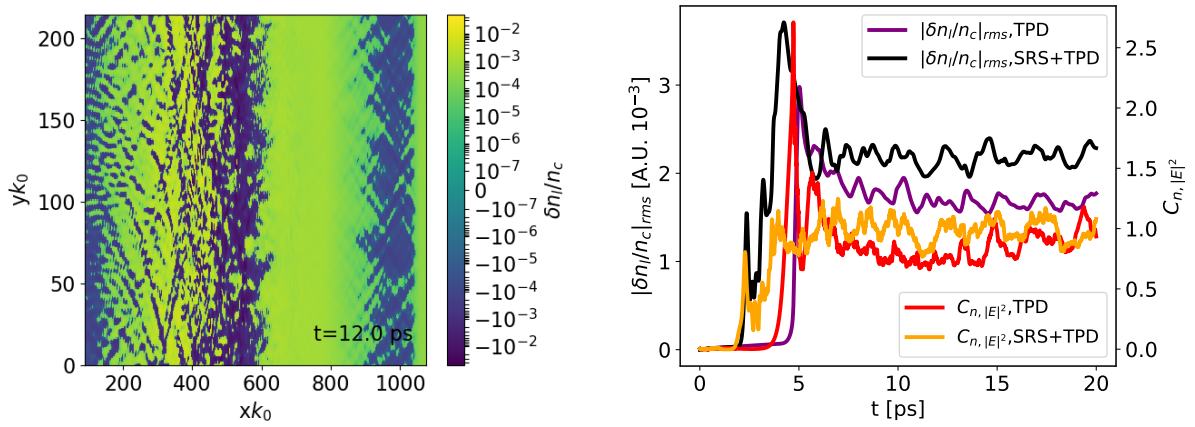

(a) (b)

Figure 4.39: a) Low-frequency electron density perturbation profile $\delta n_l/n_c$ in real space for t = 12 ps. b) Comparison between globally average $\delta n_l/n_c$ evolution in time for TPD (purple) and SRS+TPD (black) profiles, as well as the average caviton correlator in time for the same comparison (orange / red lines).

which backscatters Raman waves away from $n_c/4$. Moreover, the two structures at $k_{\parallel} \simeq \pm k_0$ in the Raman spectrum show the presence of both backscattered and forward scattered SRS as well. However, the EPW peak at $-k_0$ is lower by about 2 orders of magnitude, resulting in a weaker forward scattered SRS activity. To further support this, the calculated growth rates in these laser-plasma conditions, given by Eq. 2.155, are calculated as $\gamma_{SRS,back} \simeq 10.82$ ps^{-1} for backscattered SRS and $\gamma_{SRS,forw} \simeq 3-4$ ps^{-1} (depending on n_e/n_c) for SRS forward scattering, with a factor of $\simeq 2.5$ between the two. Overall, we conclude that backscattered SRS is dominant over forward scattered SRS here. The absolute instability also dominates over the convective one. The Raman field propagating towards lower densities is collisionally absorbed, such that a Raman field with amplitude ~ 10 times weaker than the one at $n_c/4$ reaches the simulation boundaries, as shown in Fig. 4.38b.

The IAW behavior in time for the SRS+TPD case is similar to the TPD only one, with the appearance of density regions in the plasma characterized by negative electron density perturbations at low frequency, indicating caviton presence. Starting from an unperturbed density background similar to Fig. 4.6a, a density perturbation starts to appear in the region of quarter critical density, with a delay with respect to the EPW field evolution due to the slower ion response. After the system reaches quasi-stationary conditions, the cavitons form in the region of maximum EPW activity, as shown in Fig. 4.39a. There is a spatial interval of high depression between $xk_0 \simeq (500-600)$, corresponding to the region of high EPW activity that pushes away the ions though ponderomotive force. After $xk_0 \simeq 600$ and higher, there is the presence of a region with high perturbation, beyond quarter critical, with a weakened EPW potential. The density profile is therefore less perturbed in this region, allowing for a clearer signature of the IAW modes generated by LDI cascade and cavitation and propagating away from $n_c/4$. Figure 4.39b shows the evolution in time for the spatially averaged low-frequency electron density perturbation. We observe an overall increase of $\delta n_l/n_c$ across the whole SRS+TPD scaling analysis compared to the TPD only one. This can be attributed to the higher local EPW fields in the system around quarter critical, driving a larger LDI growth rate (Eq. 2.200) due to its dependence on the EPW electric field through $v_{osc} \equiv v_{osc}^{EPW} \propto E_{EPW}$. Moreover, the larger EPW fields drive a stronger ponderomotive force on the electrons, therefore creating stronger space charge effects, resulting in stronger cavitation activity. This is shown in Fig. 4.39b for the caviton correlator diagnostic, where the SRS+TPD case (orange curve) possess a quasi-stationary average correlator of $C_{n,|E|^2} \simeq 0.98$, while the one for pure TPD is $C_{n,|E|^2} \simeq 0.87$.

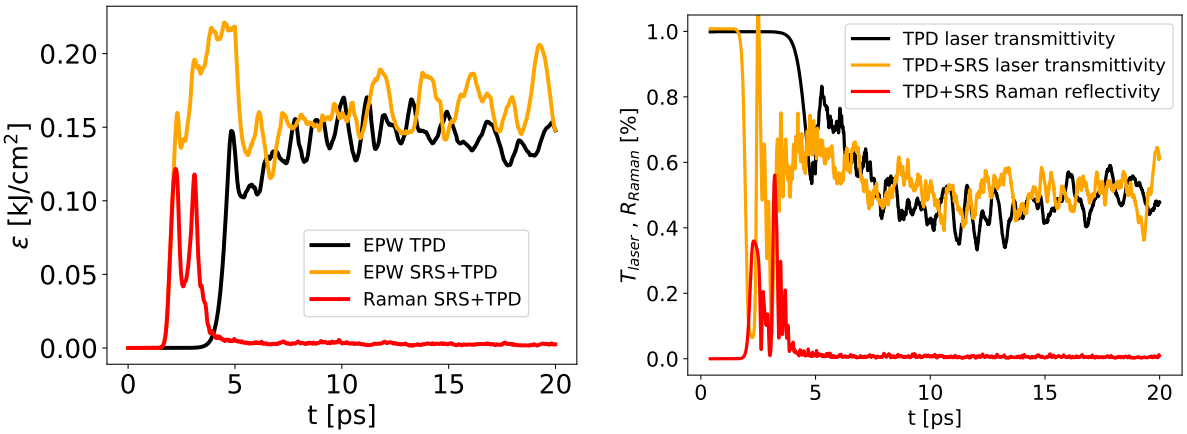

(a) (b)

Figure 4.40: a) Evolution in time of the wave energy fluence (in kJ/m^2) for the EPWs in the TPD (black curve) and SRS+TPD (orange curve), as well as for the Raman light for SRS+TPD (red curve). b) Time evolution of the laser transmission for both the TPD and SRS+TPD cases, and Raman reflectivity for the SRS+TPD one (same colors as a)).

Overall, the addition of Stimulated Raman Scattering leads to a stronger growth of EPW modes, albeit in a more limited region of space. Moreover, the instability occurs at earlier times due to a lower SRS intensity threshold and a similar growth rate than TPD in the case of study. The scattered Raman field shows the presence of light propagating in space mainly towards lower densities. This may further trigger convective SRS away from the quarter critical region, with a strong absorption of the Raman field in the plasma before it reaches the left boundary. Finally, the LDI and cavitation activity are strengthened by this increase in fields, with an increase in IAW modes and a stronger cavitation growth.

4.4.3 SRS+TPD energy metrics

The energy metrics' comparison between the TPD only and the SRS+TPD case are presented.

The laser-plasma instabilities develop earlier in the SRS+TPD case, reaching quasi-stationary conditions at shorter times, as shown in the comparison between the EPW energies in time in Fig. 4.40a, where an initial growth several picoseconds earlier in the SRS+TPD case than in the TPD one is observed. SRS+TPD reaches similar quasi-stationary levels compared to TPD only, at $\varepsilon \simeq 0.14 - 0.15$ kJ/cm^2. The TPD maximum growth rate is calculated by using Eq. 2.181, reaching $\gamma_{TPD} \simeq 11.67$ ps^{-1}, while the SRS backscattered growth rate is the one already given in section 4.4.2, $\gamma_{SRS,back} \simeq 10.82$ ps^{-1}. This leads to the conclusion that, while the two instabilities start at different times, their growth rate is relatively similar.

The Raman energy for the SRS+TPD case is also represented in Fig. 4.40a. The Raman energy growth coincides with the development of earlier EPWs, suggesting that SRS is the instability that dominates at initial times. After t $\simeq$ 2.1 ps the EPW energy outgrows the Raman one, but the Raman light still presents considerable values of energy fluence. However, after t $\simeq$ 3.1 ps. the Raman fluence starts to abrutply decrease, until reaching values close to zero in quasi-stationary conditions.

The fractional power absorbed by collisional damping follows the evolution of the wave energy fluence, quantitatively showing a slight increase from $P_{CD}^{EPW}/P_{laser} \simeq 17\%$ to $\simeq 20\%$ when adding SRS. The same occurs for the fractional power of the Raman field that is absorbed in the plasma through collisional damping. The EPW fractional power absorbed by Landau damping follows a similar profile no matter if SRS is included or not, reaching the same quasi-stationary level of $P_{LD}^{EPW} \simeq 32\% - 33\%$.

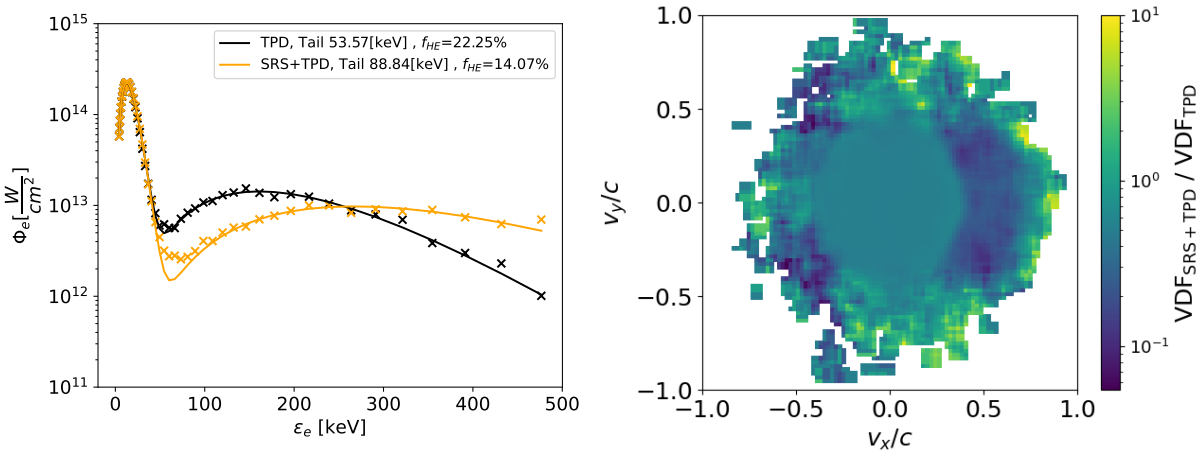

(a) (b)

Figure 4.41: a) Comparison between average spectra in quasi-stationary conditions of the electron energy fluxes for TPD and SRS+TPD systems. The laser plasma conditions are $L_n = 125$ μm, $T_e = 4$ keV, $T_i/T_e = 0.5$ and $\eta = 1.5$. b) Ratio between Velocity Distribution Functions (VDF) for the TPD and SRS+TPD cases, against v_x and v_y normalized to c.

The laser transmission is shown in Fig. 4.40b. The SRS+TPD system shows an abrupt decrease in laser transmission at times where SRS grows. At later times, since the EPW collisional and Landau damping are almost not affected from the introduction of SRS, the laser transmission does not present appreciable changes in quasi-stationary conditions when SRS is added to the physical system. Moreover, the Raman light reflectivity follows the Raman energy fluence behavior, reaching peaks of $R_{Raman} \simeq 40\% - 60\%$ in the linear growth phase before being almost negligible in quasi-stationary conditions. The high reflectivity at earlier times shows the strong Raman activity before the electron injection, coinciding with the depressions in laser transmittivity, after which it becomes negligible.

For these times, SRS is the dominant instability, therefore generating significant Raman scattered waves, which carry over the majority of the laser energy. These waves, mainly generated through backward SRS scattering (as seen in section 4.4.2) either carry the majority of their energy outside the boundaries, leading to significant laser reflectivity, or are absorbed by the plasma through collisional damping, with peaks of $P_{CD}^{Raman}/P_{laser} \simeq 12\%$. At times beyond t $\simeq$ 3.2 ps, TPD begins its linear growth phase, as seen in the TPD only scenario. This coincides with an increase in EPW energy fluence in Fig. 4.40a, and a sharp decrease in both Raman energy, P_{CD}^{Raman}/P_{laser} and reflectivity to almost zero. The growth of TPD generates stronger EPW modes than the Raman ones, as shown by the increase in EPW energy after the start of TPD growth, leading to a stronger plasma perturbation. This drives a stronger cavitation activity and LDI cascade, as illustrated by the $C_{n,|E|^2}$ and $\delta n_l/n_c$ signatures in section 4.4.2, which weakens the SRS growth rate in the caviton density depressions. As a result, the Raman field is limited to be an order of magnitude lower than the EPW one, with a reduction of 2 orders of magnitude in energy, coherently with the results in Fig. 4.40, suggesting that turbulence from TPD may limit the SRS growth [161]. This allows us to conclude that TPD dominates over SRS as soon as the instability starts growing, in accordance to the literature for OMEGA like conditions [35, 142, 162].

4.4.4 SRS+TPD Hot electron analysis

We now analyze the HE characteristics in the SRS+TPD case.

Figure 4.41a illustrates the energy flux behavior of the SRS+TPD system compared to the TPD only one. While the Maxwell-Boltzmann distribution describing the plasma bulk at low

energies are almost identical between the two cases, significant differences arise after reaching the hot electron tail energy region ($\varepsilon_e \gtrsim 50$ keV). The first part of the HE tail (from 50 to 250 keV) shows a lower electron flux in the SRS+TPD case by about a factor of 4 at lower energies. The SRS+TPD flux then overtakes the TPD only one after $\simeq 250$ keV up to the end of the recorded energy spectrum. This overall results in a decreased HE energy flux Φ_{HE} in the SRS+TPD case, leading to a lower HE conversion fraction by a factor of $\simeq 1.6$. On the opposite side, the greater flux at higher energies shows a hotter HE tail, with an increasing higher average temperature T_{HE}. This is coherent with the increased $\delta n_l/n_c$ signal, which implies a higher LDI activity, and therefore the presence of more low-k, high v_{ph} EPWs that allow the hot electrons to be stage-accelerated at higher energies.

While the HE tail flux decreases, the fractional power absorbed by Landau damping of the EPWs remains the same (as stated in section 4.4.3), and the HE temperature increases. While a more detailed analysis should be performed on this regards, we infer the reason of this lower conversion of EPW energy into hot electrons beyond 50 keV is due to the presence of SRS activity which, albeit small, disrupts the EPW generation at small wavelengths (as shown in Fig. 4.37), which are the ones that are outside the Landau cutoff circle and therefore are the most resonant with the electron velocities. At the same time, the increase in IAW activity in the SRS+TPD case implies an enhanced production of low-k EPW modes, which have a larger phase velocity and can accelerate the electrons to higher energies during staged acceleration. The reduction in the high-k EPW field would therefore explain the decreased HE population, while the increase in low-k EPWs would bring the fewer electrons to higher energies, resulting in a similar fractional power absorbed by Landau damping.

A further comparison between TPD and SRS+TPD behaviors is illustrated in Fig. 4.41b, which shows the ratio of the Velocity Distribution Function of SRS+TPD divided by the TPD one. The features encountered in the electron energy flux in Fig. 4.41a are the same in the VDF as well. The circle around $(v_x/c, v_y/c) \simeq (0, 0)$ represents the plasma bulk at average temperature T_e, which remains about the same both in the TPD and SRS+TPD case ($VDF_{SRS+TPD}/VDF_{TPD} \simeq 1$). However, the region at positive v_x/c (i.e. towards the target) shows a reduction in the VDF by a factor of $\simeq 0.3$ when SRS is included, representing the reduction in the electron flux encountered in the forward direction for the SRS+TPD case. Moreover, while there appears to be an increase in hot electron side emission, the overall HE fraction extracted from such side emission is calculated as $f_{HE} \simeq 0.55\%$ for the TPD+SRS case. We therefore conclude that HE side emission due to the presence of SRS is negligible compared to the forward and backward emissions, which accounts for $f_{HE,f} \simeq 14.07\%$ and $f_{HE,b} \simeq 3.7\%$ respectively. A more significant increase is in the forward direction at high energies between $50 - 250$ keV. This is consistent with the energy flux behavior as well, with an increase by a factor of 2 on average, and of an order of magnitude at maximum.

The results of the HE scaling analysis for the SRS+TPD system are represented in Fig. 4.42, for two of the three OMEGA-like density scale lengths considered: $L_n = 125$ and 187.5 μm. Drawing comparisons with the TPD case, there is no appreciable difference in the qualitative behavior of SRS+TPD HE quantities. The parameter scan in η still shows a plateau in f_{HE} after crossing the intensity threshold, while Φ_{HE} increases. In the T_e scan, a quadratic dependency is observed for Φ_{HE}, and a linear one for f_{HE}. T_i/T_e gives a root-like behavior for both the HE flux and fraction, controlling the plasma turbulence from LDI and LW collapse. Finally, the L_n scan still shows a dencrease in Φ_{HE}, but similar values of f_{HE}.

However, while the qualitative behaviors are the same as in TPD, the HE database for SRS+TPD shows a overall reduction for both f_{HE} and Φ_{HE} across the entire scaling when compared to their TPD counterpart (Fig. 4.13 and 4.14). For the HE conversion fraction in particular, at the largest laser plasma conditions for $L_n = 250$ μm, $T_i/T_e = 0.75$, $T_e = 5$ keV and $\eta = 1.5 - 2.0$, the values reached for the SRS+TPD case are up to $f_{HE} \simeq 33\%$, compared to the value of $\simeq 41\%$ of the TPD only scenario, for a relative reduction of about $\simeq 20\%$.

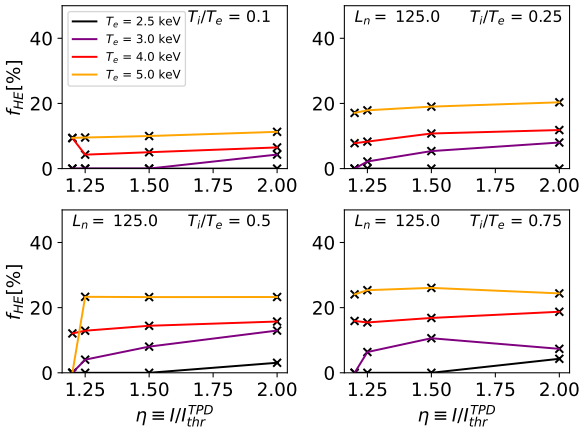

(a) f_{HE}, $L_n = 125.0$

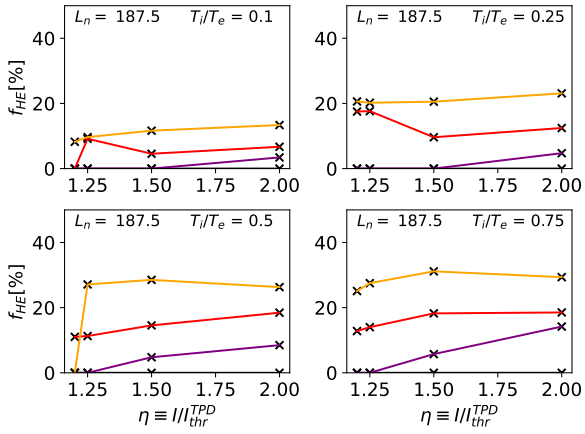

(b) f_{HE}, $L_n = 187.5$

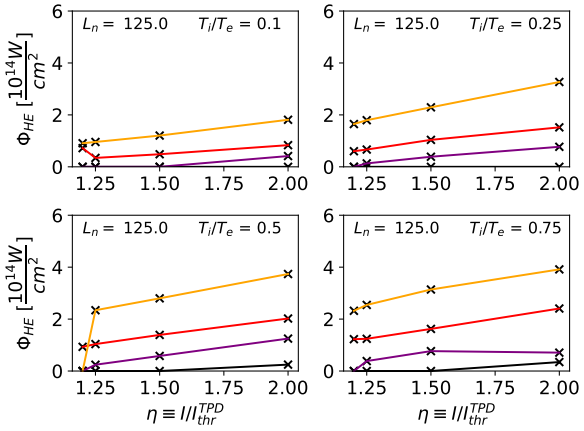

(c) Φ_{HE}, $L_n = 125.0$

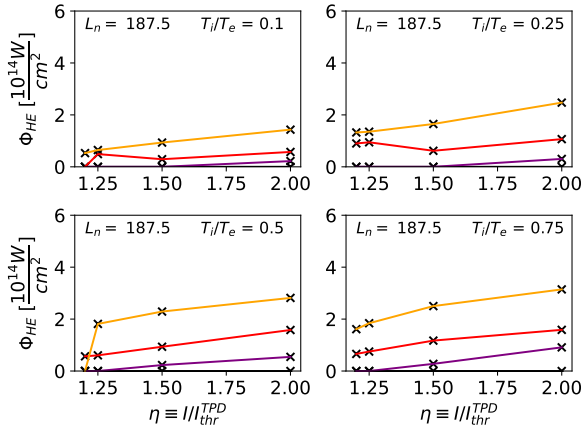

(d) Φ_{HE}, $L_n = 187.5$

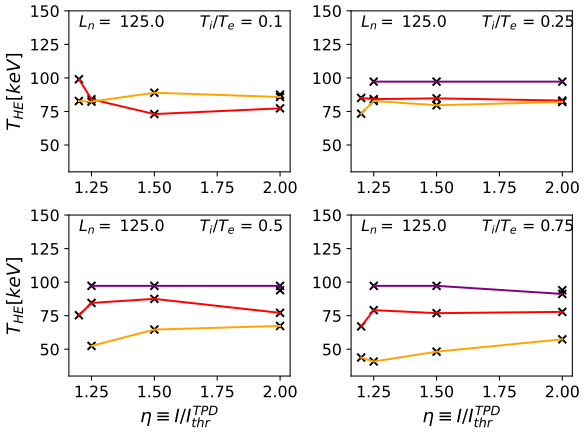

(e) T_{HE}, $L_n = 125.0$

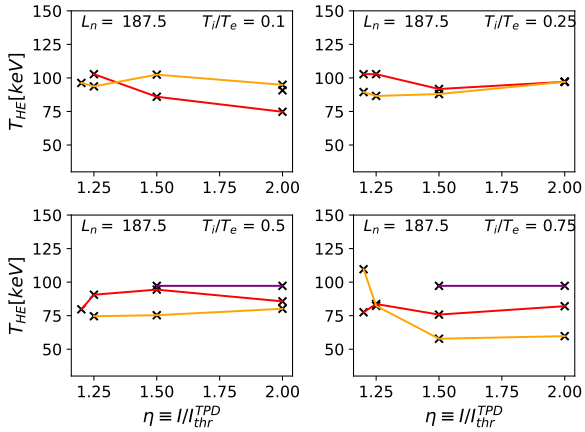

(f) T_{HE}, $L_n = 187.5$

Figure 4.42: Hot electron scaling analysis for the SRS+TPD system, both for a)-c)-e) $L_n = 125$ μm and b)-d)-f) for $L_n = 187.5$ μm.

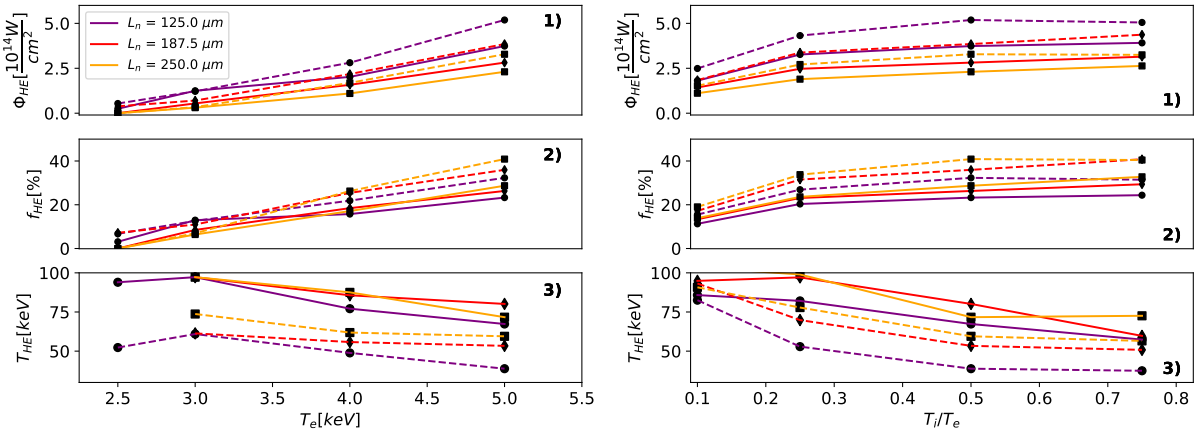

(a) (b)

Figure 4.43: a) HE quantities' scaling as a function of the electron plasma temperature T_e and for the different density scale lengths considered (different curves), with $T_i/T_e = 0.5$ and $\eta = 2.0$, while b) shows the HE scaling as a function of the ion-electron temperature ratio T_i/T_e at different L_n for $T_e = 5$ keV and $\eta = 2.0$. The full line refers to the TPD+SRS case, the dashed line the TPD only one.

This reduction is not constant, since in the same laser plasma conditions, with the exception of $L_n = 125$ μm, the two HE fractions report $f_{HE} \simeq 35\% - 40\%$ in the TPD only case, and $\simeq 25\%$ in the SRS+TPD one, leading to a decrease between $\simeq 29\% - 37.5\%$.

The HE average temperature behaviors are shown in Figs. 4.42e and 4.42f. Qualitatively, the behavior is similar to the TPD only case, but the overall temperatures reached are higher, in the $70 - 100$ keV range, in agreement to the literature [56, 57, 152], and it is caused by the stronger turbulence and the enhanced low-k modes generation from LDI cascade. The effects of the input laser-plasma conditions are the same, with η not influencing T_{HE}, T_i/T_e showing a decrease due to the weaker low-k EPW generation by turbulence, and T_e and L_n having no clear trends.

Overall, the addition of Stimulated Raman Scattering leads to a significant reduction of the HE conversion fraction across the entire scaling, but no change in scaling shape compared to the TPD only case. This is visible in Fig. 4.43, where the behavior between the SRS+TPD case (full line) and the TPD only one (dashed line) as a function of either T_e or T_i/T_e remains the same, with an overall reduction in quantities both for f_{HE} and Φ_{HE}, and an increase in T_{HE}, as previously specified. The decrease in the HE population observed in a reduced Φ_{HE} and f_{HE}, compounded with the additional reduction in HE conversion fraction and energy flux when 3D simulations are considered, can lead to HE quantities closer to experimental data. We hypothesize the presence of SRS, albeit small, is enough to disrupt the generation of EPW modes that allow resonance with the electrons, and an enhanced turbulence through the generation of additional EPW modes through the propagated scattered Raman light from absolute and convective SRS, which see a different critical density and therefore may act as a pump wave for further convective SRS at lower densities. A possible analysis to better understand such a phenomenon would be to extract the electron trajectories and the energy acquisition can be determined in the SRS+TPD case, similarly to the TPD one in Fig. 4.10 and 4.11. However, this it has not been carried out in this work due to limitations in the available computational costs, and future work is required to better explain this phenomenon.

To conclude this discussion, we show the beginning of a simple scaling law analysis for the HE conversion fraction as a function of the database independent variables (T_e, T_i/T_e, L_n and η). Note that a more comprehensive scaling law might be derived with the addition of more

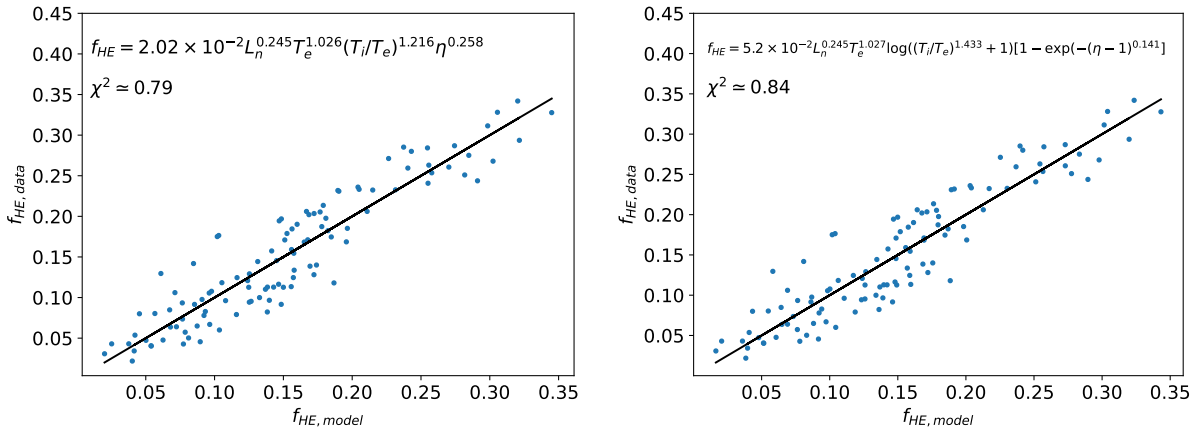

(a) (b)

Figure 4.44: Linear regression of scaling laws for the HE conversion fraction for the SRS+TPD system, for a) a simple and b) a modified power law.

physical phenomena, such as laser polarization effects, speckles, multi-beam effects, and 3D simulations. Moreover, due to the difference in datasets, this scaling law does not take yet into account the effects of a larger density scaling length, such as the ones at the National Ignition Facility (which will be discussed in section 4.4.4.1).

The HE conversion fraction data is fit with a simple power law of the form:

$$f_{HE} = 2.02 \times 10^{-2} \times \left[L_n^{0.245} T_e^{1.026} \left(\frac{T_i}{T_e} \right)^{1.216} \eta^{0.258} \right]. \tag{4.14}$$

The results are shown in the multi-variable linear regression in Fig. 4.44a. The HE conversion fraction scales roughly as $\sim 1/4$ with the density scale length, in agreement with the small changes in f_{HE} already discussed in the TPD analysis (section 4.3.5). The electron temperature relation is almost linear, similarly to the behavior displayed in Fig. 4.25b and 4.43a. The ion-electron temperature ratio is the oddest, since from Fig. 4.28 and 4.43b we observed a square-root like dependency. Finally, the laser drive strength η shows a similar behavior to L_n with a $\sim 1/4$ dependence, but this does not take into account the dependency on the instability threshold. Nonetheless, the minimum chi-square achieved by the fitted data corresponds to a figure of merit of $\chi^2 \sim 0.79$.

Several attempts were made in order to recover a similar dependency on T_i/T_e and η. An approach is to use the same definition as in [53] applied to both T_i/T_e and η. However, while it could be useful for correcting the drive strength, it was not useful for T_i/T_e. Using a shifted logarithm of the form $\log(T_i/T_e^d+1)$ appears to provide some degree of similarity, with a resulting parameter of 1.433. Moreover, the η behavior is recovered when the definition of [53] has been taken into account. However, modifying the scaling law from 4.14 always resulted in worse χ^2 values. In the light of the applied corrections, the modified scaling law becomes:

$$f_{HE} = 5.2 \times 10^{-2} \times \left[L_n^{0.245} T_e^{1.027} \log \left(\left(\frac{T_i}{T_e} \right)^{1.433} + 1 \right) \left(1 - e^{-(\eta-1)^{0.141}} \right) \right], \tag{4.15}$$

with a figure of merit of $\chi^2 \simeq 0.84$. Overall, a more detailed analysis which did not make it into this work is currently being considered.

4.4.4.1 SRS+TPD Hot electron analysis: NIF conditions

We now discuss the scaling performed for NIF-like conditions. The parameter space has been chosen with a density scale length of $L_n = 500$ μm, as shown in [57], with an electron temperature

ranging within $T_e = 4 - 6$ keV, a ion-electron temperature ratio within $T_i/T_e = 0.1 - 0.5$ and a laser drive strength from $\eta = 1.25$ to 4.0. These parameter ranges allowed for a reduced scan composed by 36 simulations.

The resulting HE energy flux and conversion fraction belonging to the NIF scan are illustrated in Fig. 4.45. In NIF-like conditions the simulations, plotted as full lines, reach energy fluxes at $\simeq 3.5 \times 10^{14}$ W/cm^2 at the highest values of η, T_e and T_i/T_e, while the HE conversion fractions reach maximum values similar to the OMEGA case, at $f_{HE,max} \simeq 36\%$.

In order to make a comparison between OMEGA and NIF-like conditions, the simulations at $L_n = 125$ μm have been shown. Therefore, the subset has been chosen to match the NIF simulations, at $T_e = 4, 5$ keV, $T_i/T_e = 0.1, 0.25, 0.5$ and $\eta = 1.25, 1.5, 2.0$.

The HE average temperature retains a similar behavior with respect to the previous analyses, reaching high temperatures (around $\simeq 100 - 120$ keV) at low drive strengths, only for the temperature to end at $\simeq 70 - 100$ keV as η increases (Fig. 4.45c. The low L_n simulations reached similar levels.

The hot electron energy flux Φ_{HE} follows a behavior similar to the scaling analyses done for both TPD and SRS+TPD in OMEGA-like conditions, increasing with the laser drive strength after a certain threshold is met, as well as with both the electron plasma temperature and $T_/i/T_e$ as well. Compared to OMEGA, the NIF scaling at its lowest considered plasma temperature ($T_e = 4$ keV) starts generating a measurable HE tail at $\eta \simeq 2$, caused by keeping the drive strength η the same despite increasing the density scale length, which in turn lowers the injected laser intensity by a factor of 4, therefore lowering both the SRS and TPD growth rate and preventing a measurable tail statistic to accumulate in quasi-stationary conditions.

According to Fig. 4.45a, the same reduction occurs for the HE energy flux, with a correlation between the reduction in the absolute TPD threshold and the one in HE energy flux. This is confirmed by the energy metrics, where the behavior is similar to Figs. 4.40 globally averaged Raman energy in quasi-stationary conditions is once more $\simeq 10^2$ times less than the average EPW energy. This would imply that, even in the considered NIF-like scaling setup, TPD is the dominant instability over Stimulated Raman Scattering, which is in contradiction to what has been observed in experiments at NIF. On this regard, it must be noted that the same conditions as in OMEGA are applied for the injected light, i.e. a plane wave in p-polarization. In the work of Gu et al. [56], a dominance of SRS for s-polarized laser light and a strong TPD presence in the case of p-polarization has been observed. This aspect could be a suggestion that the HE scaling can be improved by considering light polarization (s and p polarization, as well as polarization smoothing) in the parameter scan.

4.4.5 PIC simulations verification of SRS+TPD: SMILEI

A comparison between the LPSE results and other simulation codes has been carried out with the simulation code SMILEI (simulations performed by O. Budriga, National Institute for Laser, Romania).

SMILEI is a fully relativistic electromagnetic Particle In Cell (PIC) code that solves a discretized distribution function f_s, which represents a population of "quasi- virtual- / macro-" particles. f_s is solution of the system of equations composed by the Vlasov equation for the particles' kinetic description, and the Maxwell's equations that give the electromagnetic field from which the Lorentz's force on the particle can be derived. The subscript s denotes the different particle species with mass m_s and charge q_s. Provided a spatial grid composed by several points in space, also called "nodes", and the region between the nodes labeled as a "cell", PIC codes integrate Vlasov's equation along the continous trajectories of the quasi-particles within each cell, while the fields are solved at the nodes. The fields influence the particle trajectory within a cell through the Lorentz's force, and the particles' movement generates an electromagnetic field that modifies the fields at the nodes, therefore establishing the feedback loop consistent with the nature of a plasma. A more detailed description of the SMILEI code can be found in [91].

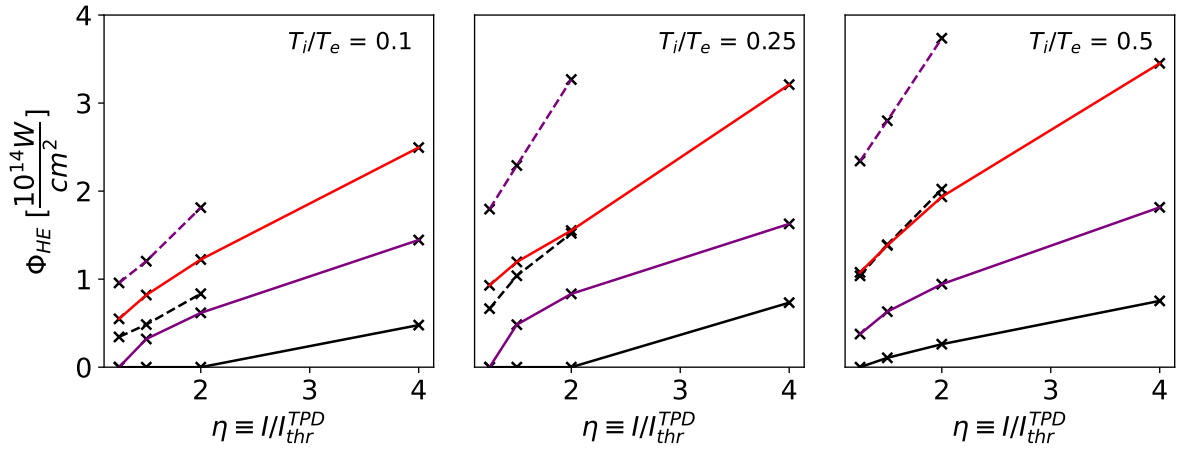

(a)

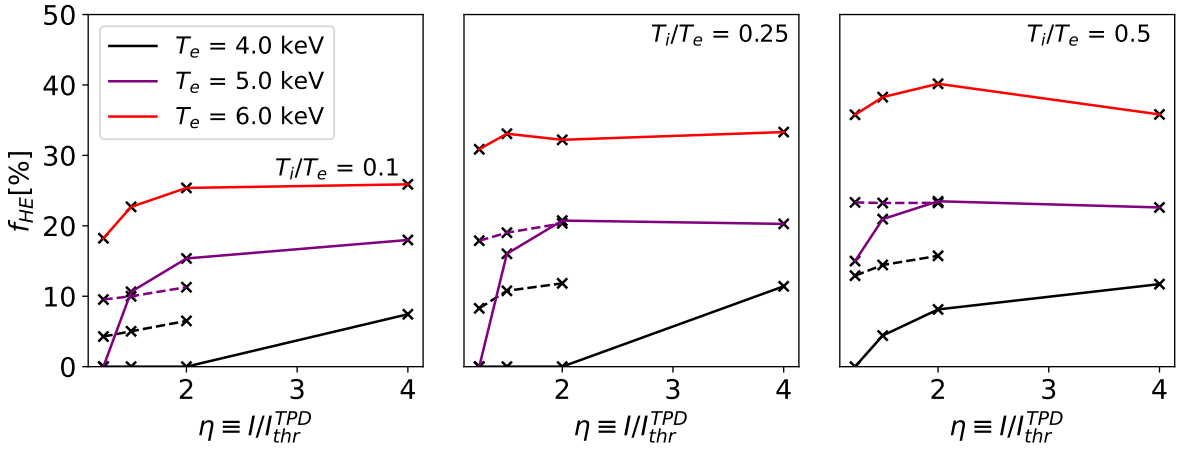

(b)

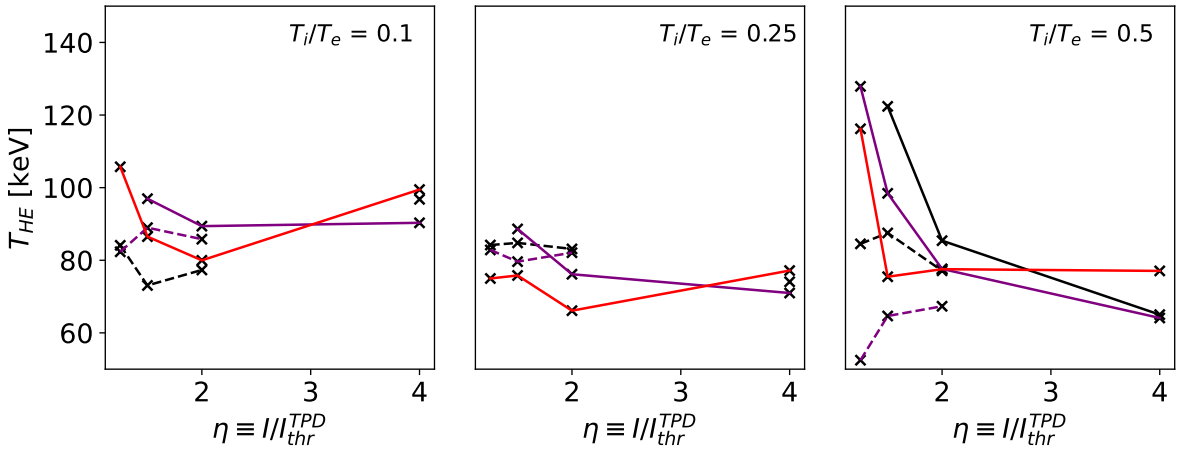

(c)

Figure 4.45: a) Hot electron energy flux b) HE conversion fraction and c) HE average temperature scaling analysis in NIF conditions. The color of the curves refer to different electron temperatures, while the different subplots refer to different T_i/T_e. The full lines represent the $L_n = 500$ μm case, while the dashed lines belong to the $L_n = 125$ μm one.

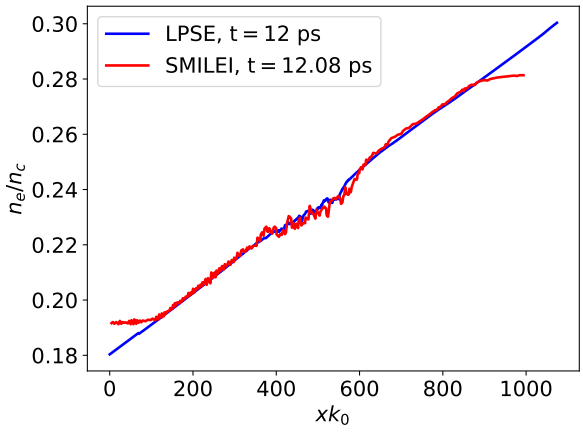

Figure 4.46: Quasi-stationary electron density profile for both LPSE (blue) and SMILEI (red) for the time t $\simeq$ 12 ps. Courtesy of O. Budriga, National Institute for Laser, Romania.

The comparison has been carried out for a single simulation, with SRS+TPD and laser pump depletion. The laser plasma conditions chosen for both the LPSE and SMILEI simulations were $T_e = 4$ keV, $T_i/T_e = 0.5$, $L_n = 125$ μm and $\eta = 1.5$. By the definition of the laser drive strength, the laser intensity injected in vacuum is $I_{laser} = 9.637 \times 10^{14}$ W/cm^2. The SMILEI simulation is chosen to follow the single ion species description of LPSE, with an average ion charge of $\langle Z \rangle = 3.5$ for a CH plasma at 50% fraction for both C and H. The plasma critical density is $n_c \simeq 9 \times 10^{21}$ cm^{-3}. The SMILEI simulation has been done in 2D, as the LPSE one, in a 56×7 μm $\times$ μm grid instead of the 60×12 μm $\times$ μm grid used by LPSE, in order to keep the same resolution on the x and y axis, with a grid step of 5 nm. As a consequence, the density extremes are ranging between $n_e/n_c = [0.18 - 0.292]$ in the SMILEI simulation with the same linear profile as the LPSE one. This does not change the physics within the simulation, since the focus was on the quarter critical region. Finally, the SMILEI simulation time has been carried for 25 ps, with a time step of 17 as.

The density profile of the SMILEI simulation closely follows the LPSE one when in quasi-stationary conditions, as shown in Fig. 4.46, despite some notable differences in the density profile at the simulation borders, due to the SMILEI's thermalized boundaries for the particles. At densities between $n_e/n_c \simeq 0.22 - 0.24$, the density profile becomes flatter, due to the turbulence generated by EPWs and Raman scattered light. At densities between $n_e/n_c \simeq 0.24 - 0.255$, the density profile is mostly distorted by the turbulent plasma due to the EPW generation and Raman scattered light, therefore inducing density profile steepening close to the resonance region.

The SMILEI code includes the evolution of macro-particles in the domain with a kinetically computed trajectory. Therefore, the reproduction of energies and velocities of such particle population is one of the main strengths of a PIC code. The usefulness in comparing the LPSE code to a PIC one is to observe the discrepancy between said particle-related quantities with the hybrid approach LPSE employs through the HPE module discussed in section 3.3.4, since the LPSE macro-particles do not generate fields, and therefore do not provide a feedback for the LPSE field solver aside from the Landau damping calculation through the velocity distribution function. While SMILEI does not has the VDF as an output, we can compare the emission given by the VDF in LPSE shown in Fig. 4.47a to the emitted electrons' distribution function (in cm^{-3}keV^{-1}) for the time snapshot at t = 14 ps in Fig. 4.47b, which is considered in steady-state regime. The figure represents only a quarter of the entire emission domain, with the assumption that the emissions at angles of $(270° - 360°)$ are symmetrical to the ones showed. The electrons ranging from $\simeq$ 50 keV to $\simeq$ 200 keV constitute the largest population, and are emitted at a maximum angle of $\alpha_{HE} \simeq (-30°, +30°)$ if the assumption of the emission being symmetrical

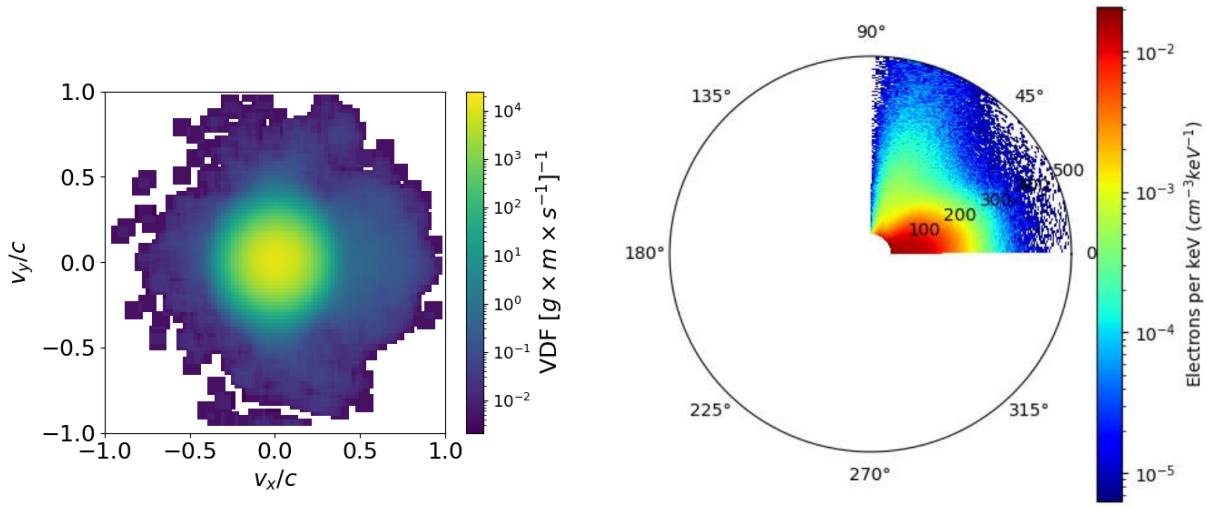

(a) (b)

Figure 4.47: a) Velocity distribution function as collected from the LPSE code and b) Electron angular distribution for t = 14 ps from the SMILEI code (Courtesy of O. Budriga, National Institute for Laser, Romania). The radial values correspond to the energy (in keV) of the emitted electrons.

is considered valid. This is consistent with the emission found by the LPSE VDF, where the electrons beyond 50 keV are emitted with a spread of about $\pm 30^\circ - 35^\circ$. A more homogeneous emission happens for electrons up to $\simeq 300$ keV. This can be attributed to electron acceleration at high energies by EPW low-k modes due to LDI cascade. Moreover, in the SMILEI data there occurs a transversal emission at $\sim 70^\circ - 80^\circ$, which could be caused by sidescattered EPW modes due to SRS [21], up to $\simeq 400$ keV. This population however is more than one order of magnitude smaller than the main population at $\simeq 50 - 200$ keV, and about 3-4 orders of magnitude lower than the bulk overall, and therefore negligible. The LPSE VDF reports a similar emission, albeit for lower energies (at velocities $\sim 0.7c$, corresponding to ~ 200 keV), and in this case too is small compared to the forward emission. Overall, the emission angle observed in LPSE has been confirmed to be similar in the SMILEI code as well, with the implication that the majority of the high energy electrons from the HE tail are emitted towards the target at a relatively narrow angle.

The differential electron energy flux has been extracted from the SMILEI simulations as well, expressed in the SMILEI code in $\mathrm{Wcm^{-2}keV^{-1}}$ (Fig. 4.48). While the plasma bulk is almost identical, the comparison between the fit and data profiles show some notable features between the data and the fit in SMILEI, starting from $\varepsilon_e \simeq 50$ keV, at the beginning of the hot electron tail. At energies between $50 - 200$ keV, the HE tails of both profiles closely match between each other, with a slight overestimation of the fit between $75 - 125$ keV, thus implying that the fit of the SMILEI data predict a similar HE generation at such energy intervals. At $\varepsilon_e \gtrsim 200$ keV, the SMILEI fit does not follow the data anymore, with the data much lower values than the fit. This might suggest that the two-temperature fit of the high-energy HE tail used is insufficient to correctly represent the HE data at the highest energies.

Moreover, comparing the SMILEI fit and LPSE one, it has been calculated that LPSE overestimates HE generation for a HE conversion fractions of $f_{HE} \simeq 14.07\%$ for LPSE, while SMILEI predicts $f_{HE,fit} \simeq 5.11\%$ for the fit and $f_{HE,data} \simeq 3.3\%$ for the data. However, the temperatures obtained for the two maxwellians with SMILEI are $T_e = 4.5$ keV for the bulk $T_{HE} \simeq 77$ keV for the HE tail which, compared to the bulk temperature $T_e = 4.24$ keV and HE tail $T_{HE} \simeq 88.84$ keV found in LPSE, account for a reasonable difference between the two fits' bulk of $\simeq 6\%$ and tail of $\simeq 13\%$ respectively.

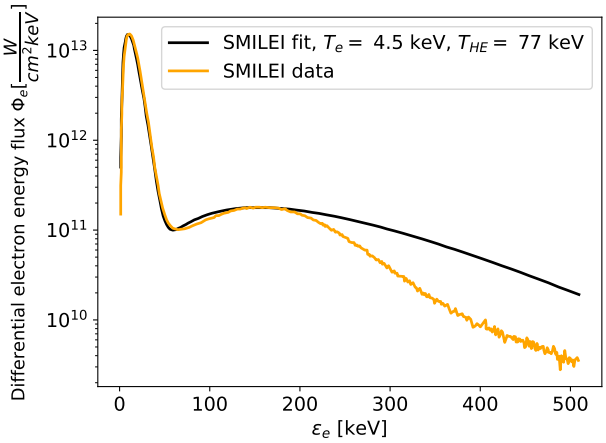

Figure 4.48: Energy spectrum of the differential electron energy flux (in $\mathrm{Wcm^{-2}keV^{-1}}$) considered beyond t = 12 ps collected by the SMILEI code (orange curve) and the two-temperature fit used for the data. The LPSE temperatures obtained are T_e = 4.24 keV and T_{HE} = 88.84 keV. Courtesy of O. Budriga, National Institute for Laser, Romania.

The differences between the LPSE fit and the SMILEI data might be caused by additional physics not considered in the LPSE code. As previously stated, the SMILEI simulation uses the same physics used for the LPSE one, considering a 2D SRS + TPD system. Laser pump depletion is enabled in both cases, for a single beam laser (no multi-beam effects) in p-polarization, incident on one of the system's boundaries. SBS and plasma flow has been turned off in both cases. However, plasma turbulence can still manifest in SMILEI. The main reason of the change for the high-energy tail not following a Maxwell-Boltzmann distribution might be caused by the particles in a PIC code generating their own electromagnetic field, which in turn interferes with the laser and Raman field as well as the EPWs in the system. Any charged particle population moving on average in a single direction will generate a current density, and therefore an electromagnetic field, proportional to their velocity. This can interfere with the interacting EPWs, therefore reducing the probability of resonating with the phase velocity of said EPW, with this interference becoming stronger at higher energies / velocities, thus resulting into a lower population of highly energetic particles and therefore a lower HE tail. Such mechanism does not occur in LPSE, where the macro-particles are influenced by the fields in the system, but they do not generate any field in return.

While the cause of LPSE overprediction of the HE generation must be investigated, the high energies at which the two temperature fit fails, and its associated lower population due to a lower electron energy flux (an order of magnitude lower on average at the highest energies), might suggest that this could be a negligible effect. However, more analysis and data are required to further confirm this aspect, as well as to derive the HE conversion fraction and energy flux related to the SMILEI case.

4.4.6 Comparison between LPSE and experiments + PIC codes from previous work

In this chapter we perform comparisons with previous experimental campaigns of LPSE and other PIC results.

The work of Ref. [43], previously reported also in [48, 49], shows such an experimental setup for OMEGA scale experiments. The campaign used special targets with an outer diameter between 415 and 500 μm, composed of a plastic (CH) ablator with thickness between 35 and 50 μm. While the core was composed by CH with Ti doping at 5%, the experiments showed the

laser to ablate ~ 12 μm of the CH shell. The experiments were performed in the optics of the Shock Ignition (SI) scheme. One of the major goals was to observe the generation of shocks at $\gtrsim 300$ Mbar at the SI laser intensities of 10^{15-16} W/cm^2, pressure required for the main shock to achieve ignition in the fuel assembly. The experimental setup included the shot of the 60 beam configuration at the OMEGA facility, with a laser energy of $I_{Laser,SB} \simeq 6 \times 10^{15}$ W/cm^2 at the initial target surface at the peak of the laser pulse. The laser was equipped with phase plates, polarization smoothing [163] and smoothing by spectral dispersion (SSD) [164]. Each beam possessed an intensity of 4×10^{14} W/cm^2 when SSD was on and 6×10^{14} W/cm^2 when SSD was off, comparable with the laser intensity injected in the LPSE simulation dataset. The measured electron and ion plasma temperatures were of $T_e = 3.6$ keV and $T_i = 0.7$ keV, respectively, which can be interpolated between the conditions of $T_e = 3-4$ keV and approximated to $T_i/T_e \simeq 0.25$ in the LPSE simulation dataset. The experimental density scale length calculated at the quarter critical density is the same as in the LPSE scaling, $L_n = 125$ μm.

For the purposes of this comparison, the main feature is the similarity of the measured hot electron conversion fraction reported in the experimental campaign for a CH plasma. Moreover, another important feature is the effects of SSD on the HE generation. All [43, 48, 49] report a time-integrated conversion efficiency of $\simeq 8\%$. In particular, this is true for [43] when SSD is off, while when SSD is turned on, a weakening in HE production by a factor of 2 (i.e. $f_{HE} \simeq 4\%$) has been observed. This would imply that including SSD in future SRS+TPD scaling analyses might be beneficial for a more detailed physical picture of HE generation. The HE conversion fractions for LPSE in similar laser plasma conditions (Fig. 4.42a) show a HE conversion fraction reaching up to $f_{HE} \simeq 8\% - 12\%$ for the highest drive strengths $\eta = 1.5 - 2$, corresponding to a laser intensity of $I_{laser} \simeq 9.6 - 12.8 \times 10^{14}$ W/cm^2, well above the single beam intensity in the experiment. While the f_{HE} obtained in LPSE is taken as an instantaneous value across the whole quasi-stationary regime, the values are promisingly close to the experimental conditions. While the HE conversion fraction is similar, the LPSE code overestimates the HE average temperature by 20 keV, which could be caused by imprecision in the fitting method for the energy flux in the LPSE codes by difficulties in interpreting the experimental data.

Another example of previous work is given in [57], where the simulation code EPOCH [60] has been used to perform two simulations for OMEGA and NIF scales, respectively. The laser intensity used is higher, at 2×10^{15} W/cm^2. While this intensity is above the one used in the LPSE scaling analysis, reaching at their highest $\simeq 1.2 \times 10^{15}$ W/cm^2 for OMEGA-like simulations, and 8×10^{14} W/cm^2 for NIF-like ones, we can extrapolate the HE conversion fraction under the assumption that the LPSE simulations reach a plateau in f_{HE} after the instabilities develop. The laser-plasma conditions for the OMEGA simulation in [57] were $L_n = 170$ μm, $T_e = 3.5$ keV, while for the NIF simulations were $L_n = 600$ μm, $T_e = 4.5$ keV. Both simulations were carried out in a CH plasma and with an ion temperature given by $T_i/T_e = 0.5$. While the simulation conditions are not exactly the same as in Figs. 4.42b and 4.45b, they can be extrapolated by using the inferred power law found in section 4.4.4, Eq. 4.15. However, we must remind that the scaling laws in section 4.4.4 has been derived without taking the HE data of the NIF scaling into account. While a scaling law for the average HE temperature has not been computed due to them having no clear trend (section 4.4.4), we can assume they possess similar temperature ranges to the preexisting scaling, between $75 - 90$ keV for OMEGA (Fig. 4.42b) and $75 - 100$ keV for NIF conditions (Fig. 4.45c). The values obtained by interpolation with the LPSE scaling data are $f_{HE} \simeq 5.7\%$ for OMEGA and $f_{HE} \simeq 10.1\%$ for NIF conditions. The work done in [57] reports HE conversion fractions for OMEGA of $f_{HE} \simeq 11.2\%$ for energies above 100 keV, much higher than the ones from LPSE. For the NIF simulation, the HE conversion fraction reached is similar, at $f_{HE} \simeq 11.2\%$ for electron energies $\varepsilon_e \gtrsim 100$ keV. While these data are promising, the NIF simulations report a SRS signature that is different than the one in this work, possessing a fraction of backscattered SRS of 23.5%, while for LPSE is of the order of $\simeq 10^{-1}\% - 10^{0}\%$, similarly to the OMEGA case. Since light polarization influences

the presence of SRS and TPD in the plasma [56], this could be caused by having considered only p-polarization in the LPSE simulations, and considering a scaling in s-polarization would provide a better comparison with the reference's data.

NIF experiments have been carried out in [63], with the support of the simulation codes DRACO [165] for deriving the laser-plasma conditions and EGSnrc [166] for Monte Carlo electron-photon transport calculations. The experiment has been conducted using a CH planar target configuration with 96 incident laser beams, half of the 192 available at NIF, divided in 32 "inner" beams (at an angle of incidence of 23.5° and 30°) and "outer" beams (at 44.5° and 50°). The plasma temperatures and density scale lengths estimated in the experiment by the code DRACO was 4.4 keV and 690 μm for the inner beams, 4.7 keV and 500 μm for the outer ones, respectively. The reported HE conversion fraction in the two cases are $f_{HE} \simeq 0.7 \pm 0.2\%$ to $2.9 \pm 0.6\%$ for the inner beam configuration, with a beam intensity between $5.9 - 14 \times 10^{14}$ W/cm^2 for the inner beams, and $6.2 - 11 \times 10^{14}$ W/cm^2 for the outer ones. Overall, there is a significant difference with the LPSE simulation results, which result in a $f_{HE} \sim \mathcal{O}(10^1)$ by using Eq. 4.15. These higher fractions can be attributed to the lack of s-polarization in the system, as well as the absence of SSD (which in [63] was included), which would reduce the f_{HE} significantly [43]. Moreover, the HE temperature observed is much lower than in the LPSE simulations ($T_{HE} \sim 75 - 100$ keV), with $T_{HE} = 45 - 55$ keV and 62 keV for the inner and outer beam configuration, respectively. This value has been calculated from a one-temperature fit of the hard x-ray spectra, instead of a two-temperature fit for the energy flux as in LPSE.

Overall, the simulations and experiments here briefly described show the LPSE scaling analysis of SRS+TPD presented in this work being a promising start for a more complete characterization of HE quantities up to experimental conditions and, in general, to the state-of-the-art for deriving HE quantities. In order to achieve this, the addition of more physics to the LPSE is required, such as smoothing by spectral dispersion (SSD), which drastically changes the HE production in the plasma system, as well as the consideration of multibeam effects [55, 145], and whether or not considering a spherical target geometry instead of a simpler planar one. The overall comparison between LPSE and the literature [43, 57, 63] has been summarized in Table 4.3.

4.5 Conclusions

In this chapter, the results of the LPSE scaling analysis have been presented. We started with identifying the main laser-plasma parameters that served as the basis of the HE database, the LPSE equations, the boundary conditions used, the damping rates calculations and the parameters used for the kinetic module of LPSE. First, this work has been done for a physical system where only TPD was included as major process, and we later added SRS.

As far as the TPD system is concerned, a single 2D TPD simulation has been analyzed, to derive a physical picture for each simulation. Care has been taken in explaining not only the behavior of the observed EPW potential and IAW field, but more importantly the derivation of the HE quantities starting from the energy metrics of each simulation, in particular the fitting of the electron energy flux as a function of the electron energy. Moreover, considerations on the electrons' direction and angle of emission have been taken through the observation of the associated velocity distribution function (VDF), as well as the derivation of the hot electrons and the end of the plasma bulk's particle trajectories and their energy acquisition in the longitudinal direction. Finally, an overall estimation of the energy balance, in particular observing the laser transmitted through the resonance region at $n_c/4$ has also been observed.

After such analysis, the scaling for 2D TPD has been considered in full. The focus was mainly in observing the changes in the HE energy flux, conversion fraction and average temperature for changing the different laser-plasma parameters considered as the basis of the database. These quantities have been found by assuming a quasi-stationary regime where the laser-plasma

	Facility	Beams and polarization	Geometry	$I_{laser,SB}$ [10^{14}W/cm^2]	T_e [keV]	T_i/T_e	L_n [μm]	Measured f_{HE}, T_{HE}	LPSE f_{HE}, T_{HE}
[57], EPOCH	OMEGA	1, ?	Planar	20	3.5	0.5	170	11.2%, $\gtrsim$ 100 keV	5.7%, 75 – 90 keV
[57], EPOCH	NIF	1, ?	Planar	20	4.5	0.5	600	11.2%, $\gtrsim$ 100	10.1%, 75 – 100 keV
[43, 48, 49], Experiment (SSD off)	OMEGA	60, PS	Spherical	6	3.6	0.195	125	7.9% 60−80 keV	8% – 11.8%, 75 – 90 keV
[63], Inner beams	NIF	32, PS	Planar	5.9 – 14	4.4	?	690	0.7 ± 0.2% - 2.9 ± 0.6%, 45 – 55 keV	∼ 10%, 75 – 100 keV
[63], Outer beams	NIF	64, PS	Planar	6.2 – 11	4.7	?	500	1.2±0.2 - 2.6 ± 0.5, 62 keV	∼ 10%, 75 – 100 keV
SMILEI	NIF	1, p-pol	Planar	9.64	4	0.5	125	3.3%, ∼ 77 keV	14.07%, 88.84 keV

Table 4.3: Comparison between previous work, both simulations and experiments, and LPSE. PS stands for "polarization smoothing".

instabilities, turbulence and pump depletion are in equilibrium. We observed that there is an increase in HE flux, but no increase in the HE conversion fraction at higher laser drive strength η values, leading to the assumption that the HE flux is proportional to the increase in laser energy, leading to a flat HE fraction, and to a behavior that is described in [53]. The electron temperature T_e instead leads to a linear increase in f_{HE}, and a quadratic one in Φ_{HE}, with a presence in all of the physics in the simulations. The T_i/T_e ratio has a square-root like behavior, due to its control over the turbulent secondary processes of LDI and LW collapse. Finally, there is a weak dependence on the density scale length L_n, with a decrease HE flux because of the longer plasma, and a higher HE temperature due to the higher probability for electrons acquire energy through staged acceleration [152]. These analyses have been completed by proposing simple scaling laws for the observed data. However, in some cases more data are required for deriving better behaviors.

After this scaling, a comparison between 2D and 3D TPD simulations has been carried out. The analysis of the EPW potential in Fourier space showed that TPD is confined in a 2D plane, emitting the majority of EPWs and therefore accelerating electrons on the longitudinal direction. The simulation metrics show a small reduction in energy fractions absorbed and an increase in transmittivity, due to an increase of the phase space from 2D to 3D. The HE energy flux and conversion fraction both slightly, while the HE temperature increases. Most notably, f_{HE} decreases almost by $\simeq 20\%$. A comparison between a reduced scaling analysis has been performed, albeit with laser pump depletion off, leading to slightly lower HE conversion fractions. We therefore infer that 3D effects in the TPD only case provide a more correct accounting of HE generation, but not significant, due to the 2D nature of the instability.

The analysis continued by including Stimulated Raman Scattering (SRS) to the 2D simulations. After a description of the LPSE equations used and database entries, comparisons between TPD and SRS+TPD have been carried out for the EPW potential and IAW fields. SRS occurs at earlier times than TPD, with SRS+TPD showing a similar behavior to the TPD only case once quasi-stationary conditions have been achieved. However, the Fourier spectrum

shows a regrouping of EPW modes towards lower wave numbers, showing less high-k EPW modes and an increase in LDI activity. The Raman field has been observed as well, showing the light being stopped at quarter critical and then propagating mainly towards lower densities, with an outgoing field of one order of magnitude lower than the one at $n_c/4$. This results into values of Raman energy and reflectivity about two orders of magnitude lower than the EPW activity, leading to the conclusion that TPD is the dominating instability in the system, which agrees with experiments at the OMEGA facility. However, despite the energies being similar to the TPD ones, the SRS+TPD system reports lower HE fluxes and fractions by a factor of $\simeq 1.58$. Therefore, it has been hypothesized that Raman generation from SRS, despite being significantly weaker than TPD, is enough to disrupt the high-k EPW generation that match electrons with resonant phase velocities. However, more work is required on this part to better understand the causes of this reduction.

The HE scaling analysis of SRS+TPD has then been carried out in a similar fashion as the TPD one. Since TPD is the dominant instability, a comparison between changing laser-plasma parameters both in the TPD and SRS+TPD case have been made, determining similar behaviors of the SRS+TPD case to the TPD scaling. A consistent reduction in HE fraction and energy flux has been observed, with a similar range of HE temperatures. At this point, a multi-variable scaling law has been proposed, encompassing all parameters in the database for the HE conversion fraction. While the results require further study, they show a promising formula to interpolate the HE fraction for conditions within the bounds of the scaling.

At this point, all the scaling analyses were done for OMEGA like values of density scale lengths. Therefore, a scaling with NIF-like conditions ($L_n = 500\ \mu$m) has been ran and compared with OMEGA-like conditions. This shows lower HE fluxes than the OMEGA ones, but a similar HE conversion fraction. Most notably, the Raman signature is still very weak compared to the literature for NIF simulations and experiments. A possible reason is that the simulations were carried out with p-polarized light, and s-polarization (where SRS would dominate) has not been considered. The effects of the polarization being important [56] imply that a future scaling analysis of SRS+TPD in s-polarization will be beneficial for the purposes of this scaling analysis, but it should be carried in 3D to capture the correct TPD behavior.

Up to this point, the scaling analysis was done with LPSE only without comparisons with codes or experiments. We performed a first comparison with the Particle In Cell (PIC) code SMILEI for one 2D SRS+TPD simulation (courtesy of O. Budriga, National Institute for Laser, Romania). A comparison of the density profile shows little difference between the two, particularly around the quarter critical region where density profile steepening is being observed. Comparing the VDF from LPSE to the angular distribution from SMILEI, we found a similar electron emission in the forward direction, with the electrons being preferentially emitted towards the ICF target at an angle of $\alpha_{HE} \simeq (-30°, +30°)$. The electron energy flux spectrum has been observed as well, identifying a good similarity between the SMILEI data and the LPSE fit up to energies belonging to the HE tail up to 200 keV, after which the SMILEI simulation shows the fit of the HE tail using a 3D Maxwell-Boltzmann distribution is not valid anymore. That said, the low statistic of the HE tail at high energies could lead to the conclusion that the LPSE and SMILEI reach a good level of agreement on the HE generation.

Finally, we made comparisons with previous work in the literature, both simulations and experiments, in order to understand which phenomena are missing in the scaling. We observed that while the HE quantities show an already promising similarity, several effects must be considered, in addition to the 3D aspect. Notably, the consideration of multi-beam effects and polarization smoothing and Smoothing by Spectral Dispersion (SSD).

Overall we conclude that, while this scaling analysis is showing promising results in the determination of the HE quantities, it needs to include more sophisticated phenomena to be included in order to make more meaningful comparisons with experimental data and be implemented into radiation hydrodynamic codes.

Chapter 5

Conclusion

The objectives of this Ph.D. were the following:

- **Investigation of hot electron generation mechanisms.** In ICF conditions, electrons can be accelerated almost exclusively by EPWs, which are in turn generated by laser plasma instabilities. An investigation of the relevant instabilities therefore must be established first.
- **Simulation of a hot electron database.** Develop a database of HE quantities by using a set of parameters that relates the laser and plasma conditions to HE characteristics.
- **Characterization of HE generation.** Provide physical explanations to the HE generation behavior depending on laser and plasma parameters. Compare similar results with simulations that included more physics (such as considering 3D effects, longer scale lengths for different facilities (NIF)).
- **Comparison with PIC code SMILEI and literature.** Validation of the LSPE results comparing them to the SMILEI PIC code, as well as comparisons with past literature and experiments.

With these objectives having been set, we present the conclusions and the current progress of this work.

5.1 Investigation of hot electron generation mechanisms

The hot electron generation in ICF plasmas is related to the activity of EPWs. These waves transfer energy to a small population of electrons in a staged process, creating a HE population characterized by higher energies than the rest of the Maxwell-Boltzmann plasma. In literature, HE generation is tied to a class of laser-plasma nonlinear couplings that require a "pump" wave to decay into two "product" waves, provided they satisfy some matching conditions both in wave number and frequency. These "parametric" instabilities are shown to be SRS, TPD and the secondary process of LDI. Moreover, the HE acceleration mechanism is due not only to the instabilities' EPWs, bu also the plasma turbulence generated by these instabilities. Weak turbulence, mainly from the multiple decay of LDI into long wavelength waves, produces a field intense enough to produce localized depressions in density profile, leading to the formation of "cavities / cavitons" that trap the EPWs and act as their resonator. These waves can transfer energy to electrons and therefore be damped, until the trapped EPW energy is not sufficient to sustain the cavity, which collapses. This process, called "LW collapse", is the origin of a strong turbulence within the plasma.

The simulation code chosen to simulate these phenomena must satisfy several conditions. First, it should resolve the kinetic scales necessary for HE generation, including strong plasma

turbulence, SRS,TPD and LDI. Here, we neglect resonance absorption (RA) and convective SRS to focus on the region at quarter critical density. Second, the prospect of resolving the other goal in this work (characterize HE generation through the establishment of a database of HE quantities) meant that the simulations had to be as computationally cheap as possible. With these goals in mind, the "Laser Plasma Simulation Environment" (LPSE) hybrid code is used. LPSE uses a linear solver for the fields of the laser light, scattered light, EPWs and an hydrodynamic description of the IAWs. This field solver uses the Zakharov model to take into account strong plasma turbulence without resorting to the complete kinetic description. The simplification consists in choosing a representative frequency for the EM waves, as well as the EPWs, instead of considering their entire Fourier spectrum. This allows for a lower computational time and the possibility of carrying out a large number of simulations. However, the downside of this simplification is that the code is unable to resolve phenomena that occur from vacuum to quarter critical, such as convective SRS, at the same time as the absolute instabilities. For the HE part, the HPE module is implemented in the code, which generates a population of virtual / macroparticles that evolve according to the fields in the system. In contrast with more refined PIC codes, these particles do not provide feedback to the field solver in the form of generated fields, with the exception of a kinetically computed Landau damping.

After these premises, LPSE has been used to perform simulations of 1D SRS, verifying the field and growth rate against theory. Moreover, a comparison between the theoretical and LPSE-calculated absolute SRS threshold served to validate the code ability to capture it. Moreover, the main features of TPD expected from theory were tested in a 2D simulation, including the growth rate. In particular, the TPD threshold was once again tested against theory. Adding LDI and LW collapse, we investigated the effects of turbulence on the system, which in this case was caused by TPD, LDI and LW collapse. In particular, the condensation towards low-k modes is observed, as well as cavitation activity. Finally, we observed the effects of HE generation on the simulation, especially through the use of energy metrics for the simulation considered, such as a decrease in laser transmittivity and a fraction of power absorbed by Landau damping. Simulations of TPD only and SRS+TPD have been carried out with the intent to completely analyze their behavior. In particular, the electron energy flux collected from each simulation was used to extract the HE quantities. The particle population was characterized by a two-temperature fit, fitting the "bulk" of the plasma following the Maxwell-Boltzmann distribution with average temperature set to the thermal plasma, and using a separate Maxwell-Boltzmann distribution fitting the high-energy hot electron "tail". The fit was found to be accurate in the majority of conditions.

5.2 Simulation of a hot electron database

The second step after testing the LPSE capabilities for the investigation of HE generation was to use the code for a wide range scan of the HE generation behavior. Before doing this scan, the key laser-plasma conditions that constitute the parameters in this database had to be identified. Moreover, this database had to be simple enough to not perform an excessive number of simulations, while at the same time being significant enough to encompass the relevant physics. These parameters have been identified to be the electron temperature T_e, the ion-electron temperature ratio T_i/T_e, the density scale length L_n, and the laser drive strength η. These parameters control the instabilities in the plasma through the damping rates, both collisional and Landau, are present in the theory of development of the field coupling equations and of turbulence, and in the laser intensity thresholds required to achieve such conditions. The simulations have been carried out for a scan of such parameters in a simplified system of a plane wave in p-polarization only, in planar geometry, with a single ion species plasma equivalent to CH. Moreover, the simulation time has been kept constant for all simulations in the scaling. The HE quantities obtained in such a way were collected under the assumption of quasi-stationary

conditions, where all the physical processes have reached equilibrium with each other in the light of limited growth due to the finite energy of the laser and other saturation mechanisms. While this assumption is not always true due to the lower growth rate at low intensities, and therefore the necessity to extend the simulation time, the events in which this does not occur belong to low parameters in the scaling, and limited in number.

A scaling of 2D TPD has been performed to model a simple first HE scaling analysis. The energy flux allowed to obtain the average temperature of the HE maxwellian, the HE energy flux and the conversion fraction. Simulations show that the electrons in these conditions reach HE conversion fractions up to 40% in the strongest laser plasma conditions considered, with a corresponding HE energy flux of $\simeq 5 \times 10^{14}$ W/cm^2. While fitting the maxwellian tail is more difficult at low values of η due to the lower HE population statistic, the HE population has been identified to possess an average HE temperature between 35 keV at the lowest T_e and L_n, to 100 keV at the highest T_e, L_n. This has been achieved most consistently at the highest values of η, where the HE tail statistic was the most developed.

A similar scaling has been done for a 2D system that included both SRS and TPD into the scaling analysis. The HE results are overall similar to the TPD only case, albeit the highest HE fluxes and conversion fractions are reduced to $\simeq 4 \times 10^{14}$ W/cm^2 and $\sim 30\%$ respectively. The HE average temperature were increase in a range between 50 and 100 keV. This suggests a competition between SRS and TPD, which has been observed to result into a negligible value of reflected Raman light after an initial growth of SRS, meaning that TPD is still the major HE generation mechanism. The SRS influence however is enough to interfere with EPW generation and mainly the TPD behavior.

5.3 Characterization of HE generation

After collecting the data, several trends and behaviors have been observed in the HE quantities (mainly the HE conversion fraction and flux) when varying parameters one by one. These results have been qualitatively common for both the TPD and SRS+TPD results, despite having some differences from a quantitative point of view.

An increase in laser drive strength injects a higher laser intensity into the system, and the instabilities are characterized by a higher growth rate because of it (and therefore develop at earlier times). Moreover, a saturation in laser transmittivity at similar quasi-stationary level occurs in the 2D TPD scaling analysis, independently on the drive strength considered. The analysis in the same laser plasma conditions of the system while progressively adding laser pump depletion, IAWs (LDI and turbulence) and the HEs lead to the hypothesis that the combination of IAWs and the kinetically computed Landau damping imposes a lower limit to the laser transmittivity and an upper one on EPW generation, while only LDI and LW collapse impose an upper limit to transmission (and a lower one on EPW growth). The HE energy flux increases for increasing η due to the higher laser energy. However, the HE conversion fraction behavior tends to stay at a similar level no matter the value of η considered after the instability threshold has been overcome, suggesting a linear dependence between the HE flux and laser intensity increase. While possessing high HE temperatures, low η simulations tends to possess a lower HE tail statistic, rendering the fit difficult. A possible individual scaling law has been inferred for 2D TPD, in an attempt to follow the scaling imposed in [53]. While the results are encouraging, more data is required due to inaccuracies around the intensity threshold.

Changes in electron plasma temperature T_e influence the growth rate when keeping constant $\eta \equiv I_{laser}/I_{thr}^{TPD}(T_e)$. As a result, higher T_e simulations have a higher growth rate. Moreover, the HE energy flux appear to increase with a quadratic behavior, which would justify the linear increase in HE conversion fraction. Overall, a higher temperature shifts the maxwellian bulk towards higher temperatures and fluxes, which allows a higher electron population towards electron velocities that are resonant with the corresponding EPW phase velocities. Moreover,

the decrease in electron-ion damping rate associated to the higher values of T_e implies a reduction in EPW energy absorbed by collisional damping, allowing for more electrons to be accelerated via Landau damping. The HE temperature behavior is similar to the one in the η scaling and almost independent on the electron temperature. Overall, this quantity is the one that gives the highest changes in conversion fraction, due to its influence in all the laser plasma instabilities.

The ion-electron temperature ratio changes the behavior of turbulence in the system. A root-like increase takes place for both the HE energy flux and conversion fraction, enhancing HE production, but with a reduced HE temperature, due to a lower staged acceleration of the HE population. This reduction in temperature has been attributed to the lower LDI activity, and therefore weaker turbulence, generating less low-k, high phase velocity EPW modes, which are responsible for acceleration of HEs at higher energies.

Finally, no significant differences were observed in both HE fraction and flux for different values of the density scale length L_n. It has been observed that the interaction region enlarges for longer plasmas, as expected from theory. However, at constant η raising the density scale length implies a lower laser intensity as well. The energy in the HE tail becomes repartitioned towards higher temperatures, due to a longer interaction region that allows for higher energies to be reached by the HEs through better staged acceleration. As a result, there is an increase in HE temperature in this case.

Both the TPD and SRS+TPD scaling analyses show the same qualitative behavior even though the SRS+TPD ones do seem to reach lower values of HE conversion fraction and energy flux. The HE temperatures on the other hand show a small increase, due to a higher LDI activity. Moreover, while in the TPD only case the scaling laws of only singular parameters were established, a simple multi-variable scaling law model has been proposed for the SRS+TPD simulation, which encompassed every quantity of the scaling. The results appear promising, but this has been a preliminary analysis, and more work is required in deriving the form of such scaling law.

After setting up the databases for both the TPD only and SRS+TPD cases, comparisons between simulations belonging to the scaling databases and the ones with additional physical effects have been made.

For the TPD only case, a comparison between 2D and 3D simulations has been carried out. The first comparisons have been made between two simulations, one in 2D and one in 3D, about HE quantities. These have been done with laser pump depletion turned on, and for this reason a full 3D scaling with pump depletion on was not possible due to the excessive computational costs. One result was that, by observation of the EPW fields, the TPD instability mainly occurs onto a plane even in a 3D space. The HE conversion fraction that has been obtained through the fits reported a small relative decrease of about $\simeq 20\%$, while the HE temperature decreased by $\sim 10\%$. Moreover, a scaling of 3D TPD without laser pump depletion has been performed and compared with its 2D counterpart. The results show similar values in HE fraction at low T_i/T_e, while several 2D simulations diverge in the high T_i/T_e case. However, the 3D ones reach stable HE fractions even without pump depletion. Overall the HE temperature does not possess a definite trend, but tends to stay in a similar interval for low T_i/T_e, while they decrease in the 3D case for high T_i/T_e. Overall, these comparisons suggest that a scaling of the 3D system, albeit computationally expensive, may be beneficial in converging the HE conversion fraction, despite the small changes due to the 2D nature of TPD.

Finally, In the SRS+TPD case, an additional scaling analysis has been made for p-polarized light in long plasmas, reaching plasma conditions at the National Ignition Facility (NIF) rather than the rest of the previous analysis which focused on OMEGA like conditions. The results of the HE energy flux were similar to the ones at shorter plasmas (i.e. lower L_n), with a reduction by about a factor of 4. Moreover, the HE conversion fractions have been observed to be similar in value to the OMEGA case, which would suggest that TPD is the dominant instability even in this case. However, this is in direct contrast with experiments, where SRS has been observed

to dominate. We therefore infer that the introduction of a scaling for s-polarized light might be important to characterize HE generation from SRS in a better way, which further justifies the need to carry out a scaling in 3D, with both SRS and TPD.

5.4 Comparison with PIC code SMILEI and literature.

A comparison between LPSE simulations and other codes has been performed for the 2D SRS+TPD case. A simulation with the PIC code SMILEI has been carried out (courtesy of Olimpia Budriga, National Institute for Laser, Romania). Several aspects have been found to agree with the LPSE simulations, such as the density profile and the emission angle. As far as the electron energy flux is concerned, there is a similar profile for the plasma bulk and for the HE tail up to 200 keV, after which the two simulation codes tend to disagree, with SMILEI reporting a lower tail. Moreover, LPSE shows to overpredict HE generation. The lower HE fractions in SMILEI might be caused by the additional physics considered in PIC codes, such as the generation of fields from the macroparticles, which interfere with the EPW field in the plasma.

Finally, a comparison with the literature has been done to further verify the validity of the data from LPSE. A comparison has been made with publisher results from the PIC code EPOCH, which returned a similar HE conversion fraction and temperature with the conditions in the study [57], as well as from several experiments in both OMEGA [43, 48, 49] and NIF [63]. Some experiments gave comparisons with the HE data within the same order of magnitude, resulting in a promising outcome for the LPSE scaling, while other gave different result similarly to the SMILEI comparison. Overall, more refined effects must be taken into account, one of which is smoothing by spectral dispersion (SSD), which has been observed to dramatically reduce the HE conversion fraction [43].

5.5 Perspectives for the future

The scaling analysis, databases and scaling laws for both TPD and SRS+TPD presented in this work are still in a simplified physical context. Every simulation has been done with a single plane wave laser beam irradiating a single ion plasma with an equivalent atomic mass and charge of CH. This laser has always been considered in p-polarization and the plasma always with a linear density gradient. For the purposes of hot electron generation, further effort will be required to introduce more detailed physical phenomena to the system and closely match the HE simulation results to the literature. We summarize here the possible modification that can be made to the scaling analysis presented in this work in order to obtain a close matching to the rest of literature.

- **3D simulations.** As shown in this work, a change in dimensions reduces the HE generation from TPD, but the qualitative HE behavior remains approximately the same. This means that a reduced scaling of SRS+TPD in 3D, with laser pump depletion, could be used to calculate reduction coefficients when passing from 2D to 3D. These coefficients could then be used on the 2D data to extrapolate what the 3D ones would be, without the need to perform the complete scaling analysis in 3D.

- **Different wavelengths.** The OMEGA and NIF facilities use Nd-YAG lasers which are frequency tripled to the third harmonic before entering the laser chamber, resulting into a laser wavelength of $\lambda_0 = 0.351$ μm. However, several private Inertial Fusion Energy companies are considering frequency doubling to the second harmonic in order to lower damage on optics at high repetition rates. Therefore, a comparison of different laser wavelengths could be considered as well. This would change the LPIs thresholds and

growth rates, resulting in a different level of HE generation. While these dependencies are already present in the set of input parameters, the results should be verified.

- **Different ion species.** Changes in plasma ion species, corresponding to a change in the ablator shell material of the ICF target, can modify HE generation by acting on the EPWs and IAWs damping rates. While CH is considered at the present time as the material that generates the most HEs, alongside pure C, it may be worth looking into different materials for HE mitigation purposes such as Si. LPSE is a code that assumes a single effective ion species, therefore the changes that could be measured would be as a function of $Z_{eff} \equiv \langle Z^2 \rangle / \langle Z \rangle$.

- **Polarization effects.** The effects of laser polarization are needed to better describe the evolution of SRS as well. While p-polarization allows to observe the evolution of TPD, simulations considering s-polarization should be introduced in order to better observe the behavior of SRS, which is especially important in long plasmas at NIF-like conditions. In a more complete way, one could also think to introduce polarization smoothing to the system, and observe the competition of the instabilities when both polarizations are at play.

- **Speckles and Smoothing by Spectral Dispersion.** In this work we have neglected the speckle pattern of real ICF beams and produced by smoothing phase plates. The speckles may change HE generation due to the instabilities developing in the speckle more rapidly. The LPIs growth may also be limited by the speckle lifetime of a few picoseconds, induced by the Smoothing by Spectral Dispersion (SSD) system, which introduces speckle dephasing through variations the laser frequency. Comparisons with the literature in chapter 4 showed that a speckled beam does not significantly change HE generation in this particular case. However, one could argue that HE generation might be affected in different conditions, since the introduction of speckles implies HEs could be produced even for simulations with intensities below the LPIs' threshold. Moreover, the introduction of SSD shows a clear reduction in HE conversion fraction. Therefore, introducing a speckled beam and SSD could lead to a reduction of this work's HE fraction results. The laser drive strength presumably would take into account speckle influence by considering their probability distribution in the definition of η, as well as introducing a correcting term that takes into account the effects of SSD as a function of the speckle lifetime.

- **Broadband effects.** The introduction of an interval of frequencies in the laser light is able to raise the instabilities' intensity threshold, therefore lowering LPIs and HE generation. The effect can be introduced in this work's scaling analysis by modifying the calculation of the TPD intensity threshold. This would lower I_{thr}^{TPD}, therefore resulting into the same HE scaling as in this work, but with the data shifting towards higher values of η. However, the possibility of broadband effects influencing HE generation should not be underestimated, and should be investigated.

- **Multibeam effects.** The laser setup in this work has been done with one single laser beam. The effects of multiple beams overlapping with each other could be considered as well. This is once more an effect that could be applied to the laser drive strength, in particular on the laser intensity. However, multibeam effects have been shown in the literature to influence the intensity thresholds as well, and therefore should be treated accordingly.

Overall, one could decide to integrate some of these effects in the current 2D scaling analysis made in this work. Here we propose an illustrative formula that could include all the previous

phenomena:

$$f_{HE} = f_{HE,2D}\left(Z_{eff}, T_e, \frac{T_i}{T_e}, L_n, \hat{\eta}(\lambda_0)\right)\chi_{3D}F_{SSD}(\tau_{speckles}), \tag{5.1a}$$

$$\hat{\eta} = \frac{\sum I_{laser}}{I_{thr}^{TPD}(N, \delta\omega/\omega_0)}F_{speckles}, \tag{5.1b}$$

where $f_{HE,2D}$ is the SRS+TPD scaling proposed in this work, depending on both the laser-plasma conditions we discussed but which would have to be expanded for, and the ion species Z_{eff}, χ_{3D} is a correction factor resulting from the 3D reduced scaling and F_{SSD} is a correction term applied for simulations using SSD, which is a function of the speckle lifetime. Moreover, the drive strength $\hat{\eta}(\lambda_0)$, depending on a different laser wavelength, would be modified as specified before, with a sum of the single beam laser intensities to take into account multibeam effects, a TPD intensity threshold (the one we used in our scaling, but it could also be referred to the SRS threshold), depending on both multibeam effects (where N is the number of beams) and broadband effects $\delta\omega_0$, and $F_{speckles}$ would take into account the speckle probability distribution in the laser signal.

Once a robust formula including the sufficient physics contribution is derived and validated, the next step is the inclusion of the scaling law into hydrodynamic codes for inline HE generation, which would in part allow for a better comparison to experiments by accounting for the evolution in time of the hydrodynamics parameters.

Bibliography

[1] AB Zylstra, AL Kritcher, OA Hurricane, DA Callahan, JE Ralph, DT Casey, A Pak, OL Landen, B Bachmann, KL Baker, et al. Experimental achievement and signatures of ignition at the national ignition facility. *Physical Review E*, 106(2):025202, 2022.

[2] AL Kritcher, AB Zylstra, DA Callahan, OA Hurricane, CR Weber, DS Clark, CV Young, JE Ralph, DT Casey, A Pak, et al. Design of an inertial fusion experiment exceeding the lawson criterion for ignition. *Physical Review E*, 106(2):025201, 2022.

[3] John Nuckolls, Lowell Wood, Albert Thiessen, and George Zimmerman. Laser compression of matter to super-high densities: Thermonuclear (ctr) applications. *Nature*, 239(5368): 139–142, 1972.

[4] Stefano Atzeni and Jürgen Meyer-ter Vehn. *The physics of inertial fusion: beam plasma interaction, hydrodynamics, hot dense matter*, volume 125. OUP Oxford, 2004.

[5] RS Craxton, KS Anderson, TR Boehly, VN Goncharov, DR Harding, JP Knauer, RL McCrory, PW McKenty, DD Meyerhofer, JF Myatt, et al. Direct-drive inertial confinement fusion: A review. *Physics of Plasmas*, 22(11):110501, 2015.

[6] JR Freeman, MJ Clauser, and SL Thompson. Rayleigh-taylor instabilities in inertial-confinement fusion targets. *Nuclear Fusion*, 17(2):223, 1977.

[7] David H Sharp. An overview of rayleigh-taylor instability. *Physica D: Nonlinear Phenomena*, 12(1-3):3–18, 1984.

[8] JD Kilkenny, SG Glendinning, SW Haan, BA Hammel, JD Lindl, D Munro, BA Remington, SV Weber, JP Knauer, and CP Verdon. A review of the ablative stabilization of the rayleigh–taylor instability in regimes relevant to inertial confinement fusion. *Physics of Plasmas*, 1(5):1379–1389, 1994.

[9] R Betti, VN Goncharov, R áL McCrory, and C áP Verdon. Growth rates of the ablative rayleigh–taylor instability in inertial confinement fusion. *Physics of Plasmas*, 5(5):1446–1454, 1998.

[10] D Pesme, S Hüller, J Myatt, C Riconda, A Maximov, VT Tikhonchuk, C Labaune, J Fuchs, S Depierreux, and HA Baldis. Laser–plasma interaction studies in the context of megajoule lasers for inertial fusion. *Plasma physics and controlled fusion*, 44(12B):B53, 2002.

[11] A Bruce Langdon and Barbara F Lasinski. Filamentation and subsequent decay of laser light in plasmas. *Physical Review Letters*, 34(15):934, 1975.

[12] F Califano, R Prandi, F Pegoraro, and SV Bulanov. Nonlinear filamentation instability driven by an inhomogeneous current in a collisionless plasma. *Physical Review E*, 58(6): 7837, 1998.

[13] P Kaw, G Schmidt, and T Wilcox. Filamentation and trapping of electromagnetic radiation in plasmas. *The Physics of Fluids*, 16(9):1522–1525, 1973.

[14] William L Kruer, Scott C Wilks, Bedros B Afeyan, and Robert K Kirkwood. Energy transfer between crossing laser beams. *Physics of Plasmas*, 3(1):382–385, 1996.

[15] P Michel, L Divol, EA Williams, S Weber, CA Thomas, DA Callahan, SW Haan, JD Salmonson, S Dixit, DE Hinkel, et al. Tuning the implosion symmetry of icf targets via controlled crossed-beam energy transfer. *Physical review letters*, 102(2):025004, 2009.

[16] IV Igumenshchev, DH Edgell, VN Goncharov, JA Delettrez, AV Maximov, JF Myatt, W Seka, A Shvydky, S Skupsky, and C Stoeckl. Crossed-beam energy transfer in implosion experiments on omega. *Physics of Plasmas*, 17(12):122708, 2010.

[17] Marshall N Rosenbluth. Parametric instabilities in inhomogeneous media. *Physical Review Letters*, 29(9):565, 1972.

[18] CS Liu, Marshall N Rosenbluth, and Roscoe B White. Raman and brillouin scattering of electromagnetic waves in inhomogeneous plasmas. *The Physics of Fluids*, 17(6):1211–1219, 1974.

[19] CS Liu and Marshall N Rosenbluth. Parametric decay of electromagnetic waves into two plasmons and its consequences. *The Physics of Fluids*, 19(7):967–971, 1976.

[20] Liang Lu. Framework of parametric instabilities in the presence of space-time fluctuations in homogeneous and inhomogenous plasmas. i. theory. *The Physics of fluids*, 31(11):3362–3370, 1988.

[21] BB Afeyan and EA Williams. Stimulated raman sidescattering with the effects of oblique incidence. *The Physics of fluids*, 28(11):3397–3408, 1985.

[22] JA Heikkinen and SJ Karttunen. Intensity saturation of stimulated raman scattering by ion-wave coupling. *The Physics of fluids*, 29(4):1291–1297, 1986.

[23] P Michel, L Divol, EL Dewald, JL Milovich, M Hohenberger, OS Jones, L Berzak Hopkins, RL Berger, WL Kruer, and JD Moody. Multibeam stimulated raman scattering in inertial confinement fusion conditions. *Physical review letters*, 115(5):055003, 2015.

[24] Seppo J Karttunen. Ion fluctuation effects on the two-plasmon decay and stimulated raman scattering. *Physical Review A*, 23(4):2006, 1981.

[25] DF DuBois, DA Russell, and Harvey A Rose. Saturation spectra of the two-plasmon decay instability. *Physical review letters*, 74(20):3983, 1995.

[26] S Weber, C Riconda, O Klimo, A Heron, and VT Tikhonchuk. Fast saturation of the two-plasmon-decay instability for shock-ignition conditions. *Physical Review E*, 85(1):016403, 2012.

[27] HX Vu, DF DuBois, DA Russell, JF Myatt, and J Zhang. Nonlinear development of the two-plasmon decay instability in three dimensions. *Physics of Plasmas*, 21(4):042705, 2014.

[28] D Turnbull, AV Maximov, DH Edgell, W Seka, RK Follett, JP Palastro, D Cao, VN Goncharov, C Stoeckl, and DH Froula. Anomalous absorption by the two-plasmon decay instability. *Physical Review Letters*, 124(18):185001, 2020.

[29] BH Ripin, FC Young, JA Stamper, CM Armstrong, R Decoste, EA McLean, and SE Bodner. Enhanced backscatter with a structured laser pulse. *Physical Review Letters*, 39(10): 611, 1977.

[30] DW Phillion, WL Kruer, and VC Rupert. Brillouin scatter in laser-produced plasmas. *Physical Review Letters*, 39(24):1529, 1977.

[31] S Hüller, P Mulser, and AM Rubenchik. Nonstationary stimulated brillouin backscattering. *Physics of Fluids B: Plasma Physics*, 3(12):3339–3352, 1991.

[32] S Hüller. Stimulated brillouin scattering off nonlinear ion acoustic waves. *Physics of Fluids B: Plasma Physics*, 3(12):3317–3330, 1991.

[33] NA Ebrahim, HA Baldis, C Joshi, and R Benesch. Hot electron generation by the two-plasmon decay instability in the laser-plasma interaction at 10.6 μm. *Physical Review Letters*, 45(14):1179, 1980.

[34] A Bruce Langdon. Nonlinear inverse bremsstrahlung and heated-electron distributions. *Physical Review Letters*, 44(9):575, 1980.

[35] Barukh Yaakobi, Christian Stoeckl, Thomas Boehly, DD Meyerhofer, and W Seka. Measurement of preheat due to fast electrons in laser implosions. *Physics of Plasmas*, 7(9): 3714–3720, 2000.

[36] VA Smalyuk, D Shvarts, R Betti, JA Delettrez, DH Edgell, V Yu Glebov, VN Goncharov, RL McCrory, DD Meyerhofer, PB Radha, et al. Role of hot-electron preheating in the compression of direct-drive imploding targets with cryogenic d 2 ablators. *Physical review letters*, 100(18):185005, 2008.

[37] T Kolber, W Rozmus, and VT Tikhonchuk. Saturation of stimulated raman scattering by langmuir and ion-acoustic wave coupling. *Physics of Fluids B: Plasma Physics*, 5(1): 138–150, 1993.

[38] S Depierreux, J Fuchs, Ch Labaune, A Michard, HA Baldis, D Pesme, S Hüller, and G Laval. First observation of ion acoustic waves produced by the langmuir decay instability. *Physical Review Letters*, 84(13):2869, 2000.

[39] S Depierreux, C Labaune, J Fuchs, D Pesme, VT Tikhonchuk, and HA Baldis. Langmuir decay instability cascade in laser-plasma experiments. *Physical review letters*, 89(4): 045001, 2002.

[40] Vladimir E Zakharov et al. Collapse of langmuir waves. *Sov. Phys. JETP*, 35(5):908–914, 1972.

[41] Martin V Goldman. Strong turbulence of plasma waves. *Reviews of modern physics*, 56 (4):709, 1984.

[42] R Betti, CD Zhou, KS Anderson, LJ Perkins, W Theobald, and AA Solodov. Shock ignition of thermonuclear fuel with high areal density. *Physical review letters*, 98(15): 155001, 2007.

[43] W Theobald, A Bose, R Yan, R Betti, M Lafon, D Mangino, AR Christopherson, C Stoeckl, W Seka, W Shang, et al. Enhanced hot-electron production and strong-shock generation in hydrogen-rich ablators for shock ignition. *Physics of Plasmas*, 24(12):120702, 2017.

[44] WL Shang, R Betti, SX Hu, K Woo, L Hao, C Ren, AR Christopherson, A Bose, and W Theobald. Electron shock ignition of inertial fusion targets. *Physical review letters*, 119 (19):195001, 2017.

[45] William Kruer. *The physics of laser plasma interactions*. crc Press, 2019.

[46] Shalom Eliezer. *The interaction of high-power lasers with plasmas*. CRC press, 2002.

[47] Susanne Pfalzner. *An introduction to inertial confinement fusion*. CRC Press, 2006.

[48] W Theobald, R Nora, W Seka, M Lafon, KS Anderson, M Hohenberger, FJ Marshall, DT Michel, AA Solodov, C Stoeckl, et al. Spherical strong-shock generation for shock-ignition inertial fusion. *Physics of Plasmas*, 22(5):056310, 2015.

[49] R Nora, W Theobald, R Betti, FJ Marshall, DT Michel, W Seka, B Yaakobi, M Lafon, C Stoeckl, J Delettrez, et al. Gigabar spherical shock generation on the omega laser. *Physical review letters*, 114(4):045001, 2015.

[50] R Betti, AR Christopherson, BK Spears, R Nora, A Bose, J Howard, KM Woo, MJ Edwards, and J Sanz. Alpha heating and burning plasmas in inertial confinement fusion. *Physical review letters*, 114(25):255003, 2015.

[51] AR Christopherson, R Betti, CJ Forrest, J Howard, W Theobald, JA Delettrez, MJ Rosenberg, AA Solodov, C Stoeckl, D Patel, et al. Direct measurements of dt fuel preheat from hot electrons in direct-drive inertial confinement fusion. *Physical Review Letters*, 127(5): 055001, 2021.

[52] MJ Rosenberg, AA Solodov, W Seka, RK Follett, JF Myatt, AV Maximov, C Ren, S Cao, P Michel, M Hohenberger, et al. Stimulated raman scattering mechanisms and scaling behavior in planar direct-drive experiments at the national ignition facility. *Physics of Plasmas*, 27(4):042705, 2020.

[53] HX Vu, DF DuBois, JF Myatt, and DA Russell. Hot-electron production and suprathermal heat flux scaling with laser intensity from the two-plasmon–decay instability. *Physics of Plasmas*, 19(10):102703, 2012.

[54] J Zhang, JF Myatt, RW Short, AV Maximov, HX Vu, DF DuBois, and DA Russell. Multiple beam two-plasmon decay: linear threshold to nonlinear saturation in three dimensions. *Physical Review Letters*, 113(10):105001, 2014.

[55] RK Follett, JG Shaw, JF Myatt, DH Froula, and JP Palastro. Multibeam absolute stimulated raman scattering and two-plasmon decay. *Physical Review E*, 101(4):043214, 2020.

[56] Yan-Jun Gu, O Klimo, VT Tikhonchuk, and S Weber. Multi-dimensional kinetic simulations of laser radiation absorption and electron acceleration in inhomogeneous underdense plasma. *Nuclear Fusion*, 61(6):066014, 2021.

[57] AG Seaton and TD Arber. Laser-plasma instabilities in long scale-length plasmas relevant to shock-ignition. *Physics of Plasmas*, 27(8):082704, 2020.

[58] A Colaïtis, X Ribeyre, E Le Bel, G Duchateau, Ph Nicolaï, and V Tikhonchuk. Influence of laser induced hot electrons on the threshold for shock ignition of fusion reactions. *Physics of Plasmas*, 23(7):072703, 2016.

[59] A Tentori, Arnaud Colaïtis, W Theobald, A Casner, D Raffestin, A Ruocco, J Trela, E Le Bel, K Anderson, M Wei, et al. Experimental characterization of hot-electron emission and shock dynamics in the context of the shock ignition approach to inertial confinement fusion. *Physics of Plasmas*, 28(10):103302, 2021.

[60] TD Arber, Keith Bennett, CS Brady, A Lawrence-Douglas, MG Ramsay, NJ Sircombe, P Gillies, RG Evans, Holger Schmitz, AR Bell, et al. Contemporary particle-in-cell approach to laser-plasma modelling. *Plasma Physics and Controlled Fusion*, 57(11):113001, 2015.

[61] Sea Agostinelli, John Allison, K al Amako, John Apostolakis, H Araujo, Pedro Arce, Makoto Asai, D Axen, Swagato Banerjee, GJNI Barrand, et al. Geant4—a simulation toolkit. *Nuclear instruments and methods in physics research section A: Accelerators, Spectrometers, Detectors and Associated Equipment*, 506(3):250–303, 2003.

[62] Jason F Myatt, John G Shaw, Russell K Follett, Dana H Edgell, Dustin H Froula, John P Palastro, and Valeri N Goncharov. Lpse: A 3-d wave-based model of cross-beam energy transfer in laser-irradiated plasmas. *Journal of Computational Physics*, 399:108916, 2019.

[63] MJ Rosenberg, AA Solodov, JF Myatt, W Seka, P Michel, M Hohenberger, RW Short, R Epstein, SP Regan, EM Campbell, et al. Origins and scaling of hot-electron preheat in ignition-scale direct-drive inertial confinement fusion experiments. *Physical review letters*, 120(5):055001, 2018.

[64] S Weber and C Riconda. Temperature dependence of parametric instabilities in the context of the shock-ignition approach to inertial confinement fusion. *High Power Laser Science and Engineering*, 3, 2015.

[65] A Colaïtis, G Duchateau, X Ribeyre, Y Maheut, G Boutoux, L Antonelli, Ph Nicolaï, D Batani, and V Tikhonchuk. Coupled hydrodynamic model for laser-plasma interaction and hot electron generation. *Physical Review E*, 92(4):041101, 2015.

[66] Gianluca Pucella and Sergio E Segre. *Fisica dei plasmi*. Zanichelli, 2010.

[67] John D Lawson. Some criteria for a power producing thermonuclear reactor. *Proceedings of the physical society. Section B*, 70(1):6, 1957.

[68] Nikita Anatolievich Popov, Viktor Alekseevich Shcherbakov, Vladimir N Mineev, Robert Meerovich Zaidel, and Aleksandr I Funtikov. Thermonuclear fusion in the explosion of a spherical charge (the problem of a gas-dynamic thermonuclear fusion). *Physics-Uspekhi*, 51(10):1047, 2008.

[69] L John Perkins, R Betti, KN LaFortune, and WH Williams. Shock ignition: A new approach to high gain inertial confinement fusion on the national ignition facility. *Physical review letters*, 103(4):045004, 2009.

[70] Max Tabak, James Hammer, Michael E Glinsky, William L Kruer, Scott C Wilks, John Woodworth, E Michael Campbell, Michael D Perry, and Rodney J Mason. Ignition and high gain with ultrapowerful lasers. *Physics of Plasmas*, 1(5):1626–1634, 1994.

[71] Max Tabak, DS Clark, SP Hatchett, MH Key, BF Lasinski, RA Snavely, SC Wilks, RPJ Town, R Stephens, EM Campbell, et al. Review of progress in fast ignition. *Physics of Plasmas*, 12(5):057305, 2005.

[72] DH Froula, DT Michel, IV Igumenshchev, SX Hu, B Yaakobi, JF Myatt, DH Edgell, R Follett, V Yu Glebov, VN Goncharov, et al. Laser–plasma interactions in direct-drive ignition plasmas. *Plasma Physics and Controlled Fusion*, 54(12):124016, 2012.

[73] R Bingham, R Short, E Williams, D Villeneuve, and MC Richardson. The filamentation instability at short wavelengths. *Plasma physics and controlled fusion*, 26(9):1077, 1984.

[74] A Colaïtis, G Duchateau, X Ribeyre, and V Tikhonchuk. Modeling of the cross-beam energy transfer with realistic inertial-confinement-fusion beams in a large-scale hydrocode. *Physical Review E*, 91(1):013102, 2015.

[75] JF Myatt, RK Follett, JG Shaw, DH Edgell, DH Froula, IV Igumenshchev, and VN Goncharov. A wave-based model for cross-beam energy transfer in direct-drive inertial confinement fusion. *Physics of Plasmas*, 24(5):056308, 2017.

[76] AM Hansen, KL Nguyen, D Turnbull, BJ Albright, RK Follett, R Huff, J Katz, D Mastrosimone, AL Milder, L Yin, et al. Cross-beam energy transfer saturation: ion heating and pump depletion. *Plasma Physics and Controlled Fusion*, 64(3):034003, 2022.

[77] AG Seaton, L Yin, RK Follett, BJ Albright, and A Le. Cross-beam energy transfer in direct-drive icf. i. nonlinear and kinetic effects. *Physics of Plasmas*, 29(4):042706, 2022.

[78] DP Turnbull, IV Igumenschev, D Edgell, RC Shah, OM Mannion, C Stoeckl, D Jacob-Perkins, A Shvydky, R Janezic, et al. 3d simulations capture the persistent low-mode asymmetries evident in laser-direct-drive implosions on omega. *Physical Review Letters*, 129(9):095001, 2022.

[79] Jean-Paul Watteau. La fusion thermonucléaire inertielle par laser: l'interaction laser-matière, vol. 1, partie 1. Technical report, P00020745, 1993.

[80] JF Drake and YC Lee. Temporally growing raman backscattering instabilities in an inhomogeneous plasma. *Physical Review Letters*, 31(19):1197, 1973.

[81] A Simon, RW Short, EA Williams, and T Dewandre. On the inhomogeneous two-plasmon instability. *The Physics of fluids*, 26(10):3107–3118, 1983.

[82] JP Palastro, EA Williams, DE Hinkel, L Divol, and DJ Strozzi. Kinetic dispersion of langmuir waves. i. the langmuir decay instability. *Physics of Plasmas*, 16(9):092304, 2009.

[83] DF DuBois and HA Rose. Statistical theories of langmuir turbulence. i. direct-interaction-approximation responses. *Physical Review A*, 24(3):1476, 1981.

[84] HX Vu, DF DuBois, DA Russell, and JF Myatt. Hot-electron generation by "cavitating" langmuir turbulence in the nonlinear stage of the two-plasmon–decay instability. *Physics of Plasmas*, 19(10):102708, 2012.

[85] DW Forslund, JM Kindel, and EL Lindman. Theory of stimulated scattering processes in laser-irradiated plasmas. *The Physics of Fluids*, 18(8):1002–1016, 1975.

[86] JS DeGroot and JE Tull. Heated electron distributions from resonant absorption. *The Physics of Fluids*, 18(6):672–678, 1975.

[87] JR Albritton and AB Langdon. Profile modification and hot-electron temperature from resonant absorption at modest intensity. *Physical Review Letters*, 45(22):1794, 1980.

[88] JP Palastro, JG Shaw, RK Follett, A Colaïtis, D Turnbull, AV Maximov, VN Goncharov, and DH Froula. Resonance absorption of a broadband laser pulse. *Physics of Plasmas*, 25 (12):123104, 2018.

[89] Duncan Barlow, T Goffrey, K Bennett, RHH Scott, K Glize, W Theobald, K Anderson, AA Solodov, MJ Rosenberg, M Hohenberger, et al. Role of hot electrons in shock ignition constrained by experiment at the national ignition facility. *Physics of Plasmas*, 29(8): 082704, 2022.

[90] Arnaud Colaitis. Multi-scale description of the laser-plasma interaction: application to the physics of shock ignition in inertial confinement fusion. Technical report, Université de Bordeaux, 2015.

[91] Julien Derouillat, Arnaud Beck, Frédéric Pérez, Tommaso Vinci, M Chiaramello, Anna Grassi, M Flé, Guillaume Bouchard, I Plotnikov, Nicolas Aunai, et al. Smilei: A collaborative, open-source, multi-purpose particle-in-cell code for plasma simulation. *Computer Physics Communications*, 222:351–373, 2018.

[92] James Clerk Maxwell. Viii. a dynamical theory of the electromagnetic field. *Philosophical transactions of the Royal Society of London*, (155):459–512, 1865.

[93] Oliver Heaviside. Xi. on the forces, stresses, and fluxes of energy in the electromagnetic field. *Philosophical Transactions of the Royal Society of London.(A.)*, (183):423–480, 1892.

[94] J Willard Gibbs. Velocity of propagation of electrostatic force. *Nature*, 53(1379):509–509, 1896.

[95] H.A. Lorentz. *Proc. Amsterdam, Enc. Math. Wiss., V 2, Heft. 1, S.200*, 254, 1902.

[96] Leon Rosenfeld. Theory of electrons. 1951.

[97] P Mazur and BRA Nijboer. On the statistical mechanics of matter in an electromagnetic field. i: Derivation of the maxwell equations from electron theory. *Physica*, 19(1-12): 971–986, 1953.

[98] SR De Groot. The maxwell equations: Nonrelativistic multipole expansion to all orders. *Physica*, 31(6):953–958, 1965.

[99] G Russakoff. A derivation of the macroscopic maxwell equations. *American Journal of Physics*, 38(10):1188–1195, 1970.

[100] Lord Rayleigh. Vii. on electrical vibrations and the constitution of the atom. *The London, Edinburgh, and Dublin Philosophical Magazine and Journal of Science*, 11(61):117–123, 1906.

[101] Irving Langmuir. Oscillations in ionized gases. *Proceedings of the National Academy of Sciences*, 14(8):627–637, 1928.

[102] Lewi Tonks and Irving Langmüir. Oscillations in ionized gases. In *Plasma and Oscillations*, pages 122–139. Elsevier, 1961.

[103] William Crookes. V. the bakerian lecture.—on the illumination of lines of molecular pressure, and the trajectory of molecules. *Philosophical Transactions of the Royal Society of London*, (170):135–164, 1879.

[104] Nicholas A Krall and Alvin W Trivelpiece. Principles of plasma physics. *American Journal of Physics*, 41(12):1380–1381, 1973.

[105] Ludvik Martinu and Daniel Poitras. Plasma deposition of optical films and coatings: A review. *Journal of Vacuum Science & Technology A: Vacuum, Surfaces, and Films*, 18(6): 2619–2645, 2000.

[106] Mounir Laroussi. Low-temperature plasma jet for biomedical applications: a review. *IEEE transactions on plasma science*, 43(3):703–712, 2015.

[107] Erich Hückel. Zur theorie der elektrolyte. *Ergebnisse der exakten Naturwissenschaften*, pages 199–276, 1924.

[108] Hideki Yukawa. On the interaction of elementary particles. i. *Progress of Theoretical Physics Supplement*, 1:1–10, 1955. URL https://doi.org/10.1143/PTPS.1.1.

[109] Ernest Rutherford. Lxxix. the scattering of α and β particles by matter and the structure of the atom. *The London, Edinburgh, and Dublin Philosophical Magazine and Journal of Science*, 21(125):669–688, 1911.

[110] LC Woods. *The Particle Kinetics of Plasmas. By IP SHKAROFSKY, TW JOHNSTON and MP BACHYNSKI. Addison-Wesley, 1966. 35.00.*, volume 50. Cambridge University Press, 1971.

[111] SI Braginskii. Transport phenomena in a completely ionized two-temperature plasma. *Sov. Phys. JETP*, 6(33):358–369, 1958.

[112] SI Braginskii and MA Leontovich. Reviews of plasma physics, 1965.

[113] Mitsuru Honda. Coulomb logarithm formulae for collisions between species with different temperatures. *Japanese Journal of Applied Physics*, 52(10R):108002, 2013.

[114] Pieter PJM Schram and Pieter PJM Schram. *Kinetic theory of gases and plasmas*, volume 46. Springer Science & Business Media, 1991.

[115] Ludwig Boltzmann. *Lectures on gas theory*. Courier Corporation, 2012.

[116] Abraham Bers and Jean-Loup Delcroix. *Physique des plasmas. 2*. EDP Sciences, 2012.

[117] Tudor Wyatt Johnston and John M Dawson. Correct values for high-frequency power absorption by inverse bremsstrahlung in plasmas. *The Physics of Fluids*, 16(5):722–722, 1973. URL https://doi.org/10.1063/1.1694419.

[118] Donald Gary Swanson. *Plasma waves*. Elsevier, 2012.

[119] A Vlasov. On the kinetic theory of an assembly of particles with collective interaction. *Russ. Phys. J.*, 9:25–40, 1945.

[120] Burton D Fried and Samuel D Conte. *The plasma dispersion function: the Hilbert transform of the Gaussian*. Academic Press, 2015.

[121] LD Landau. On electronic plasma oscillations. *J. Phys. USSR*, 10:25, 1946.

[122] Francis F Chen et al. *Introduction to plasma physics and controlled fusion*, volume 1. Springer, 1984.

[123] Takayasu Tanaka. Manley-rowe relations in energy transportsamong plasma waves. *Journal of the Physical Society of Japan*, 60(8):2645–2654, 1991.

[124] D Pesme, G Laval, and R Pellat. Parametric instabilities in bounded plasmas. *Physical Review Letters*, 31(4):203, 1973.

[125] Kyoji Nishikawa. Parametric excitation of coupled waves i. general formulation. *Journal of the physical society of Japan*, 24(4):916–922, 1968.

[126] Kyoji Nishikawa. Parametric excitation of coupled waves. ii. parametric plasmon-photon interaction. *Journal of the Physical Society of Japan*, 24(5):1152–1158, 1968.

[127] AA Galeev and RZ Sagdeev. Parametric phenomena in a plasma. *Nuclear Fusion*, 13(4): 603, 1973.

[128] Abraham Bers. Space-time evolution of plasma instabilities-absolute and convective. In *Basic plasma physics. 1*. 1983.

[129] Richard J Briggs et al. *Electron-stream interaction with plasmas*, volume 187. MIT press Cambridge, MA, 1964.

[130] Edward James Brambley. *The acoustics of curved and lined cylindrical ducts with mean flow*. PhD thesis, University of Cambridge, 2007.

[131] EA Williams and TW Johnston. Phase-inflection parametric instability behavior near threshold with application to laser–plasma stimulated raman scattering (srs) instabilities in exploding foils. *Physics of Fluids B: Plasma Physics*, 1(1):188–194, 1989.

[132] James F Drake, Predhiman K Kaw, Yee-Chun Lee, G Schmid, Chuan S Liu, and Marshall N Rosenbluth. Parametric instabilities of electromagnetic waves in plasmas. *The Physics of Fluids*, 17(4):778–785, 1974.

[133] RK Follett, JG Shaw, JF Myatt, C Dorrer, DH Froula, and JP Palastro. Thresholds of absolute instabilities driven by a broadband laser. *Physics of Plasmas*, 26(6):062111, 2019.

[134] Liang Lu. Framework of parametric instabilities in the presence of space-time fluctuations in homogeneous and inhomogenous plasmas. i. theory. *The Physics of fluids*, 31(11):3362–3370, 1988.

[135] Liang Lu. Framework of the parametric instabilities in the presence of space-time fluctuations in homogeneous and inhomogeneous plasma. ii. applications. *Physics of Fluids B: Plasma Physics*, 1(8):1605–1615, 1989.

[136] Mufei Luo, Stefan Hüller, Min Chen, and Zhengming Sheng. On the role of bandwidth in pump and seed light waves for stimulated raman scattering in inhomogeneous plasmas. *Physics of Plasmas*, 29(3):032102, 2022.

[137] DF DuBois, Bandel Bezzerides, and Harvey A Rose. Collective parametric instabilities of many overlapping laser beams with finite bandwidth. *Physics of Fluids B: Plasma Physics*, 4(1):241–251, 1992.

[138] YC Lee and PK Kaw. Temporal electrostatic instabilities in inhomogeneous plasmas. *Physical Review Letters*, 32(4):135, 1974.

[139] BF Lasinski and AB Langdon. Linear theory of the 2 ω pe instability in inhomongeneous plasmas. *Laser Program Annual Report 1977*, 2:4–49, 1978.

[140] Martin V Goldman. Parametric plasmon-photon interaction: Part i. threshold for amplification of plasmons. *Annals of Physics*, 38(1):95–116, 1966.

[141] Martin V Goldman. Parametric plasmon-photon interactions: Part ii. analysis of plasmon propagator and correlation functions. *Annals of Physics*, 38(1):117–169, 1966.

[142] RK Follett, JG Shaw, JF Myatt, JP Palastro, RW Short, and DH Froula. Suppressing two-plasmon decay with laser frequency detuning. *Physical Review Letters*, 120(13):135005, 2018.

[143] JF Myatt, HX Vu, DF DuBois, DA Russell, J Zhang, RW Short, and AV Maximov. Mitigation of two-plasmon decay in direct-drive inertial confinement fusion through the manipulation of ion-acoustic and langmuir wave damping. *Physics of Plasmas*, 20(5): 052705, 2013.

[144] RK Follett, JA Delettrez, DH Edgell, VN Goncharov, RJ Henchen, J Katz, DT Michel, JF Myatt, J Shaw, AA Solodov, et al. Two-plasmon decay mitigation in direct-drive inertial-confinement-fusion experiments using multilayer targets. *Physical Review Letters*, 116(15):155002, 2016.

[145] RK Follett, H Wen, DH Froula, D Turnbull, and JP Palastro. Independent-hot-spot approach to multibeam laser-plasma instabilities. *Physical Review E*, 105(6):L063201, 2022.

[146] David Turnbull, AV Maximov, Duc Cao, AR Christopherson, DH Edgell, RK Follett, Varchas Gopalaswamy, JP Knauer, JP Palastro, Alex Shvydky, et al. Impact of spatiotemporal smoothing on the two-plasmon–decay instability. *Physics of Plasmas*, 27(10): 102710, 2020.

[147] Russell Follett, Arnaud Colaitis, Dustin Froula, Dana Edgell, David Turnbull, and John Palastro. Validation of ray-based cross-beam energy transfer algorithms. *Bulletin of the American Physical Society*, 2022.

[148] Akira Hasegawa. Stimulated modulational instabilities of plasma waves. *Physical Review A*, 1(6):1746, 1970.

[149] DA Russell and DF DuBois. 3 2 ω 0 radiation from the laser-driven two-plasmon decay instability in an inhomogeneous plasma. *Physical review letters*, 86(3):428, 2001.

[150] R Sagdeev, G Solov'ev, V Shapiro, V Shevchenko, and I Yusupov. Plasma turbulence and dissipation of a strong electromagnetic wave in the vicinity of the n/sub c//4 resonance. *Sov. Phys.-JETP (Engl. Transl.);(United States)*, 55(1), 1982.

[151] Leonid Ivanovič Rudakov and VN Tsytovich. Strong langmuir turbulence. *Physics Reports*, 40(1):1–73, 1978.

[152] R Yan, C Ren, J Li, AV Maximov, WB Mori, Z-M Sheng, and FS Tsung. Generating energetic electrons through staged acceleration in the two-plasmon-decay instability in inertial confinement fusion. *Physical review letters*, 108(17):175002, 2012.

[153] Baolian Cheng, Thomas JT Kwan, Yi-Ming Wang, SA Yi, Steven H Batha, and F Wysocki. Ignition and pusher adiabat. *Plasma Physics and Controlled Fusion*, 60(7):074011, 2018.

[154] Vadim N Tsytovich. Nonlinear effects in a plasma. *Soviet Physics Uspekhi*, 9(6):805, 1967.

[155] Nicolaas Bloembergen and PS Pershan. Light waves at the boundary of nonlinear media. *Physical review*, 128(2):606, 1962.

[156] Sam L Musher, Alexander M Rubenchik, and Vladimir E Zakharov. Weak langmuir turbulence. *Physics Reports*, 252(4):177–274, 1995.

[157] RK Follett, JF Myatt, JG Shaw, DT Michel, AA Solodov, DH Edgell, B Yaakobi, and DH Froula. Simulations and measurements of hot-electron generation driven by the multibeam two-plasmon-decay instability. *Physics of Plasmas*, 24(10):102134, 2017.

[158] TR Boehly, RS Craxton, TH Hinterman, JH Kelly, TJ Kessler, SA Kumpan, SA Letzring, RL McCrory, SFB Morse, W Seka, et al. The upgrade to the omega laser system. *Review of Scientific Instruments*, 66(1):508–510, 1995.

[159] O Klimo and VT Tikhonchuk. Laser–plasma interaction studies in the context of shock ignition: the regime dominated by parametric instabilities. *Plasma Physics and Controlled Fusion*, 55(9):095002, 2013.

[160] AA Solodov, MJ Rosenberg, W Seka, JF Myatt, M Hohenberger, R Epstein, C Stoeckl, RW Short, SP Regan, P Michel, et al. Hot-electron generation at direct-drive ignition-relevant plasma conditions at the national ignition facility. *Physics of Plasmas*, 27(5): 052706, 2020.

[161] AV Maximov, JG Shaw, and JP Palastro. Nonlinear transmission of laser light through coronal plasma due to self-induced incoherence. *Physical Review E*, 102(2):023205, 2020.

[162] M Hohenberger, W Theobald, SX Hu, KS Anderson, R Betti, TR Boehly, A Casner, DE Fratanduono, M Lafon, DD Meyerhofer, et al. Shock-ignition relevant experiments with planar targets on omega. *Physics of Plasmas*, 21(2):022702, 2014.

[163] TR Boehly, VA Smalyuk, DD Meyerhofer, JP Knauer, DK Bradley, RS Craxton, MJ Guardalben, S Skupsky, and TJ Kessler. Reduction of laser imprinting using polarization smoothing on a solid-state fusion laser. *Journal of applied physics*, 85(7):3444–3447, 1999.

[164] S Skupsky, RW Short, T Kessler, RS Craxton, S Letzring, and JM Soures. Improved laser-beam uniformity using the angular dispersion of frequency-modulated light. *Journal of Applied Physics*, 66(8):3456–3462, 1989.

[165] PB Radha, VN Goncharov, TJB Collins, JA Delettrez, Y Elbaz, V Yu Glebov, RL Keck, DE Keller, JP Knauer, JA Marozas, et al. Two-dimensional simulations of plastic-shell, direct-drive implosions on omega. *Physics of Plasmas*, 12(3):032702, 2005.

[166] Iwan Kawrakow. Accurate condensed history monte carlo simulation of electron transport. i. egsnrc, the new egs4 version. *Medical physics*, 27(3):485–498, 2000.